Title
Characterization and simulation of additively manufactured metallic cellular features and components

Permalink
https://escholarship.org/uc/item/6f78q7b0

Author
Dong, Connie Q

Publication Date
2021

University of California
Santa Barbara

Characterization and simulation of additively manufactured metallic cellular features and components

A dissertation submitted in partial satisfaction
of the requirements for the degree

Doctor of Philosophy
in
Materials

by

Connie Q. Dong

Committee in charge:

Professor Matthew R. Begley, Chair
Professor Frédéric Gibou
Professor Tresa M. Pollock
Professor Frank W. Zok

March 2022

The Dissertation of Connie Q. Dong is approved.

Professor Frédéric Gibou

Professor Tresa M. Pollock

Professor Frank W. Zok

Professor Matthew R. Begley, Committee Chair

December 2021

Characterization and simulation of additively manufactured metallic cellular features and components

by

Connie Q. Dong

To Elin F. LaBreck, who really wanted this dedicated to her.

Acknowledgements

I am incredibly grateful to everyone who has helped me over the past years. My advisor, Matthew Begley, has been instrumental towards this work and his guidance and support has been invaluable. I would also like to thank my committee member, Frank Zok, for his indispensible experimental advice and resources. I am grateful to the rest of my committee, Frédéric Gibou and Tresa Pollock, for their insight and expertise. I have been fortunate to collaborate with the Begley, Daly, Gianola, and Zok group members both past and present. Much of the experimental work in this dissertation was done with the assistance and/or advice of Rachel Collino, Avery Samuel, Amanda Ruschel, Glenn Balbus, Paul Shin, Michelle Harr, and Sara Messina. I had a lot of input and guidance for the simulation work from Stephen Sehr, Eric Clough, Leanne Friedrich, and Virginia Collier. I would also like to acknowledge the many lab staff members who have helped me with this research, including Kirk Fields, Joshua Johnson, and David Bothman. Finally, I would thank my family and my fiancé, Mitchell, for their endless support, especially in the many stumbles I've made along the way.

This work was supported by the Air Force Research Laboratory (AFRL) [Contract No. FA8650-16-1-5232.2], the Institute for Collaborative Biotechnologies (ICB) [Contract No. W911NF-09-D-0001], and the Los Alamos National Laboratory (LANL) [Contract No. 521997 and Contract No. 618302]. The work used the Microfluidics Laboratory at the California Nanosystems Institute and the Mechanical Test Lab at UCSB.

Curriculum Vitæ

Connie Q. Dong

Education

2022	Ph.D. in Materials (Expected), University of California, Santa Barbara.
2016	B.Mat.Se. in Materials Science & Engineering, University of Minnesota, Twin Cities.

Publications

C.Q. Dong, R.R. Collino, S.P. Donegan, J.D. Miller, M.R. Begley. *Effective properties for millimeter-scale struts and strut intersections (nodes) fabricated via EBM.* Submitted to *Additive Manufacturing.* 2021.

C.Q. Dong, A.F. Samuel, L.A. Kuettner, B.M. Patterson, C. Montgomery, C.A. Britt, F.W. Zok, A.M. Beese, J.S. Carpenter, M.R. Begley. *Effective geometry and properties of L-PBF stainless steel 316L thin strut intersections (nodes) built with varying processing conditions.* In Preparation. 2021.

C.Q. Dong, A.F. Samuel, M. Leary, F.W. Zok, J.D. Miller, M.R. Begley. *Strain maps and failure analysis of SLM Ti-6Al-4V lattices measured by in situ DIC on a primitive scale.* In Preparation. 2021.

S.A. Messina, **C.Q. Dong**, G.H. Balbus, J.H. Shin, T.M. Pollock, D.S. Gianola, M.R. Begley. *The impact of geometry and microstructure on the failure of milli-meter scale EBM Ti-6Al-4V struts.* In Preparation. 2021.

Abstract

Characterization and simulation of additively manufactured metallic cellular features and components

by

Connie Q. Dong

Additive manufacturing (AM) empowers the creation of novel open-celled architectures that can achieve dramatic performance gains through topology. Lattice structures with millimeter-scale features, specifically, yield the most notable performance gains in applications that require high specific strength and stiffness, enhanced energy absorption ability, and improved heat transfer. For metal AM features at this length scale, process-structure-property relationships become intrinsically linked to geometry because the widths of the struts in the lattices consist of only several melt pools. This process-properties coupling greatly complicates the design and development cycle. One strategy to speed up the design process is to characterize lattice sub-components, or "primitives", and use their effective properties in process-informed models of larger scale structures. To explore the feasibility of this approach, extensive characterization of the effective properties of both lattice primitives and multi-celled lattices is needed.

In this work, experimental and computational techniques are used to advance the understanding of the mechanical response of metal AM lattices. The effective properties needed to predict the response of lattice primitives made of AM Ti-6Al-4V were determined using CT measurements and validated against experimental and FEA. The effective properties are shown to be highly dependent on printed geometry. The methods used to define effective properties are then applied to AM SS316L to quantify the effect of processing conditions upon effective properties of struts and nodes. Samples built with processing conditions that resulted in a higher energy density were found to have increased distributed porosity but not necessarily decreased strength. In addition, thin strut-based samples were found to display increased hardening relative to bulk properties. After understanding how to determine effective properties in struts and nodes, AM Ti-6Al-4V lattices are examined with CT and tested using in situ DIC and evaluated to determine if lattice primitives behave as expected in larger scale lattice structures. The results of these tests demonstrate some unexpected localizations in the lattices, warranting further exploration of local material properties.

This work makes several critical advances towards improving the design of printed lattice structures. Its foremost contribution is a method of determining the effective geometry of printed strut-based structures based on intuitive, direct measurements of the structure from CT. By using this method, the effective mechanical properties can be inferred, and advances in the understanding of the influence of print orientation, processing condition, and sample size upon the mechanical properties of lattice primitives are made. This work also provides insight into the behavior of strut intersections (nodes) in isolation and within lattice structures. Nodal behavior within lattice structures was found to heavily depend upon degree of constraint, orientation within the lattice, and nodal geometry.

Contents

List of Figures

Chapter 1

Introduction

1.1 Motivation

Additive manufacturing enables the creation of novel structures that cannot be easily manufactured via conventional, subtractive means. Notably, AM is an attractive pathway to generate architected cellular such as those shown in Fig. 1.1(a-b), which can obtain dramatic performance gains through topology. This enhancement in performance is especially prominent in structures with millimeter scale features that lead to high specific strength and stiffness, energy adsorption capability and improved heat transfer [24–31]. These properties make AM components attractive across a broad range of industries, from biomedical to aerospace, with a range of applications in medical implants, fuel nozzles, heat pipes, etc.

Metal printing at the millimeter scale inherently creates significant challenges in the design and development of cellular structures. As shown schematically in Fig. 1.1c, powder bed fusion fabrication involves melt pools that are tens to hundreds of microns, such that struts and thin walls in architected materials are limited to a few passes. The interaction between the size of the melt pool and the component feature size leads to

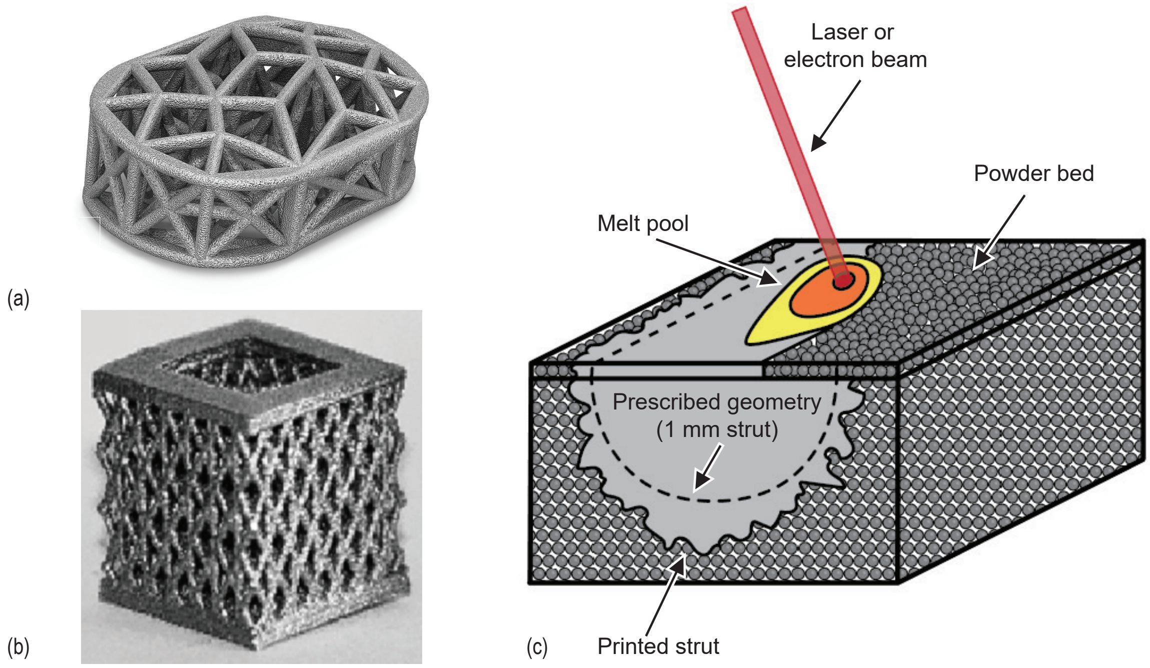

Figure 1.1: (a) EBM Ti6Al4V anterior spine truss system by 4Web Medical [1]. (b) NiTi bone scaffold from Wang, et al. [2]. (c) Schematic displaying creation of a thin-walled structure using powder-bed AM.

heat conduction and solidification pathways that are typically very different from bulk components, leading to strong coupling between material microstructure and component geometry. This coupling represents a paradigm shift in the conceptual framework needed for design; one can no longer assume properties are independent of the geometry of the application. The commonly used term “design for additive manufacturing” refers to the fact that design features often need to be defined specific to a process and its intrinsic constraints.

Strut-based cellular structures enable high impact applications and present a clear opportunity for design for additive manufacturing by limiting the feature space to struts defined only by diameter, length and print orientation, and strut intersections or “nodes”. Conceivably, one can develop libraries of struts mechanical performance that are used in simulation frameworks to account for printing-controlled features, thus capturing the coupling between process and geometry and enabling process-informed designs. Naturally, this strategy requires an understanding of this coupling (i.e. whether it is weak or pronounced – presumably weak coupling can be ignored in simulations) and quantification of the key system features that control this coupling. Further, one must identify effective properties of the struts that can be used as inputs in simulations; i.e., effective size (printing often does not reproduce input geometry), modulus, yield strength, hardening, fracture strain, defect densities, etc.

While this approach is broadly discussed, there is a critical need to establish quantitative links between geometry, effective properties and performance in millimeter scale struts. This requires extensive simultaneous characterization of strut shape (including surface defect geometry) and mechanical response, such that effective properties controlling strut response can be identified, understood, and tabulated for simulation frameworks. This is the focus of this dissertation. Following an introduction into additive manufacturing in Section 1.2, a primer on surface roughness in metal powder-bed AM in Section 1.3, and a description of prior studies on architected cellular structures in Section 1.4 (both provide background context), the scope of the work and key focus areas are outlined in Section 1.5.

1.2 Additive manufacturing

In powder-bed AM, a high energy beam selectively melts a pattern into a layer of metal powder in a manner dictated by a computer aided design (CAD) file. This layer of powder is usually several powder particles thick. The build platform upon which the powder rests upon is then lowered and a new layer of metal powder is raked over the previous layer. The process then repeats so the “slices” of the final product are cumulatively built until complete. After the build is complete, the excess, unmelted powder is removed through high-pressure blowing [4, 32].

There are two main techniques in powder-bed AM – electron beam melting (EBM) and selective laser melting (SLM). SLM is also known as laser powder bed fushion (L-PBF). The main difference between the techniques is their power source; EBM utilizes electron beams while SLM uses laser beams. Because of this difference in power source, the resultant operating environment between the techniques are different. In EBM, a high vacuum environment is necessary to maintain the strength of the electron beam. Additionally, the powder bed is usually preheated to a temperature that is roughly 80% of the melt temperature (usually 600–1000 °C) of the powder and that temperature is maintained throughout the process. SLM operates in an inert gas environment and the build plate is heated no more than 200 °C, which is considerably lower than the build temperature in EBM. EBM is usually faster than SLM because of the higher power of the electron beam. The powder particles in EBM tend to be larger, resulting in rougher builds as compared to those built via SLM [4, 18, 32].

Powder-bed AM has been mostly used to print objects made from titanium alloys, specifically Ti-6Al-4V, though it is slowly becoming more popular to print with other alloys based on steel, nickel, or aluminium. The work in this dissertation focuses primarily on parts built from EBM and SLM Ti6Al4V and SLM stainless steel 316L (SS316L) but the findings and methedology are broadly applicable toward other metal powder-bed AM systems. Ti6Al4V is popular because of its high specific strength, low density, corrosion resistance, relatively low elastic modulus, and proven biocompatibility [4, 5, 8, 18, 33–38]. SS316L can be viewed as an alternative to Ti6Al4V due to its lower cost, higher ductility, and lower sensitivity to residual stress and cracking [39]. The broad majority of the literature reports on the microstructure and mechanical properties of Ti6Al4V [4,8,18,32].

Processing parameters in powder-bed AM have been shown to significantly influence the resultant microstructure, and thus properties, of the printed metal components.

Machine parameters, such as power and velocity, and other variables, such as preheat temperature and postprocessing heat treatment, influence the cooling rates during and after solidification of the part [18]. Because of this process-properties relationship, there have been several studies focused on controlling resultant microstructure through various scan strategies and remelting techniques [40–43]. However, these techniques for microstructural control rely on heat transfer through multiple build layers, which is not a luxury thin parts possess, since they have dimensions on the order of the widths of several melt pools, as illustrated in the schematic in 1.1(c). Additionally, thin parts have been demonstrated to have significantly different microstructure and mechanical properties than bulk parts as a result of differences in printing strategies and solidification pathways [22, 44–48]. It is thus integral to characterize thin-walled parts directly when trying to connect processing parameters to properties.

Studies trying to connect resultant properties to processing parameters have primarily focused on the effect of power, scanning speed, scanning strategy, layer thickness, and hatch distance [12, 49–55]. Initially, researchers have commonly focused on assessing the stability of scan tracks based on a performance matrix of power and scan speed to develop ideal process windows for fully dense parts [49, 56]. They then extend this by incorporating other variables into a single energy density term that they attempt to connect to porosity and other defects, surface roughness, and overall densification levels [33, 56]. For SLM, the energy density, E_{SLM} is defined as:

$$E_{SLM} = \frac{P}{vhd} \tag{1.1}$$

where P is laser power, v is scan speed, h is hatch/scan distance/spacing, and d is layer thickness [56, 57]. For EBM, the acceleration voltage, U, and the electron beam current, I, are accounted for in the P term so that energy density, E_{EBM} is represented as [56, 58, 59]:

$$E_{SLM} = \frac{4UI}{\pi v h} \tag{1.2}$$

There has been a strong focus on connecting the energy density to resultant porosity in AM parts since residual porosity since significantly degrade the resultant mechanical properties of a completed build. In particular, Gong, et al. [60] found that if the energy density is too low, the build will suffer from lack of fusion defects, which are characterized by large, irregular pores that form due to insufficient melting between layers. As energy density increases, porosity will generally decrease, but at some point, the energy density can be too high, and porosity will begin increase again [60]. When the energy density is too high, "keyholing", which is a phenomenon by which relatively equiaxed pores are created due to the recoil pressure from overheating the melt pool causing spatter ejection, will occur [56]. Additionally, too high of an energy density can result in vaporization of low-melting point constituents within the metal powder, which will also result in round, regularly shaped pores that tend to be on the order of tens of microns [61]. The results that Gong, et al. [60] found on the relationship of energy density and porosity has been corroborated by other sources in the literature [56, 61–66]. However, it has also been shown that machine specifics, such as scan strategy, have an influence on the optimal energy density for fully-dense parts, so it is difficult to determine a universal energy density at which porosity can be optimized for AM parts [56].

Surface roughness has also been found to be correlated to energy density in a similar manner as porosity. In general, the energy densities that minimize porosity will also minimize surface roughness [67]. At low energy densities, insufficient melting results in unmelted powder particles clinging to the surface of the build, resulting in a rough build [33, 67, 68]. At energy densities high enough to avoid lack of fusion defects but still lower than optimal, a phenomenon known as “balling”, may occur [69, 70]. During balling, the molten track has a shrinking tendency to decrease its surface energy under surface tension, resulting in the appearance of coarsened balls upon the surface of the build [70]. This phenomenon usually results in less surface roughness than the surface roughness caused by insufficient melting but more surface roughness than the optimal energy density [66–68]. At energy densities much higher than optimal, surfaces are again much rougher than they would be at optimal energy density because of splatter ejection and powder loss [66–68].

Energy density and the process parameters it encompasses do not tell the complete story when it comes to process-induced defects. Besides scan strategy, which was mentioned earlier, other variables, such as direction of gas flow, build preheat temperature, etc., may have a strong influence on the quality and performance of the resultant build [13, 14, 49, 71]. One of the most important factors that energy density does not account for is print orientation. Print orientation is defined as the orientation of the sample relative to the build plate. ASTM standards assign the build direction to be the z-axis in a right-handed coordinate system while x and y are orthogonal directions in the build-plane [72]. The primary focus of connecting print orientation to resultant properties in powder-bed AM has been on relationships relative to the build direction (z-direction).

For thin-walled parts, print orientation has been shown to strongly influence resultant microstructure. For as-printed powder-bed AM parts, grains tend to be columnar and oriented in the build direction [44, 73–75]. As a result, if the same part is printed in different orientations, the resultant properties may be different due to the orientation of these grains. This body of work is primarily focused on characterizing the influence of process-informed defects upon mechanical properties of thin powder-bed AM parts, so microstructural variations due to varying processing factors will not be deeply discussed.

It is just important to mention that sample size/thickness, orientation, and processing parameters can strongly influence the resultant microstructure of these printed parts, potentially resulting in significant variations in microstructure within the same part.

Besides microstructure, print orientation can also influence resultant geometry in thin-walled parts [21, 23, 29, 76, 77]. Suard, et al. [29] found that nominally round beam-like struts printed parallel to the build plate tended to be larger and more elliptical in shape in comparison to their counterparts which were built perpendicular to the build plate. This oversizing of parts printed parallel to the build plate is thought to be a result of overmelting due to the heat flux, which is conducted from the beam through the part to the build plate, during the print process [29, 44, 78]. This overmelting effect has also been observed and documented in other studies [21, 77]. As a result of this size difference in parts printed in different orientations, mechanical properties based on nominal size can be erroneous as a stronger response from overmelted parts may be misattributed to internal (microstructural) factors instead of the actual culprit, geometric differences.

The size of parts not built perpendicular to the build plate can also be subject to an effect called “staircasing”, which is inherent to the AM process. Staircasing is a phenomenon by which curved surfaces and oblique/inclined surfaces are represented by “stair steps” which have a thickness equivalent to the layer thickness [79–82]. This staircasing effect can result in dimensional mismatch between the CAD file and the resultant printed part [79–81, 83]. Additionally, this effect can cause significantly more surface roughness on the “downskin”, which is the surface facing the build plate, of parts in comparison to the “upskin” [67,79,81,82]. This surface roughness can sometimes serve as a notch defect to the part, which can result in a reduction in mechanical strength [84].

While additive manufacturing is an excellent manufacturing technique for the creation of thin-walled structures with complex geometry, the strong process-properties coupling that occurs can make it difficult to predict the resultant performance of printed products.

Factors such as part size, energy density, and print orientation play a significant role in the resultant properties of printed parts as described in detail earlier. It is thus critical to fully characterize process-properties relationships in printed AM parts, especially in relation to thin parts, in order to accurately predict the behavior of printed lattices.

1.3 Surface roughness in powder-bed AM

As mentioned in the previous section, surface roughness plays an important role in contributing to the as-printed geometry of metal powder-bed AM parts. The origins of surface roughness is dependent upon the process selection, powder feedstock, processing parameters, and part design [85,86]. This section will provide a brief overview as to how these factors contribute to the surface roughness of powder-bed AM parts.

The process itself plays a role in the resultant surface roughness of metal AM parts. Although the printing process itself is very similar between L-PBF and EBM, the deviations in power source result in parts with significantly different surface roughnesses since the surface roughness is highly dependent upon build rate, beam diameter, layer height, melt pool size, and powder feedstock, which are all influenced by the power source [85]. The impact of these specific factors will be discussed in detail later. L-PBF has a maximum build rate of 20-35 cm^3/hr, a typical melt pool size of 0.1-0.5 mm, and a layer height of 20-100 µm [87]. EBM has a higher maximum build rate (due to higher energy density and scan speeds) of 80 cm^3/hr, larger melt pool size of 0.2-1.2 mm, and larger layer height of 50-200 µm, relative to L-PBF [87]. These differences manifest as L-PBF parts having a smoother finish, with an arithmetic surface roughness (R_a) of 4-11 µm while EBM parts have a R_a ranging from 25-35 µm [87].

There is generally considered to be two sources of surface roughness – (1) surface roughness due to the "staircasing", as was described earlier in Section 1.2, and (2) surface roughness due to incomplete melting and "balling", which was also described earlier in Section 1.2 [85, 86]. Because staircasing is reliant upon the layer thickness, surface roughness due to this affect can be reduced by using smaller layer thickness values [85,86]. However, using a smaller layer thicknesses will result in a much longer build time so there must be a balance between part accuracy and build time. The surface roughness due to staircasing can also be reduced by avoiding parts built at steep print orientations through proper selection of build direction [85, 88, 89]. For some geometries, it may be unavoidable to have some portions of the part built at a steep incline.

Incomplete melting during the printing process causes powder particles to stick to the surfaces of the build, resulting in an average surface roughness on the same order of magnitude as the powder diameter [69,85,90,91]. Balling can occur when the scan speed is too high, which results in an elongated melt pool that can break into small islands due to Raleigh instability [69,85,92]. Because of the surface tension gradient within the melt pool, the "balls" formed from the melt pool are dragged to the outer corners, causing surface roughness at the edges of a solidified track [66–69, 85, 93]. The surface roughness due to incomplete melting and balling can be avoided through careful selection of process parameters and powder selection. These factors will be discussed in detail below.

Characteristics of the powder feedstock, such as the alloy type, the powder particle size distribution (PSD), and the powder morphology, influence the resultant surface roughness of metal AM parts. Different alloys will vary in their interactions with the heat source due to their different compositions [85]. Some of these alloys have concentrations of elements that have a tendency to migrate to the surface of the molten liquid, which influences the surface tension of the melt pool [85]. This, in turn, influences the resultant shape of the molten pool, which impacts the surface finish of the printed parts [85, 94]. Besides the composition of the alloy, the thermo-physical properties of the alloy, such as liquidus temperature, solidus temperature, density, viscosity, thermal conductivity, specific heat, and temperature coefficient of surface tension, can impact resultant roughness due to their influence upon the melt pool shape [94, 95].

The powder PSD and morphology is highly dependent upon powder manufacturing process. The alloy powders are mainly made in four different ways – gas atomization (GA), rotary atomization (RA), plasma rotation electrode process (PREP), and water atomization (WA) [85]. GA involves atomization of the molten alloy by a high pressure flow of argon and nitrogen gas [96]. In RA, molten metal is flung from a rotary disk, solidified, and collected as powder [97]. During PREP, the end of a metal bar is melted using an electric arc or plasma before being rotated about its longitudinal axis, centrifugally ejecting fine, molten droplets that are collected as solidified powder [98]. WA involves using a high pressure water jet to atomize and solidify molten metal droplets as powder [99].

The GA process creates powders that are spherical in morphology but have a dimpled surface texture and can have satellite particles [100]. Powders made from GA have the least uniform size distribution relative to other powder manufacturing methods [101]. Broad PSD can lead to higher values of surface roughness since the smallest particles can be prone to forming large agglomerates that increase the packing's porosity [102]. RA powders exhibit smooth surfaces but are not spherical [100, 101]. PREP powders are perfectly spherical in shape and have smooth surfaces [100]. These powders have the most uniform size distribution out of all the powder manufacturing processes [100, 101]. WA powder creates irregularly shaped particles with coarse surface roughness [103]. Powders with uniform size distribution promote homogeneous melting, good structure, interlayer bonding, mechanical properties, and surface finish [85, 104, 105]. Components made from WA powders exhibit the highest amount of surface roughness relative to other powder processing methods [101]. Powders with uniform size distribution and good surface finish, such as ones made from PREP, produce the smoothest parts [85, 102]. However, this higher quality powder is more expensive to manufacture [85].

In terms of particle size, small particles (10-20 µm diameter) lead to increased surface roughness due to their tendency to form large agglomerates with highly variable packing fractions [106]. For these small particles, cohesion and wetting are dominant over gravity driven flows, and it is generally not recommended to use particles this small to create parts [106]. Gravity-driven settling dictates the equilibrium configuration for larger particles and provides a more uniform and favorable packing fraction as compared to smaller particles [106]. However, the resultant surface finish for larger particles is limited by their size since larger particles are more difficult to fully melt [85]. This results in parts made with larger particles having a rougher finish in comparison to parts made with smaller particles [85].

Besides powder characteristics, processing parameters must be carefully optimized to provide the smoothest surface finish. In general, increased power leads to decreased surface roughness values. Increased power leads to larger melt pools, allowing for more complete melting and smaller surface notches [85,107]. However, too high of a power may lead to non-uniform solidification rate and high thermal stresses, which may be detrimental to surface finish [104]. This is because too high of a power can cause “keyholing”, which is a mode of melting which results in the formation of plasma and the evaporation of metal [107,108]. This phenomenon was described earlier in Section 1.2 and, in addition to excessive porosity, results in an unstable melt flow and spatter (splashing of molten material), which both increase surface roughness [88, 109].

Increased scan speed produces smaller melt pools and larger surface notches, and thus increased surface roughness [107]. The effect of increased scan speed leading to increased surface roughness is exacerbated by the faster speeds causing more melt pool instabilities and balling [88, 107]. The nominal layer thickness must be carefully chosen in order to balance surface roughness due to staircasing and unstable melt flow against surface roughness due to uneven powder layers. Too large of a layer thicknesses results in discontinuities in the melt track, which results in porosity and surface irregularities in printed parts [88]. Besides resulting in a more stable melt flow, smaller layer thicknesses also reduce the surface roughness due to staircasing since particles adhering to the edges can fill in the "gaps" between layers [79]. However, if the layer thickness is too small, the powder layers will be discontinuous and not suitable for continuous melting [106]. Lastly, the scan strategy itself can influence the surface roughness. Wang, et al. demonstrated that, despite using the same parameters, the surface roughness of printed components can vary significantly depending on the scan strategy [110]. While surface roughness is an important consideration for metal printed components, care must be taken to balance the considerations of parameter selection for surface roughness against other variables, such as porosity, which may be exacerbated by the optimal parameters for a smooth surface finish.

Finally, the design of the part itself can limit the surface roughness of the finished component. While there are some geometries which can be oriented so that surface roughness due to staircasing can be mitigated, there are others which will have inclined features no matter which orientation is chosen. These inclined features will have differing surface roughness on their "upskin" (upward facing surface relative to the build direction) compared to the "downskin" (downward facing surface). The upskin surface is usually less sensitive to incline angle than the downskin surface [3]. This is due to the differences in heat transfer phenomena occurring on the surfaces. For the upskin, heat conduction primarily goes through the previously solidified layer while for the downskin, heat transfer occurs across loose powder particles [3, 29]. In addition, on the downskin surface, the melt pool depth extends beyond the geometry prescribed, creating protrusions along the downskin that increase the surface roughness [3]. This effect is illustrated in Fig. 1.2 and occurs because the melt pool depth is equivalent to or larger than the diameter of the powder. This does not occur on the upskin side since the beam rasters over the previously solidified layer rather than loose powder. Additionally, the presence of support structures can also influence resultant surface roughness. Removal of these support features may leave remnants which can contribute to surface roughness.

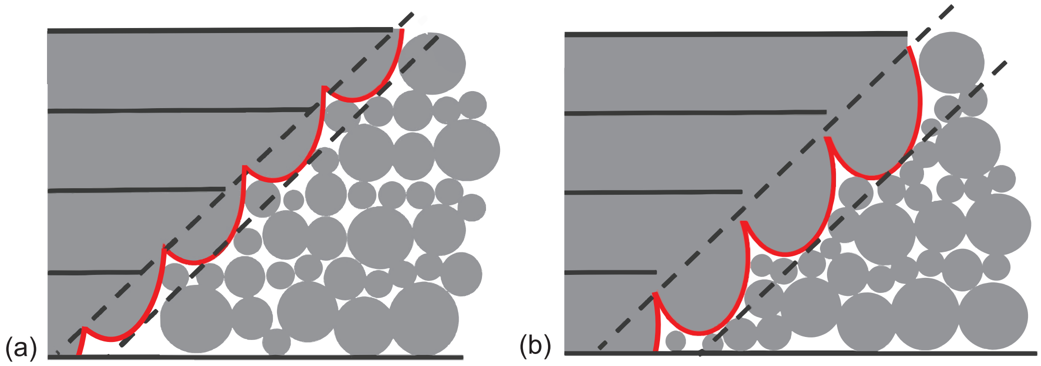

Figure 1.2: Schematic depicting resultant surface roughness (highlighted in red) along the downskin of an inclined feature with a melt pool depth (a) equivalent to the median powder particle size, which results in minimal downskin roughness, and (b) larger than the median powder particle size. Adapted from Tian, et al. [3].

1.4 Lattice structures

Lattice structures belong to a class of materials known as cellular solids. Lattices are defined to be regular, architected materials made of thin-beam like structures called struts. These struts connect at intersections, known as nodes. Gibson & Ashby [24] developed the theory of predicting the mechanical properties for lattice structures. They created powerful models which related the relative density, which is defined as the density of the lattice divided by that of the solid from which it is made, to both the relative modulus and relative strength of the lattice [24]. Similar to the definition of relative density, the relative modulus and relative strength are defined as the modulus and strength of the lattice divided by the relative modulus and strength of the solid from which the lattice is made, respectively.

However, as shown from 1.3, traditional cellular solid theory is insufficient to predict the mechanical properties of powder-bed AM structures. Both the relative modulus and strength of a variety of printed metal lattices were found to relate to the relative density by a factor lower than what was predicted by cellular solid theory. Upon closer inspection of the printed lattices, it is clear that these structures fail to follow some of the assumptions built into cellular solid theory. Cellular solid theory assumes that the struts in the lattice structure behave as ideal, slender beams. Further, it fails to account for any impact the nodes may contribute to mechanical response. However, as shown from the example images in 1.3(b), it is clear that the struts are far from ideal, as they exhibit significant surface roughness. In addition, the nodes of the struts consist of a significant amount of material that likely contributes to the response.

The idea that nodes can contribute significantly to the mechanical response in lattice structures has been explored by Hammetter, et al. [6]. Hammetter, et al. described four different failure modes by which lattices can deform under compression. These modes are elastic strut buckling, nodal yielding followed by elastic strut buckling, strut yielding followed by plastic buckling, and strut yielding with no softening [6]. These failure modes are strongly dependent upon lattice topology but in general, lattices with very thin struts (relative density less than 5%) that tend to be oriented more parallel (as opposed to perpendicular) to the compression direction will fail by elastic strut buckling. Lattices with very thick struts (relative density greater than 30%) will tend to fail via strut yielding with no softening. Lattices with relative densities between 5-30% tend to be fail either by nodal yielding or strut yielding, with lattices with thinner struts tending to fail via nodal yielding. Some examples of the strain localization in lattices due to node vs strut failure is shown in a 1.4, which is adapted from Hammeter, et al [6]. In practicality, most lattices tend to be built with relative densities around to 10-20%, which

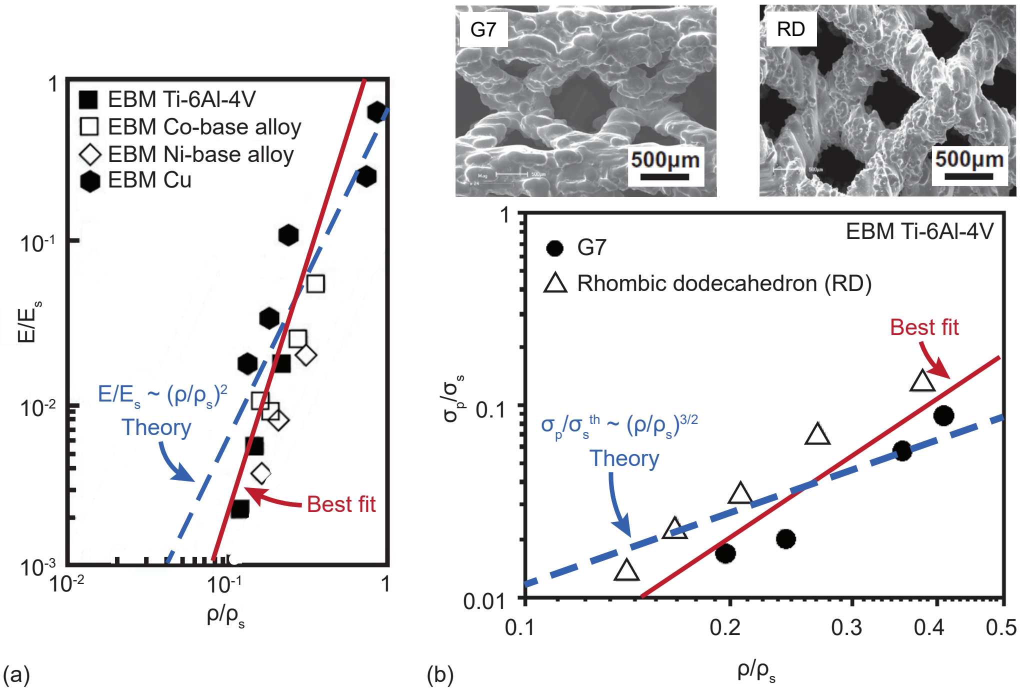

(a) (b)

Figure 1.3: Cellular solid theory predictions in compared to best fit of (a) relative modulus vs relative density of several printed lattice structures adapted from Murr, et al. [4] and (b) relative strength vs relative density of two EBM Ti6Al4V lattices with different unit cell geometries adapted from Li, et al. [5].

makes nodal yielding a highly relevant failure mechanism that should be accounted for in predicting mechanical response.

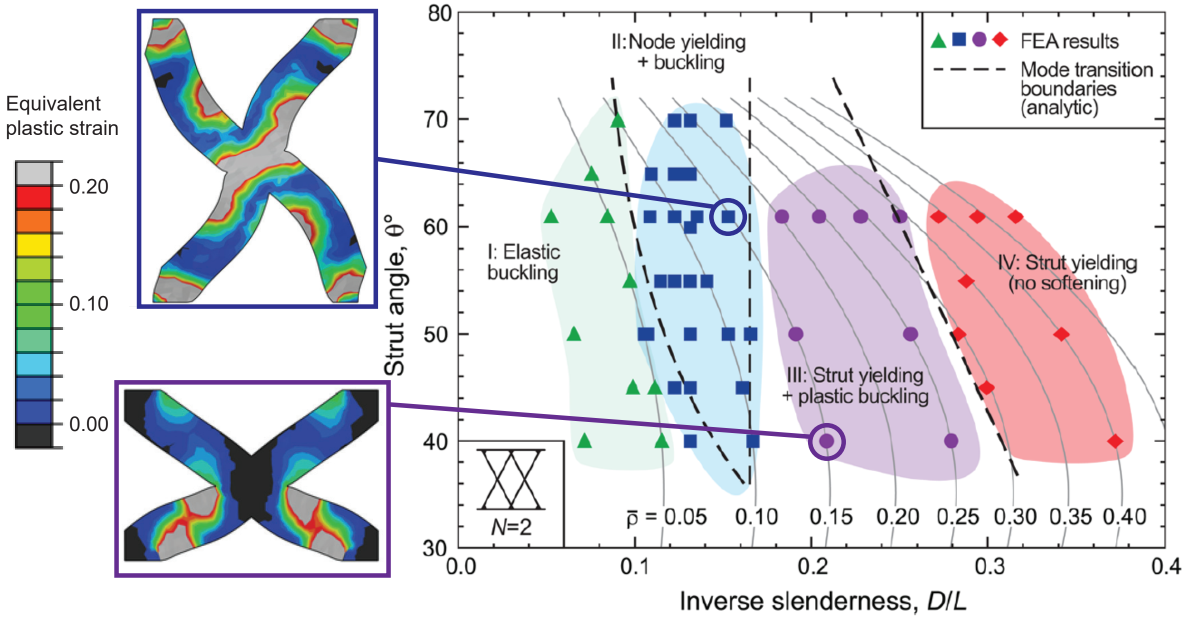

Figure 1.4: Failure modes observed in FEA simulations for a two layer lattice with varying strut angle and relative density. Images of the contours of equivalent plastic strain for two of the failure modes are shown. Adapted from Hammetter, et al. [6].

The most accurate way to simulate the behavior of lattice structures is to use a fully resolved 3D finite element analysis (FEA). However, for more complex geometries, this method is computationally prohibitive and time consuming. Some make 3D FEA more efficient through a coarser mesh that is not fully resolved. However, this method only produces accurate elastic predictions; results are nebulous when trying to predict plastic behavior.

Others have attempted to use models using beam elements to attempt to simulate the behavior of lattice structures. Beam elements are one of the lowest order geometric elements in FEA. Their formulation consists of two key assumptions. The first is the assumption of slenderness, meaning that the dimension of the cross-section is small relative to the typical dimension along the axis of the beam [111]. The second assumption is that plane sections remain plane, meaning that beam cross-sections remain plane under deformation [111]. The second assumption is not necessarily reflective of real deformation, so a shear correction factor, based on the geometry of the cross-section is introduced into the beam element formulation [112, 113]. While these beam-based models are very efficient, they fail to capture any nodal deformation since by design, they neglect to include any material in the node. This can make beam-based models very inaccurate in predicting plastic mechanical behavior of lattice structures for lattices that do not have a low relative density.

To reduce computational cost but maintain the fidelity of 3D FEA, Gorguluarslan, et al. [114] developed a hybrid modeling method with solid elements in some regions and beam elements in others to predict lattice mechanical behavior. While this technique is faster than fully-resolved 3D FEA, it is difficult to implement and it is still relatively computationally expensive because the regions that are modeled with solid elements are the regions that require a fine mesh. Other authors have attempted to adapt beam-based models to account for nodal deformation by increasing the diameter of the beams near the nodal region [115, 116]. However, this method only works for limited geometries and at low relative densities, where nodal behavior is not as important [6].

In order to truly capitalize on the freedom of design that AM allows, simulations that can efficiently predict the mechanical behavior of printed lattices are necessary. These simulations must not only accurately capture strut and nodal deformation that occurs in lattice structures due to topology, they must also account for the process-properties coupling that arises as described in the previous section. This is an outstanding challenge that this work hopes to address.

1.5 Scope, key issues, and organization

This dissertation is organized so that Chapter 2 provides an overview of the experimental and numerical methods critical to this work while Chapters 4-6 contain the work that addresses the key goals, highlighted below.

- **Characterization of of strut geometry and mechanical response to identify effective properties as a function of print orientation:** Chapter 3 involves extensive geometric and mechanical characterization of EBM Ti-6Al-4V strut primitives printed at various print orientation. It quantifies the geometry, using several different area metrics, as a function of print orientation and computes effective area with validation against mechanical test results. The results of this study demonstrates how failing to account for effective geometry can lead to unrealistic material properties. Further, this work also evaluates how the effective geometry for elastic and plastic properties may not necessarily be the same through comparisons of results using the different area metrics.

- **Identification of a method to efficiently extract effective properties from lattice-based structures:** Chapter 4 utilizes the methodology to extract effective area in Chapter 3 and extends it by demonstrating that this method is effective in lattice primitives built in a different material system (L-PBF SS316L) and that the effective area can be computed from surface roughness measurements. Chapter 4 uses the effective area to infer mechanical properties based on macroscopic deformation. The inferred properties are then used to draw quantitative insight into how processing conditions can influence resultant mechanical properties and how local property variations, such as variations in microstructure, may influence resultant strain localization.

- **Understanding the role of strut intersections (nodes) in lattice deformation:** Chapters 3 and 4 provide some preliminary insight into the mechanical behavior of nodes through mechanical testing of node primitives. Chapter 5 builds upon this previous work by analyzing how nodes deform in two different SLM Ti-6Al-4V lattice structures. This work provides a deeper understanding on how the degree of constraint, orientation within the lattice, and nodal geometry influence nodal deformation and resultant macroscopic deformation and failure in lattice structures. In addition, it fully characterizes the lattices prior and post deformation so that a complete picture of the initial and final state of the lattices can be painted.

- **Quantification of the impact of local intrinsic and surface features to macroscopic performance:** Chapters 3 to 5 heavily allude to the influence of defects and local property variations upon macroscopic performance. Chapter 6 quantitatively begins investigating these local property variations through property mapping via nanoindentation. The resultant property maps quantify the mechanical property variations in strut and cell lattice primitives and highlights how print orientation and topology influence macroscale and mesoscale properties. In addition, they demonstrate that the mechanical properties in isolated lattice primitives may not necessarily be the same as those of primitives that are apart of a larger-scale structure.

Chapter 2

Characterization Methods

This chapter provides a broad overview of the experimental and numerical methods essential to this body of work. The techniques covered are image analysis of CT scans, mechanical testing with in situ digital image correlation, nanoindentation, and finite element analysis simulations. Each section provides some basic background information on the individual technique, references with more detailed information, and some best practices or pitfalls that may occur with inexperienced users. The goal of this chapter is provide a basic understanding of all the techniques critical to this dissertation so that the reader is not confused about technical details.

2.1 Image analysis in Fiji/ImageJ

Fiji (Fiji Is Just ImageJ) [117] and its in-house plugin, TransformJ [118], was used to analyze the geometry of all of the x-ray computed tomography (CT) scans of AM metal struts. Fiji's in-house 3D Viewer plugin [119] was used to visualize the structures. The online documentation [120] for Fiji is very thorough, so a brief overview for the image analysis process will be provided along with a more detailed explanation of an image analysis algorithm essential to this work.

2.1.1 Image area analysis

To begin, the CT images were imported as a .tif stack into Fiji/ImageJ. If not already in an 8-bit format, the image stack was converted into that format by going to the Image>Type menu. Individual struts from the structure were cropped out into separate stacks by using the Image>Duplicate... and Image>Crop tools. These individual struts were then rotated using the TransformJ>TransformJ Rotate plugin tool so that the strut axis is aligned out-of-plane (the viewer should be able to see the cross-sections straight on). The image stack was then thresholded using Image>Adjust>Threshold... and making sure “Stack Histogram” was checked. For the images in this work, the Default thresholding method was appropriate for most cases. Different image thresholding methods may be appropriate depending on the quality and contrast of the CT images.

After preparing the image stack for analysis, the desired measurements were selected using the Analyze>Set Measurements menu. These measurements will vary depending on the desired information but in general, the Area, Fit Ellipse, Centroid, and Stack Position were selected. If wanting to determine the true area of the cross-section, the next step would be to analyze the image stack by using Analyze>Analyze Particles... tool. Then, various preferences to make image analysis easier, such as setting a size range, setting a circularity range, and/or checking “Exclude on Edges”, were set before running the analysis. If the inscribed area is desired, a few more steps are required before running the analysis. These steps are described in detail in the “Inscribed area algorithm” section (Section 2.1.2) ahead. An example script that will go through a stack of images and do the area analysis that will run as an ImageJ Macro is provided in Appendix A.

2.1.2 Inscribed area algorithm

The inscribed (I) area that is described by the maximum inscribed ellipse of a cross-section was computed using Fiji/ImageJ's in-house operations. After thresholding (binarization), the CT image underwent multiple "Open" operations, followed by "Erode" operation(s). For the cell samples, the struts underwent five "Open" operations followed by two "Erode" operations. In the node samples, the struts underwent five "Open" operations, followed by one "Erode" operation. The influence of these operations will be described in further detail below. Images from two sample strut cross-sections, one with a relatively rough surface and one with a relatively smooth surface, are used as examples to highlight how these operations work.

To create an ellipse from the binarized image, FIJI's "Fit Ellipse" function was used. This function creates an ellipse with the equivalent area to the binarized cross-section. In order to create the maximum-inscribed ellipse for each cross-section, we must first approximate the area of the maximum-inscribed ellipse from the binarized cross-section. This is when the "Erode" operation becomes useful. The "Erode" operation reduces the area of the binarized cross-section by removing pixels from the edges of the cross-section. Both Figures 2.1(b) and 2.2(b) show what the example cross-sections in Figures 2.1(a) and 2.2(a) and resultant ellipse created from that cross-section look like under multiple erode operations. For both example cross-sections, we see that a single "Erode" operation does not reduce the binarized cross-sectional area enough to approximate a maximum inscribed ellipse. On the other hand, applying the "Erode" operation three times seems to take off too much material from the cross-sectional area. For these sample images, applying the "Erode" operation twice seems to result in an ellipse that best approximates a maximum inscribed ellipse. For the smoother strut (Figure 2.1), especially, we see that the resultant binarized cross-section and fit ellipse created from it approximates a

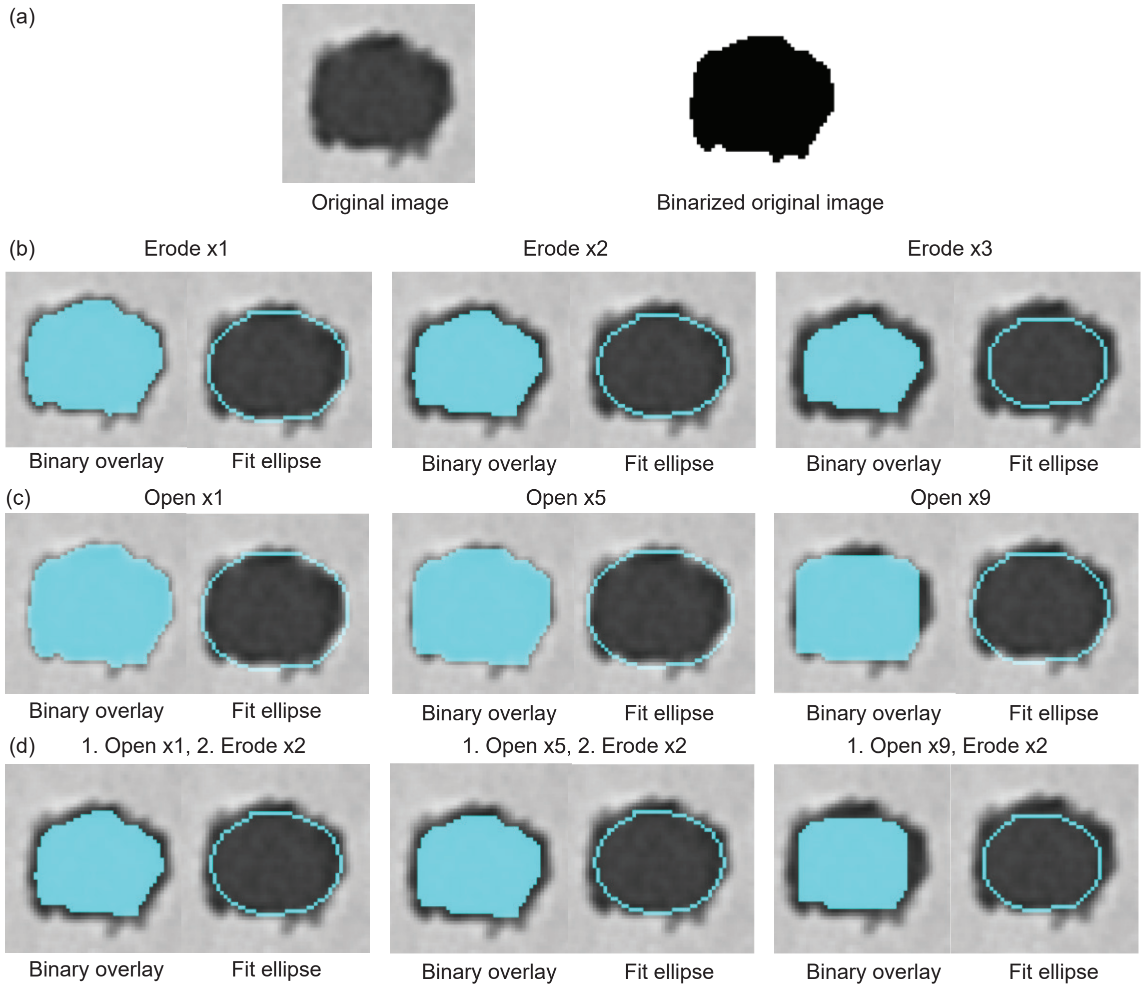

Figure 2.1: (a) Example cross-section from a strut of the cell with a smoother shape from CT and the same image binarized. (b) Examples of the resultant cross-section shape overlaid over the original image after various 'Erode' operations, and the corresponding fit ellipses from those cross-sections. (c) Examples of the resultant cross–section shape overlaid over the original image after various 'Open' operations, and the corresponding fit ellipses from those cross-sections. (d) Examples of the resultant cross-section shape overlaid over the original image after various 'Open' operations followed by 2 'Erode' operations, and the corresponding fit ellipses from those cross–sections.

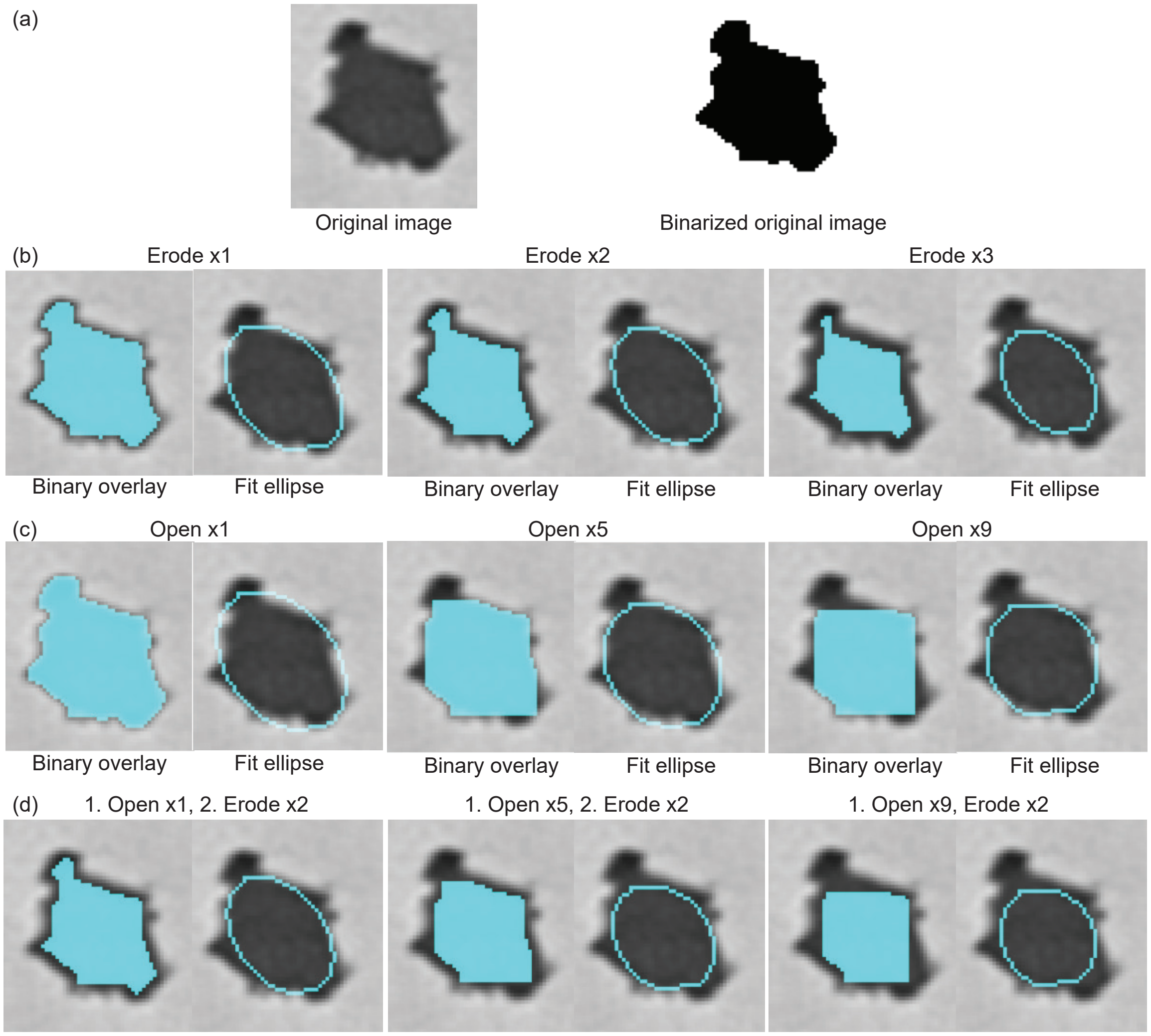

Figure 2.2: (a) Example cross-section from a strut of the cell with a rougher shape from CT and the same image binarized. (b) Examples of the resultant cross-section shape overlaid over the original image after various 'Erode' operations, and the corresponding fit ellipses from those cross-sections. (c) Examples of the resultant cross-section shape overlaid over the original image after various 'Open' operations, and the corresponding fit ellipses from those cross-sections. (d) Examples of the resultant cross-section shape overlaid over the original image after various 'Open' operations followed by 2 'Erode' operations, and the corresponding fit ellipses from those cross-sections.

maximum inscribed ellipse very well. However, for the rougher strut, (Figure 2.2), we run into a slight issue.

The “Erode” operation uniformly reduces the area of the binarized cross-section, without affecting its shape at all. For very rough/irregularly-irregularly shaped cross-section, this poses a problem because it will count asperities as part of the effective area, causing the resultant fit ellipse to be larger than the maximum inscribed ellipse. To resolve this issue, we need to remove the asperities from the binarized cross-section before creating a fitted ellipse. This is what the “Open” operation does. The “Open” operation removes pixels uniformly around the edge of the cross-section, but then adds in more pixels around the edge of the cross-section. This results in the removal of isolated regions of roughness, which creates a smoother cross-section. Figures 2.1(c) and 2.2(c) provide a visual of what the example cross-sections in Figures 2.1(a) and 2.2(a) and resultant ellipse created from that cross-section look like under multiple “Open” operations.

A single “Open” operation does not have a much of an effect on the resultant binarized cross-sectional area. This is shown in both Figures 2.1(c) and 2.2(c) in the lefternmost image; the binarized cross-section with the “Open” operation applied to it overlaps the original image almost perfectly. However, if too many “Open” operations are applied, the binarized cross-sectional area will reduce by far too much and approach a square shape. We thus need enough “Open” operations to remove any potential asperties but not too many that we reduce the effective cross-sectional area as well. Through trial and error, we found that using five “Open” operations for these samples was appropriate.

For this study, we found that using the five “Open” operations, followed by the appropriate number of “Erode” operations was a suitable method to create the maximum inscribed ellipse for the strut cross-sections. It should be stated though that this is not the only way to determine the maximum inscribed ellipse. It is probably possible to do so through some other combination of FIJI binary operations but this algorithm is what we found worked for us across a variety of different cross-sectional area shapes. The quality of results from using methods like this will depend on the voxel size of the images, the contrast of the object and background of the images, and the roughness of the objects.

2.1.3 Image surface roughness analysis

To determine the surface roughness of individual struts, image stacks of individual struts were prepared in the manner described under the "Inscribed area analysis" section (Section 2.1.1). However, instead of using TransformJ>TransformJ Rotate to rotate the struts so that the strut axis is aligned in-plane at an angle of 0° or 90°. The image stack was then thresholded using the same method to threshold the image stack of the strut cross-sections as described in Section 2.1.1. If necessary, the image stack was reduced so that only the relevant slices were present using the Image>Duplicate... tool and choosing only the relevant slices to duplicate and save.

After thresholding/binarization, the Analyze>Analyze Particles... tool was run so that Bare Outlines were shown as the result. It is convenient to set the measurements for this step to determine Area, since the preferences can then be changed so that only the solid section of the strut is selected by adjusting the size. The resultant outlines are then converted into a pixel grid by using the Image>Transform>Image to Results tool. A script that splits the image into half (to separate the upskin and downskin of the strut) and then determines the coordinates of the upskin and downskin surfaces was then run on each pixel grid of the image slice. A sample script that does this is provided in Appendix A. The coordinates of the surface points can then be analyzed in an appropriate data analysis software (e.g., Mathematica, Matlab, etc.) to determine the desired roughness metrics.

2.2 Mechanical testing using Digital Image Correlation (DIC)

Digital Image Correlation (DIC) is an optical technique that can capture full-field strain measurements through the tracking of the shape, deformation, and motion of solid objects. This method was used to track displacements and strains for the mechanical tests in Chapters 4 and 5. The mechanical tests in Chapter 3 relied on laser extensometry and crosshead displacement in combination with FEA to track displacements. This section will provide a broad overview of the important concepts in DIC but is by no means an in-depth explanation of DIC. For further reading on DIC, *Image correlation for shape, motion and deformation measurements: Basic concepts, theory and applications* by Schreier, et al. [121] and work by Rajan, et al. [122] are recommended. For this work, the DIC systems of VIC-2D and VIC-3D (Correlated Solutions, Irmo, SC) were used to make the DIC measurements.

The basic principle of DIC involves tracking a pattern (usually called a speckle pattern) in a sequence of images as an object deforms. The first image in the sequence, defined as the reference image, is of the undeformed object and it is the baseline to which the other images in the sequence are compared to. The speckle pattern of the deformed images are compared to that of the reference image and the displacement between the reference and deformed images' patterns are calculated. The following section will provide a walk-through of each of the steps taken in the DIC process.

2.2.1 Speckle patterning

The first step in DIC involves patterning the sample to be imaged/tested with a speckle pattern. The quality of the speckle pattern is of utmost importance to producing accurate measurement results. The ideal pattern should be high-contrast and random with consistent dot sizes. Ideally, there should be an equal amount of white and black on the surface. If the pattern is too sparse, too dense, or the speckles are too large or too small, noise and uncertainty will be introduced into the measurement as the software will have difficulty distinguishing unique subsets of the speckle pattern. An example of a good speckle pattern can be found in Fig. 2.3.

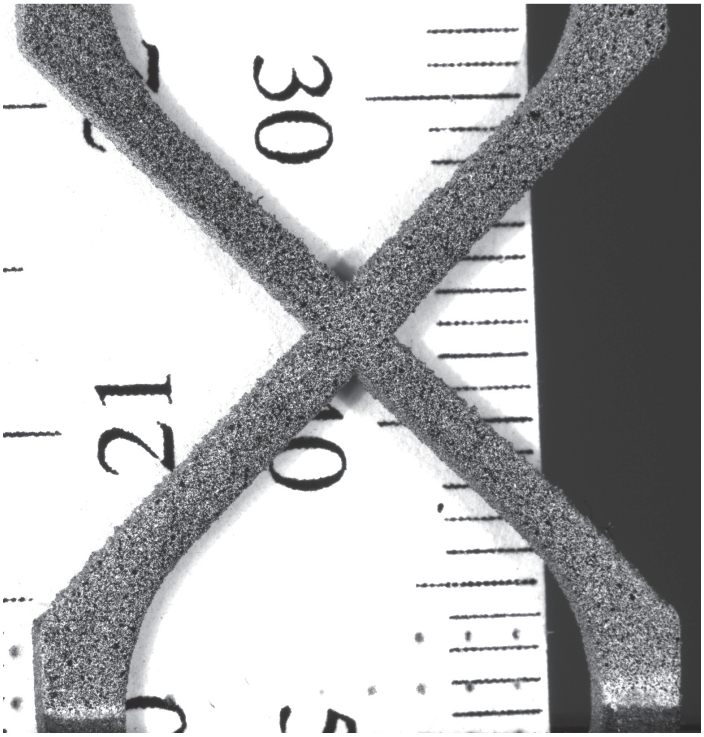

Figure 2.3: Example of sample with a speckle pattern that will provide good correlation in a DIC software.

Spraypainting and airbrushing are commonly used to apply a speckle pattern for macroscale objects, with airbrushes leading to a finer speckle size with a narrower size distribution than spray paint [122]. For this work, an airbrush was used to speckle the samples. First, a layer of flat white paint was used to cover the sample to be measured. This layer was used a background layer to provide maximum contrast for the speckles. Additionally, the samples were made of metal so it was necessary to paint over them with a matte layer so that the sample did not overexpose the images taken with the camera. Atop the flat white layer, speckles were applied using a Paasche air-brush filled with water-soluble black paint. If the paint was too thick, a small amount of polar solvent, such as ethanol or methanol, was used to thin the paint so that the airbrush would spray more evenly. Care must be taken to ensure the layers of paint were not too thick. If the paint is too thick, at high deformation, the paint will flake off and the region with paint removed can no longer be correlated to the reference image. Similarly, if the paint is too old, the paint will harden too much and flake off at high deformation. It is thus recommended to perform the experiment within a week of painting, ideally closer to 24 to 48 hours.

In practice, it is best to use DIC on a sample with black speckles upon a white background. Theoretically, a layer of flat black covered with white speckles should produce a similar result to a sample with black speckles upon white. However, the author has found that black speckles upon a white background yield better measurements than white speckles upon a black background.

2.2.2 Subsets and step sizes

DIC involves the tracking of subsets, which is a collection of unique pixels, of the patterned object. For the best image quality, each subset should ideally have 3-5 speckles and each speckle should be 3-7 pixels across its diameter [121]. Thus, one should have a clear idea of the field of view one wishes to image before deciding how to pattern their sample. The DIC software determines the center of each subset and then tracks the location of the subset center as the object deforms. With multiple subsets, DIC is able to compute a field of displacements. Two important dimensions to note in DIC are the subset size and the step size, which are both measured in units of pixels. The subset size is the height/width of the subset square in the reference image while the step size is the distance between subset centers. The step size helps dictate the spatial resolution in DIC, with smaller step sizes yielding more DIC data points to track. In general, a step size that is ten times smaller than the subset size should be used.

2.2.3 Image capturing and calibration

The work in this dissertation uses both 2D DIC and 3D DIC techniques to capture sample deformation. 2D DIC involves a single camera pointing perpendicular to the speckled sample of interest. This technique does not account for any out-of-plane motion so it is ideal for very thin or very thick samples that have negligible out-of-plane deformation. Otherwise, out-of-plane motion introduces error into the measurement for 2D DIC. 3D DIC involves imaging using two cameras that use triangulation to determine out-of-plane deformation. This method of determining out-of-plane deformation is valid as long as the sample remains in focus. 3D DIC will thus not accurately capture extreme out-of-plane motion. Additionally, it must be noted that 3D-DIC still only measures displacements on the surface of a material and not within the volume of the material. The only way to capture volume displacements is to use an imaging system that can view the inside of a material, such as x-ray tomography or confocal microscopy. This technique is called digital volume correlation (DVC) and is beyond the scope of this body of work.

Once the sample is prepared, the camera(s) should be setup so that the region of interest is in the field of view. The appropriate image magnification should be used so that the region of interest and the predicted deformation will be fully captured by the camera(s), e.g., if testing in tension, leave extra room in the direction of the loading so that parts of the sample will not go outside the field of view once it is pulled. Care should be taken to light the sample evenly along the region of interest. The lighting should be intense enough to saturate the pixels but not too intense so that pixels are overexposed. In practice, the ideal lighting should be that in the DIC software, the sample looks barely overexposed (just a few pixels overexposed). It is recommended that polarizing filters are placed orthogonally on the lights; this helps decrease error, increase contrast, and attenuate saturated pixels [123].

Before the experiment can be performed, calibration must be done to relate the image deformation captured by the camera to real dimensions. For 2D DIC, this calibration is straightforward since it only requires a line of known length to be related to pixel dimensions. One way to do this is to place a ruler within the field of view before testing. 3D DIC requires the cameras to be calibrated with respect to one another so the calibration for this technique is a bit more complex. The 3D-DIC calibration procedure will vary depending on the DIC software packaged used but for the VIC-3D system, this procedure involved imaging a glass calibration grid that was backlit with a diffuse LED panel. The grid was incrementally rotated and moved within the field of view and 25 to 50 calibration images were taken. The software would then go through the calibration images and indicate whether or not the calibration procedure was sufficient. If not, the process needs to be redone until sufficient calibration is obtained.

2.2.4 Strains

In the DIC software used in this work, the strain values are determined by a strain filter. A strain filter is a multiplicative factor that is used to determine the virtual strain gauge size. The total strain smoothing area is given by the strain filter multiplied by the step size. The smaller the step size, the larger the strain filter needed since the strain should be averaged over at least two subsets. This is especially important when the step size is less than the subset size since neighboring DIC data points will not be completely independent.

2.2.5 Noise floor and error evaluation

Before starting the experiment, it is recommended to capture repeated, static images of the setup and speckle pattern. Then, the noise floor of a particular measurement, e.g., vertical displacement, can be determined by evaluated the root mean square (RMS) value from the static images. Compare these values to the anticipated values for your experiment – this noise floor should be orders of magnitude lower than the expected displacements and strains.

Strains in some regions, especially near the edges of the sample, may appear to be erroneously high due to edge effects. To evaluate whether this is a real strain or an erroneous one, determine whether the strain evolves over the experiment. If it fails to change, it is likely a fictitious strain due to an edge effect. Additionally, if it is located in a subset that contains a speckle that is abnormally large (takes up most of the subset), it may be a fictitious strain since significantly larger speckles can sometimes be interpreted as false strains.

2.2.6 Mechanical test setup

All of the mechanical tests in this work were performed on a Material Test System 810 servohydraulic load frame at room temperature under a quasi-static strain rate (approximate strain rate between 10^{-3}–10^{-4} s^{-1}). Fig. 2.4 shows an example setup for a mechanical test involving both 2D and 3D DIC. While the specific details for the mechanical tests in this work can be found in the individual chapters, it is important to note a couple commonalities to all of the tests. First, all of the tests were completed under displacement control. Second, the choice of load cell was made so that the maximum

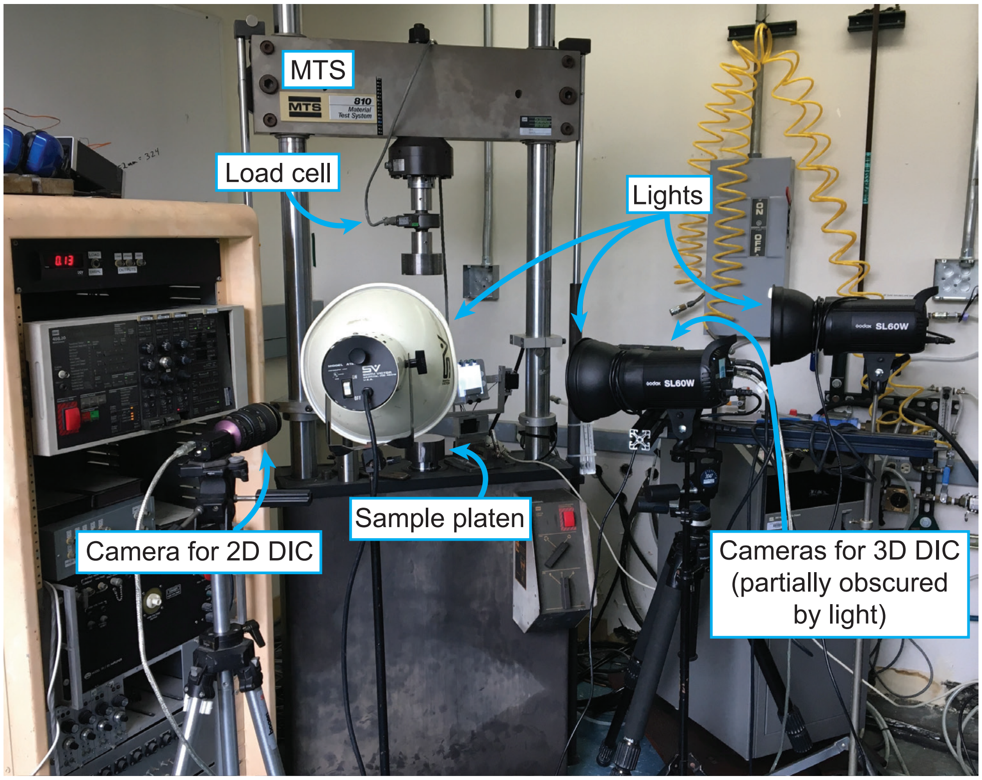

Figure 2.4: Example mechanical test setup involving both 2D and 3D DIC.

load rating of the load cell was approximately twice the maximum load anticipated for the mechanical tests. If the load cell is too large, the load-displacement data will be too noisy. The maximum load estimates for the individual mechanical tests were estimated using FEA prior to the test using a reasonable estimate for the material properties.

2.3 Nanoindentation

Nanoindentation using an iNano Nanoindenter (Nanomechanics Inc., Oak Ridge, TN) was used to probe local mechanical property variations on AM lattice primitives in Chapter 6. Indentation is a technique that is commonly used to characterize the plastic properties of solid materials. It involves pushing a hard tip with known material properties into a sample with unknown properties. From this experiment, the modulus and hardness, which is related to material strength, of the sample can be determined. Indentation is generally classified into macroindentation, microindentation, and nanoindentation. These indentation scales differ from each other in their applied loads and indentation depth, with macroindentation usually having loads greater than 10 N, microindentation with loads between 2 to 10 N, and nanoindentation with loads below 2 N. The different indentation scales probe different amounts of material volume and their results are generally not easily correlated to each other. Further, various indentation tips can be used for each type of indentation test. Even within the same indentation scale, the use of different tips will require some sort of conversion to be able to compare the results from different tests.

This work used a Berkovich tip to probe several EBM Ti6Al4V lattice primitives to depths greater than 500 µm. Ideally, an indentation scale greater than nanoindentation would have been used since the intention was to probe material properties averaged over many grains instead of just a couple. However, the instrumentation at the facilities at UCSB were limited to only nanoindentation for practical reasons. This section is intended to provide a broad overview on some of the rationale behind the indentation setup in this work, while the results can be found in Chapter 5. For a more in-depth reading on the theory and mechanics behind indentation, Johnson's *Contact mechanics* book [124] is recommended.

2.3.1 Sample preparation

Prior to indentation, it is ideal if samples are as clean and flat as possible. In this work, the samples were ground to the region of interest and then polished using colloidal silica on a vibratory polisher for several days. Care must be taken to avoid scratching the sample during this process since scratches could break the indenter tip and they introduce plastic deformation into the sample that could misrepresent material properties. Additionally, the polishing process needs to be done gently (low load) since the process introduces a thin layer of plastic deformation to the sample surface; using too much load during the polishing process can result in more unnecessary plastic deformation that the indenter will have to push past to measure results representative of the material properties. Prior to being tested, the indenter must be calibrated to a material with known properties. In this case, calibration was done on fused silica.

2.3.2 Indentation spacing

As an indenter tip pushes into the material it is testing, it plastically deforms the material, creating a plastic zone which spreads outwards from the indenter. Traditionally, Johnson's model [124, 125], based on expansion of a spherical cavity in an elastic-plastic material, has been used to describe the resultant plastic zone formed by indentation. This model relates the plastic zone radius to the radius of the imprint given the sample's modulus, yield strength, and the angle of the indenter tip. More recent literature [126–128] has expanded and improved upon this model, and it is generally believed that the plastic zone is 5-10 times the depth of the indent for metals [129–132].

In practice, this means that when setting up many indents to probe a large swath of material with nanoindentation, the indents need to be spaced out sufficiently so that their measurements are independent of one another. To be safe, indents in this work were planned to be at least 10 µm away from each other as the planned indentation depth was 1 µm. A visualization of a Berkovich indenter and the resultant plastic zone can be found in Fig. 2.5.

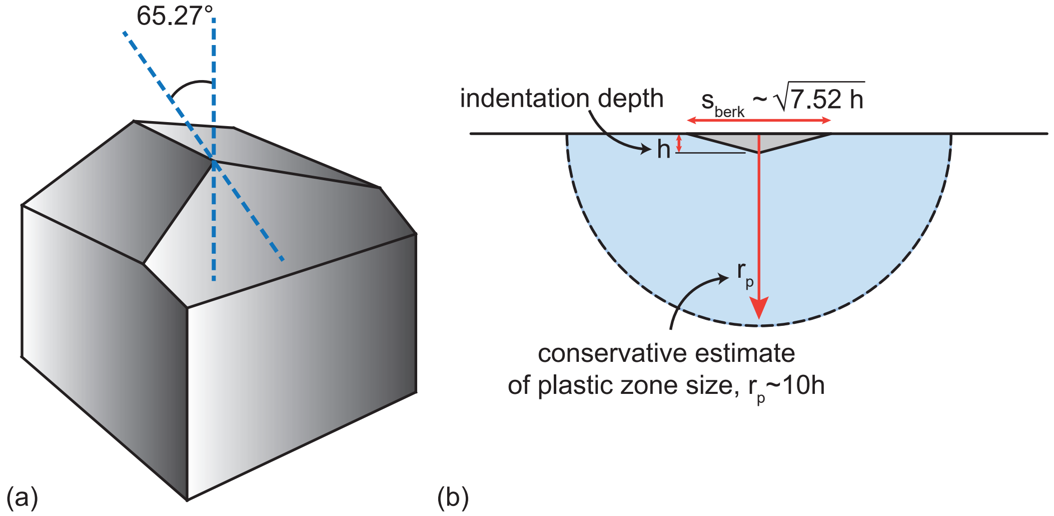

Figure 2.5: (a) Geometry of a Berkovich indenter. (b) Schematic depicting width of indenter and conservative plastic zone estimate in relation to indenter depth for a Berkovich tip.

2.3.3 Hardness and material strength

Scientists have long sought to connect harness to mechanical properties of materials. Traditionally, Tabor [133, 134] established an empirical relationship in which hardness is approximately three times the yield strength. This equation is only valid for ideally plastic materials that do not work harden [133, 135]. The analysis also relies on a relationship between yield strength and critical shear fracture stress, which is based on the Tresca and von Mises yield criterions [133, 134], which both neglect the effect of the normal stress upon the shear stress during deformation. This makes Tabor's empirical relationship unsuitable for many materials, such as work-hardening metals, ceramics, crystalline materials, etc. Other publications have reported an empirical relationship between hardness and ultimate tensile strength in which the hardness is approximately three times the ultimate tensile strength [136, 137]. This relationship to ultimate tensile strength was found to have good agreement among carbon and alloy steels with different pretreatments [134, 136]. This brings up the issue: what does hardness physically represent?

This question is difficult to answer because the relationships between strength and hardness vary for different material classes [134,137,138]. The most accurate, yet tedious, way to estimate mechanical properties from hardness measurements is to either derive a relationship using the indenter morphology, material hardening, indentation loading, and hardness or to develop empirical relationships for a given material class based on many hardness and strength measurements [134, 138–140]. For Ti6Al4V, specifically, which is the material this work nanoindents, an empirical relationship has been developed by Hickey [141] to relate Vickers hardness and ultimate tensile. This relationship, however, is of limited utility, since the hardness measurement is strongly influenced by the orientation of the underlying HCP α phase [142]. For AM Ti6Al4V, Keist & Palmer [142] have demonstrated that hardness and strength are linearly correlated. From this, the bottom line is that hardness has the most utility in qualitatively comparing mechanical strength within a material system for the same experimental conditions. In this work, the nanindentation results are used to qualitatively compare EBM Ti6Al4V of different print orientation and geometry.

2.4 Numerical methods

Finite Element Analysis (FEA) simulations of all of the lattice structure-based geometries in this work were conducted in ABAQUS FEA (Dassault Systémes, Vèlizy-Villacoublay, FR). These simulations were used to further understand the deformation mechanisms and material properties of the AM samples. All simulations were conducted using a quasi-static analysis or with a loading rate that was within the quasi-static regime using displacement control. ABAQUS has no built-in system of units and it assumes that the user uses consistent units. For all simulations in this work, SI (mm) units were used with lengths defined in mm, force in N, time in s, stress in MPa, and density in tonne/mm^3. This overview assumes that the reader has a basic understanding of FEA and will provide a brief background into the element types and setup used in the FEA in this work. For a more thorough understanding of the theory behind FEA, *Concepts and Applications of Finite Element Analysis* by Cook, et al. [112] is strongly recommended. Additionally, the ABAQUS documentation [111] can be found online if details of the ABAQUS analysis is desired. Some sample scripts to generate beam, 2D, and 3D FEA simulations can be found in Appendix B.

2.4.1 Element types and mesh convergence

The simulations in this work used beam elements (specifically Timoshenko-Mindlin element named B21 in ABAQUS), 2D plane stress elements (CPS4R and CPS8R in ABAQUS), and 3D continuum brick elements (C3D8R in ABAQUS). A schematic depicting the shape of these elements with their nodes labeled is shown in Fig. 2.6. In general, lower order geometric elements were used for parametric studies but were validated against higher order element simulations before use. All simulations used peak load as a mesh convergence metric for load-displacement convergence. Strain contour convergence was evaluated on a more qualitative metric; strain contours were visually inspected for “smoothness” so that no individual element outlines could be distinguished. The amount of elements across a minimum dimension is always lower for load-displacement convergence than it is for strain distribution convergence. General contact was implemented for the higher geometric order (2D and 3D) FEA.

The beam elements used each had two nodes, each with displacement and rotational degrees of freedom at each node. The spatial strain variations in these elements are linear and the cross-sectional shape was either circular or rectangular, depending on their

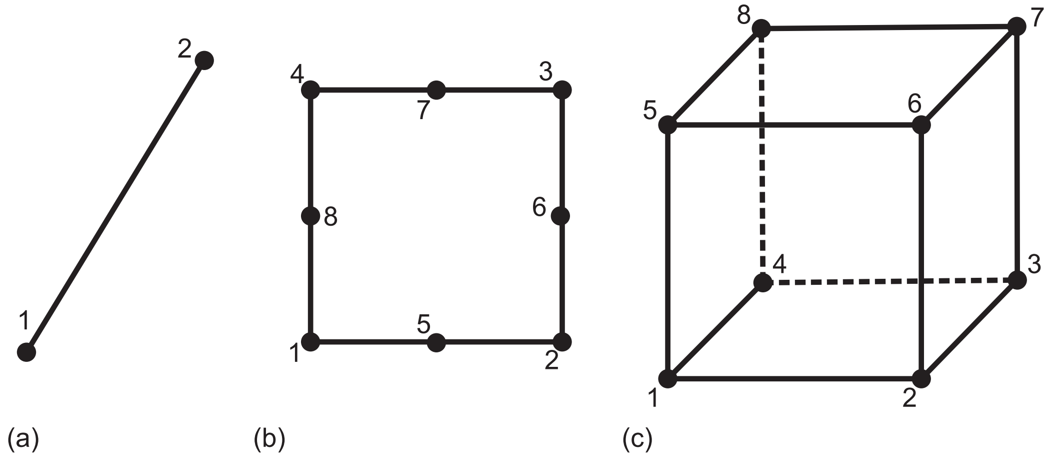

Figure 2.6: FEA elements used in this work with nodes labeled. (a) B21 beam element. (b) CPS8R 2D plane stress element. (c) C3D8R 3D continuum brick element.

intended geometry. These elements are quite good at capturing the strain distribution across long, slender objects, such as struts in lattice structures, but they fail to capture any kind of nodal deformation, without any adaptations. For this work, these elements were used to evaluate the effectiveness of using beam elements to represent lattice structures and to develop more efficient simulation methods. In general, a minimum of ten elements across the minimum dimensions were needed for load-displacement convergence but twenty elements were optimal for strain convergence.

The 2D plane stress elements used in this work have eight nodes each. These elements are appropriate when the thickness of a structure is small relative to its in-plane (lateral) dimensions. Plane stress elements are defined in the x-y plane, with all loading and deformation assumed to act in-plane (out-of-plane normal and shear stresses are zero). In this work, 2D plane stress elements were used to approximate most of the geometries, as they were found to produce approximately the same load-displacement and strain distribution results as fully-resolved 3D FEA but at a lower simulation cost. In general, a minimum of twenty elements across the minimum dimension (usually the strut thickness) were needed for the struts and nodes of the lattice structures simulated, with fewer elements need in the region away from the struts (e.g., the frame at which the sample was gripped). The elements in the regions away from the area of interest (usually the node) were usually five times the size of the elements in the node, but this number varied depending on the actual geometry of the sample.

3D continuum brick elements were used to validate that a lower geometric order element was appropriate or if the lower geometric order elements could not suitably be used. These elements have twenty nodes each. In general, a minimum of five elements across the minimum dimension were needed for load-displacement convergence. A minimum of ten elements were required for strain distribution convergence. Simulations using 3D continuum brick elements took significantly longer (five to hundreds times longer) than simulations using lower geometric order elements.

2.4.2 Simulation scheme: implicit vs. explicit

All of the higher geometric order simulations used an implicit, quasi-static (Abaqus/Standard) scheme in the analysis. For the beam elements, an explicit, dynamic scheme (Abaqus/Explicit) was used. An implicit method is time-independent and determines the deformation by solving equations of equilibrium throughout the loading. An explicit method solves for the acceleration at each time step and is thus time dependent. All simulations were supposed to simulate behavior under quasi-static loading so care must be taken when selecting a loading rate for the beam simulations so that the rate does not impact the resultant deformation.

The rationale for the different schemes depending on the element type is as follows. For the higher geometric order simulations, both an implicit and explicit scheme were used initially to run the analysis. It was found that the implicit and explicit schemes yielded the same result but the implicit scheme had a shorter computational time than the explicit. For FEA using the beam elements, an implicit scheme failed to converge to a solution at times because of buckling, which is a dynamic event, that would occur as the geometry would transition from one state to another. Some buckling modes had eigenvalues very close to each other, which made it difficult for the implicit solver to find a solution since there were multiple solutions that were energetically similar. It was thus necessary to use an explicit scheme to ensure a solution could be found while using the beam elements. The explicit scheme would automatically incorporate the first (lowest order) eigenmode into the analysis to determine a solution in the analysis. It was found that using an implicit scheme with a small amount of the first eigenmode (as a buckling imperfection) would yield the same result as the explicit scheme but it was more convenient to use the explicit scheme in the beam simulations.

2.4.3 Step size/loading rate

For the higher geometric order simulations, a step size of 1.0 was used for all simulations. Since time does not play a role in implicit simulations, it is standard to use a step size of 1.0. For the beam simulations, the length of the step size matters as it dictates the loading rate. In this reduced-order simulations, a couple methods were implemented to ensure the loading rate would not influence the resultant deformation. First, the displacement was defined by a periodic loading amplitude defined by a cosine as shown below in Eq. 2.1

$$a = \frac{1 - \cos(\pi t/t_s)}{2} \tag{2.1}$$

where a is the loading amplitude, t_s is the user-defined step time, and t is the time in the simulation. This periodic loading amplitude avoids any sudden accelerations at the beginning of the simulation that could potentially happen if a ramp amplitude was used instead. Second, different loading rates, in the form of different step sizes for the same displacement, were evaluated for their impact upon peak load. The shortest step time which did not cause a change in peak load was then chosen as the step time at which to run the beam analysis. Additionally, the kinetic energy (ALLKE) of the simulation was compared to the internal energy (ALLIE) of the simulation for the chosen step time. If the kinetic energy was significantly lower (at least a couple orders of magnitude) than the internal energy of the simulation, then this helped confirm that the loading rate was not significantly influencing the deformation in the system.

Chapter 3

Effective properties for millimeter-scale struts and strut intersections (nodes) in lattice primitives fabricated via EBM

3.1 Introduction

Additive manufacturing (AM) empowers the development of architected cellular materials that achieve dramatic performance gains through topology. These gains are most notable in structures with millimeter-scale features, which lead to high specific stiffness and strength, enhanced heat transfer, and biocompatibility [24–27, 29–31]. For metal thin-walled or strut-like features, process-structure-property relationships can be intrinsically tied to component geometry, which defines thermal conduction pathways that strongly impact solidification [5, 29–31, 34, 35]. This implies that the geometry and mechanical response of thin struts often depend on (i) their orientation relative to the build direction, (*ii*) their absolute size (when feature dimensions are comparable to melt pool dimensions), and (*iii*) the local topology of intersecting walls and struts.

The implicit connections between feature properties and processing poses a significant challenge to design and characterization of AM cellular structures. Ideally, process-informed models of individual struts and strut intersections (or nodes), like those seen in Fig. 3.1(a,b), can be used to predict the response of larger scale features, such as unit cells in lattice structures (Fig. 3.1c). This approach would dramatically accelerate the design and development of lattices by narrowing the requisite scope of process-informed models to sub-scale features, or 'primitives', which are then used to predict the performance of a wide variety of full-scale topologies.

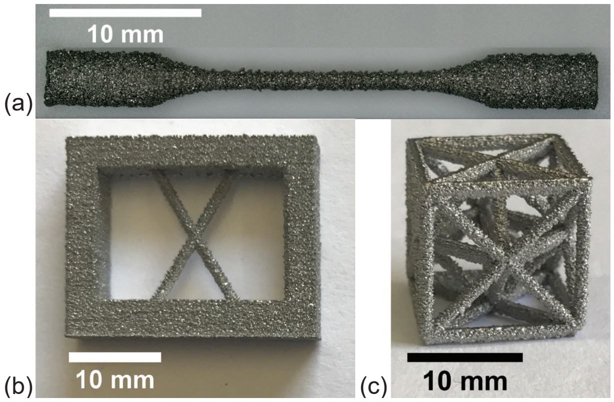

Figure 3.1: Printed primitives of lattice structures for this study. (a) Strut. (b) Multi-strut intersection (node). (c) Multi-node structure (cell).

Toward that end, this work characterizes the geometry and mechanical response of individual struts and a single connection between struts (node); simulations are conducted to infer effective combinations of geometric parameters and mechanical properties needed for accurate simulations. The study utilizes millimeter-scale Ti-6Al-4V features fabricated with electron beam melting (EBM), which are commonly used in biomedical applications due to its low density, corrosion resistance, low elastic modulus (compared with steels or cobalt nickel alloys), and proven biocompatibility [5, 8, 34–38].

The coupling of process and properties in AM materials is a rapidly growing field with extensive characterization of microstructure and process build defects [5, 7–9, 12, 20, 31, 34–36, 38, 44, 143–145]. However, the vast majority of this work focuses on bulk components, which have physical dimensions much greater than that of the melt pool. This contrasts many lattice materials whose dimensions are comparable to the melt pool; many of the conclusions stemming from bulk components will not be applicable due to differences in printing strategies and solidification pathways [45, 46]. Similarly, while there is a growing number of studies of 3D printed lattice structures, the scope is often limited in scope to the overall macroscopic response of specific topologies [5, 30, 34, 35]. The focus on macroscopic response makes translations of their insights to alternative topologies difficult (if not impossible).

This work makes the following important advances. First, the relationships between print orientation and resultant component geometry are determined with a method that directly translates geometric characterization into inputs that are used for simulations. This goes beyond previous work that has also used X-ray computed tomography (CT) to characterize the geometry of printed struts [20, 29, 84, 145]. Specifically, this work uses CT-measured geometry in greater detail than Suard, et al. [29], who used a more indirect method to determine the appropriate geometry for simulations. Second, the geometry measured by CT is used to infer material properties for the nodes and predict their mechanical behavior using FEA, which is compared to experimental results. While others [20–23] have used the real geometry of printed components to infer mechanical properties, they do not impose consistency between their reported modulus and strength values, resulting in highly unrealistic reported modulus. The results of this study provide realistic effective material properties from geometry and insight into using printed component geometry for a simulation framework for larger scale lattices. Finally, a comparison of node tests and simulations highlights the importance of surface defects in peak load and post-buckling response.

3.2 Methods

In the present study, the geometry of individual struts at various orientations was characterized using CT imaging of nodes (Fig. 3.1b) and simple lattice cells with an octet geometry (Fig. 3.1c). The cells were only used to collect orientation-dependent data from a single specimen; future publications will address their mechanical response, which is highly sensitive to defects, as demonstrated in this paper for the node geometry. Imaging of two different multi-strut structures provides insight regarding the variability of strut geometry with respect to overall architecture. Individual struts (Fig. 3.1a) printed at several orientations with respect to the build direction were tested in tension, to determine effective CT-based estimates of strut area and yield stress that capture measured response. Compression testing was also performed on the node primitives, to evaluate the feasibility of using effective strut properties to predict node response. As such, the approach involved a combination of characterization, testing and simulation.

3.2.1 Printing

Primitive samples of struts, nodes, and cells, shown in Fig. 3.1, were fabricated in Ti-6Al-4V by an EBM system (Arcam A Series, Arcam, Sweden) using a 70 µm melt theme. Additional details on the powder characteristics are available in the work by Dong, et al. [146]. Samples were printed with either a nominal strut diameter of 1 mm or 1.25 mm. Strut primitives were printed at three different orientations relative to the build plate, 0°, 45°, and 90°, with a minimum sample size of four per orientation for each nominal strut diameter. Node primitives were printed at two print orientations, 0° and 90°, with a sample size of four per orientation for each nominal strut diameter. Cell primitives were all printed at the same orientation, with a minimum sample size of eleven for each nominal strut diameter.

All samples were hot isostatically pressed (HIP) upon fabrication per ASTS F2924-14 or ASTM F3001-14 specifications [147]; components were processed under inert atmosphere at not less than 100 MPa within the range of 894 °C to 995 °C and held at the selected temperature within ± 15 °C for 180 ± 60 minutes before cooling under inert atmosphere to below 425 °C.

3.2.2 CT imaging

Four nodes and two cells were analyzed by x-ray computed tomography (CT) using a North Star Imaging System equipped with a Perkin Elmer detector with a pixel pitch of 200 × 200 µm. An average of 1440 projections were used to perform the reconstructed images. The node reconstructed images have a voxel size of either 34.38 µm or 34.44 µm over a length of approximately 20 mm. The reconstructed images for the cells have a voxel size of 27 µm over a length of approximately 17 mm. FIJI (ImageJ) software with its built-in plugins were used to quantitatively analyze the images [117].

As discussed in detail in Section 3.3, the CT images were post-processed to determine the variation in cross-sectional area along the length of the struts, using a spatial discretization equal to the voxel size. Two area estimates form the basis of the study: (1) the true cross-sectional area determined via image processing of cross-section slices, and (2) the area of an inscribed ellipse that neglects areas associated with local surface roughness. The statistics enabled by the data-rich CT images are discussed in Section 3.3, along with the implications of using various area measures to compare mechanical testing and simulated response. It should be noted that the CT results from the cells (Fig. 3.1c) were used to interpret mechanical tests; this is reasonable as the cell geometry consisted of struts with the same print orientation as the individual struts tested (Fig. 3.1a).

3.2.3 Mechanical testing

Mechanical testing was done on a Material Test System 810 servohydraulic load frame at room temperature under a displacement rate of 0.1 mm/min (approximate strain rate of 2×10^{-4} s^{-1}). Strut primitives were tensile tested to failure using custom-built stainless steel grips. Node primitives (as seen in Fig. 3.1b) were electrical discharge machined (EDM) to remove select parts of their frame to create flat, parallel surfaces for testing. These samples were secured between two hardened steel platens using superglue, and then loaded in compression until the first strut fracture. Several unloading cycles in the initial stages of loading were included to determine experimental stiffness.

Laser extensometry was used to measure the displacement between the grips in all cases; however, post-processing of the strut tensile data strongly suggested slippage of the reflective markers. As such, strut tensile results are reported in terms of cross-head displacement. Finite element calculations were conducted to account for the deformation in the tapered region of the struts to accurately connect measured stiffness to the stiffness of the gauge section.

3.2.4 Finite element simulations

Finite element simulations of the strut tensile tests were conducted to account for the tapered region and connect extracted stiffness to measured areas, using a modulus estimated from indentation tests on polished strut cross-sections. These simulations utilized purely elastic, axisymmetric finite elements in ABAQUS. Outside of the gauge region, the dimensions were determined from optical images of the struts, which produced a gauge length of 13.3 mm, a grip radius of 1.65 mm, and taper region length of 5.256 mm. To establish consistency between the measured and predicted stiffness, the uniform radius in the gauge section was varied using extracted areas from CT scans of the struts (in the cell primitives with the same orientation). The stiffness of the entire simulated geometry is compared to the measured stiffness that includes contributions from both the gauge and taper regions. All simulations used a modulus of 120 GPa (based on the indentation), which is the same modulus reported by the manufacturer [148]. The axisymmetric FEA used between 8,000 to 11,000 4-node bilinear axisymmetric quadrilateral elements.

The compression tests of the nodes were simulated in ABAQUS using elastic-linear hardening in two-dimensional, plane stress FEA. (Supplemental calculation illustrated that 3D simulations produce identical load-displacement response of the node specimens.) While Ti-6Al-4V exhibits very little strain hardening, a small amount of hardening (0.4% of the elastic modulus) stabilizes non-linear iterations during elastic-plastic buckling, without significantly impacting the macroscopic response. As with the strut modeling, the elastic modulus was assumed to be 120 GPa [148]. A parameter study was conducted to determine the combination of effective strut size (based on CT scans) and yield stress that accurately capture the node response. The 2D FEA used between 40,000 to 44,000 8-node quadratic plane stress quadrilateral elements. Additional simulations incorporating a surface defect in a strut were conducted using the same material formulation.

3.3 Results & Discussion

3.3.1 Geometry Characterization

Examples of volume reconstruction of the cell and node primitives are shown in Fig. 3.2a and Fig. 3.2b, respectively. Individual struts of different print orientations relative to the build direction, isolated from the parent cell shown in Fig. 3.2a, are shown in Fig. 3.2c. In this study, the 0° print orientation is defined as parallel to the build direction (vertical) while the 90° orientation is defined as perpendicular to the build direction (horizontal). Representative cross-sections from each of the isolated struts are also shown for each orientation. As expected and shown from Fig. 3.2, the as-printed structures display significant differences in both total area and shape, with the 90° struts tending to have larger and more elliptical cross-sections (elongated in the build direction) than the 0° and 45° struts. Three different estimates of the effective area of the struts were extracted from the CT imaging as follows.

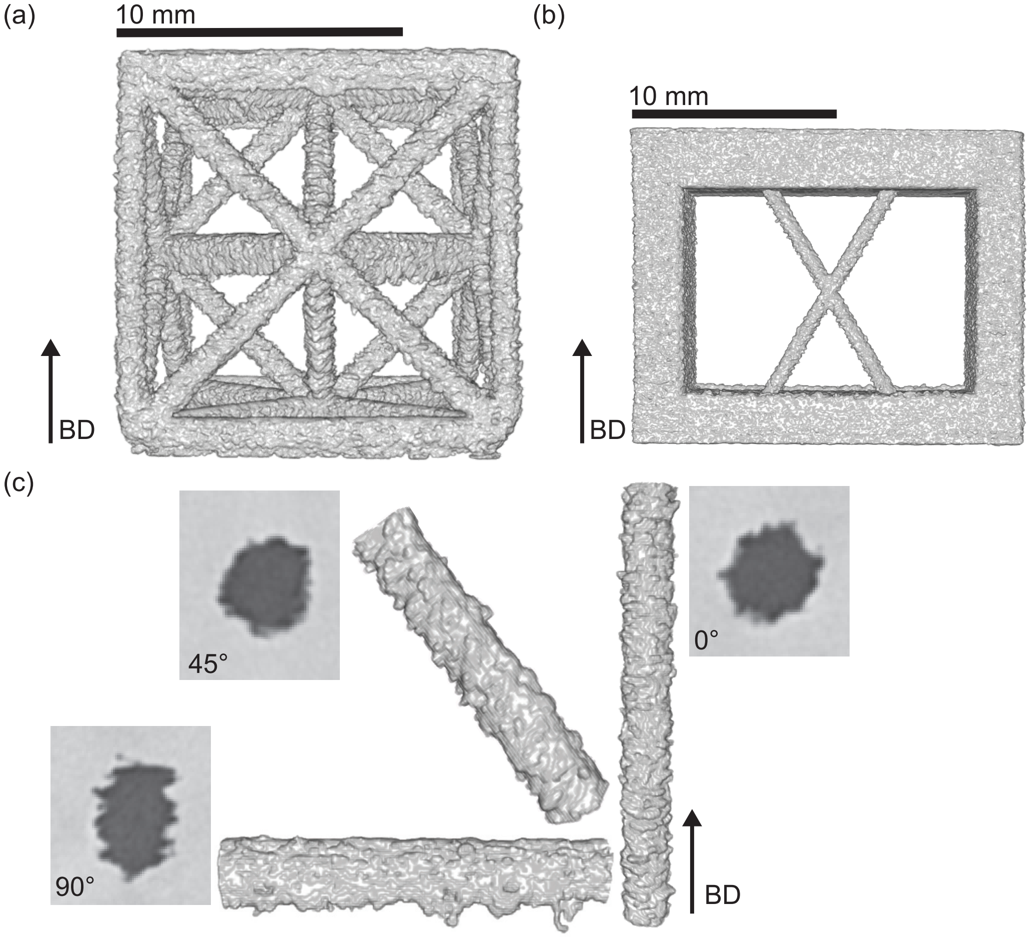

Figure 3.2: Examples of reconstructed CT volumes of primitives oriented relative to their build direction (BD). (a) Cell with 1 mm nominal strut diameter. (b) Node with 1 mm nominal strut diameter. (c) Isolated struts (not to scale) from the cell in (a) with representative axial cross-sections. The representative cross-sections highlight print-orientation dependent variations in geometry and surface roughness.

For the first metric, defined as the true (T) area, each individual image slice in the strut was binarized to isolate the cross-sectional area from the background. The area of the binarized section was then computed using FIJI's in-house 'Analyze Particles' function to calculate the area of each slice. An illustrative result of this process is shown in Fig. 3.3(a); it represents the upper bound on the effect of surface roughness upon cross-sectional area. The second metric, defined as the inscribed (I) area, serves as the lower bound on cross-sectional area, and can be visualized in Fig. 3.3(b). To obtain the I measures, the binarized areas were subject to several operations that removed the surface roughness and reduced the area such that the resultant shape approximated the maximum inscribed ellipse of the cross-sectional area. A full description of the process used to generate the I areas can be found in the Supplemental Information. The third and final metric is an average over the T and I area estimates, denoted as $\overline{\mathrm{I,T}}$, computed for each cross-sectional slice.

The results of these area analyses are shown in Fig. 3.3(c-f) in the form of non-standard box plots, for various strut orientations relative to the build direction. The area metrics are normalized by the nominal area of the struts, which is the strut cross-sectional area prescribed by the computer aided design (CAD) file, and statistics are based on averaging over all CT slices. The white bar in the center of the box in Fig. 3.3(c-f) represents the average value of the averages computed for all struts within a given print orientation; the box is bounded by the average value of the average standard deviation over all struts within a print orientation of the primitive. The whiskers indicate the absolute maximum and minimum values across all struts within a given print orientation. There are two prominent features of the data that factor into the subsequent discussion of mechanical response.

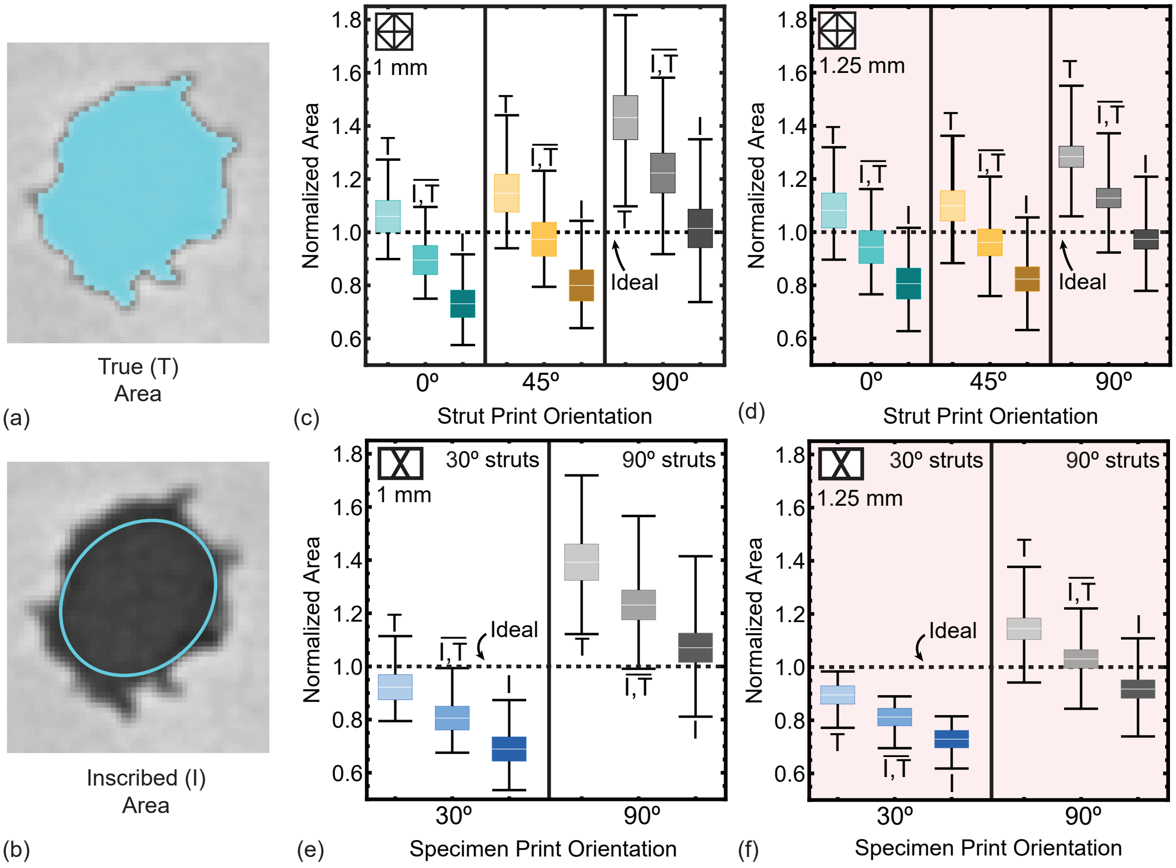

Figure 3.3: Non-standard box plots of the three different metrics of printed area normalized to nominal area grouped by strut print orientation, for cell primitives with nominal diameter of (a) 1 mm and (b) 1.25 mm, and for node primitives with nominal diameter of (c) 1 mm and (d) 1.25 mm. The three area metrics given are the true (T) area, the inscribed (I) area, and the average of the true and inscribed ($\overline{\text{I,T}}$) areas. The T and I areas can be as visualized in (a,b).

First, in both node and cell primitives of both nominal sizes, 90° struts are significantly larger than struts printed in any other orientation. This is a general trend that holds over both specimen topology and nominal strut size. As pointed out in previous efforts [29, 44, 78], this is a consequence of differences in heat conduction; for 90° struts, the heat of the melt pool is conducted primarily into the underlying powder, leading to elliptical cross-sections with larger areas. For other orientations, the heat of the melt pool is directed through previously solidified portions of the strut, leading to more equiaxed cross-sections that are smaller than the 90° struts. The implications of these variations in strut size are discussed in conjunction with the mechanical response in Section 3.3.2.

Second, while the trends in strut size vs orientation are consistent across all specimens, there can be significant differences in absolute size when comparing struts from different specimens. This is seen, for example, in comparing the 90° strut sizes in Fig. 3.3(c,e), as well as those in Fig. 3.3(d,f); recall that the 90° struts in the node primitive mean than the 'X' lies parallel to the build plane. The struts in the cell primitive are 10-20% larger than corresponding struts in the node primitives. This disparity is presumably a consequence of differences in the density of strut cross-sections in a given print layer, which impacts both thermal gradients in the layer and the time spent on any given layer. That is, the cell primitives have a greater density of struts, implying more time spent on a given layer and higher temperatures. This leads to more melting and therefore larger strut sizes.

As a final note on geometry, it is interesting to note that printing the planar node primitives parallel to the build direction (creating struts at 30°) leads to consistently undersized struts, regardless of the metric. The 30° struts in the nodes are noticeably smaller than the 45° struts in the cells; presumably, this is a consequence of the greater strut density (in the plane of the print layer) in the cells.

Besides the cross-sectional area, the surface roughness of the upskin, downskin, and two sides perpendicular to the upskin and downskin (denoted as “left” and “right”) of the struts were computed from the CT of the cell and node primitives. The average roughness and standard deviation of the arithmetic roughness ($\mathrm{R_a}$) and root-mean-square (RMS) roughness ($\mathrm{R_{RMS}}$) for the struts in the cell primitives are shown in Fig. 3.4. The measurements of valley and peak roughness ($\mathrm{R_v}$ and $\mathrm{R_p}$) are shown in Fig. 3.5. Similar measurements for the surface roughness of the struts in the node primitives are found in Fig. 3.6. The surface roughness measurements are averaged over all of the struts within a specific orientation. For each strut, the surface roughness of a specific side was averaged over five slices. A complete tabulation of the average, standard deviation, maximum, and minimum of these surface roughness measurements can be found in Appendix C.

From the $\mathrm{R_a}$ and $\mathrm{R_{RMS}}$ measurements of the struts in the cell primitives, it is evident that the 0° and 45° struts have similar roughnesses across all sides while the 90° have a significantly lower upskin roughness, higher downskin roughness and lower side roughnesses than the struts of the other orientations. This pattern holds true across both sizes of struts and there are only minor differences in surface roughness magnitude across struts. The pattern for the 90° struts is the same when it comes to $\mathrm{R_v}$ and $\mathrm{R_p}$. However, the 0° struts are subject to more severe valleys but similar peaks as the 45° struts across all of the sides. This suggests that the 0° are more defect prone in comparison to the 45° struts.

Similar to the cell primitives the surface roughness of the struts in the node primitives display minimal differences in regards to strut size. The pattern of lower upskin and side surface roughnesses and higher downskin surface roughness are maintained for the 90°

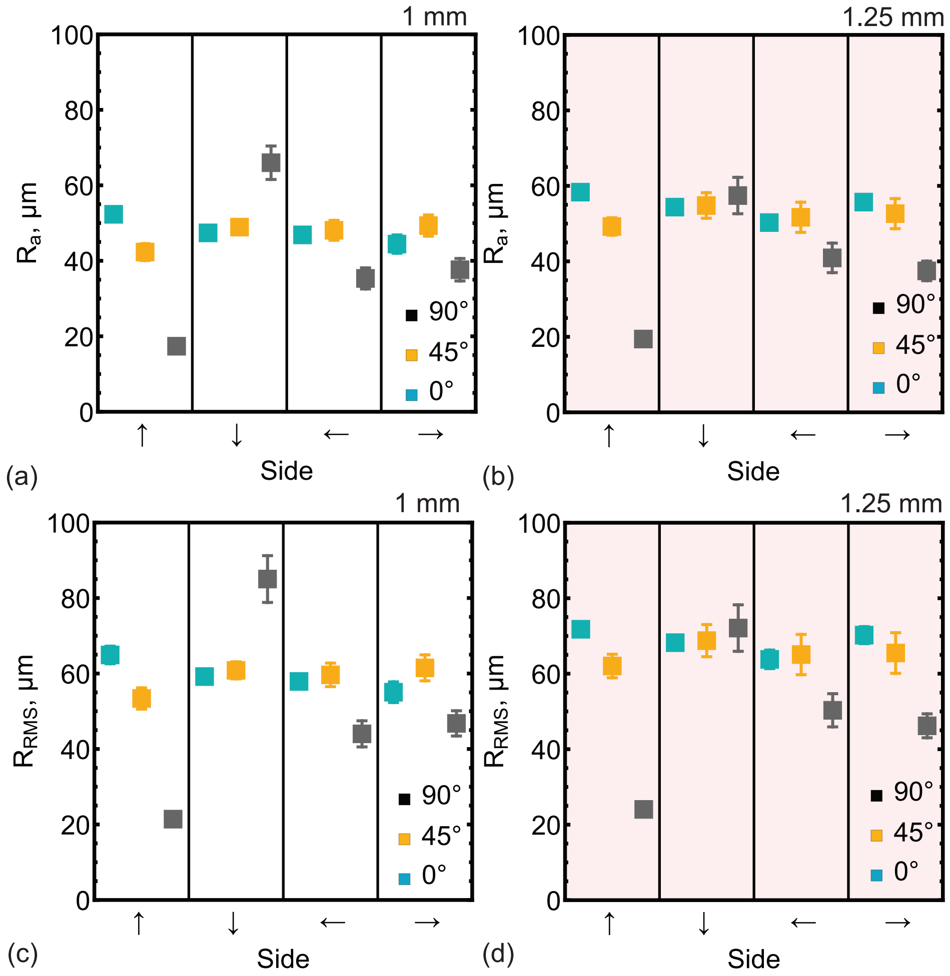

Figure 3.4: Average surface roughness and standard deviation of R_a for the (a) 1 mm and (b) 1.25 mm struts and R_{RMS} for the (c) 1 mm struts and (d) 1.25 mm struts from the cell primitives. Note that the 0° doesn't have a true "upskin" or "downskin" so the values reported in those rows are just for sides that were arbitrarily labeled "upskin" or "downskin.

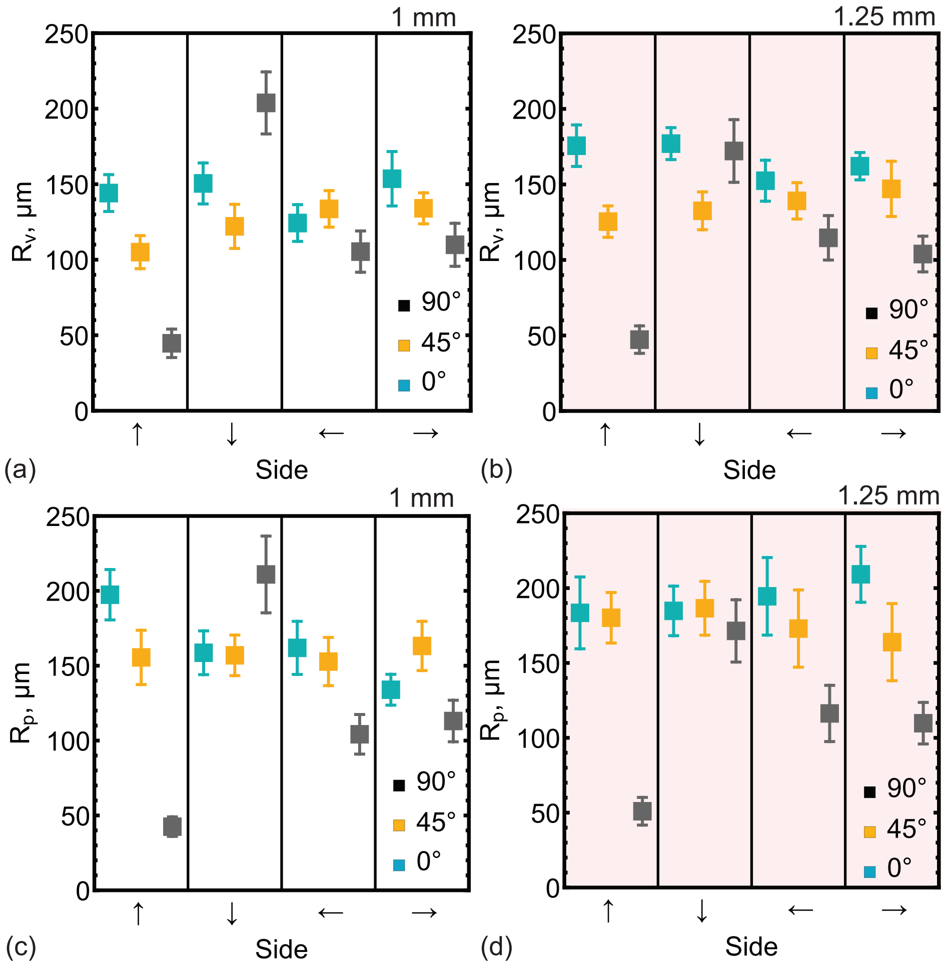

Figure 3.5: Average surface roughness and standard deviation of R_v for the (a) 1 mm and (b) 1.25 mm struts and R_p for the (c) 1 mm struts and (d) 1.25 mm struts from the cell primitives. Note that the 0° doesn't have a true "upskin" or "downskin" so the values reported in those rows are just for sides that were arbitrarily labeled "upskin" or "downskin.

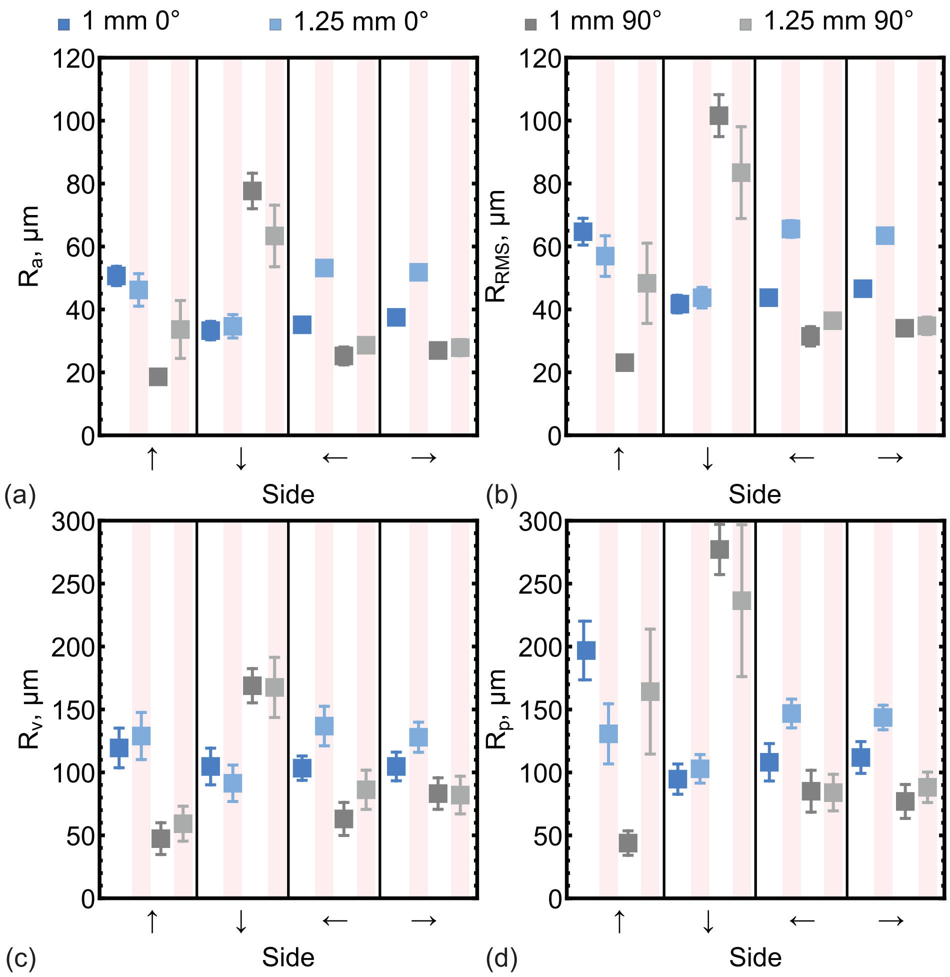

Figure 3.6: Average surface roughness and standard deviation of (a) R_a,(b) R_{RMS}, (c) R_v, and (d) R_p for the struts in the node primitives.

samples as compared to the 0° samples.

3.3.2 Mechanical response of struts

The measured mechanical response of the struts is shown in Fig. 3.7 for all print orientations and both nominal strut sizes. The stiffness (obtained via unloading segments) and the peak loads are provided in Table 3.1. As expected based on the area measurements shown in Fig. 3.2, struts printed at higher angles to the build direction are stiffer and have higher peak loads than those printed at lower angles. While precise ductility measures cannot be extracted due to the slip of the reflective tabs during laser extensometry, estimates based on the 13.3 mm uniform gage section length (which dominates deformation at higher loading) indicate failure strains $\epsilon_f \sim 1.5\%$ for the smaller (1 mm) diameter struts, and $\epsilon_f \sim 2.5\%$ for the larger (1.25 mm) diameter struts. Note that there is significant variability in failure strain from test to test.

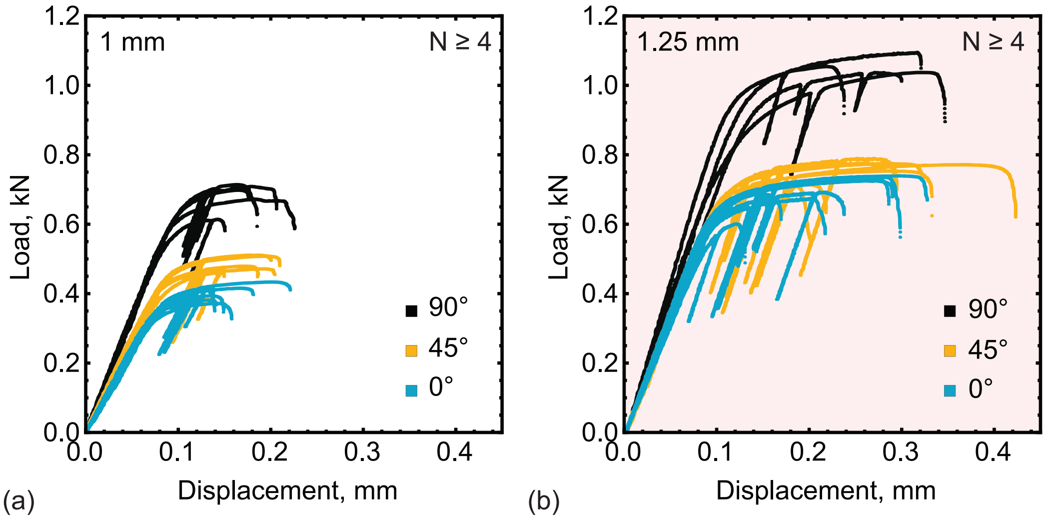

Figure 3.7: Load-displacement from tensile tests of the strut primitives printed from the same CAD file with print orientations of 0°, 45°, and 90° relative to the build direction and nominal diameters of (a) 1 mm and (b) 1.25 mm.

Orientation	Stiffness, kN/mm		Yield Load, kN		Peak Load, kN	
(N ≥ 4)	1 mm	1.25 mm	1 mm	1.25 mm	1 mm	1.25 mm
0°	4.99 ± 0.08	7.72 ± 0.22	0.393 ± 0.020	0.668 ± 0.032	0.400 ± 0.022	0.701 ± 0.044
45°	5.72 ± 0.10	8.12 ± 0.39	0.468 ± 0.021	0.707 ± 0.021	0.483 ± 0.021	0.759 ± 0.031
90°	7.18 ± 0.14	9.71 ± 0.22	0.664 ± 0.037	0.947 ± 0.073	0.678 ± 0.041	1.058 ± 0.027

Table 3.1: Strut tensile stiffness, yield load, and peak load with standard deviation.

The first question that arises is whether the variations in cross-sectional area explain differences in stiffness, and if so, which of the area metrics are predictive. To address

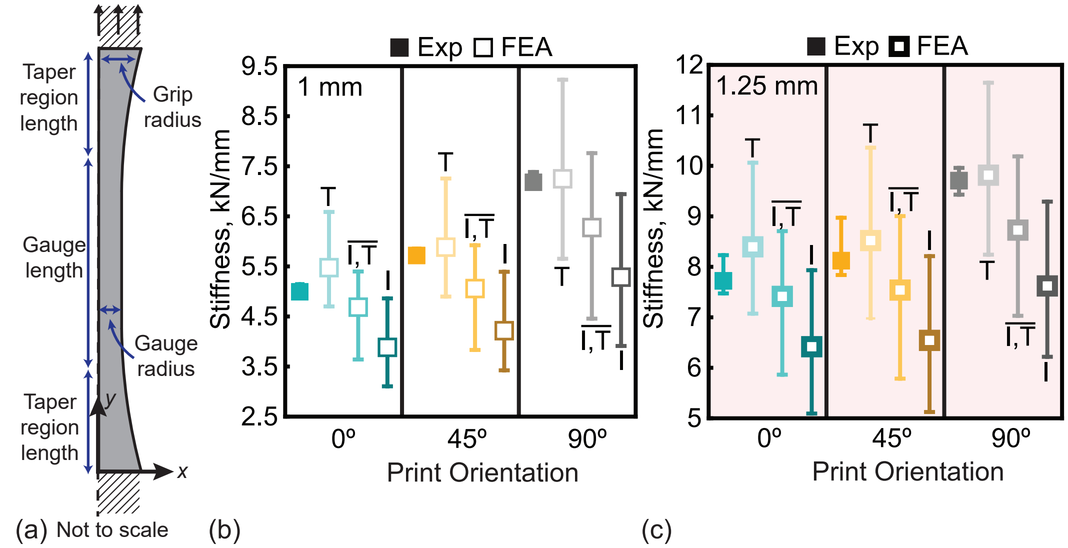

Figure 3.8: (a) Schematic of geometry and boundary conditions of axisymmetric FEA of the gauge and taper region of the strut primitives. Comparison of the experimental (Exp) stiffness to FEA stiffness for nominal diameters of (b) 1 mm and (c) 1.25 mm, using gauge radius dimensions based on the the area metrics from Fig. 3.3(c,d). The bounds indicate the maximum and minimum values while the marker provides the average.

this, CT-based area estimates were combined with finite element analysis to predict the stiffness of the specimens (FEA was used to ensure the tapered sections between the grips were properly accounted for when using cross-head displacements; as one might expect, the role of the tapered region is rather negligible). Fig. 3.8 provides a comparison of the experimental stiffness and that predicted with FEA that utilizes the three area metrics outlined in Section 3.3.1. The elastic modulus is taken to be 120 GPa; extensive nanoindentation arrays along polished struts cross-sections of all orientations yielded an average modulus of 119.9 ± 5.0 GPa [149].

The comparison illustrates that the true (T) area metric accurately predicts stiffness for larger diameter specimens (i.e. 90° struts), and slightly over-predicts stiffness for smaller diameter specimens (i.e., 0° and 45° struts). The inscribed (I) area metric clearly under-predicts the structural stiffness of the struts, indicating that the length-scale of the asperities in the axial direction is sufficient for them to carry a significant fraction of the load. Since the true (T) area slightly over-predicts stiffness, there is *some* effect of the surface roughness, as cross-sections with larger areas than the inscribed ellipse have a slightly lower average stress than the core of the strut.

While it is tempting to conclude that the true (T) area is the only metric needed to predict mechanical response, the results of Fig. 3.9 clearly indicate otherwise. Here, the measured peak load is combined with CT-based area metrics to predict the effective ultimate strength of the struts. Values from the literature for EBM-printed Ti-6Al-4V are also included, for both bulk and small-scale components. Estimates based on true (T) area produce anomalously low effective yield strengths, while those based on inscribed (I) ellipses are more consistent with prior studies.

Considerations of net-section yielding in materials with low-hardening provide a clear rationale for using the inscribed (I) metric, as the peak load will be reached when plasticity localizes in the narrowest cross-section (note that the material lacks sufficient hardening to spread plastic deformation in the axial direction). Averaging the inscribed and true area metrics ($\overline{\mathrm{I,T}}$) leads to results in the range of previously reported values, but are still 20% lower than the values reported by Persenot, et al. [20], who also studied HIP slender structures and reported mechanical properties inferred from CT geometry. Simply put, strut yielding is controlled by local defects while elastic response is relatively insensitive to them.

Even after accounting for differences in surface defects (as captured by the inscribed (I) area metric), clear evidence of orientation-dependent material behavior remains. Note

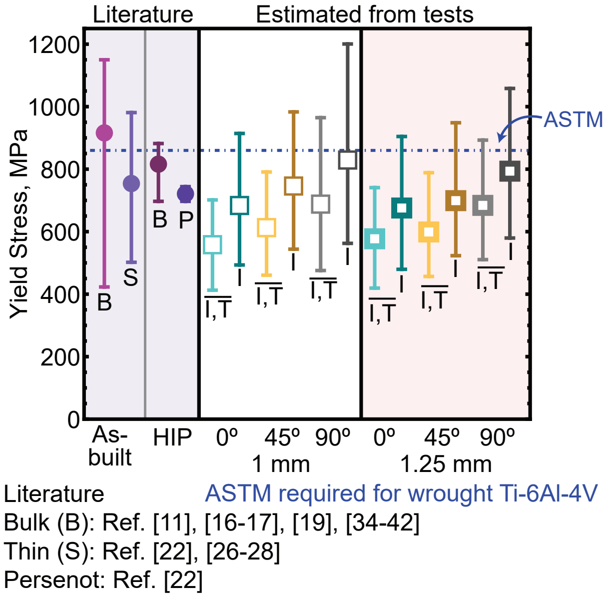

Figure 3.9: Comparison of reported yield stress from literature and ASTM required yield stress for wrought Ti-6Al-4V to those estimated using the I and $\overline{\text{I,T}}$ area metrics from Fig. 3.3(c,d). The literature value comparisons include as-built (no heat treatment) and HIP bulk (B) parts [7–19] and thin parts (S) tested by [20–23]. Persenot, et al. [20] was the only author to report thin HIP (P) parts (parts were printed in 0° orientation). The estimated values were computed by dividing the 0.2% offset yield load from the tensile test in Fig. 3.7 by the I or $\overline{\text{I,T}}$ areas in Fig. 3.3(c,d). The bounds display the maximum and minimum while the marker represents the average value

from Fig. 3.9 that regardless of the area metric used, there is still a 15-20% difference in yield strength between the 0° and 90° strut angles. Preliminary studies of local indentation hardness along struts from the cell primitives show similar variations; characterization of the underlying microstructural origins of the difference is complicated by the anisotropy of Ti-6Al-4V and is currently on-going [149].

It is worth noting that the true material yield stress in the struts is likely immaterial for the design and simulation of lattices; explicit representation of surface defects in a printed lattice is difficult (if not impossible) to define and prohibitively expensive to simulate. In essence, effective measures of area and yield stress are needed to accurately capture strut response; once such properties are identified for struts, the question remains as to whether or not they are applicable to other multi-strut structures. This is addressed in the next section.

3.3.3 Mechanical response of nodes

The load-displacement responses of the node primitives shown in Fig. 3.1b are depicted in Fig. 3.10, for two different orientations and two difference strut sizes (four tests for each condition). The 0° degree specimens imply that the plane of the ‘X’ is aligned with the build direction, while the 90° specimens imply the ‘X’ is printed laying down parallel to the build plate. The image of a collapsed node in Fig. 3.10b is representative of the post-buckling deformation that occurs after peak load has been reached. Finite element simulations were conducted with various combinations of strut sizes (defined by CT area metrics) and yield stress values. Tables 3.2 and 3.3 summarize the measured stiffness and peak loads from the node tests, along with the FEA predictions using strut-

Stiffness, kN/mm	Node			
	1 mm, 0°	1 mm, 90°	1.25 mm, 0°	1.25 mm, 90°
Exp (N ≥ 4)	6.27 ± 0.10	9.72 ± 0.82	9.05 ± 1.67	12.83 ± 3.15
$\overline{\text{T}}$	7.71 (+23%)	11.04 (+14%)	11.59 (+28%)	14.12 (+10%)
$\overline{\text{I,T}}$	6.75 (+7.7%)	**9.77** (+0.5%)	10.53 (+16%)	**12.75** (-0.6%)
I	**5.80** (-7.5%)	8.52 (-12%)	**9.48** (+4.8%)	11.36 (-11%)

Table 3.2: Comparison of experimental node stiffness (mean and standard deviation) to simulation stiffness with percent difference.

based properties. The property combinations that yield the closest agreement for each case are highlighted in bold. Illustrations of the predicted load-displacement response of the nodes are shown in Fig. 3.11 for several property combinations.

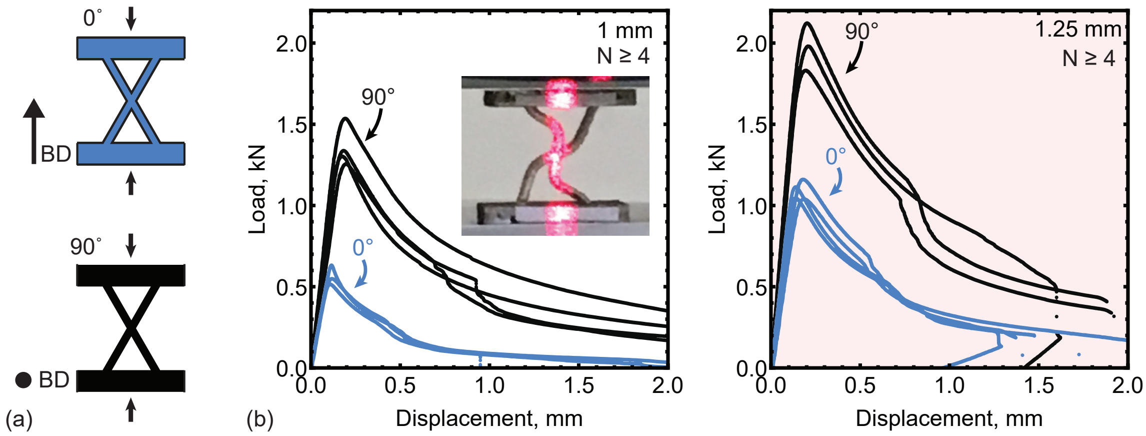

Figure 3.10: (a) Schematic depicting testing direction relative to build direction for compression tests of nodes with print orientations of 0° and 90°. Load-displacement from compression tests of nodes with nominal strut diameters of (b) 1 mm and (c) 1.25 mm.

As with the strut tests, the area metrics that accurately capture the stiffness of the structures are first considered; a comparison of measured and predicted values is given in Table 2. The $\overline{\text{I,T}}$ metric produces the smallest error over all cases (two sizes and two orientations), with excellent agreement for the 90° specimens. The $\overline{\text{I,T}}$ metric over-predicts the stiffness for the two 0° specimens, though it should be noted that the largest error

Peak Load, kN	Node			
	1 mm, 0°	1 mm, 90°	1.25 mm, 0°	1.25 mm, 90°
Exp	0.58 ± 0.06	1.37 ± 0.12	1.09 ± 0.06	1.98 ± 0.15
Area Metric	I	$\overline{\mathrm{I,T}}$	I	$\overline{\mathrm{I,T}}$
$\sigma_y^{\overline{\mathrm{I,T}}}$	**0.57** (-1.7%) (613 MPa)	1.14 (-17%) (688 MPa)	0.92 (-16%) (599 MPa)	1.49 (-25%) (684 MPa)
$\sigma_y^{\overline{\mathrm{I,T}}}$ Range	0.47–0.67 (543–682 MPa)	0.89–1.40 (564–813 MPa)	0.78–1.07 (533–665 MPa)	1.19–1.80 (564–804 MPa)
σ_y^{I}	0.68 (+17%) (746 MPa)	**1.36** (-0.7%) (829 MPa)	**1.07** (-1.2%) (699 MPa)	**1.72** (-13%) (793 MPa)
σ_y^{I} Range	0.57–0.79 (671–821 MPa)	1.11–1.64 (704–954 MPa)	0.92–1.23 (627–771 MPa)	1.42–2.05 (674–913 MPa)

Table 3.3: Comparison of experimental node peak load (mean and standard deviation) to peak load of simulations with best fit area metric from Table 3.2 with percent difference.

(1.25 mm diameter specimen) falls within the standard deviation of the tests. In all cases, the true (T) area metric significantly over-predicts the stiffness. While the inscribed (I) area metric provides the minimum % error for the 0° print orientations, the error is only marginally better for the smaller struts, and there is large standard deviation of the larger struts. With the strut tests, the true (T) area metric had the smallest overall error but the $\overline{\mathrm{I,T}}$ metric is only slightly worse (error-wise). When considering both the struts and nodes together, the $\overline{\mathrm{I,T}}$ metric is arguably the "best practice" metric for accurately estimating stiffness across all print orientations.

A comparison of measured and predicted peak loads for the nodes is provided in Table 3. The results illustrate that, as with the struts, the best predictions are obtained with the elevated yield stress values obtained from struts using the inscribed (I) area metric. Note that in all cases, the measured peak loads fall within the predicted standard deviation arising from the yield stress based on the I metric (the results for the 90°, 1 mm struts are the single outlier; this is likely due to the role of defects, discussed below). The peak loads of the node specimens are significantly underestimated if one utilizes the

$\overline{\mathrm{I,T}}$ area metrics for the struts. As was the case with the struts, this provides strong supporting evidence that inferring material yield stress values from stiffness-derived area metrics will underestimate response.

While the above discussion focused on the best single area metric and yield stress metric that minimized error across all specimens, it is clear that for any single case, the best predictions are based on different property combinations. A comparison of the measured and simulated load-displacement response (Fig. 3.11) reveal two interesting features that highlight the challenge of extracting properties of AM-printed structures.

First, the simulated response shows a stable 'hardening' response after initial yielding in all cases, despite the fact there is no hardening in the material. This stems from the fact that the simulated strut intersection yields prior to strut yielding; increasing loads are required to spread plastic deformation from the intersection into the struts themselves. In contrast, the experiments exhibit significant softening after the onset of initial onset of non-linearity, and peak loads obtained at smaller applied displacements. One possibility is that the intersection region has a higher yield stress than the struts; this would presumably elevate the load at which non-linearity is evident and make the transition from intersection yielding to strut yielding more abrupt.

Second, the transition from intersection yielding to strut yielding is likely strongly impacted by the presence of isolated surface defects, represented by the extremes of the measured areas. Consider, for example, the case for the node with the 1 mm diameter struts printed in the 0° orientation, Fig. 3.11(a,b). This case is likely to be more prone to the influence of surface defects, as they are larger in comparison to the nominal area. For sufficiently large defects, strut yielding may coincide with node yielding, such that

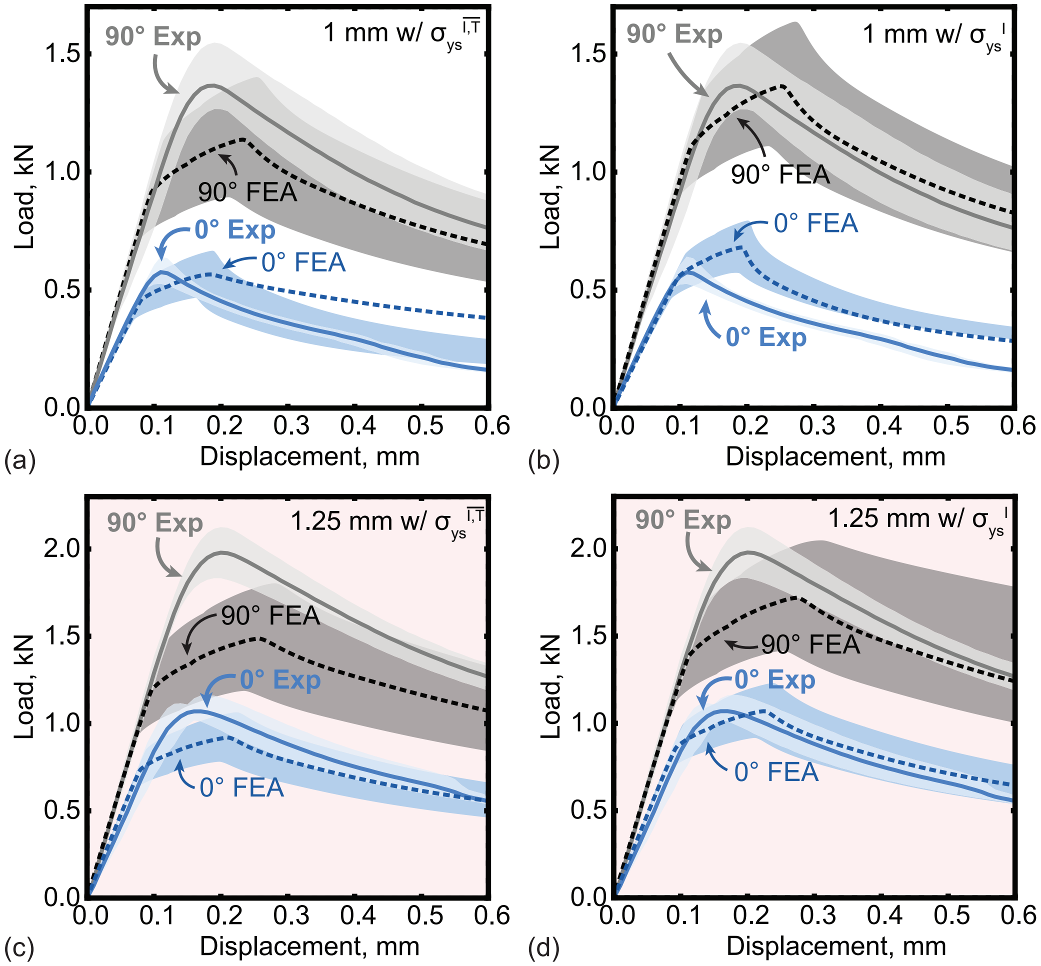

Figure 3.11: Comparison of interpolated load-displacement (showing average load--displacement bounded by the range) of experimental node (Exp) compression to 2D FEA of nodes using the best fit area metrics from Table 3.3. 1 mm nominal diameter nodes with yield stress based on (a) $\overline{\text{I,T}}$ metric and (b) I metric from Fig. 3.9. 1.25 mm nominal diameter nodes with yield stress based on (c) $\overline{\text{I,T}}$ metric and (d) I metric from Fig. 3.9.

the onset of yielding coincides with peak load. Further, the response after peak loading would likely lead to lower loads (for a given displacement), due to the formation of a plastic hinge at the defect.

To corroborate the hypothesized role of defects, additional simulations were conducted with a small notch defect, as shown in Fig. 3.12a. Numerous simulations were run with notch depths defined by the difference of the minimum inscribed area metric and maximum of the true area metric, which correspond to depths that were 12-31% of the effective strut width. The notch height was set to 0.1 mm; additional simulations with larger heights showed negligible differences. Simulated notch locations are shown in Fig. 3.12a; those further from the ends of the struts had the most marked impact and the results are shown in Fig. 3.12b. Note that the simulations with defects bring the onset of non-linearity and peak load into coincidence; further, simulations that use yield strengths based on the inscribed area metric bracket the experimental peak load, and bring post-buckling response into closer agreement.

These results make a compelling case that the details of response near the peak load are strongly influenced by the presence of surface defects, which alter the transition from node yielding to strut yielding. That said, these effects are limited to the *displacement* at which peak load is reached; in nearly all cases, the peak load is reasonably predicted with the estimate of yield strength based on inscribed (I) area.

Finally, while the yield stress estimated from inscribed areas provides the closest estimate of peak load (see Fig. 3.11(b,d) and Table 3.3), the data suggests that the one is still likely to underestimate peak loads using the yield stress inferred from the struts. That is, the experiments fall within the standard deviation resulting from yield stress

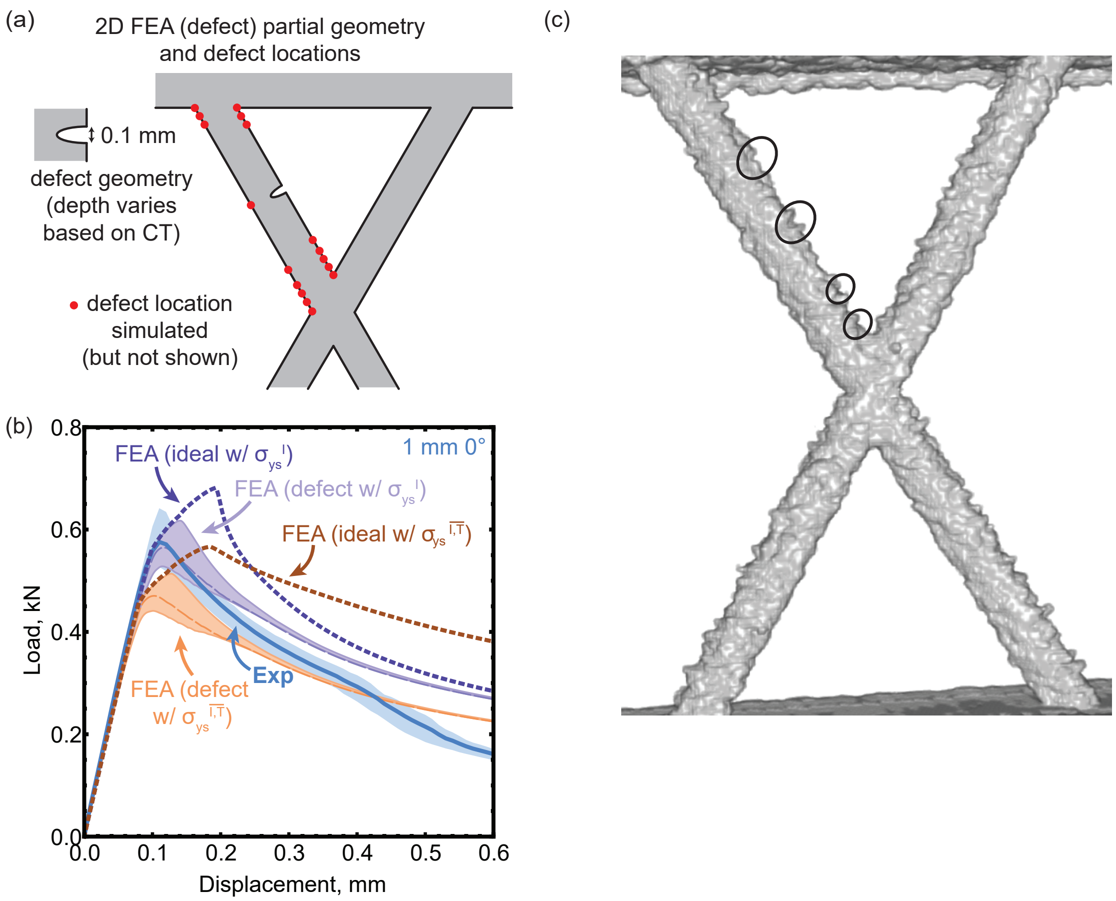

Figure 3.12: (a) Schematic depicting the location of the defect incorporated in the simulations shown in (b) along with red dots marking all the locations of defects simulated but not shown. (b) Load-displacement of 2D FEA of compression test of a 0° node with nominal strut diameter of 1 mm, using the average I geometry with a central strut defect incorporated (as shown in schematic in (a)) compared to the ideal (no notch) case and experimental (Exp) results. The notch size varies based on comparisons of the minimum I area. The minimum defect depth (highest peak load within the defect simulations) was based on the ratio of the min I area to the avg I area. The maximum defect depth was based on the ratio of the min I area to the max T area. The “average” defect depth (dotted line within the defect simulations) was based on the ratio of the min I area to the max I area. (c) CT reconstruction of one of the 1 mm 0° nodes with several print defects along one strut highlighted. Note that the lines on the CT image are voxels from the CT reconstruction and not print layers.

variations, but have consistently higher loads than the average. This would naturally arise if the material in the strut intersection exhibits a higher yield stress than the struts; future studies are needed to determine if such a difference arises from differences in the thermal history of the nodes.

3.4 Conclusions

Extensive geometric characterization and mechanical testing of HIP EBM Ti6-Al-4V lattice primitives has revealed a strong print orientation dependence on the resultant geometry and mechanical response of the parts. The main conclusions from these experiments and simulations are as follows:

- Cross-sectional area metrics from CT scans illustrate variations with print orientation that are broadly consistent across different geometries. The average of the true area and inscribed area metrics ($\overline{\mathrm{I,T}}$), in general, produces the most consistent predictions of strut and node stiffness prior to the loss of linearity.

- The yield stress inferred from strut tests strongly suggests that strut yielding is controlled by local yielding at locations with minimal cross-section; using the area metric that matches stiffness leads to anomalously low estimates of yield stress, which fail to predict peak loads. Estimating the yield stress from inscribed area metrics leads to values that are consistent with the literature for bulk specimens.

- Building off of the previous two points, accurate simulations will require effective strut sizes and properties that are derived from different area metrics, chosen to ensure consistency with actual stiffness and peak loads.

- The peak load of node specimens (strut intersections) is best captured using estimates of yield stress based on inscribed area measurements on struts, supporting the conclusions based on strut behaviors.

- Differences between simulations and the experiments suggest that the local properties and extreme defects likely have a significant impact on the displacement associated with peak load and post-buckling behaviors. These differences are most pronounced for smaller struts with orientations aligned with the build direction. Future investigations will focus on mechanical properties of strut intersections and defect sensitivity of these structures.

Chapter 4

Effective geometry and properties of L-PBF stainless steel 316L thin strut intersections (nodes) built with varying processing conditions

4.1 Introduction

Additive manufacturing (AM) empowers the development of complex geometries, which cannot be easily created using conventional, subtractive methods. AM notably allows for the creation of architected, cellular materials, which can achieve dramatic performance gains in material properties [24–27, 29]. Most applications that demand high specific stiffness and strength, enhanced energy absorption capability, and improved heat transfer require millimeter-scale thin walls or struts to reach beneficial relative densities with a reasonable number of cells [24–28, 150]. For features with this length-scale or smaller, properties are intrinsically tied to component geometry, which defines thermal conduction pathways that strongly impact melting and solidification [28, 29, 45, 73, 75, 151–157]. As a result, the mechanical response of strut-like features can be different from those of bulk properties, which poses significant challenges to the design of the topology utilized in printed lattices.

Ideally, the response of multi-celled lattice structures can be predicted using process-informed models of individual struts and strut intersections (or nodes). This would dramatically accelerate the design process of lattices by reducing the characterization needed for these simulations to simple sub-structures, defined here as "primitives". Towards that goal, this work characterizes the effect of input processing parameters and sample thickness upon the geometric characteristics and mechanical performance of the simple lattice "X" primitive shown in Fig. 4.1. This study is focused on millimeter scale struts comprising stainless steel 316L (SS316L), although a similar study on Ti-6Al-4V is available [146]; the principal distinction of the two studies is that SS316L exhibits much greater strain hardening and ductility [39], and as such, requires a more sophisticated treatment of plastic properties.

In order to develop process-informed models useful to design, one must account for differences between nominal (CAD-based) geometry and as-printed geometry, as well as deviations from bulk material response that may arise due to small sample size. In this work, CT imaging of the samples prior to deformation are used to address the first challenge, while the second is addressed with a combination of finite element simulations and mechanical testing with in situ digital image correlation (DIC). Effective material properties in the structure (taken to be spatially uniform) are inferred by comparing macroscopic load-displacement response of the structure to simulations with various input material parameters. Insight regarding the accuracy of the material model and potential role of spatial property variations is obtained by comparing DIC strain maps to those generated

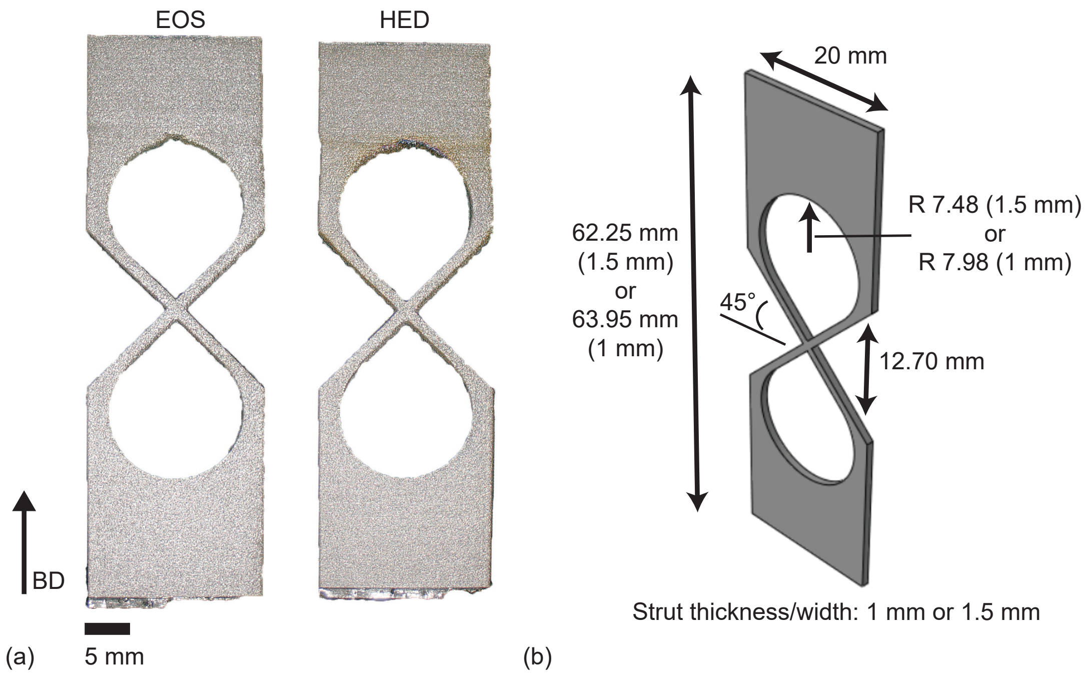

Figure 4.1: (a) Optical images of the L-PBF SS316L printed “X” primitives. (b) Schematic depicting the prescribed dimensions of the specimens.

from finite element models.

This work extends the growing body of work focused on the characterization of processing and microstructure in AM materials [39, 61, 73, 75, 151–153, 157–181]. However, many of these studies only focus on bulk components, which have physical dimensions much greater than the melt pool; a central objective of this study is to determine whether characterization of bulk specimens is applicable to lattice materials, which have dimensions on the order of the melt pool [45,73,75,156]. While studies of thin-walled structures fabricated via AM continue to emerge, work to date is primarily focused on the overall macroscopic response of specific topologies or on topology optimization [170–179]. Because macroscopic lattice response is heavily dependent on a given topology, it is difficult (and often impossible) to translate the insights of these studies to other topologies.

Prior work on thin-walled structures made of laser powder bed fusion (L-PBF) SS316L [73, 75, 151, 172, 179–187] has highlighted the need for more detailed connections between geometry, material properties and macroscopic response. These studies are primarily focused on characterizing the resultant microstructure of thin parts or they mechanically test struts with little regard to actual printed area. Without careful attention to the difference between nominal and as-printed geometry, one can infer unrealistic (at worst) or ambiguous (at best) material properties, notably elastic moduli [172, 179, 181–186, 188]. Efforts to fully quantify both geometry and mechanical properties are arguably more advanced for titanium alloys fabricated with electron beam melting (EBM) (e.g. [20–23, 29, 146, 188, 189]). That said, studies that rigorously connect geometry, material properties, measured initial stiffness, peak load and post-yielding response are limited. The authors' prior work in Ti-6Al-4V provides a review of this literature, and illustrates that the approach taken here may be broadly applicable to the characterization of thin struts and strut intersections fabricated from a variety of materials via different methods [146].

The important contributions of this paper, which largely follow the sequence of characterization and analysis used, are presented as follows. Section 2 presents an overview of the fabrication, characterization and analysis methods: printing, pre-test CT imaging, mechanical testing with in situ DIC imaging, and finite element simulations. In Section 3, CT area measurements are used to identify effective areas that bring simulated and measured stiffness into agreement. This section also makes the case that one can infer effective area measurements from surface roughness parameters, which has important implications for future approaches that do not perform full CT characterization of the specimens. Section 4 utilizes qualified area metrics to conduct a comparison of simulated and measured post-yielding response of the specimens and infer elastic-plastic properties of the material in the specimen. Section 5 provides a discussion of the broader implications of the study using a comparison of simulated and measured strain maps, and consideration of porosity in the specimens. Key conclusions are summarized in Section 6.

4.2 Methods & Illustrative Results

In this study, lattice “X” primitives (Fig. 4.1) with nominal square cross-sections were printed to have a thickness of 1 mm or 1.5 mm, using two sets of processing conditions, which on aggregate translate to having one set with a higher energy density than the other. Although energy density has some limitations in fully capturing variations in processing conditions between different builds, for simplicity the samples having the aggregate higher energy density will be referred to as HED [49,71]. The printed primitives were then characterized using x-ray computed tomography (CT) to quantify the role of processing condition and nominal thickness upon printed area, surface roughness, and internal porosity. Then, the samples were tested in tension, with the objective of determining how processing condition influences primitive response. Effective strut area and material properties were determined by a comparison of measured response to finite element simulations which used various estimates based on CT imaging and manufacturer-provided (manuf.) mechanical properties.

4.2.1 Printing

Primitive samples with an “X” geometry, shown in Fig. 4.1, were fabricated using SS316L powder with an average particle size of 22.7 µm by an EOS selective laser melting (SLM) system (EOS M290, EOS GmbH, Germany) using the default manufacturer parameters and a set of parameters that result in a higher energy density than the default. The parameters using the default (EOS-recommended) and the higher energy density (HED) can be found in Table 4.2. The chemical composition of the powder used for the samples is shown in Table 4.1, as first tabulated by Britt, et al. [151]. The rationale behind the selection of the parameter set for the HED samples can be found in the same study [151]. All samples were printed in the same build orientation (shown in Fig. 4.1) on the same build plate made of 1030 carbon steel. Upon the build plate, samples of the same thickness were spaced 0.35 mm apart while samples of different thicknesses were placed 20 mm apart for improved buildability and support. A bi-directional scan pattern with 60° rotations was used between each build layer. In addition, different energy contours were used for the top (upskin) and bottom (downskin) 120 µm of each inclined surface, with the parameters indicated in Table 4.2. There were two samples per nominal thickness and process parameter set for a total of eight samples that were analyzed in this study.

Fe	Cr	Ni	Mo	Mn	Si	N	O	C	Cu	S	P
64.7	18.07	13.13	2.26	0.91	0.71	0.072	0.03	0.02	0.015	0.011	0.006

Table 4.1: Chemical composition of the powder used for the samples. The average particle size was 27.7 µm.

Process	Laser power, W	Laser speed, mm/s	Hatch distance, µm	Layer thickness, µm	Energy density, J/mm^3
EOS	214.2	928.1	100	40	57.7
HED	100	250	109.2	40	91.6
Upskin	150	515	100	40	72.8
Downskin	74	951	90	40	21.6

Table 4.2: Processing parameters.

4.2.2 CT imaging

All samples were analyzed by x-ray computed tomography using a ZEISS Xradia Versa 520. The reconstructed images have a voxel size of 12.6 µm over a length of approximately

12 mm. FIJI (ImageJ) software with its built-in plugins was used to quantitatively analyze the images [117]. For every length equivalent to the voxel size along the struts in the primitives, the cross-sectional area and porosity was determined via image processing. Additionally, for every length equivalent to the voxel size through the thickness of the samples, the upskin and downskin surface roughness of each strut was determined. This was done by (1) creating an outline of the surface roughness from the strut lengthwise (example shown in Fig. 4.2f), (2) determining the coordinates of the upskin and downskin roughness, respectively, and (3) computing the mean line for each set of roughness coordinates, in addition to using the coordinates to compute the relevant roughness metrics of R_a, R_RMS, R_v, and R_p (arithmetic mean roughness, root-mean-square roughness, maximum valley depth, maximum peak height) [190]. For the nodes in the primitives, 15 images around and including the minimum cross-section in the node for the 1 mm nominal thickness and 22 images for the 1.5 mm nominal thickness were analyzed to determine the cross-sectional area and porosity. Representative reconstructions of the CT images as well as example cross-sections used to determine cross-sectional area, porosity, and surface roughness are shown in Fig. 4.2.

4.2.3 Mechanical testing

Mechanical testing was done on a Material Test System 810 servohydraulic load frame at room temperature under a displacement rate of 0.5 mm/min (approximate strain rate of 6.6×10^{-4} s^{-1}). The “X” primitives were pulled in tension using hydraulic wedge grips. Samples were tested to failure as shown in Fig. 4.3(a). The stiffness of the elastic regime and yield load were determined from these tensile tests – Fig. 4.3(b) illustrates how these parameters were determined. Table 4.3 tabulates the stiffness, yield load, and failure displacement from all samples. In all tests, full field strain measurements were made

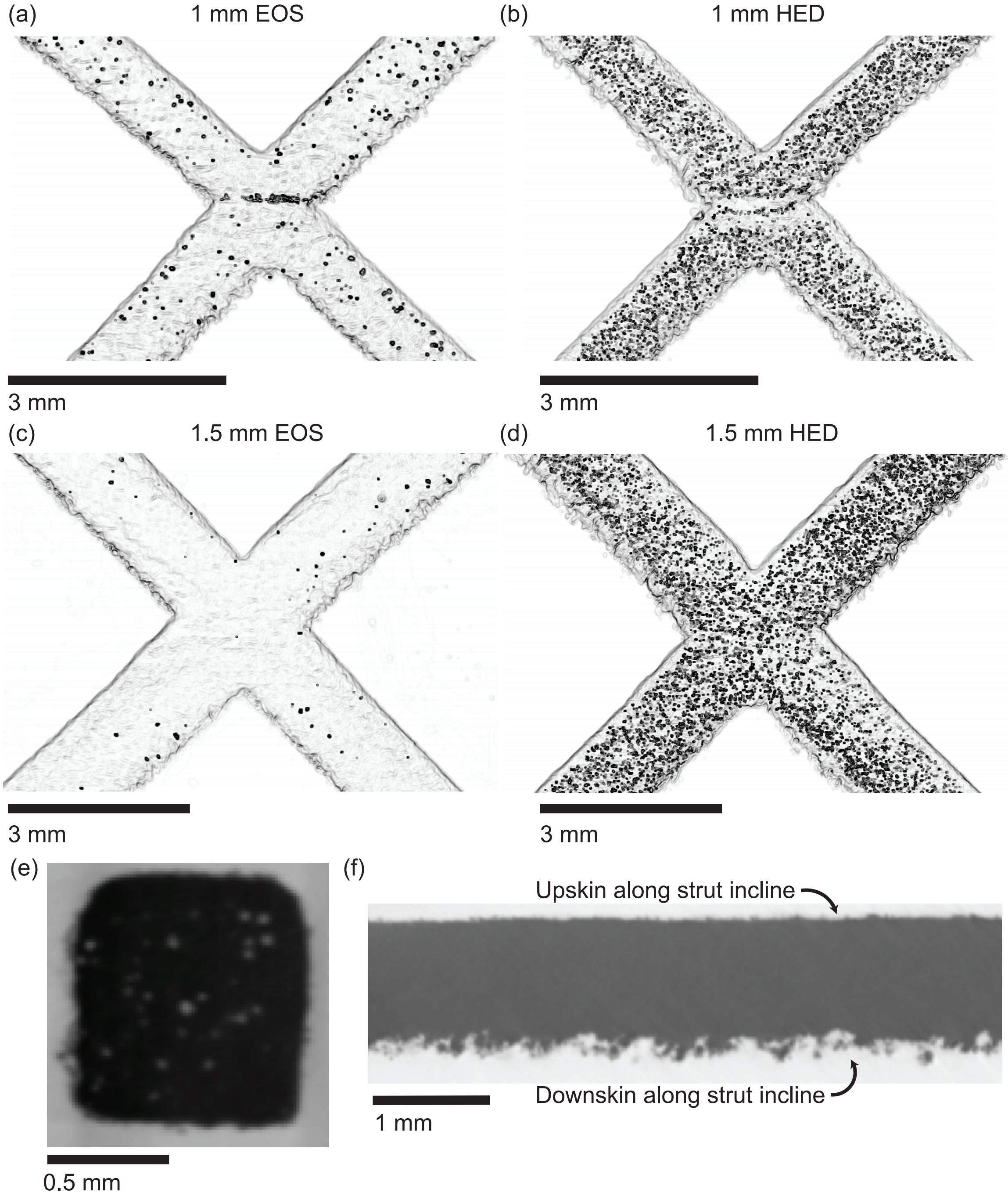

Figure 4.2: (a-d) Representative reconstructed CT scans of all "X" primitives. Example cross-sections used for calculating (e) area and porosity and (f) surface roughness.

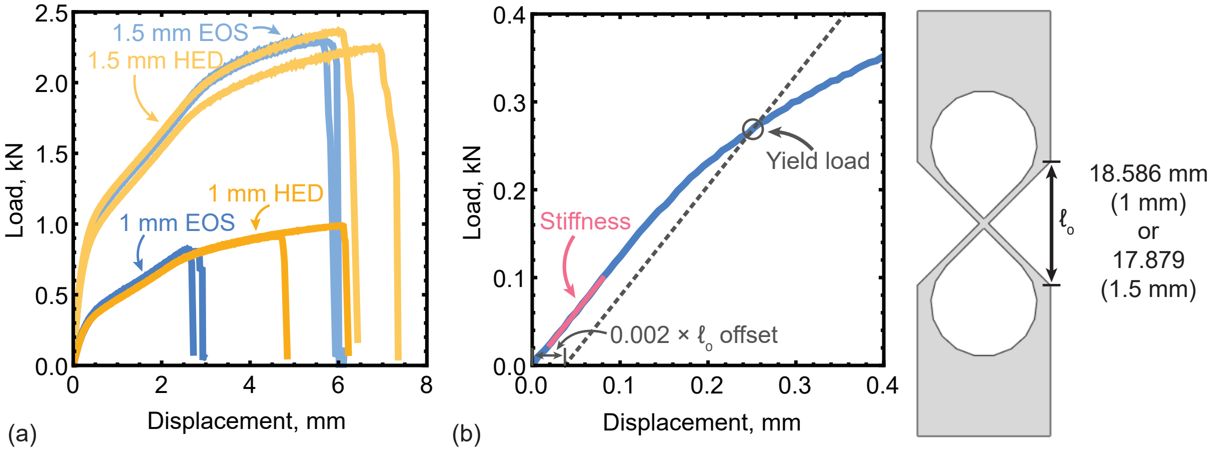

Figure 4.3: (a) Full range load-displacement from all tension tests. (b) A single tension test at low displacement with graphics illustrating how stiffness and yield load were computed.

Process	Stiffness, kN/mm		Yield load, kN		Failure displacement, mm	
	1 mm	1.5 mm	1 mm	1.5 mm	1 mm	1.5 mm
EOS	1.24 ± 0.03	4.04 ± 0.01	0.251 ± 0.028	0.660 ± 0.002	2.68 ± 0.13	5.51 ± 0.14
HED	1.20 ± 0.01	4.18 ± 0.30	0.251 ± 0.009	0.663 ± 0.044	5.34 ± 1.00	6.42 ± 0.56

Table 4.3: Measured sample tensile stiffness, yield load, and failure displacement with standard deviation.

using 2D Digital Image Correlation (DIC) (Vic-2D, Correlated Solutions, Columbia, SC). The purpose of these measurements were to (1) obtain an accurate measure of macroscale displacement and (2) ascertain if the processing variations led to strain localization in these structures. The strains and displacements were defined with respect to the global coordinate system, characterized by the tension direction and its normal. Images were taken using a scale factor of 13.6 µm/pix and were correlated using a subset size of 17–19 pixels (231–258 µm) and a step size of 2 pixels (27.2 µm). Prior to testing, the samples were coated in flat white paint before being speckled with a Paasche airbrush filled with water-soluble black paint, as per the best practices outlined by Rajan, et al [122].

4.2.4 Finite element simulations

Finite element simulations of the “X” primitives under tension were conducted to determine effective strut size and to compare inferred material properties based on processing condition to the manufacturer-provided properties. These simulations utilized elastic-plastic two-dimensional plane stress finite elements or three-dimensional continuum brick finite elements in ABAQUS, with plasticity defined by input yield stress and ultimate tensile stress fit to the form of an exponential based on the Hollomon strain-hardening equation [191]. The 3D FEA results yielded identical load-displacement results to the 2D FEA results but had minor variations in surface strain distributions. Initial simulations were based on the average manufacturer-provided yield stress and ultimate tensile stress [192] with strain hardening behavior based on the hardening exhibited by L-PBF SS316L tensile specimens in Suryawanshi, et al [160]. Subsequent simulations to determine effective material properties used input yield stress and ultimate tensile stress that deviated from manufacturer-stated properties. All simulations used a modulus of 180 GPa and density of 7.9 g/cm^3. A small amount of horizontal displacement that was 16.7% of the vertical displacement was prescribed to mimic the slight sample misalignment seen in DIC of the experiments. These boundary conditions are illustrated in Fig. 4.4(a). The 2D FEA used between 42,000 to 57,000 8-node quadratic plane stress quadrilateral elements while the 3D FEA used 537,000 to 1,102,000 20-node quadratic continuum brick elements. The 3D FEA results were used for comparison of the von Mises strain contours to DIC, as illustrated in Fig. 4.4b, while the 2D FEA results were used for parameter sweeping to determine the best-fit material properties and for load-displacement comparisons to experiment as shown in Fig. 4.4(c-f). Tables 4.4 and 4.5 summarize how the stiffness and yield load compare from the experiment to the simulation for various effective areas, as will be discussed.

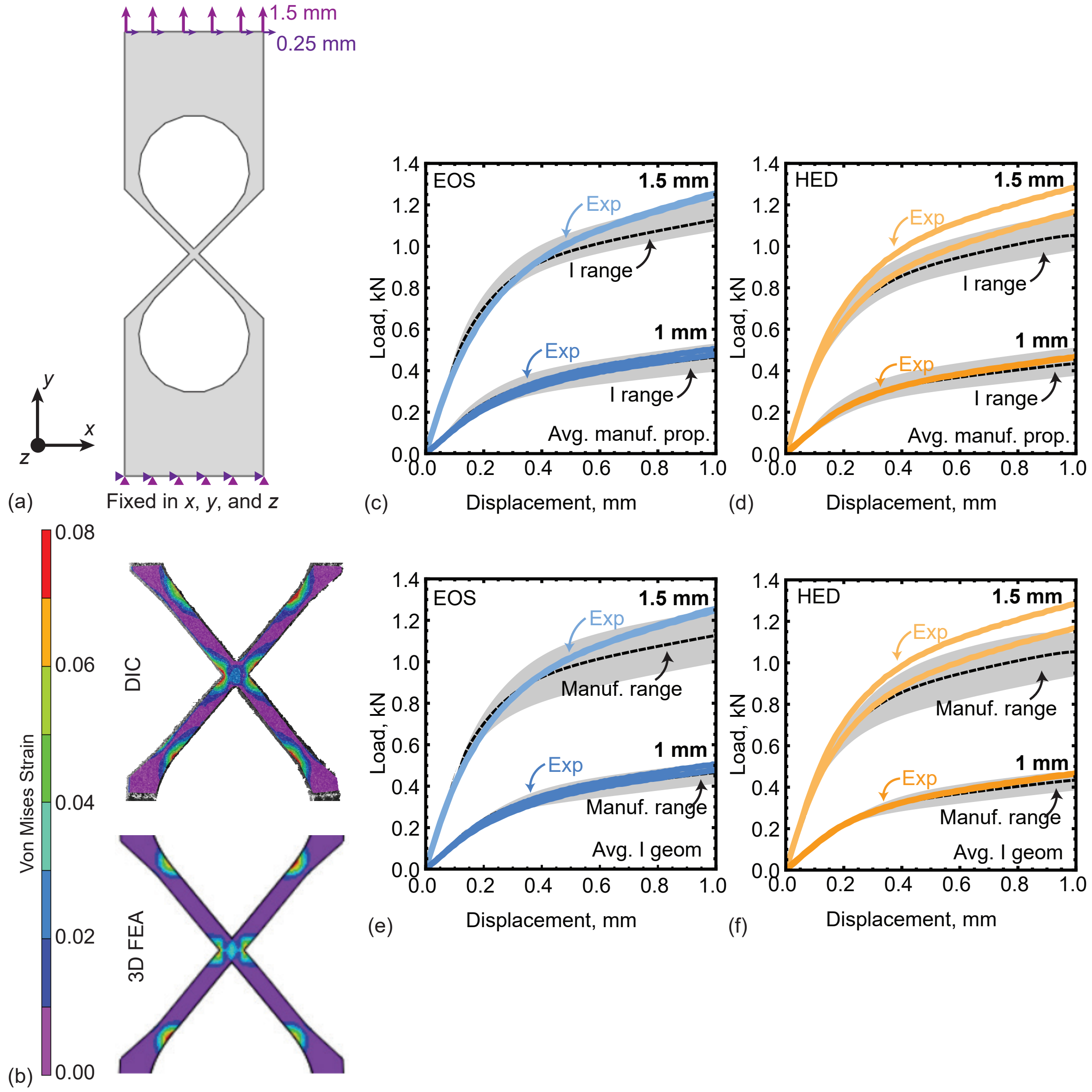

Figure 4.4: (a) Schematic illustrating boundary conditions for FEA that incorporate a slight horizontal displacement based on displacement observed in the DIC. (b) Example of von Mises strain contours from DIC as compared to 3D FEA. Comparison of load-displacement for experimental (c) EOS and (d) HED to simulations using the average nominal (manuf.) properties and varying I geometry. Comparison of load--displacement for experimental (e) EOS and (f) HED to simulations using the varying nominal (manuf.) properties and average I geometry.

Stiffness, kN/mm	Primitive			
	1 mm, EOS	1 mm, HED	1.5 mm, EOS	1.5 mm, HED
Exp	1.24 ± 0.03	1.20 ± 0.01	4.04 ± 0.01	4.18 ± 0.30
FEA, Nom	1.52 (+23%)	1.52 (+27%)	4.77 (+18%)	4.77 (+14%)
FEA, T	$1.50^{+0.32}_{-0.30}$ (+21%)	$1.34^{+0.40}_{-0.26}$ (+12%)	$4.80^{+0.50}_{-0.40}$ (+18%)	$4.40^{+0.70}_{-0.40}$ (+5.3%)
FEA, I	$\mathbf{1.32}^{+0.28}_{-0.28}$ (+6.5%)	$\mathbf{1.21}^{+0.32}_{-0.24}$ (+0.8%)	$\mathbf{4.45}^{+0.50}_{-0.29}$ (+10%)	$\mathbf{4.00}^{+0.60}_{-0.40}$ (-4.3%)

Table 4.4: Comparison of experimental stiffness (mean and standard deviation) to simulation stiffness (using manufacturer-provided properties) with percent difference.

Yield Load, kN	Primitive			
	1 mm, EOS	1 mm, HED	1.5 mm, EOS	1.5 mm, HED
Exp	0.251 ± 0.028	0.251 ± 0.009	0.660 ± 0.002	0.663 ± 0.044
FEA, Nom	0.305 (+22%)	0.305 (+22%)	0.723 (+9.5%)	0.723 (+9.0%)
FEA, I	$0.277^{+0.040}_{-0.041}$ (+10%)	$0.260^{+0.046}_{-0.036}$ (+3.6%)	$0.684^{+0.062}_{-0.037}$ (+3.6%)	$0.631^{+0.071}_{-0.046}$ (-4.8%)

Table 4.5: Comparison of experimental yield load (mean and standard deviation) to simulation yield load (using manufacturer-provided properties) with percent difference.

4.3 Results

4.3.1 Geometric characterization and effective areas

Examples of the reconstruction of the "X" primitives from CT are shown in Fig. 4.2, with the internal porosity shown in black. These images are of the entire thickness of the sample, making the internal porosity appear more extreme than it is in reality. The EOS samples are significantly less porous than their HED counterparts of the same thickness. All samples, except for the 1 mm EOS primitives, have relatively uniform porosity. The source of the anomalous localized porosity in the center of the node in the 1 mm EOS sample is a printing error that was not discovered until after the samples had been imaged with CT. Instead of interpreting the geometry of the 1 mm EOS sample as an "X", the printer interpreted the geometry as a "V" resting atop a horizontally reflected "V". This caused the printer to use the upskin and downskin processing parameters around the center of the node for the 1 mm EOS sample, resulting in the localized porosity.

Two different estimates of the effective cross-sectional area were extracted from the CT – a true (T) area and an inscribed (I) area, as visualized in Fig. 4.5(a-b). The T area, which represents the upper bound on the effective cross-sectional area, was computed from an area calculation of a binarized image of each slice of the strut cross-section. The I area, which is essentially the continuous load-bearing area, was calculated by computing the area of the binarized cross-section of each slice after the surface roughness was removed with some smoothing operations. All area calculations incorporate the internal porosity into their computation.

The results of these area analyses are shown for the struts in Fig. 4.5(c-d) and nodes in Fig. 4.5(e-f) of the "X" primitives in the form of non-standard box plots. The area metrics for the struts are normalized to the nominal strut area, and statistics for all area calculations are based on averaging over all measured CT slices. The white bar in the center of the box in Fig. 4.5(c-f) represents the average value of the averages computed for all struts given a thickness and process. The box is bounded by the average value of the average standard deviation while the whiskers indicate the absolute maximum and minimum within the sample grouping. There are a couple important features to note that are relevant to the discussion of the mechanical response.

First, deviations from the optimized manufacturer parameters appear to result in struts that are undersized relative to nominal. This is contrary to some previous studies, which have reported that struts tend to be oversized relative to their nominal dimensions [155, 171, 178] but in line with others that report observations similar to the ones presented here [173, 174, 187]. Prior studies have shown that process parameters, specifically laser power, layer thickness, and scanning speed, can affect strut dimensions and

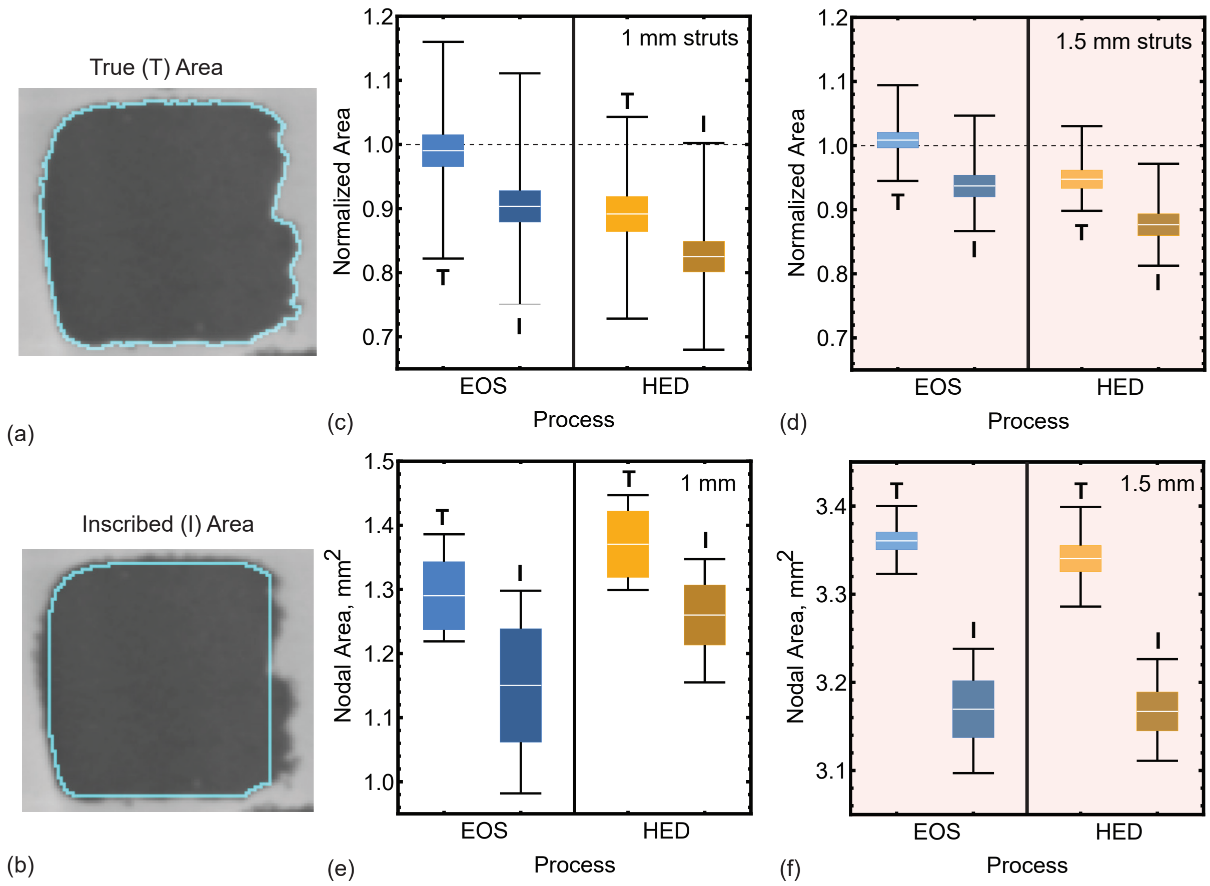

Figure 4.5: A schematic visualizing the (a) true and (b) inscribed areas. Non-standard box plots of true (T) and inscribed (I) strut areas for the (c-d) strut areas and (e-f) nodal areas of the "X" primitives.

properties, even in parts built from the same base powder [155,180]. In addition, differing lattice topologies can result in struts of the same orientation having different geometric variations [173]. For this study, the undersized strut size implies that attempting to simulate the mechanical response using nominal properties will result in over-predictions in stiffness and strength. Second, while the nodal area for the 1.5 mm samples is approximately the same across both processing types, for the 1 mm thickness, the EOS samples have a noticeably smaller nodal area as compared to the HED samples. This is likely due to the printing error mentioned earlier, that resulted in the upskin and downkin parameters being used to build the center of the node in the 1 mm EOS samples, causing porosity to be localized in the center of the node.

From the reconstructions in Fig. 4.2, the upskin roughness is much smaller than the downskin. Conventional methods of surface roughness of R_a and R_RMS, as well as R_v and R_p, computed from the CT scans, confirm this. The results of these measurements (average value bounded by absolute maximum and minimum) are in Fig. 4.6(a-c), with a schematic illustrating the meaning of the roughness parameters in Fig. 4.6d. These findings are consistent with the results in other studies [67, 79, 81, 170, 171] and can be attributed to partially bonded particles and to the stair step shape of the strut. Because all samples used the same upskin and downskin parameters, it was unsurprising to find that their roughness values were not significantly different from each other within an up/downskin grouping. Additionally, the upskin roughness corresponds well with the roughness reported by the manufacturer [192]. These findings suggest that surface roughness is independent of part size.

The porosity of the struts and nodes were determined separately, and the average values bounded by the maximum and minimum are in Fig. 4.7. It is unusual that the

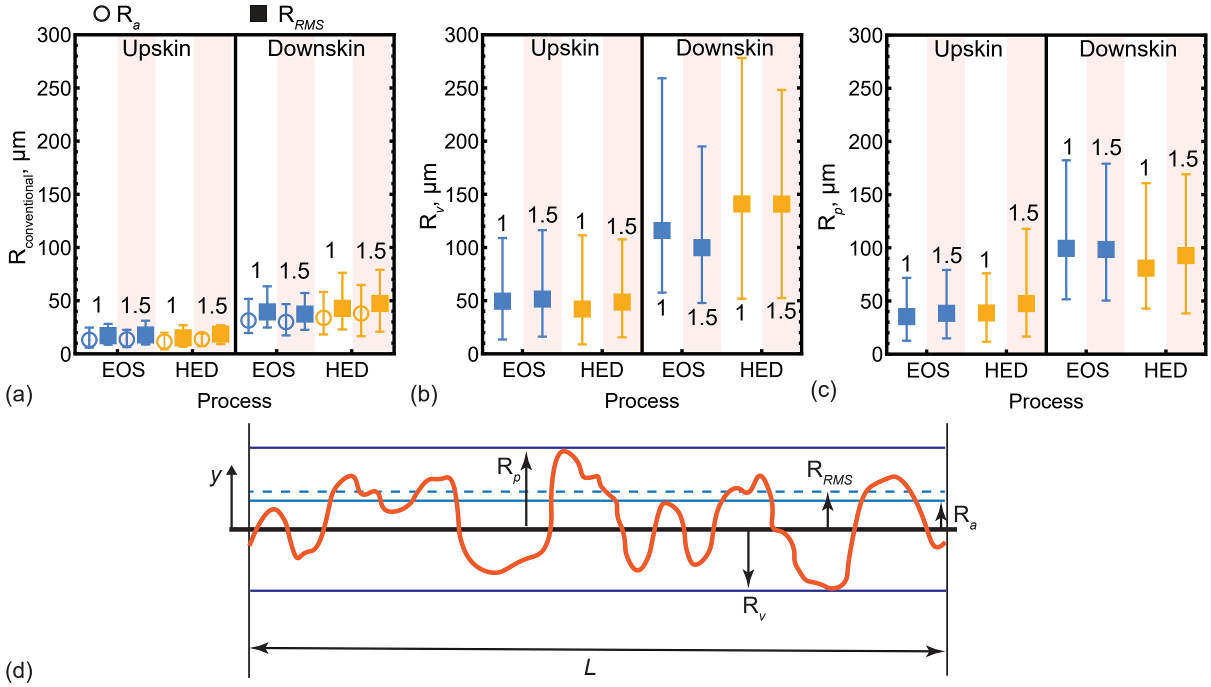

Figure 4.6: Surface roughness measurements of (a) R_{a} and R_{RMS}, (b) R_{v}, and (c) R_{p} of upskin and downskin for each process and thickness. The bounds represent the maximum and minimum. (d) A schematic visualizing roughness metrics computed in (a-c).

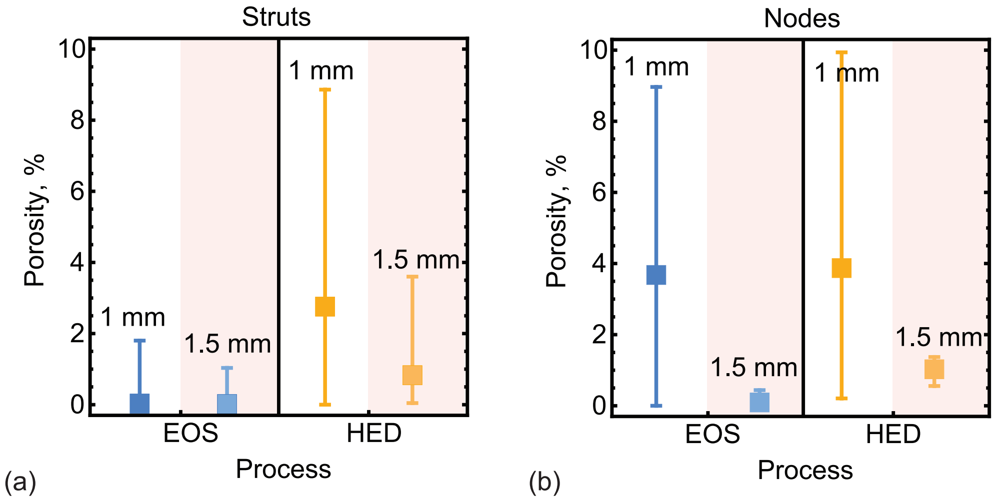

Figure 4.7: Internal porosity for (a) struts and (b) nodes. The bounds represent the maximum and minimum.

HED samples are significantly more porous than the EOS samples since previous studies report that porosity tends to decrease with increasing energy density [61,62,165,166,170]. However, Cherry, et al. [61] has shown that increasing energy density beyond an energy density that has minimal porosity can result in increased porosity due to vaporization of low melting elements. This is likely the case here, since the morphology of the pores as shown in Fig. 4.2, is congruent with gaseous porosity as described by Cherry, et al. [61]. The nodal porosity in the 1 mm EOS and HED samples do not follow this pattern, most likely because of the printing error in the 1 mm EOS samples.

As a final note on geometry, the thicker samples tended to be less porous than their thinner counterparts. This is at odds with the results from Wang, et al. [182] who found that porosity did not vary with sample thickness but is in agreement with Abele, et al. [187] who found that thicker parts tended to be more dense than thinner parts. The origin of this phenomena may be due to differences in interlayer time between the parts, with thicker parts having a longer interlayer time due to their increased sized. Although studies on the effects of interlayer time in L-PBF SS316L are limited, Mohr, et al. [193] found that for certain parameter sets, parts built with shorter interlayer times can result in significantly more porosity than those with longer interlayer times due to differences in melt pool behavior. These results suggest that parameters optimized to build fully-dense bulk samples will not work as well to create fully-dense thin samples.

4.3.2 Elastic-plastic properties using effective areas

The measured mechanical response of all samples is shown in Fig. 4.3a with the stiffnesses, yield loads, and displacement at failure provided in Table 4.3. DIC measured strain contours of von Mises strain at loads of 500 N and 800 N for the 1 mm samples and 1300 N and 2000 N for the 1.5 mm samples are shown in Fig. 4.8. Interestingly, the differences in processing parameters do not seem to significantly affect the stiffness and strength of the HED samples relative to their EOS counterparts.

All samples failed via a horizontal through-crack through the center of their nodes. Notably, the 1 mm EOS samples tended to fail at a much lower displacement in comparison to their HED counterparts. At initial glance, this may seem counter-intuitive, given that the 1 mm HED samples are significantly more porous than the 1 mm EOS samples, as shown in Fig. 4.2(a-b). However, in the 1 mm EOS samples, the porosity is highly localized in the center of the node, causing the samples to have a similar nodal porosity to the 1 mm HED samples, as shown in Fig. 4.7b. This porosity localization at the failure location causes elevated strain concentrations in the node. This is illustrated through comparison of the measured von Mises strain maps in Fig. 4.8. In the 1 mm samples, the strain is much higher in the center of the node in the EOS sample as compared to the HED

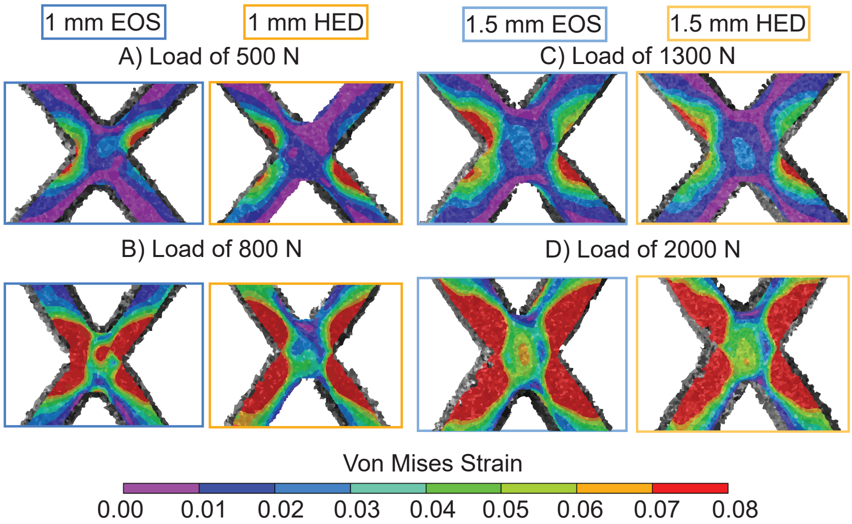

Figure 4.8: DIC images of von Mises strain contours at loads of 500 N and 800 N for the 1 mm samples and 1300 N and 2000 N for the 1.5 mm samples.

sample. For the 1.5 mm samples, the strain in the center of the node is approximately the same from process to process. These results suggest that for this geometry, changes in processing conditions that result in significantly more distributed porosity have minimal effect on mechanical performance, unless the porosity is highly localized in the node.

To draw insight into the material properties of these samples, the effective area of the struts, as determined via stiffness matching, must be determined. The simulated stiffness using the nominal area as well as CT-based T and I areas from Fig. 4.5(c-f) in comparison to the experimental stiffness are shown in Table 4.4. It is clear from these results that inputting the nominal properties or T area metric significantly over-predicts the stiffness in all samples. On the other hand, the I area metric provides excellent agreement with the experimental results in all cases, except with the 1.5 mm EOS sample (a slight over-prediction). This discrepancy is likely due to the simulation geometry being based entirely on averages over the strut area without consideration to the local nodal geometry. For some samples, the actual nodal geometry is well approximated by the actual strut geometry; in others, the node is relatively under- or over-sized. Supplemental simulations that incorporate the actual nodal geometry into the simulation instead using a node defined by the strut geometry helped reduce the percent error in stiffness among all samples without significantly affecting other simulation metrics, such as yield load and hardening rate. However, these simulations with separate nodal and strut geometries are tedious to implement and do not provide significantly different results. In general, the I metric provides the most reasonable estimate of effective area in these samples.

After establishing that the I area metric produces the most appropriate effective area for these samples with regard to stiffness, simulations using the I area metric were used to infer plastic properties. Table 4.5 compares the yield load from the experiments to simulations using both the nominal area and the I geometry. The yield load is defined by the intersection of the load-displacement curve with a line that is parallel to the stiffness and intersects the abcissa at a 0.2% of the gauge length, as illustrated in Fig. 4.3b. All simulations summarized in Table 4.5 used the manufacturer-provided material properties. As shown from Table 4.5, the simulations using the I geometry predict the yield load far more accurately than the simulations using the nominal area and, with the exception of the 1 mm EOS case, are within 5% of the experimental result. Although both stiffness and yield load are accurately predicted with simulations using the I area and manufacturer-provided material properties, upon closer inspection of the comparison of simulation to experiment of the load-displacement curves in Fig. 4.4(c-f), there are significant discrepancies in the plastic regime.

For the simulations using the range in I area in Fig. 4.4(c-d), the hardening rate of the thinner samples matches the experimental results well but the hardening rate predicted for the 1.5 mm samples is much lower than what occurs in the experiment. This suggests that there is some thickness dependence on mechanical properties since within a processing parameter set, the agreement between simulation and experiment is different depending on the sample thickness. Wang, et al. [182] found that increased strut thickness results in decreased hardening, which is contrary to the results shown in Fig. 4.4(c-d) (the 1.5 mm samples have a higher hardening rate than the 1 mm samples). However, Bultman, et al. [185] found that increased strut diameter resulted in increased hardening, which is in agreement with the results reported in this study. The caveat with both of these studies is that they did not rigorously define the effective area for their struts so it is impossible to make an unambiguous comparison between their work and the work in this study. This difference in hardening rates between the 1.5 mm and 1 mm samples persists even if the range of properties from the manufacturer is varied (as opposed to varying the range in area) as shown through Fig. 4.4(e-f). In addition, the amount of hardening that the 1.5 mm samples undergo is beyond the range predicted by the manufacturer. These results indicate that relying on bulk manufacturer material properties to predict hardening behavior of printed, thin-walled specimens may lead to significant errors.

4.4 Discussion

4.4.1 Characterization of effective areas

As noted in the previous section, the I area metric was found to be the best measure of effective area in these samples based on stiffness as shown in Table 4.4. Fully characterizing individual samples with CT is a time consuming process, such that it is highly desirable to identify a method to estimate the effective area using surface measurements. The I area metric is essentially the T area reduced by the surface roughness. For these samples, as shown in Fig. 4.5(c-d), the T area approximates the nominal area well, when accounting for porosity. By taking the nominal length measurements and knowing the average surface roughness and porosity, the I area can then be estimated with the equation below:

$$A = \left[\left(h_0 - \left(\overline{R_{\uparrow}} + \overline{R_{\downarrow}} \right) \right) \left(1 - \phi \right) \right]^2 \tag{4.1}$$

where A = area, h_0 = nominal thickness, $\overline{R_{\uparrow}}$ = average upskin roughness (conventional metric), $\overline{R_{\downarrow}}$ = average downskin roughness (conventional metric), and ϕ = porosity.

This equation was developed by subtracting the surface roughness from the nominal thickness and multiplying that difference by the percentage of solid material. The product was then squared to determine the effective area since the cross-sections of the struts in the samples are nominally square. An open question was which roughness metric to use to reduce the nominal thickness. The average R_{a} and average R_{RMS} from the samples were chosen to be evaluated over R_{v} or R_{p} because they are more robust to outliers so they will be more representative of the average geometry.

A comparison of the I area from Fig. 4.5(c-d) to the effective area estimates from Eq. 4.1 using the average R_{a} and average R_{RMS} from Fig. 4.6a and porosity from Fig. 4.7(a) is shown in Fig. 4.9. The range in predicted effective area is bounded by the range of predictions using the average roughness from individual samples within a grouping, while the average value is computed by using the aggregate average roughness over all samples within a processing condition and thickness combination. As shown from Fig. 4.9, the predictions using the average R_{RMS} are in better agreement overall. While Eq.

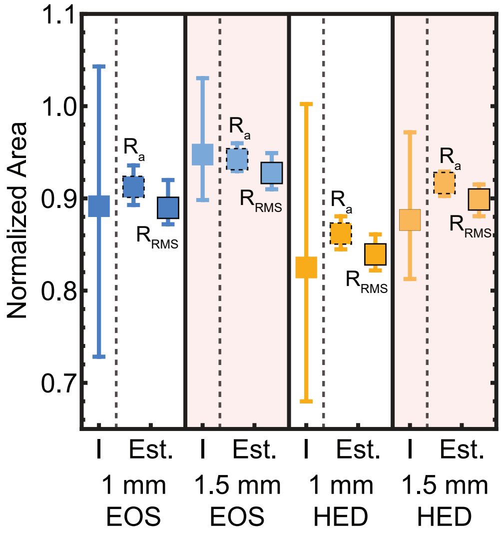

Figure 4.9: Comparisons of the inscribed (I) area from the CT to area estimates (Est.) from Eq. 1.1 using conventional roughness metrics. The bounds on the I area represent the maximum and minimum. The bounds on the Est. are based on the range Eq. 1.1 provides by inputting conventional roughness metrics from an individual sample.

4.1 is limited to this specific print and geometry, the quality of agreement between this simple equation and the effective area suggests that using surface roughness to estimate effective area in other geometries seems to be a promising venue to quickly determine effective print area for accurate simulations.

4.4.2 Plastic properties using effective areas

Simulations using the manufacturer-provided properties proved to be sufficient in matching the yield load but insufficient in capturing the appropriate hardening rate, as shown in Fig. 4.4(c-f). To assess the material properties defining the correct hardening rate for each sample, simulations with the fixed average I geometry and varied initial yield stress (YS) and ultimate tensile stress (UTS) were run to improve agreement between predicted and measured response. The outcome of the properties for the best-fit simulations was, in general, a lower yield stress than the average reported by the manufacturer (but still within the range of manufacturer properties), and a higher ultimate tensile stress than that reported by the manufacturer. The precise values of YS and UTS for the best-fit simulations are shown in Fig. 4.10 with a comparison to the values reported by the manufacturer, for reference. The mechanical properties shown in Fig. 4.10(a-b) match some of the samples with reported mechanical properties by Röttger, et al. [180] and have a similar degree of hardening (ratio of UTS to YS) as that reported by Hanzl, et al. [153] and Wang, et al. [182]. The amount of hardening in this study is far greater than that reported by many of the studies with mechanical properties on L-PBF SS316L [39,152,158,160,185,194] but with the exception of Wang, et al. [182] and Röttger, et al. [180,182], all of the reported properties are for bulk samples, which more than likely have a different microstructure. Additionally, Röttger, et al. [180] demonstrated that mechanical properties can vary significantly for a given sample geometry and using the same powder batch of L-PBF SS316L parts, so it is difficult to directly reasonably compare mechanical properties among different studies without rigorously accounting for the processing parameters.

The best-fit material properties suggest that the processing condition with higher energy density results in a slight increase in YS while maintaining the same UTS as the lower energy density parts. It is difficult to compare these results to other studies because there are limited studies on how energy density influences resultant material properties in L-PBF SS316L parts. Additionally, previous studies [61, 166] that do report results on the influence of energy density upon strength focus on bulk samples, which may not necessarily have the same properties as thin samples. Additionally, they do not show stress-strain or load-displacement results, instead they rely on hardness as a proxy for strength [61,166]. Both studies report that up to an energy density of 125 J/mm^3, higher

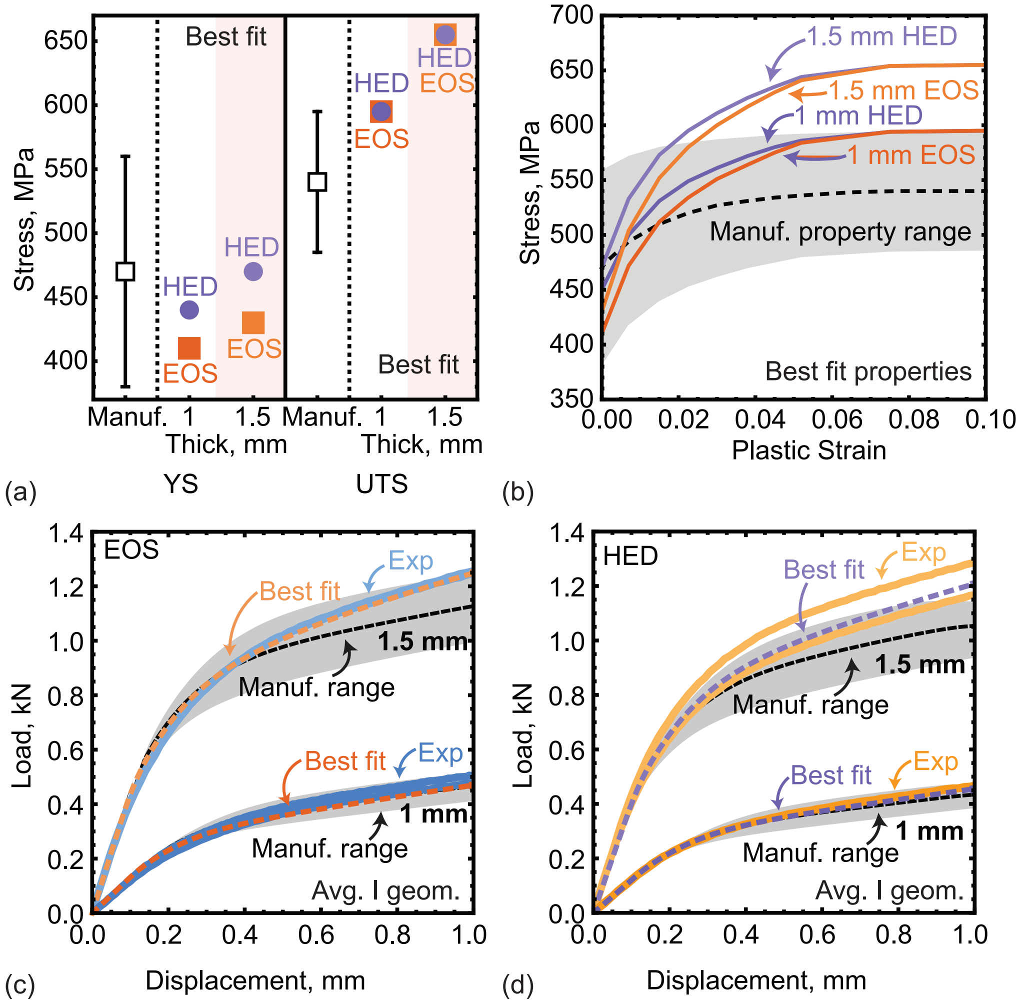

Figure 4.10: (a) Yield stress (YS) and Ultimate Tensile Stress (UTS) provided by manufacturer (manuf.) as compared to FEA best fit values. (b) Strain hardening using manufacturer-provided YS and UTS as compared to FEA best fit strain hardening. Load-displacement of FEA using best fit and manufacturer-based YS and UTS as compared to experimental results for (c) EOS and (d) HED.

energy densities result in higher hardnesses [61,166]. However, Cherry, et al.'s [61] results suggest that hardness is not monotonic with energy density.

In addition to the relationship between energy density and strength, there also appears to be a size effect of strength, with thicker parts having higher YS and UTS than their thinner counterparts. This thickness dependence of strength agrees with the results reported by Wang, et al. [182], who found that thicker struts tended to be stronger than thinner struts and corroborated their results by showing that thicker struts tended to be harder than thinner struts. Notably, Wang, et al. [182] only measured the diameter of the struts in his study from optical micrographs of longitudinal sections and did not rigorously define an effective area based on CT, mechanical tests, and FEA, as done in this study. To the authors' knowledge, this study is the first of its kind to use rigorous measurements of effective area to report a size effect of strength in L-PBF SS316L struts.

It is important to emphasize that the approach taken here assumes isotropic, homogeneous plastic response; this is clearly an assumption that warrants future study of spatial property variations within the primitive. Evidence of such variations appears in Fig. 4.11, which displays comparisons of the von Mises strain contours of a sample of each process to 3D FEA simulations using the best-fit and average manufacturer properties. Clearly, the extent of plastic deformation in the nodal region is suppressed relative to either prediction. The increased hardening levels of the best-fit properties suppress plastic deformation in the node relative to the manufacturer properties, with moderately improved local agreement at the center of the node and along the strut faces extending from the node. It is entirely possible that equivalent results can be obtained by including enhanced hardening only at the nodes; that is, the material yield stress may be position-dependent.

Previous indentation studies showed significant variations in hardness in similar specimens [151]. However, additional study is needed to translate those hardness variations into effective yield stress and hardening rate, which can be convoluted in such tests. It should also be noted that the connection between indentation on lateral surfaces and the yield stress in the direction of the struts requires careful consideration of the crystalline structure and grain size/orientation. Simply put, future study should focus on establishing a rationale basis to describe gradients of such spatial property variations, e.g. through indentation property mapping and constitutive descriptions tied to microstructural characterization [195].

Finally, it is also interesting to note that impact the concentration of voids at the mid-plane of the 1 mm EOS specimen is clearly evident, with much larger localized strains in the node region. It is possible that strains are elevated in the node due to the presence of voids, such that the isotropic hardening rate obtained via calibration based on macroscopic results is overestimated. If so, local hardening around the voids would presumably have to be dramatic to compensate for the loss of material in the voids. That is, hardening due to strain concentrations associated with voids would have to compensate for the reduced net section of the node. Further, local hardening in the node would have to compensate for any hardening decrease that arises from decreased deformation in the struts.

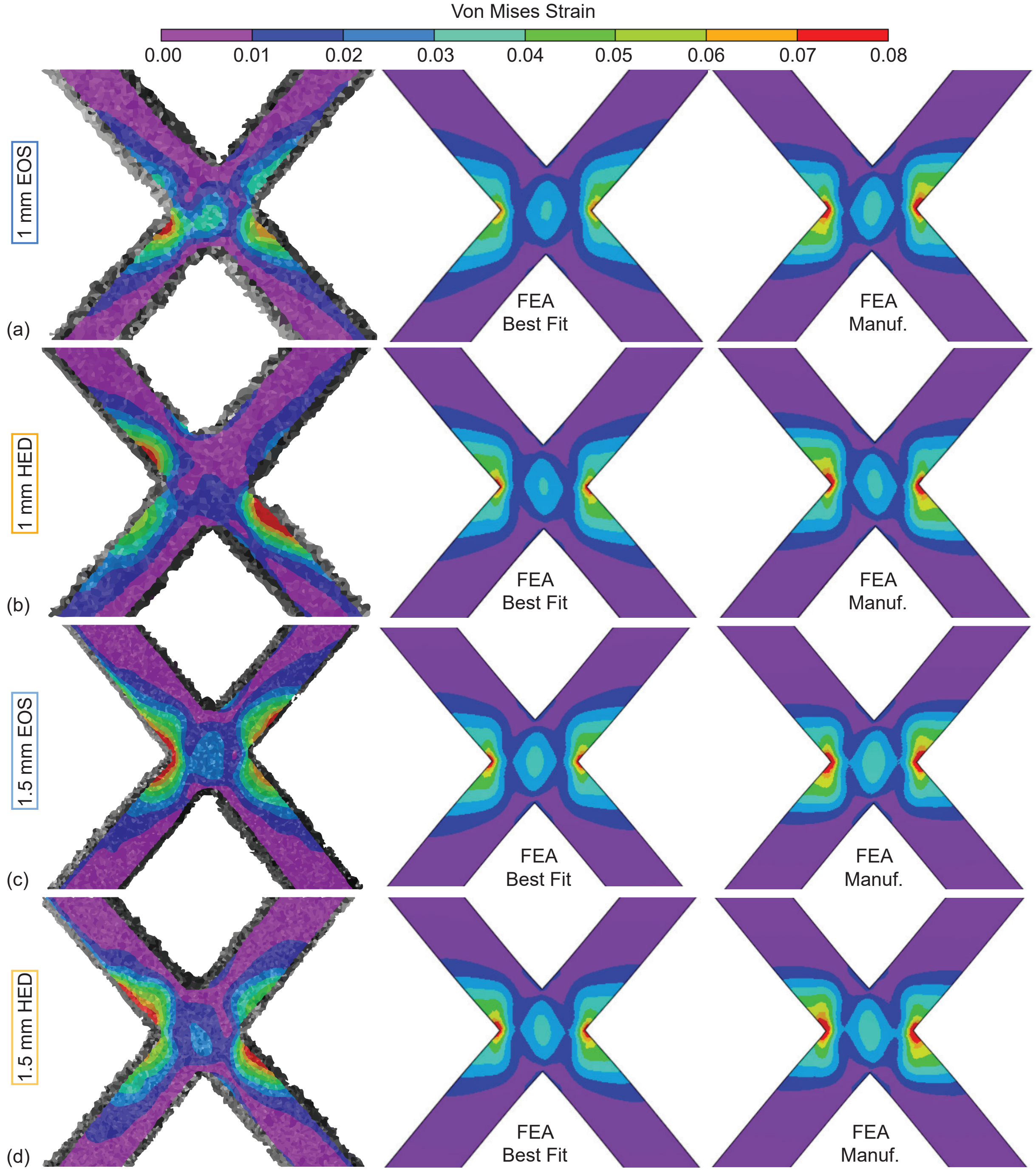

Figure 4.11: Comparison of DIC von Mises strain to von Mises strain from FEA using average I geometry and average manufacturer (manuf.) properties or best fit properties for each sample type at a macroscale displacement of 1 mm.

4.5 Conclusions

The results of this work provide insight into the influence of processing conditions and part thickness on the resultant geometry and mechanical properties of thin-walled L-PBF SS316L lattice primitives. The primary findings are as follows:

- Samples built with higher energy density have significantly increased distributed porosity with minimal change in mechanical properties. Localized porosity has the greatest influence on mechanical performance of these lattice-based “X” primitives due to strain localization within the node.
- The presence of surface roughness introduces uncertainty in defining an effective area for simulation inputs. However, using the inscribed cross-sectional areas of a strut as an effective area produces accurate stiffness measurements and more appropriate peak loads.
- The effective area of thin-walled printed structures can be estimated from average measurements of surface roughness and porosity.
- Sample thickness has a significant effect on mechanical properties, with thicker samples exhibiting significantly more hardening than thinner samples with the same processing parameter inputs. Simulations based on manufacturer-provided material properties will result in reasonable predictions for thin-walled samples up to yield.

Chapter 5

Strain maps and failure analysis of SLM Ti-6Al-4V lattices measured by in situ DIC on a primitive scale

5.1 Introduction

Additive manufacturing (AM) empowers the development of architected cellular materials, which cannot easily be created through conventional, subtractive means. These cellular materials, commonly referred to as lattice structures, can achieve dramatic performance gains through topological design [24–27,29]. For most applications that demand high specific strength and stiffness, improved heat transfer, and enhanced energy absorption capability, lattice structures are required to have millimeter-scale features to reach a beneficial relative density with a reasonable number of cells [24–27, 150]. For features of this length scale in metal AM, process-structure-property relationships are intrinsically tied to component geometry, which defines thermal conduction pathways that strongly influence solidification [29, 73, 146, 196]. This means that lattice geometry cannot be decoupled from its processing so printed structures may perform differently from ideal due to defects, such as porosity and surface roughness, which are induced during the printing process [79, 146, 196–200].

Much of the previous work on metal AM lattice structures has been focused on the macroscopic behavior of specific geometries [5, 30, 34, 35, 116, 201–206]. Because material and geometric heterogeneities can significantly play a role in the stiffness and strength of lattice structures relative to their prescribed properties, there has been growing interest in understanding deformation mechanisms that govern lattice behavior at the lattice substructure (e.g., struts and nodes) or "primitive" level [146, 196, 197, 200, 207, 208]. One method that has gained popularity in experimentally assessing deformation mechanisms in lattices is digital image correlation (DIC). DIC is a non-contact, optical method that relies on image storage, tracking, and registration to extract measurements such as full-field displacement and strains [209].

While it has become more common to use DIC techniques to evaluate deformation in lattice structures, many of these DIC studies on lattices provide no information upon the deformation occurring at the primitive level and instead display strains averaged over a unit cell [201, 205, 206, 210–214]. Other studies do not provide quantitative assessments of strains at the primitive level because they use 2D DIC techniques on inherently 3D surfaces which undergo significant out-of-plane motion that obfuscates the true strains experienced by the surface [209, 215–218]. There are a few studies that display quantitative strains at the primitive and macroscale level but all of these studies are focused upon microlattices, which have feature sizes near the minimum feature size of the printer, which makes them more prone to defects in comparison to millimeter scale lattices [73, 175, 196, 219–222]. Additionally, some of these studies do not display the temporal evolution of strain throughout the test, which can bring insight into failure mechanisms in lattices [73, 221, 222].

To further the understanding of strain evolution and failure mechanisms in millimeter-scale lattice structures, in situ DIC was used to evaluate the mesoscale and macroscale deformation of two different lattice structures, named “FCC” and “FCZ” (shown in Fig. 5.1). Rather than evaluating lattices with extreme differences in geometry, the lattices evaluated in this study are very geometrically similar, with the only difference between the “FCC” and “FCZ” geometries being the addition of a cross-brace in the z direction in the “FCZ” lattice. This additional strut increases the average strut connectivity of the nodes in the “FCZ” lattice. The study of the evolution of deformation in both lattices allows us to quantify the effect of an additional cross-brace upon macroscopic mechanical properties and mesoscale strains. Additionally, the geometries of the lattices in this study are appropriate for use of 2D DIC as the imaged faces are inherently planar. 3D DIC upon an adjacent face of the lattice was done to ensure out-of-plane motion induced minimal effects upon the apparent strains on the face imaged by 2D DIC. The strains observed by the DIC are validated against finite element analysis (FEA) simulations.

The utility of surface strain measurements upon predicting failure in lattice structures is also evaluated in this work. X-ray computed tomography (CT) was used to characterize the geometry of the lattices pre-compression and evaluate failure modes post-compression. This study is the first of its kind to fully characterize lattice structures using CT before and after mechanical testing with in situ DIC. The use of CT in combination with the DIC enables a complete picture of how deformation evolves in these metal AM structures as they are compressed. Best practices in terms of analyzing the lattice primitives within the context of deformation are also discussed. The results of this

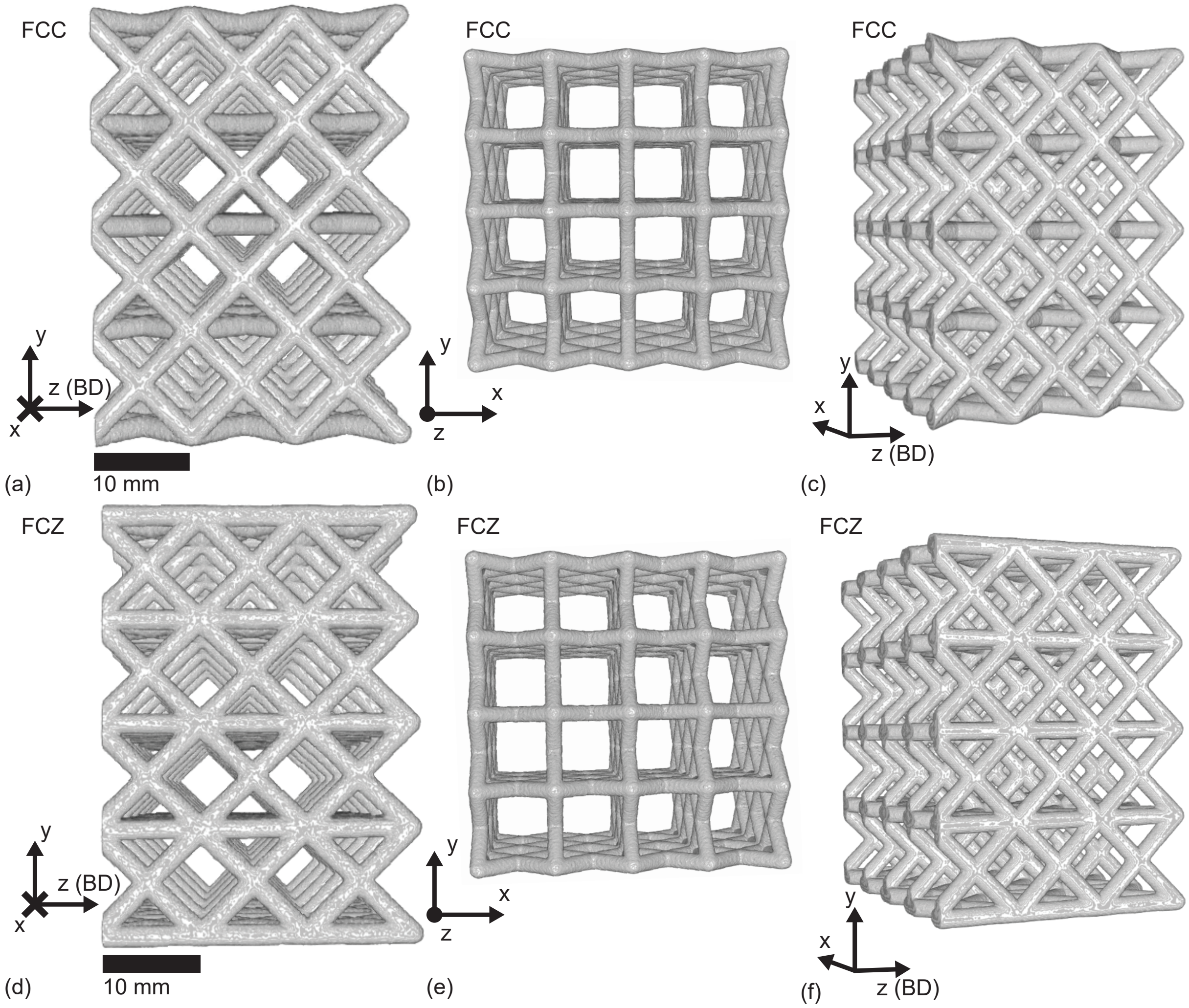

Figure 5.1: Reconstructed CT images of the SLM Ti6Al4V printed lattices in this study. The (a) -x, (b) +z, and (c) oblique views of the "FCC" lattice. The (d) -x, (e) +z, and (f) oblique views of the "FCZ" lattice. Note that the lines on the CT image are voxels from the CT reconstruction and not print layers.

work provides a greater understanding on how topology influences strain localization in lattices and their primitives and provides a clearer picture of how to best utilize surface strain measurements in understanding mesoscale behavior of lattices.

5.2 Methods

In the present study, the two lattice geometries of "FCC" and "FCZ" (Fig. 5.1) were printed to have nominally circular struts with a diameter of 2 mm and a cell size of 10 mm. The samples were characterized using CT after being printed to evaluate print quality and to characterize their geometry. They were then tested in compression while using DIC until first few failures to characterize their mechanical behavior. Post-compression samples were then characterized via CT again to determine failure locations and failure types.

5.2.1 Printing

Lattice samples with "FCC" and "FCZ" geometries, shown in Fig. 5.1, were fabricated using Ti6Al4V powder by an EOS selective laser melting (SLM) system (EOS GmbH, Germany) using the default manufacturer parameters. Complete details on the powder characteristics are available in the work by Dong, et al. [223]. Samples were printed at the same orientation relative to the build plate with a nominal strut diameter of 2 mm and a nominal cell size of 10 mm. There was only one sample per geometry.

5.2.2 CT imaging

All samples were analyzed by x-ray computed tomography (CT) using a Bruker SKYSCAN 1275 equipped with a Perkin Elmer Dexela 1512 detector with a pixel pitch of 75 µm. The reconstructed images have a voxel size of 35 µm over a length of approximately 40 mm. FIJI (ImageJ) software with its built-in plugins was used to visualize the images and determine failure locations [117].

5.2.3 Mechanical testing

Mechanical testing was done on a Material Test System 810 servohydraulic load frame at room temperature under a displacement rate of 0.48 mm/min (approximate strain rate of 2×10^{-4} s^{-1}). The lattices were compressed between two vacuum greased, hardened steel platens, as shown in Fig. 5.2, until first few failures before unloading, as indicated in Fig. 5.3. In all tests, full field strain measurements were made using 2D Digital Image Correlation (Vic-2D, Correlated Solutions, Columbia, SC) on the -x face and 3D Digital Image Correlation (Vic-3D, Correlated Solutions, Columbia, SC) on the +z face as indicated in Fig. 5.2. For the 2D DIC, images were taken using a scale factor of 23.8 µm/pix and were correlated using a subset size of 21 pixels (500 µm) and a step size of 2 pixels (47.6 µm). Prior to testing, the lattice faces were first coated in flat white paint and then speckled using a Paasche airbrush with black water-soluble paint, as per the best practices outlined by Rajan, et al [122]. The purpose of these DIC measurements were to (1) obtain an accurate measure of macroscale displacement and (2) observe strain localization in these structures. The displacements were defined with respect to the global coordinate system, characterized by the compression direction and its normal. The strains were defined in both the global coordinate system and by the strut coordinate

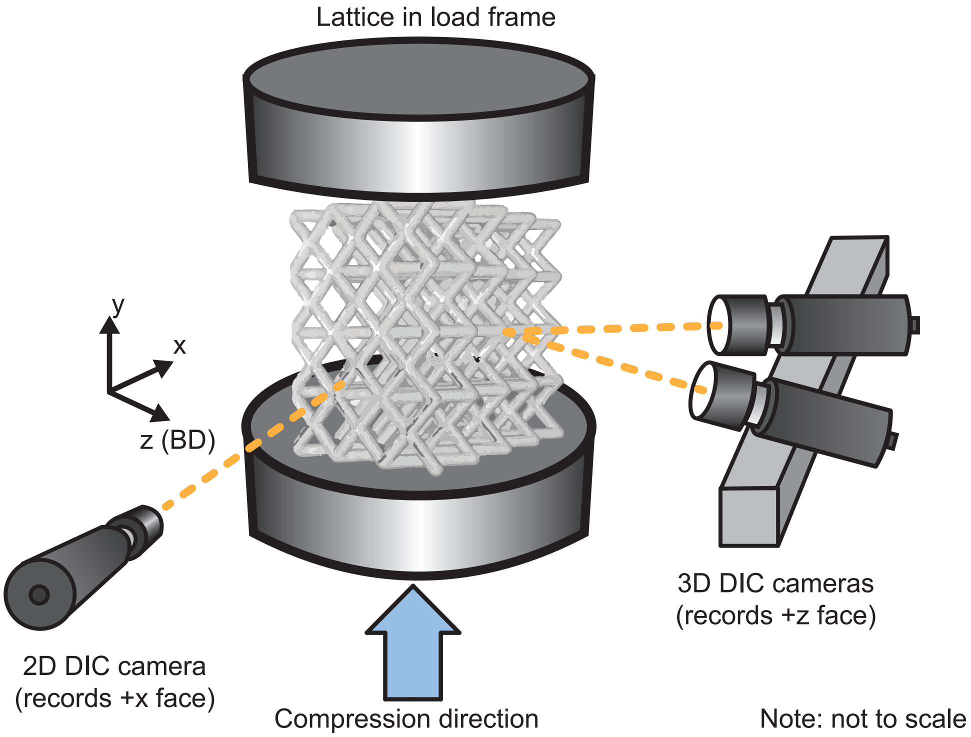

Figure 5.2: Schematic depicting the loading and DIC camera setup of the compression test of the lattice.

system, defined by the strut axis and its normal.

5.2.4 Finite element simulations

Finite element simulations of the -x face (face imaged by the 2D DIC) for both lattice geometries under compression was conducted to provide a qualitative comparison of a strain map to the experiment. Strain maps from the FEA were scaled to the same magnitude as the DIC for the appropriate comparison. These FEA simulations utilized elastic-plastic two-dimensional plane stress finite elements in ABAQUS with a modulus of 120 GPa and yield stress of 880 MPa, which are values commonly reported by metal AM manufacturers for Ti6Al4V [148]. While Ti6Al4V exhibits very little strain hard-

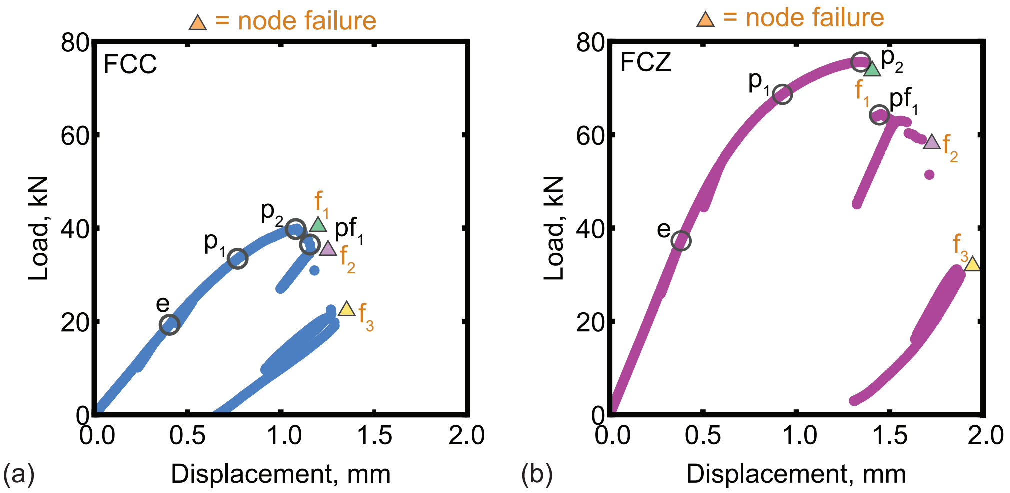

Figure 5.3: Load-displacement curves from the (a) FCC and (b) FCZ lattice compression tests. The displacements at which node failure occurs is marked by a triangle and the sequences of failure are marked by f_1, f_2, and f_3. Four displacements for each load-displacement curve are marked which indicate a point in the elastic regime (e), two points in the plastic regime but before failure (p_1 and p_2), and the point after first failure (pf_1).

ening, a small amount of hardening (0.4% of the elastic modulus) was included in the simulation as it stabilizes non-linear iterations during elastic-plastic buckling, without significantly impacting the macroscopic response. For both geometries, the bottom of the lattice was fixed while the top had a prescribed linear, distributed compressive displacement so that one end was displaced by 2 mm over the length of the simulation while the other was displaced by 2.3 mm (for the FCC geometry) or 2.26 mm (for the FCZ geometry). These values were chosen based on the slight misalignment seen in the DIC of the experiments. In addition, a small amount of horizontal displacement was also prescribed based on the experimental misalignment. For the FCC geometry, this amounted to a horizontal displacement that was 18.6% of the average vertical displacement while for the FCZ geometry, a horizontal displacement that was 10.3% of the average vertical displacement was prescribed. The 2D FEA for the FCC geometry used 177,566 4-node linear plane stress quadrilateral elements while the 2D FEA for the FCZ geometry used

104,652 8-node quadratic plane stress quadrilateral elements.

5.3 Results

5.3.1 Geometric and mechanical characterization

Reconstructed CT images of the printed “FCC” and “FCZ” lattices before mechanical testing are shown in Fig. 5.1 from several different viewpoints. Geometric analysis of the pre-compression CT images revealed that, on average, the struts are within 2-3% of their dimensions prescribed by their computer aided design (CAD) file and have nominally round cross-sections. The cell size and macroscopic dimensions of the printed lattices similarly matched their prescribed measurements. This accuracy between printed geometry and designed geometry is better than that reported by Van Bael, et al. [224], however the nominal sizes of features in this study are about an order of magnitude larger than the samples studied by Van Bael, et al. and the minimum feature size of SLM machines. Printed lattices had no notable defects – the surface roughness of the struts was approximately the same regardless of orientation (no significant upskin vs downskin differences) and there was no apparent porosity. This suggests that the processing parameters used to create these lattices were at an optimal energy density to create fully dense components [60, 61].

A schematic displaying the experimental setup for the mechanical tests is shown in Fig. 5.2. The -x face was chosen to be imaged for 2D DIC since all of the struts were in the same plane relative to the camera. The +z face was chosen to be imaged for the 3D DIC since the struts were not not in the same plane (inherently 3D) so it was thought that there would be greater out-of-plane motion in the +z face in comparison to the -x face. Although the 3D DIC results are not shown in this paper, they were used to determine the amount of out-of-plane motion experienced by the -x face. Because the 2D DIC camera was located far away relative to the amount of out-of-plane motion, the maximum apparent strain induced from out-of-plane motion would be 0.0018, and this would occur right after failure (at point pf_1 in Fig. 5.3) [218]. The amount of out-of-plane apparent strain is small relative to the in-plane strains experienced on the 2D DIC face at point pf_1. Thus the 2D DIC results shown in this study can be taken as quantitative strains.

The load-displacement results from the mechanical tests for both lattices is shown in Fig. 5.3. The measured sample unloading stiffness, yield load (defined by a 0.02% offset), and load at first failure are tabulated in Table 5.1. Each load-displacement result has four points marked on it which are labeled e (elastic), p_1 (plastic, point 1), p_2 (plastic, point 2), and pf_1 (post-first failure) which are locations at which different DIC images are shown in this study. Additionally, there are three triangles which mark load drops shown in the load-displacement that indicate when the structure experienced failure or a set of failures of nodes. Three sets of failure occurred in each lattice and are marked accordingly by f_1, f_2, and f_3. Unsurprisingly, the "FCZ" structure is much stronger, stiffer, and more ductile than the "FCC" structure due to its additional horizontal cross-brace which assists the lattice against collapse. The additional constraint of the horizontal cross-brace in the "FCZ" structure helps the lattice deform in a more stretch-dominated manner than the "FCC" lattice [221, 225].

Fig. 5.4 displays optical images that were used for the DIC which have the locations of the first and second sets of failure (f_1 and f_2) marked. The failure locations during f_3 were

Geometry	Stiffness, kN/mm	Yield load, kN	Load at first failure, kN
FCC	60.3	33.5	39.9
FCZ	109.1	58.3	75.2

Table 5.1: Measured sample unloading stiffness, yield load, and load at first failure.

not discernible from the optical images. For the “FCC” lattice in Fig. 5.4a, the location of first failure was an interior horizontal node. During second failure, horizontal nodes diagonal to the first failed node began to fail before subsequent shearing collapse along the diagonal of the lattice. The “FCZ” lattice also experienced macroscopic shearing but in a different plane. The “FCZ” lattice first experienced failure in a node in the bottom corner. During the second set of failure, the entire bottom row of the lattice began to shear.

Fig. 5.5 displays the von Mises strain maps from the DIC for both tests at the points of e, p_1, and f_1. The locations at which failure occurred are also indicated according to the colors in Fig. 5.4. In both lattices, strain begins to localize in the bulk at the exterior of the struts and nodes, at point e, which is prior to any evident macroscopic yielding. In addition, strain also localizes in the center of the nodes with a strut connectivity of four. Interestingly, this pattern of strain localization does not occur in the nodes with a strut connectivity of six in the “FCZ” lattice. As both lattices are loaded further to point p_1, the strain localizations look largely the same as they did at point e. However, in the “FCZ” lattice, strain also begins to localize at the lower bottom node, where the point of first failure will occur. By point pf_1, several of the points at which failure occurs or will occur have missing data, indicating that correlation is lost due to severe deformation. While the von Mises strain maps from the DIC provide information on how strain localizes on the lattice surfaces as whole, they do not provide any kind of directionality, which is useful in determining how struts and nodes are deforming as the

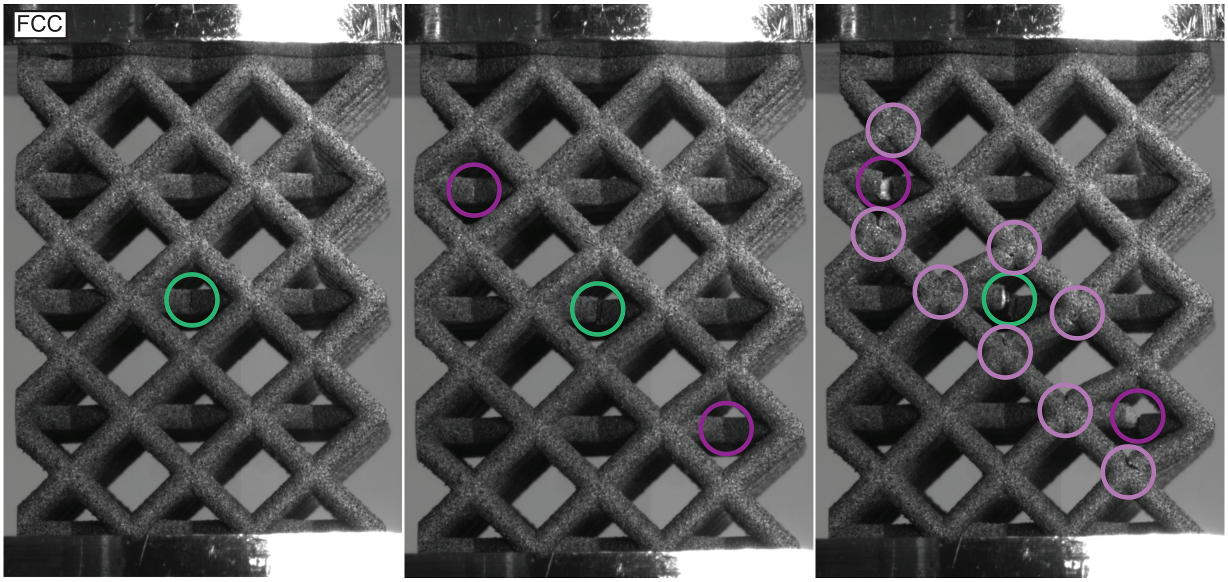

(a) f_1 failure locations f_2 initial failure locations f_2 subsequent failure locations

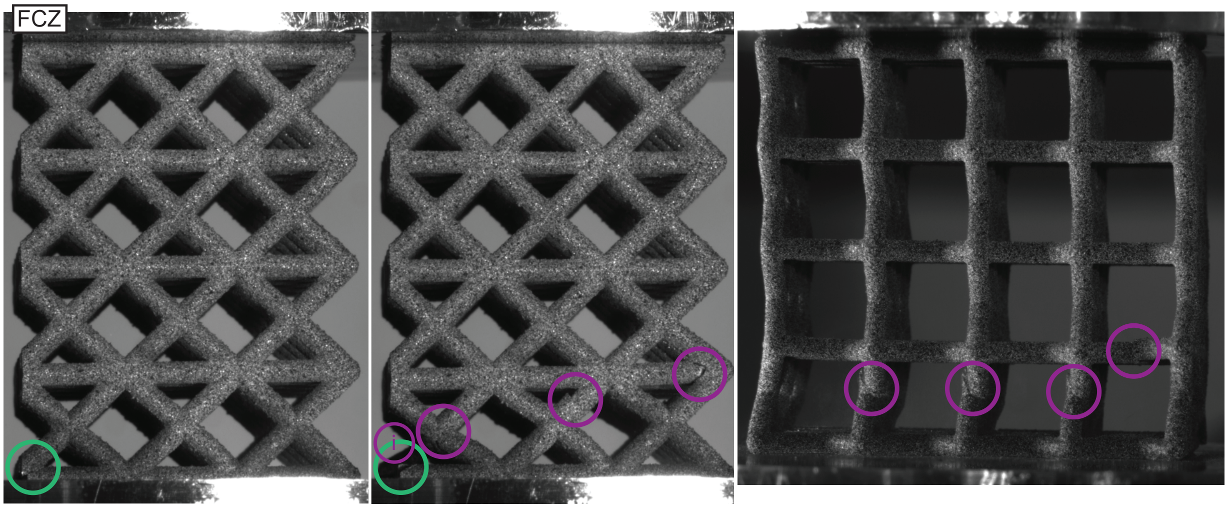

(b) f_1 failure locations f_2 failure locations (-x face) f_2 failure locations (+z face)

Figure 5.4: Optical images that were used for DIC which indicate the locations at which failure occurred for the first (f_1) and second (f_2) failure sets for the (a) "FCC" and (b) "FCZ" lattices. Note that the "i" indicated within a circled region represents interior nodes failing.

lattice is loaded. This will be explored in the next section.

5.3.2 Primitive DIC strains compared to FEA

The struts and nodes of both lattices were visualized separately in different coordinate systems and compared to FEA results, which were scaled to the strain values of the DIC. The ϵ_{yy} strain contours of the struts are shown in a coordinate system that has the yy direction aligned with the strut axis in Fig. 5.6, while the ϵ_{yy} strain contours of the nodes are shown in a coordinate system that has the yy direction aligned with the compression direction in Fig. 5.7. Both Fig. 5.6 and Fig. 5.7 have the failure locations from Fig. 5.4 overlaid and colored according to Fig. 5.4.

For both lattice structures in Fig. 5.6, a boundary effect on strain localization in the struts is apparent from the DIC strain contours; this effect is validated against the FEA. For a depth roughly equivalent to a unit cell, struts near the exterior have different strain localization patterns than struts in the interior of the face. Additionally, the degree of constraint has an influence on strain localization; diagonal struts that have no imposed boundary conditions along the vertical exterior of the lattice experience lower ϵ_{yy} strains than struts in the interior but higher strains that struts adjacent to the compression platens.

For the “FCC” lattice in Fig. 5.6, the struts near the platens are splaying outward in a stretch-dominated matter, as the lattice is compressed based on the tensile ϵ_{yy} strains. Interestingly, despite these exterior struts experiencing high tensile strains, they do not fail first. The interior struts along the surface are primarily bending as the structure is

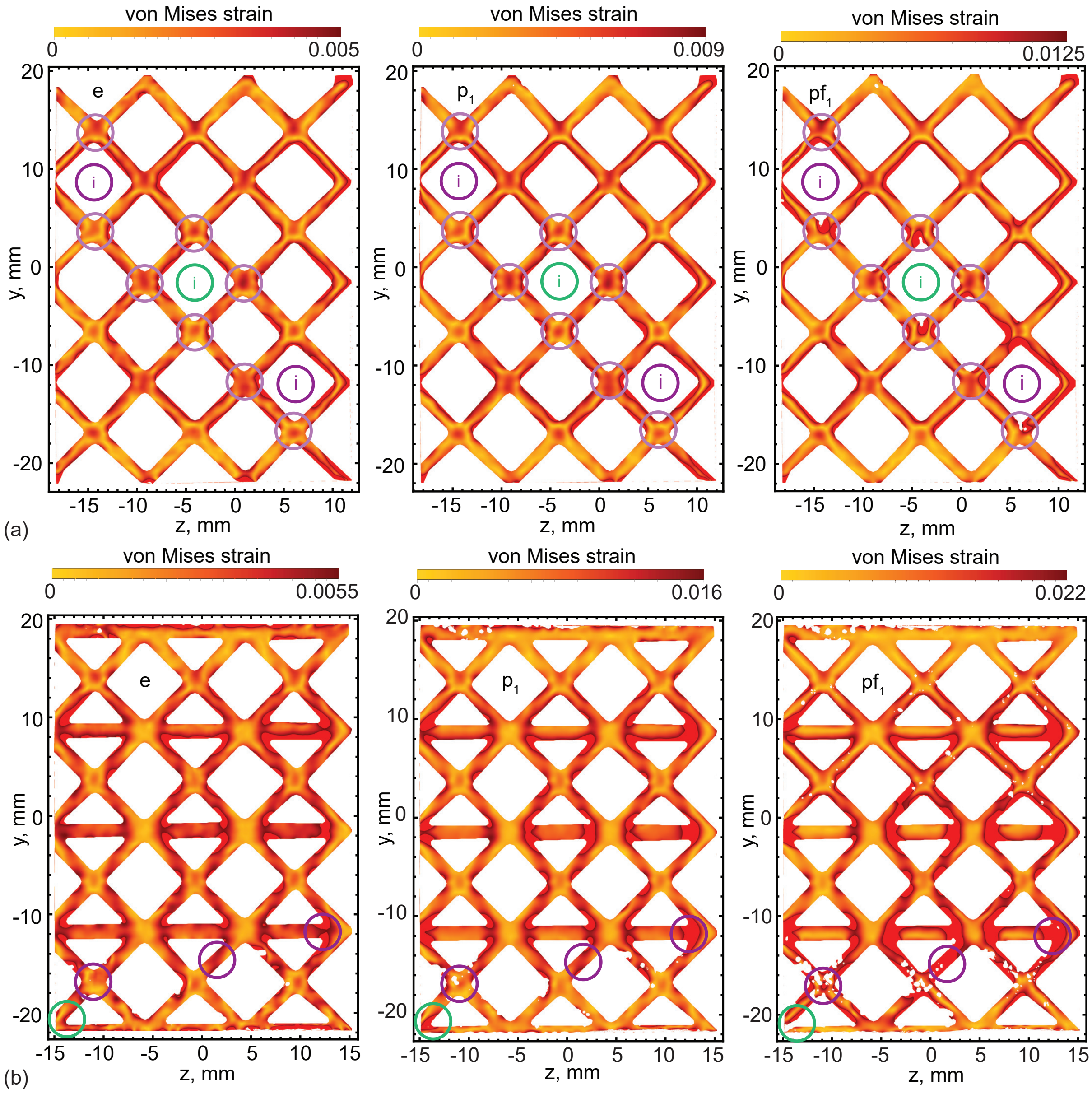

Figure 5.5: Von Mises strain contours from the DIC for the (a) FCC and (b) FCZ lattices at the points of e, p_1, and pf_1 as indicated in Fig. 5.3. The failure locations seen from Fig. 5.4 are indicated and colored accordingly.

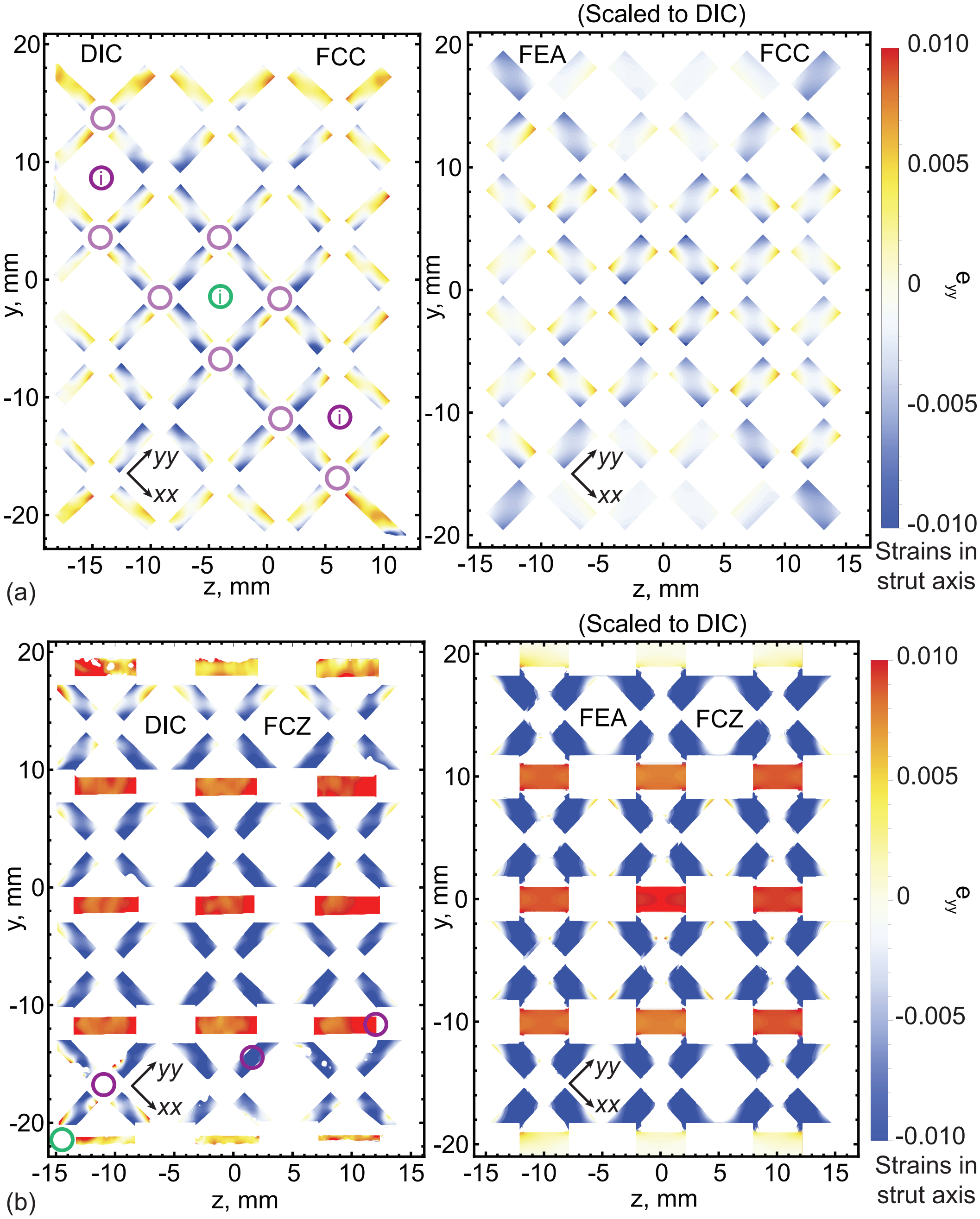

Figure 5.6: Comparison of ϵ_{yy} strain contours of the struts from the DIC to the FEA at point p_1 for the (a) FCC and (b) FCZ lattice. Note that the coordinate system of the strains is aligned with the strut axis and that strains in the FEA are scaled to strains in the DIC. The failure locations seen from Fig. 5.4 are indicated and colored accordingly in the DIC images.

compressed, based on the patterns of tensile ϵ_{yy} strains along opposite ends of the struts that are experiencing mostly compressive ϵ_{yy} strains. The patterns in strain localization observed in the DIC are similarly echoed in the FEA, with the exception of the struts near the imposed boundary conditions, which do not undergo the stretch-dominated splaying that occurs in the experiment. This deviation could be because the degree of constraint imposed in the horizontal direction in the FEA is stricter than that of the experiment. Another possibility is that the printing process induces local defects or microstructural differences in the struts near the exterior that causes them to behave differently than what simulations would suggest. Variations in the mechanical properties near the exterior boundary in comparison to the interior have been observed in the nanoindentation work by Messina, et al. [195].

The diagonal struts in the “FCZ” lattice in Fig. 5.6 also bend under macroscopic compression but not to the same degree as those in the “FCC” lattice. The amount the diagonal struts can bend is more constrained due to the horizontal crossbars in the “FCZ” lattice, which experience high tensile ϵ_{yy} strains as they stretch to support the structure. Similar to the “FCC” lattice, the FEA strain maps of the “FCZ” lattice display a similar pattern of strain localization to the DIC with the exception of the struts near the applied boundary conditions. The struts near the platens in the DIC appear to experience higher tensile strains in comparison to their counterparts in the FEA. As discussed earlier, these differences could be due to the differences in constraint between simulation and experiment or local material variations due to process-property coupling arising from the printing process. Differences in strain localization due to strut orientation and proximity to external boundaries has also been observed in previous studies who have done DIC on lattice structures [73, 175, 196, 221].

In the nodal strain maps in Fig. 5.7, the nodes with a strut connectivity of four in both lattice structures counter-intuitively display tensile ϵ_{yy} strains in their interior. This phenomenon is validated by the FEA, which also shows a similar pattern of the nodes experiencing tensile strains in their interior with compressive strains around the exterior. These tensile strains are a result of the bending in the diagonal struts, shown in Fig. 5.6, compressing the material around the exterior of the nodes, which results in tensile strains in the interior of the nodes. The nodes with a strut connectivity of six in the "FCZ" lattice do not experience the high tensile ϵ_{yy} strains in the interior and instead, are predominantly compressive. This is due to the horizontal struts in the "FCZ" lattice, shown in Fig. 5.6, which compress the material in the nodes with a strut connectivity of six.

In both lattices, there is a significant difference in the location of the highest strain localization between the FEA and DIC. As mentioned earlier, this deviation could be due to the differences in boundary conditions or from local properties that differ from the uniform isotropic properties imposed in the simulations, such as variations in microstructure. Radlof, et al. conducted FEA simulations of the lattices they imaged with in situ DIC and reported similar results – their FEA reported a similar pattern of strain but at a different location than the DIC [219]. They attributed this deviation between experiment and simulation to geometrical imperfections [219]. However, Boniotti, et al. [222] conducted 3D FEA by modeling the as-designed geometry from CT while using a uniform elastic-plastic material model. They then compared the resultant strain contours from the CT-based FEA to those observed in DIC and found that, even when using the as-manufactured geometry in simulation, the patterns of strain localization in the FEA did not match with that of the experiment. This suggests that local material variations play a crucial role in strain localization.

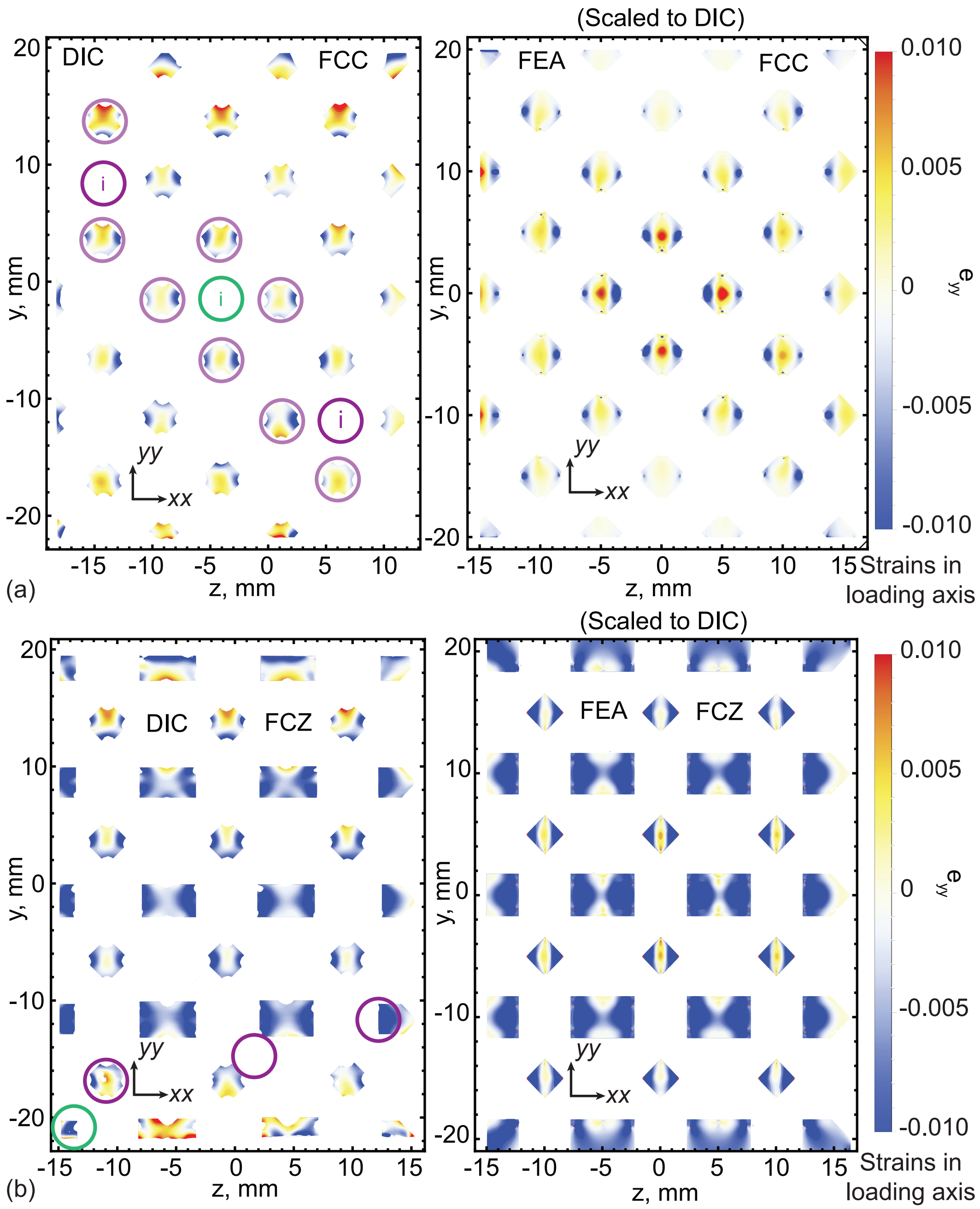

Figure 5.7: Comparison of ϵ_{yy} strain contours of the nodes from the DIC to the FEA at point p_1 for the (a) FCC and (b) FCZ lattice. Note that the coordinate system of the strains is aligned with the loading direction and that strains in the FEA are scaled to strains in the DIC. The failure locations seen from Fig. 5.4 are indicated and colored accordingly in the DIC images.

5.4 Discussion

5.4.1 Surface strain localization and failure location

Fig. 5.8 displays the von Mises strain for both the DIC and FEA of both lattices at point p_2, which is just prior to first failure of the lattice structures. Similar to previous figures, the failure locations from Fig. 5.4 are also superimposed upon the DIC results. In the "FCC" lattice, the FEA shows a pattern of strain localization with the highest strains forming an "X" pattern across the entire face of the lattice. The DIC for the "FCC" also displays this pattern, though it is more subtle, and additionally has high strains localizing along the exterior of the struts with no constraint on the farthest right of the lattice. From this pattern, it may be expected that the lattice would fail first at one of the nodes in the interior on the surface. As shown from the failure locations, the location of first failure is actually at one of the horizontal struts in the interior of the lattice. Additionally, the locations on the surface at which failure occurs are not the locales of highest strain.

For the "FCZ" lattice in Fig. 5.8b, the strain contours for the FEA are highest around the horizontal joints in the interior and in the nodes with a strut connectivity of four in the interior. The DIC shows a similar pattern of strain localization, though strain contours tend to be more asymmetric than those shown in the FEA. Based on the pattern of strain localization in the "FCZ" lattice, it is unclear where one would expect failure to first occur. Although the indicated failure locations do experience a significant amount of strain localization, it would not be intuitive to expect failure to occur at these loca-

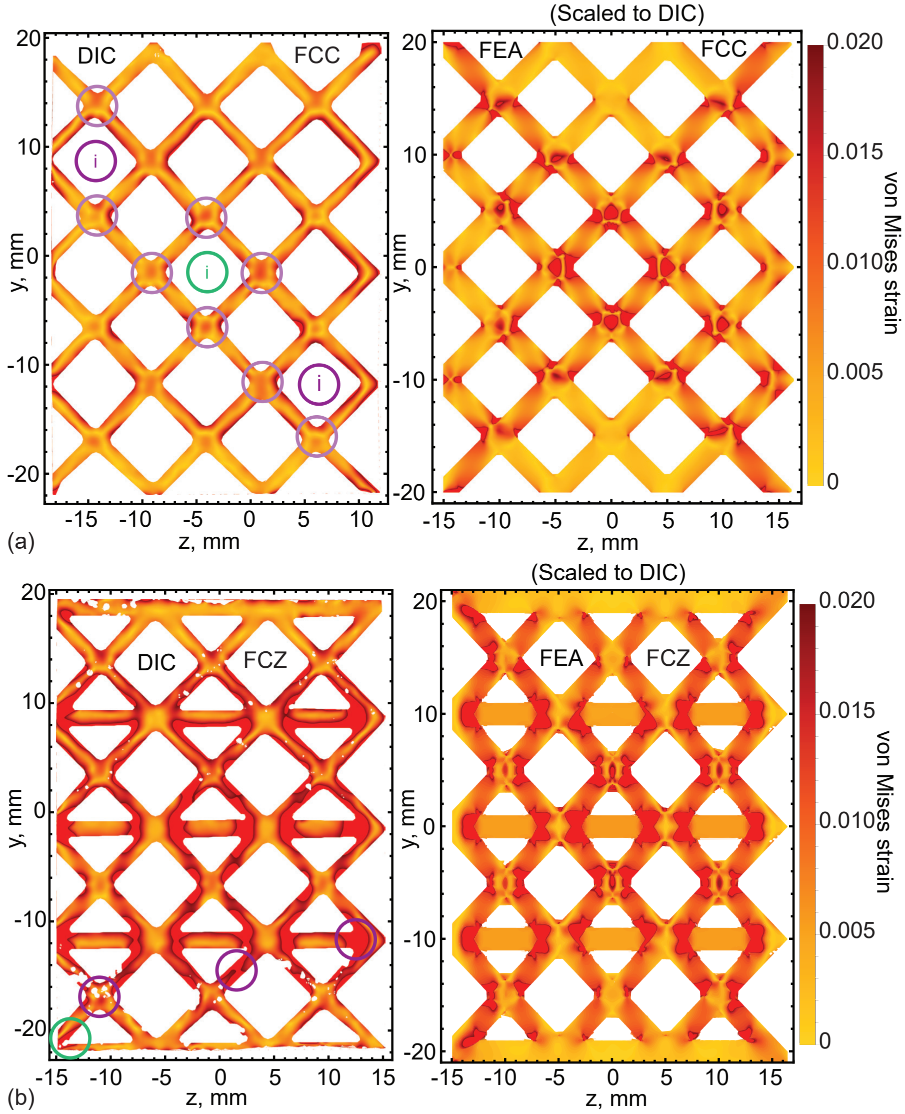

Figure 5.8: Comparison of von Mises strain contours from the DIC to the FEA at point p_2 for the (a) FCC and (b) FCZ lattice. Note that strains in the FEA are scaled to strains in the DIC. The failure locations seen from Fig. 5.4 are indicated and colored accordingly in the DIC images.

tions since there are many other locations, such as along the intersection of the interior horizontal struts to the nodes with a strut connectivity of six, which experience equally prominent strain localization.

The patterns of strain localization compared to failure locations in both lattices suggest that surface strains have limited ability to predict failure location. This is congruent with many of the other studies that also found that strain localization did not necessarily predict failure [196,212,216,219–221], but opposite the few studies that found that strain localization did correlate with failure location [201, 211, 213, 214]. The utility in surface strain measurements likely depends upon the quality of the measurement and upon the lattice geometry and defect population.

Although surface strains may not necessarily inform failure locations, they do provide informative information about how strain localizes in lattice structures. Specifically, the differences in strain localization that occurs in struts near the external boundaries in comparison to struts in the bulk. Struts at external boundaries appear to experience less strain than struts in the bulk. This difference in strut strains at external boundaries in comparison to those in the bulk persists to depths comparable to the cell size and has also been reported in previous studies [226–229]. This insight into the boundary effect has implications for lattice design; depending on the end-use, it may be optimal to use a different geometry along the external boundary.

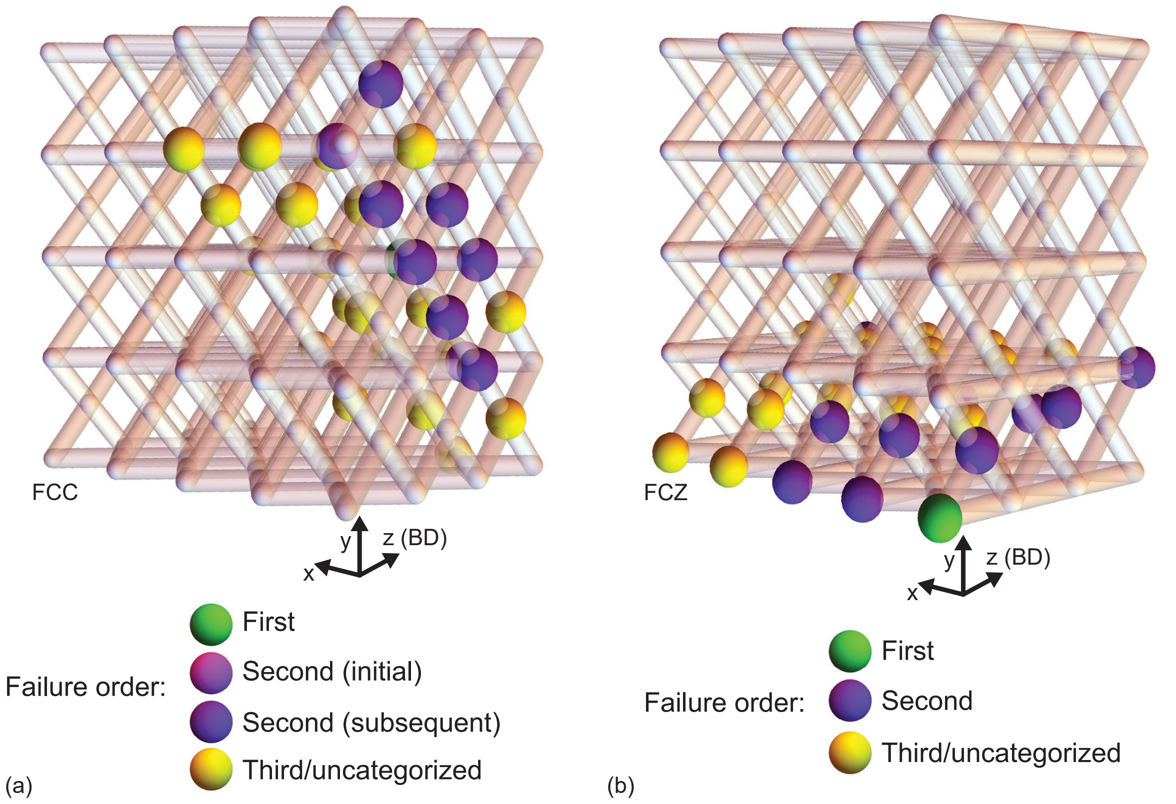

Figure 5.9: Schematic of the ideal (a) FCC and (b) FCZ lattice structures with the failure location and failure sequence indicated based on Fig. 5.4.

5.4.2 Topology and failure modality

The post-compression CT was analyzed for defect locations and failure modes. The results of this analysis is overlaid a schematic of the ideal lattice structures in Fig. 5.9, with the failure order marked as seen in Fig. 5.4. Macroscopically, both lattices failed via shearing of the nodes. This mode of macroscopic failure has been observed in other studies that tested geometries similar to the ones in this study [220, 221]. The “FCC” lattice sheared in the YZ direction near the -x face while the “FCZ” lattice sheared in the Z direction near the -y face.

Fig. 5.10 displays reconstructed CT images of the select nodes from the lattices post-compression. The selected nodes were chosen based on their failure order, as indicated by Fig. 5.9. These differing failure modes illustrate the effect of constraint and geometry upon nodal and strut failure. For the “FCC” node, the node that fractured during first failure, shown in Fig. 5.10a, experiences a “cup-cone” failure that results in complete separation of one part of the node from the other. This mode of failure is due to the high tensile strains the node undergoes as the lattice is compressed. In Fig. 5.10(b-c), the nodes that failed during the second set of failure in the “FCC” lattice experienced a precursor to the “cup-cone” failure observed during first failure. In some cases, this results in one of the struts nearly shearing off, as shown in Fig. 5.10b. The interior node that failed during the third set of failure, shown in Fig. 5.10d, experienced the least-severe form of failure with only a small crack forming at the middle of the node. The node on the exterior -z face that was binned in the third set of failure/uncategorized (Fig. 5.10e) displays shearing of the node, which is different from the modes leading to “cup-cone” failure experienced by the other nodes. This illustrates how nodal orientation and degree of constraint results in a different failure modality.

Despite both lattices experiencing some form of macroscopic shearing, the failure modes exhibited by features the “FCZ” lattice are very different from those in the “FCC’ lattice. For first failure in the “FCZ” lattice, shown in Fig. 5.10f, the struts has completely sheared off from both nodes it was connected to. A less severe version of this strut shearing is exhibited by the node in Fig. 5.10g which failed during the second set of failure; the strut has completely sheared off one of the nodes it is connected to but is still connected to the lattice by the other node. Some features on the +z face, such as that shown in Fig. 5.10h, instead experience shearing of the strut instead of shearing of the strut from the node. This type of failure that originates from the center of the strut is relatively rare in comparison to failure that originates from the node and is likely due to

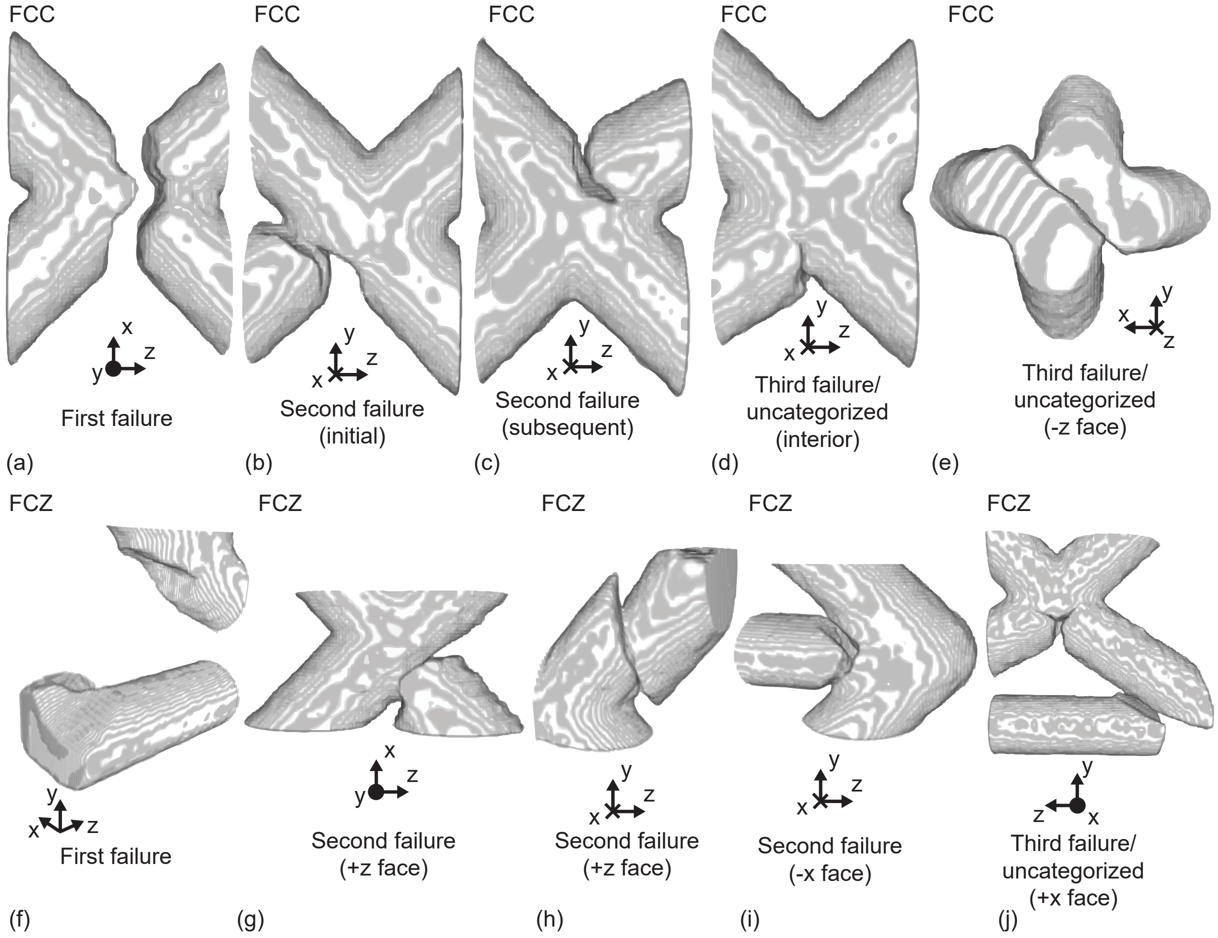

Figure 5.10: Reconstructed CT images from the post-compression (a-e) FCC and (f-j) FCZ lattice of various features of interest based on failure sequence. Note that the layers shown on the images are due to the image reconstruction and are not build layers.

local geometric or material variations in the strut. A third mode of failure, shown in Fig. 5.10i and occuring during the second set of failure, results in the horizontal strut debonding from the node on the -x. This occurs because of the high tensile strains experienced by the horizontal struts, as shown in Fig. 5.6. The various modes of failure exhibited by features during the second set of failure illustrates how orientation of features within the lattice influences failure modality. The last image, shown in Fig. 5.10j, is of a feature that was binned in third failure/uncategorized. The mode of failure exhibited is a precursor to the severe form of failure experienced during the first set of failure. In this image, the strut has debonded from the horizontal node in the exterior, and a large crack, originating from the center of the other node it is connected to, has partially sheared off the strut.

In comparison to the “FCC” lattice, the “FCZ” lattice experienced more severe forms of failure, with several of the struts missing by the end of the test. This is due to the higher strains the “FCZ” lattice experienced due to the addition of the cross-brace. The “FCZ” lattice also displayed more failure modes than the “FCC” lattice. The various failure modes displayed by both lattices highlight how topology influences both macroscopic failure and lattice primitive failure.

While the stress state is nodes has a complex spatial distribution, significant insight can be gained from beam-based analyses that do not explicitly model the nodes. Fig. 5.11 illustrates the surface strains obtained from a 3D Bernoulli-Euler elastic beam analysis of the lattices, for the struts that were characterized with DIC. For both the FCC and FCZ lattices, the strut location with the highest predicted von Mises strains correspond to the observed failure sites: i.e., the center, horizontal strut on the interior of the FCC and the corner angled struts in the FCZ. Further, the 3D FEA beam model correctly predicts the stiffness of both specimens, and, assuming a yield strain in the material of

0.009, predicts the onset of initial yielding to be close to the points identified by point "e" in Fig. 5.3. It should be noted that while this is the prediction for the onset of initial yielding in the elastic beam-based model, the macroscopic response does not exhibit significant non-linearity until plasticity has spread across a significant number of nodes or struts.

While the beam-based model does not model the nodes explicitly, the average strain in the nodes can be predicted from the beam results by computing the average stress in the nodal volume using the reaction forces at the ends of the struts forming the node. The results of this computation are also shown in Fig. 5.12, which plots the maximum principal strain magnitude in the nodes (assuming spherical nodal intersections), color-coded to indicate strain magnitude. For the FCC structure, the average nodal strains are lower than those predicted at the ends of the strut elements, a consequence of the complex deformation states in the nodes. Nevertheless, failure occurs in the node with the highest predicted tensile value of strain, even though other nodes have higher compressive principal strains. For the FCZ structure, failure occurs at a node with the highest compressive principal strain (bottom left corner); while there are high tensile strains at the nodes in the center of the lattice, the strain level of these locations is smaller than the peak strain in the FCC. A consistent interpretation of these results is that the tensile failure strain in the material is smaller than the compressive failure strain; as such, the FCC fails due to tension at a node because it reaches that limit first, while the FCZ reaches the compressive limit in the bottom corner before the tensile limit is reached elsewhere.

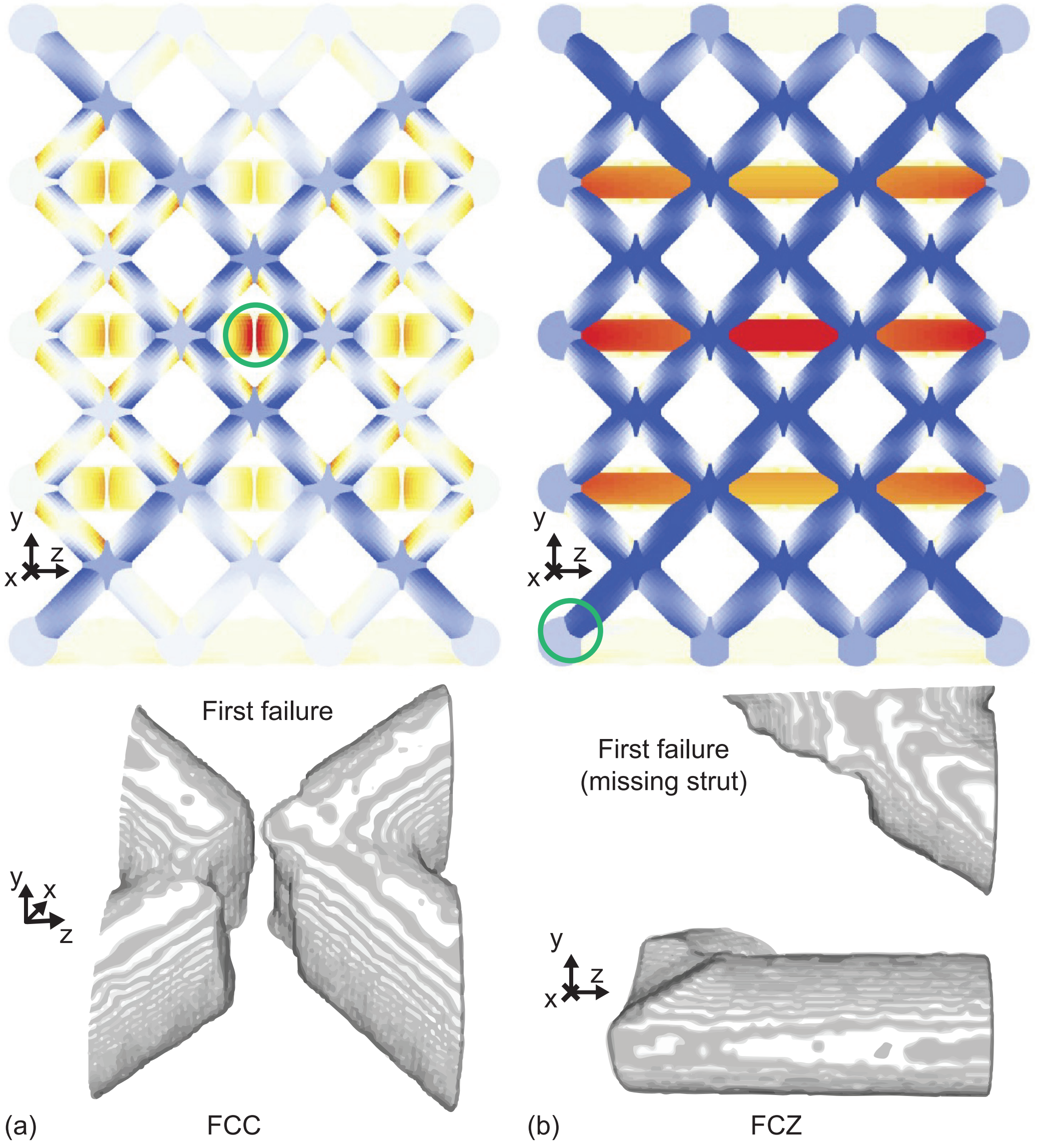

Figure 5.11: 3D beam FEA with strains in the strut axis along with the site of first failure from post-compression CT for (a) FCC and (b) FCZ lattices. The average nodal vertical stress is provided at the strut intersections.

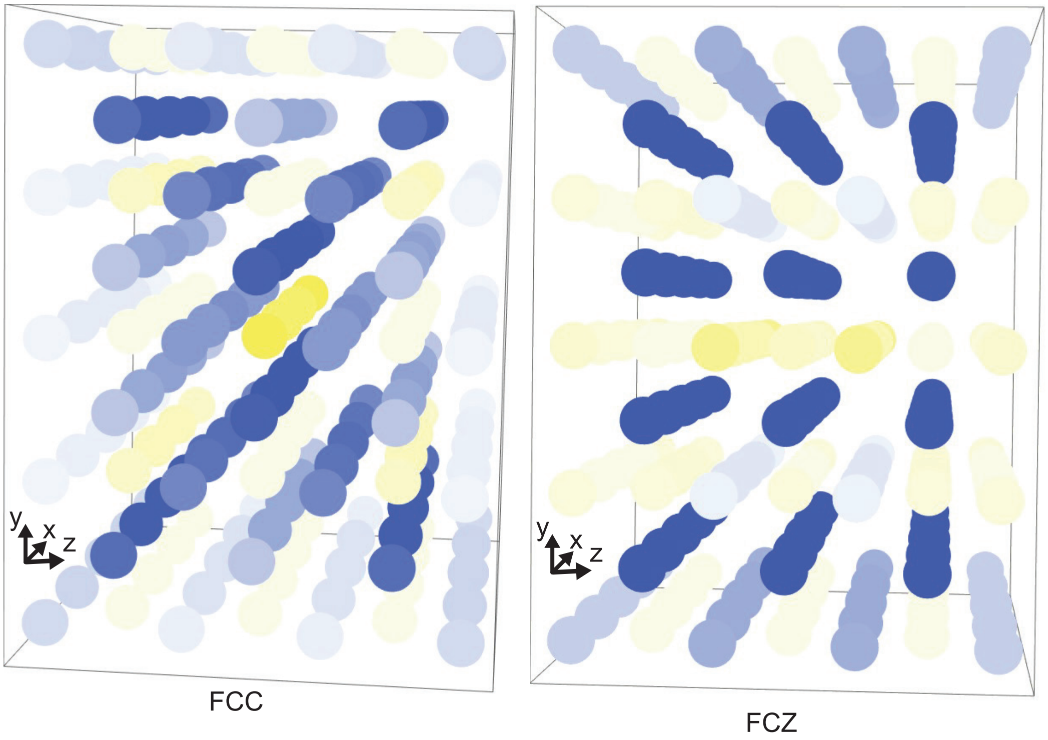

Figure 5.12: Average nodal strain computed from 3D beam FEA for (a) FCC and (b) FCZ lattices. Blue indicates compression while yellow indicates tension.

5.5 Conclusions

The results of the work provides insight into how lattice geometry influences strain localization and failure modes in lattice primitive features (struts and nodes). In addition, it also provides insight into how to best utilize surface strain measurements for in situ testing of lattice structures. The primary findings from this work are as follows:

- The addition of the horizontal cross-brace to the unit cell of a bend-dominated lattice structure will make the lattice structure significantly stronger, stiffer, and more ductile.
- Boundary effects that result in different strain localization patterns persist to a depth approximately equivalent to a unit cell.
- While von Mises strain maps provide information on how strain localizes on the lattice face, they do not provide detailed information on how lattice primitives, struts and nodes, are deforming within the structure. To best visualize primitive lattice deformation, one should display the struts in a coordinate system with the strains aligned with the strut axis while the strain in the nodes should be visualized in a coordinate system aligned with the loading direction.
- The addition of a horizontal cross-brace in the unit cell of a bend-dominated lattice structure significantly reduces the amount of bending the struts experience.
- Strut connectivity significantly influences strain localization in nodes. Nodes with a strut connectivity of four experienced tensile strains in their center due to the bending of their connecting struts. Nodes with a strut connectivity of six did not experience this unexpected phenomenon due to stabilization from the horizontal cross-brace.

- Surface strain measurements have limited utility in predicting failure location in lattice structures. Their ability to predict failure location is highly dependent upon lattice topology and defect population.
- Failure mode of lattice primitives is highly dependent upon orientation relative to the macroscopic loading direction and degree of constraint. Highly constrained nodes experience more severe forms of failure, e.g., “cup-cone” failure.

Chapter 6

Spatial maps of local variations in modulus and hardness of EBM Ti-6Al-4V millimeter-scale struts and strut intersections (nodes) measured by nanoindentation

6.1 Introduction

Additive manufacturing (AM) enables the creation of complex geometries, such as architected cellular solids, which cannot easily be fabricated via conventional, subtractive means. These architected materials, known as lattice structures, can achieve dramatic performance gains by means of their topology [24–27, 29]. Lattice structures with millimeter-scale features, specifically, can achieve notably high specific stiffness and strength, enhanced energy absorption capability, and improved heat transfer [24–27, 29–

31]. For metal AM thin-walled features of this length scale, process-structure-property relationships are intrinsically tied to component geometry, which dictates thermal conduction pathways that strongly influence solidification [5, 28–31, 34, 35, 152]. This implies that mechanical properties of printed thin struts depends on their orientation relative to the build direction, the local topology of intersecting struts (nodes), and their absolute size.

The coupling of process and properties poses a significant challenge towards the characterization and design of AM metal lattices. Ideally, process-informed models of lattice sub-features, or "primitives" of struts and strut connections (nodes) could be used to predict the behavior of lattices themselves. This approach, which involves the input of isotropic properties based on characterization of lattice primitives into Finite Element Analysis (FEA) simulations, has been attempted in previous studies with mixed results [146, 200]. While macroscopic load-displacement is able to predicted through averaging of primitive properties, local features, such as strain localization patterns, still deviated in comparison to experimental validation. These local discrepancies may be the result of local variations in material properties, which occur over a great enough length scale to significantly influence strain localization.

To explore these local variations in material properties, this work uses nanoindentation to qualitatively measure variations in mechanical properties in lattice primitives of struts and the faces of a unit cell (which consists of a node and several struts), shown in Fig. 6.1 and Fig. 6.2. Contour maps of modulus and hardness from the nanoindentation are generated along with the average value with 95% confidence interval (CI) over 1 mm intervals across the length probed are shown to demonstrate how local properties vary in thin, millimeter-scale lattice primitives. This study specifically uses Ti-6Al-4V features

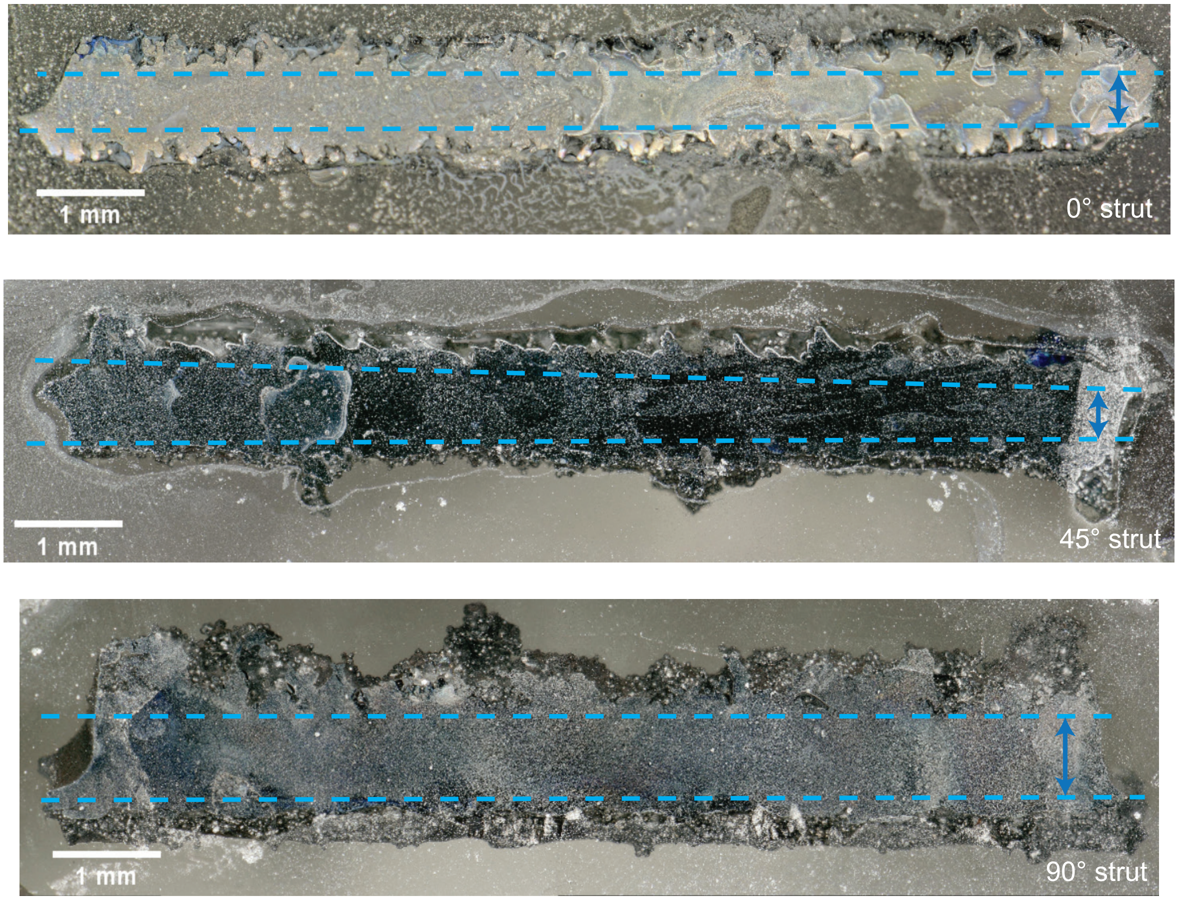

Figure 6.1: Example cross-sections of struts with dashed lines showing the region that as viable for indentation.

fabricated via electron beam melting (EBM), which are commonly used in biomedical applications due to its low density, low elastic modulus (compared with steels or cobalt nickel alloys), corrosion resistance, and proven biocompatibility [5, 8, 34–38].

There has been growing interest in using indentation to evaluate the properties of thin-walled powder bed AM materials. Majority of previous studies only use indentation to measure the hardness of struts to compare to benchmark values [8, 12, 14, 230–236]. In addition, the broad majority of studies that use indentation on AM metals report

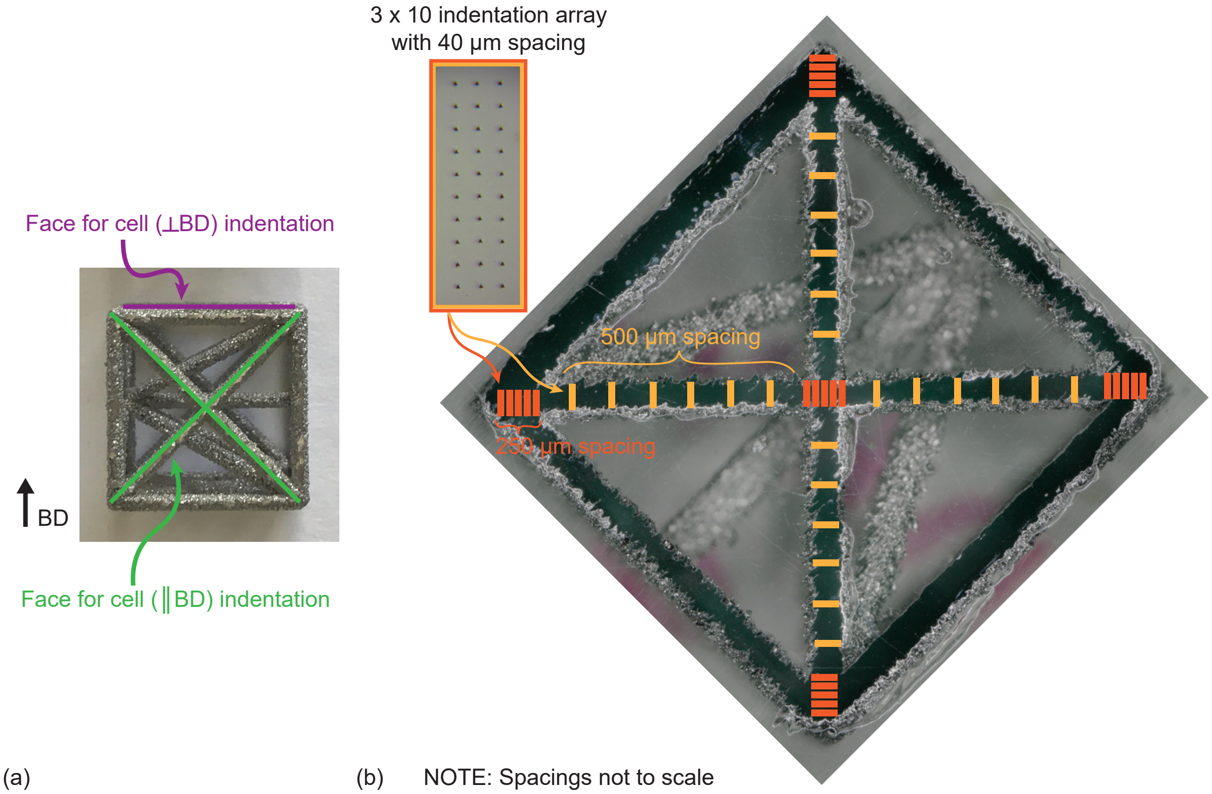

Figure 6.2: (a) Example of a cell in this study with the two faces that were indented indicated relative to the build direction. (b)Example cross-section of the cell that was indented with a schematic depicting the indentation array spacing across the sample.

microhardness values for purposes other than evaluating spatially varying properties [8, 14, 156, 230–238]. There are a few studies of note that have used microindentation as a tool to probe local material variations in powder bed AM metals spatially but were limited in the number of measurements they could produce due to their choice of indenter size [182, 239, 240]. Of the studies that use nanoindentation on metal AM materials, most of these were limited in length scale over which they indented or they did not use nanoindentation to evaluate spatially varying properties [241–245]. Everitt, et al. [246] notably used nanoindentation to investigate the mechanical properties across a single meltpool but only indented across a very small region. A couple of other studies have used nanoindentation to investigate local material property variations but only to determine how properties changed for AM metals in which a material gradient was intentionally created [247, 248]. To the authors' knowledge, this study is the first of its kind to extensively use nanoindentation to provide spatial maps of local property variations in EBM Ti-6Al-4V struts and nodes due to differences in print orientation and local geometry.

This work makes the following important contributions. First, it demonstrates the utility of using nanoindentation to probe local material property variations in powder bed AM lattice structures. Second, it evaluates the impact of print orientation upon hardness and modulus of EBM Ti-6Al-4V struts. Then, it evaluates the impact of topology (strut vs. node) upon hardness and modulus for the face of a unit cell of a lattice that consists of multiple struts and nodes. It also compares the role of topology to the role of print orientation, in terms of influence upon mechanical properties. Lastly, it compares the mechanical properties of struts printed in isolation to those of the same print orientation that are apart of a multi-strut cell. These results provide greater insight into how print orientation and local geometry influence the resultant mechanical properties of thin-walled EBM Ti-6Al-4V structures.

6.2 Methods

In this study, the local material properties of three individually printed struts at various orientations (Fig. 6.1) and struts comprising the face of two simple lattice cells with an octet geometry (Fig. 6.2) were probed with nanoindentation. One of the cells was indented on a face that was parallel to the build direction (∥BD) while the other was indented on a face that was perpendicular to the build direction (⊥BD). Refer to Fig. 6.2, which shows this graphically. Hardness and modulus maps were generated from the indentation results to draw insight into how print orientation and local topology influence material properties.

6.2.1 Printing

Primitive samples of struts and cells, shown in Fig. 6.1 and Fig. 6.2, were fabricated in Ti-6Al-4V by an EBM system (Arcam A Series, Arcam, Sweden) using a 70 µm melt theme. Complete details on the powder characteristics are available in the work by Dong, et al. [146]. All samples were printed with a nominal strut diameter of 1 mm. Strut primitives were printed at three different orientations relative to the build plate, 0°, 45°, and 90°, in which 0° is defined to be parallel to the build direction. Cell primitives were all printed at the same orientation.

All samples were hot isostatically pressed (HIP) upon fabrication per ASTS F2924-14 or ASTM F3001-14 specifications [147]; components were processed under inert atmosphere at not less than 100 MPa within the range of 894 °C to 995 °C and held at the selected temperature within ± 15 °C for 180 ± 60 minutes before cooling under inert atmosphere to below 425 °C.

6.2.2 Nanoindentation

Prior to testing, samples were mounted in an epoxy, ground to the widest point in the strut thickness, and polished in a solution of colloidal silica on a Buehler Vibromet vibratory polisher (Buehler, Lake Bluff, IL). Nanoindentation experiments were performed using a Nanomechanics iMicro Nanoindenter (Nanomechanics Inc., Oak Ridge, TN) equipped with a 1 N load cell. Hardness measurements were performed with a Berkovich tip diamond indenter. The strut samples were tested at an indentation strain rate of 0.4 s^{-1} while the cell samples were tested at an indentation strain rate of 0.6 s^{-1}. The tip area function of the Berkovich tip was calibrated on fused silica before and after all experiments to ensure that the tip area function did not change significantly throughout the course of the test. The reported hardness values are extracted from 500 nm penetration depths.

For the strut samples, indents were spaced every 50 µm across a minimum length of 16 mm and every 75 µm across the diameter within the region viable for indentation, as shown in Fig. 6.1. For the cell samples, indentation arrays consisting of a 3 x 10 (length x diameter) indentation points spaced 40 µm apart were placed across the interior struts on the indented face. These indentation arrays were spaced 250 µm apart in the nodes and 500 µm apart along the struts as illustrated in Fig. 6.2. This choice of uneven spacing was to provide more data in the nodal regions. For the cell with the face indented along the build direction (||BD), these indentation arrays were placed across both interior strut ligaments. For the cell with the face indented within the same build plane (⊥BD), the indentation arrays only occurred across one of the interior strut ligaments because the machine broke before it could test the other ligament. The machine is currently fixed but further assistance from someone in the Gianola group will be required for any future tests.

The nanoindentation results for the struts on aggregate are over a minimum sample size of 1437 for each strut. For the results that are binned in 1 mm intervals, the 0° strut has a minimum sample size of 99 for each interval, except for its last interval, which has a sample size of 49. The 45° strut has a minimum sample size of 60 for each 1 mm interval while the 90° strut has a minimum sample size of 132 for each interval. The 95% confidence intervals (CI) for the struts were computed by using a t-value associated with samples having 40 degrees of freedom, which is 2.021. Degrees of freedom are an estimate of the number of independent independent values in a data sample. The degrees of freedom is generally taken to be one minus the sample size. For the cell (∥BD) sample, a total of 2538 indents were made while for the cell (⊥BD) sample, a total of 1204 indents were made. The cell (∥BD) sample had a minimum sample size of 56 indents for each 1 mm interval while the cell (⊥BD) sample had a minimum sample size of 49 for each interval. Similar to the struts, the 95% CI for the cells used a t-value associated with samples have 40 degrees of freedom.

6.3 Results & Discussion

6.3.1 Struts

The indentation maps of the individually printed struts reveal that print orientation can significantly influence average hardness but does not significantly influence average modulus. They also demonstrate that significant property gradients can exist from one end of the strut to the other. Contour maps displaying the hardness and modulus across 10 mm of the indented region of all struts are shown in Fig. 6.3. From the contour maps of hardness in Fig. 6.3a, it is apparent that the 90° struts are much harder, suggesting that struts built in this orientation are significantly stronger than struts built in the 0° or 45° orientations [133,134,142]. Unlike the 0° and 45° struts which have "hard" regions recurring sporadically across the length, the 90° has various "soft" spots that recur. The size of these "spots" are on the order of the size of prior β grains of different orientations seen in previous studies on the literature for EBM Ti-6Al-4V parts [44,156]. Changes in orientation of Ti-6Al-4V can result in a strength difference of up to 44%, which is similar to the percent variation in hardness exhibited in these contour maps [136]. Interestingly, the trend in hardness does not extend to modulus, implying that for these materials, hardness is not correlated to modulus. From the modulus maps in Fig. 6.3b, the 45° struts appear to have a much lower modulus than the 0° and 90° struts.

The trends seen from the contour maps in Fig. 6.3 are echoed in the box plots displaying the aggregate average, standard deviation, min, and max for hardness and modulus for the struts in Fig. 6.4. The trend in hardness in Fig. 6.3a, with 90° being much stronger than struts in other orientations, is generally consistent with the trend in strength, after correcting for effective geometry, from tensile tests of similar struts from the same build in Dong, et al. [146]. The variations in modulus on aggregate, shown in Fig. 6.4b, do not

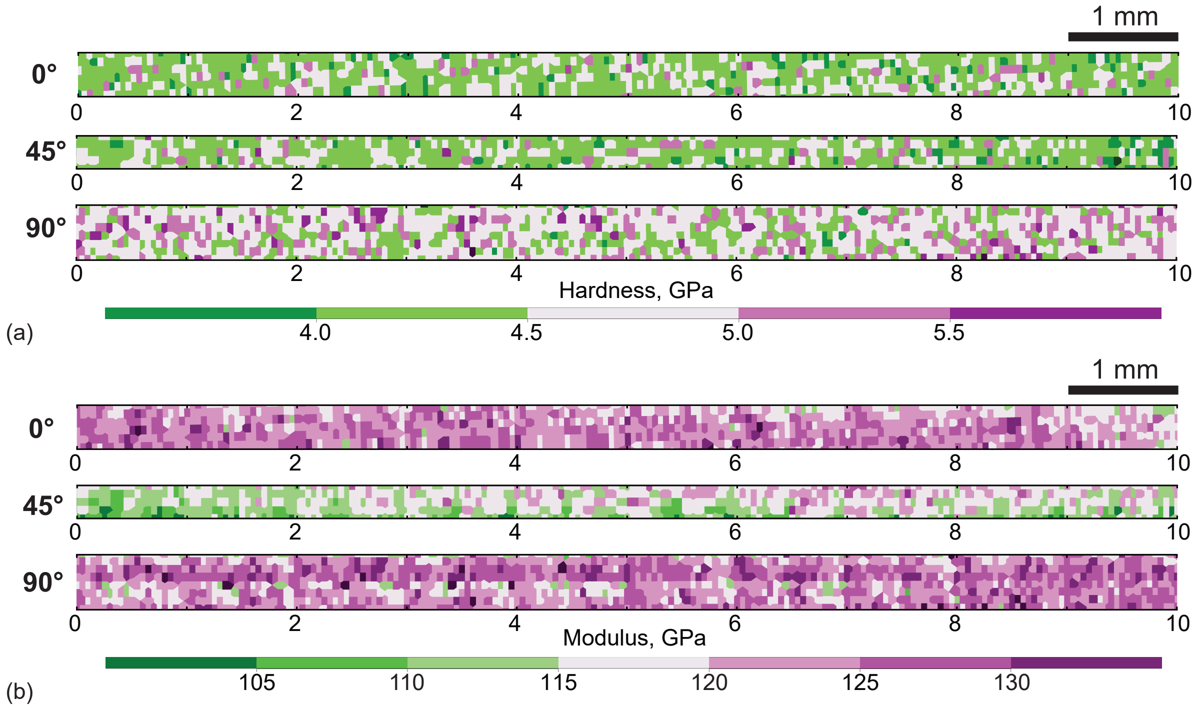

Figure 6.3: Contour maps of (a) hardness and (b) modulus across most of the length of the indented 0°, 45°, and 90° 1 mm struts.

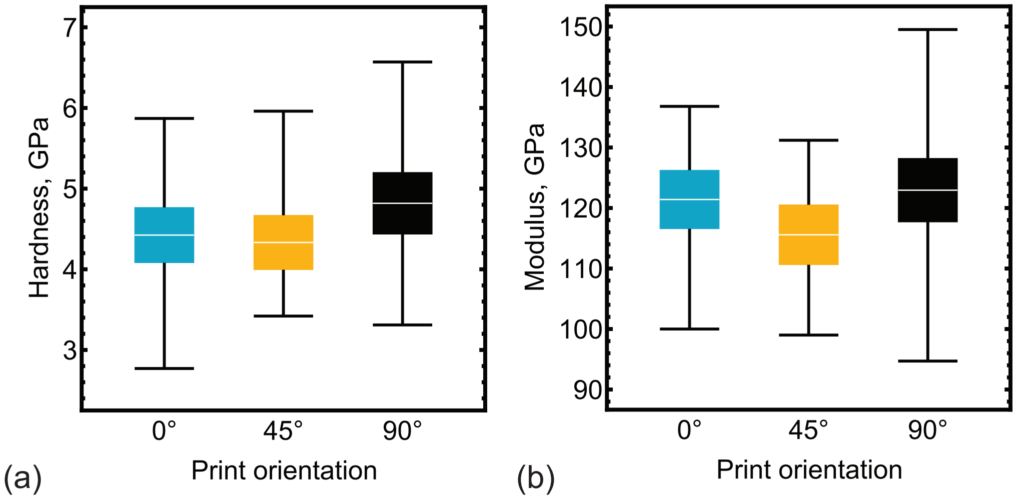

Figure 6.4: Box plots of (a) hardness and (b) modulus with the white bar displaying the mean, the colored region showing the bounds of a standard deviation, and the whiskers showing the max and min for all indented struts.

appear to be as dramatic as suggested from Fig. 6.3. The largest percent difference in average modulus between struts of different orientation is 6% and the average modulus deviates from the manufacturer's value of 120 GPa by 1-3% [148]. This suggests that on average, modulus in thin-walled structures does not vary significantly from that of bulk structures.

Although contour maps of mechanical properties like the ones shown in Fig. 6.3 are information-rich, it is useful to quantitatively report these local variations across the indented length for ease of comparison. The average hardness and modulus, with 95% CI, within every 1 mm interval along the entire indented length for all struts is shown in Fig. 6.5. A dotted line that represents the aggregate average value is also provided for convenience in Fig. 6.5. From these graphs, it is obvious that hardness and modulus are not correlated for these structures. The 0° strut displays relatively consistent hardness along the entire indented length but has significant differences in modulus from one end to the other. Both the 45° and 90° struts also display some kind of gradient in modulus, with the 45° strut having a much more dramatic difference from end-to-end. Interestingly, the 45° strut displays an almost opposite gradient in hardness in comparison to its modulus trend. The hardness of the 90° struts varies non-monotonically across the indented length. Gradients in microhardness due to distance from build plate have been observed in prior results by Wang, et al. in an EBM Ti-6Al-4V part but their results are not consistent with ours [239]. This may be because of the completely different geometry (an impeller) that Wang, et al. evaluated [239]. In general, modulus seems to vary more wildly locally than hardness in these thin-walled structures. These results reveal that significant variations in local properties can occur over the feature size, highlighting the importance to necessity to account for these variations for accurate prediction of performance.

6.3.2 Cells

Contour maps of hardness and modulus for the cell (||BD) are shown in Fig. 6.6 while contour maps for the cell (⊥BD) are shown in Fig. 6.7. For cell (||BD), the hardness is lower at the exterior nodes but then increases along the strut to the center node. This pattern is echoed in the modulus for cell (||BD) except for the strut leading to Node IV. For the cell (⊥BD), there does not appear to be a significant gradient in modulus or hardness from the exterior to the interior node. Like for the strut contour maps in Fig. 6.3, there are various "hard" or "soft" spots that sporadically occur along the struts, which likely reflect variations in microstructure.

Quantitative measurements of hardness and modulus for every 1 mm interval with 95% CI are shown in Fig. 6.8 for cell (||BD) and Fig. 6.9 for cell (⊥BD). The gradient

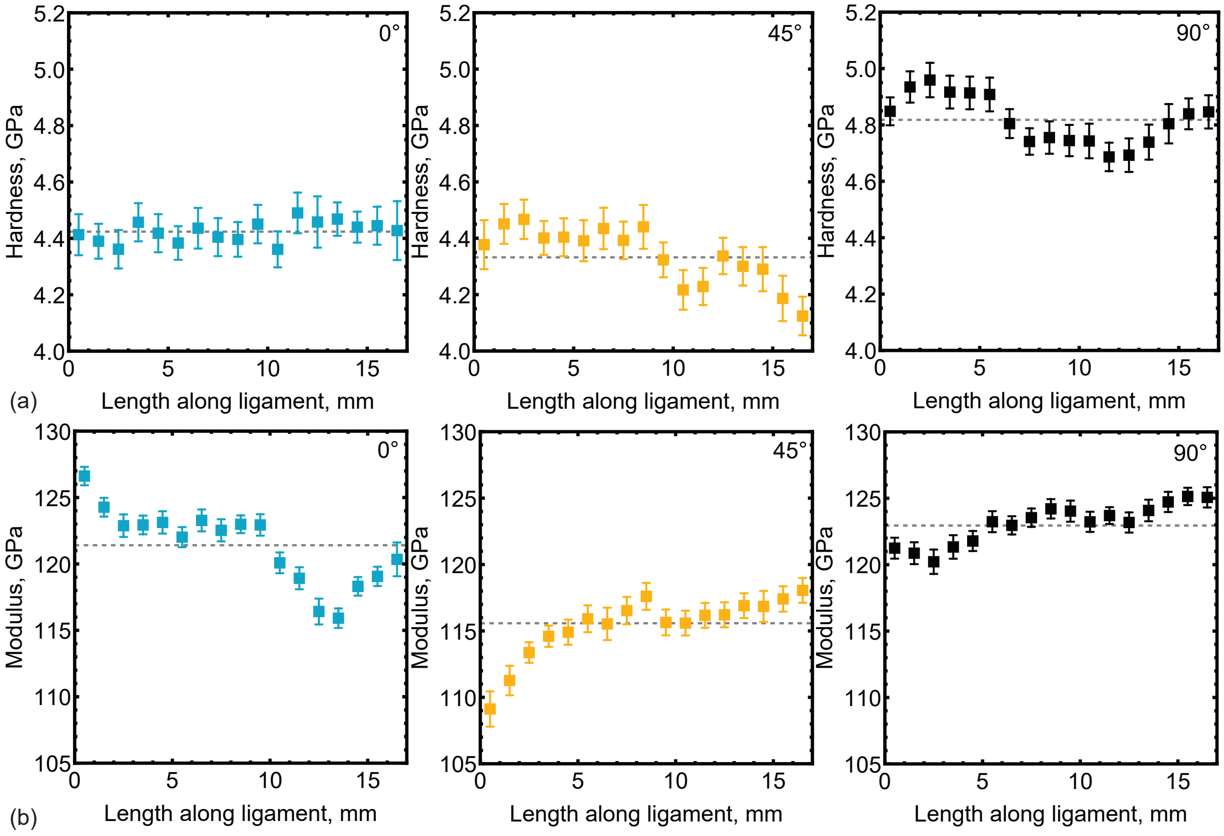

Figure 6.5: The average (a) hardness and (b) modulus within each 1 mm region indented in the struts bounded by the 95% confidence interval. The overall average for each orientation is given by the dashed line.

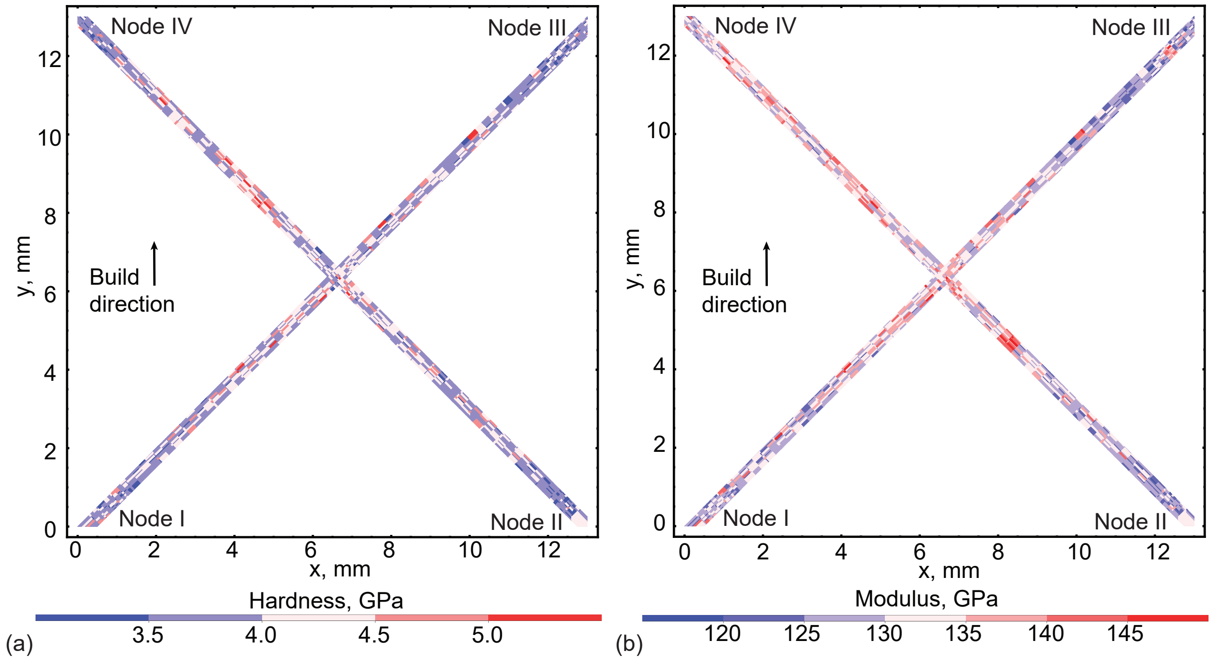

Figure 6.6: Contour maps of (a) hardness and (b) modulus across the indented region of the cell face (‖BD) with the nodes and build direction labeled.

in hardness and modulus from the exterior nodes to the center node seen in Fig. 6.6 is confirmed in Fig. 6.8. The results in Fig. 6.8a confirm that the center node is significantly harder than both the exterior nodes and average hardness of the cell face. These results are mirrored in the modulus in Fig. 6.8b, with the center node having a significantly higher modulus than average and the exterior nodes. The behavior of the center node having significantly higher hardness and modulus than the exterior nodes and overall average is not echoed in the cell(⊥BD), as shown in Fig. 6.9. Unlike with the cell (‖BD), many of the measurements in the cell (⊥BD) are relatively similar to each other and tend to vary randomly around the overall average. These results suggest that the effect of build orientation upon mechanical properties is much stronger than variations in topology (e.g., node vs. strut).

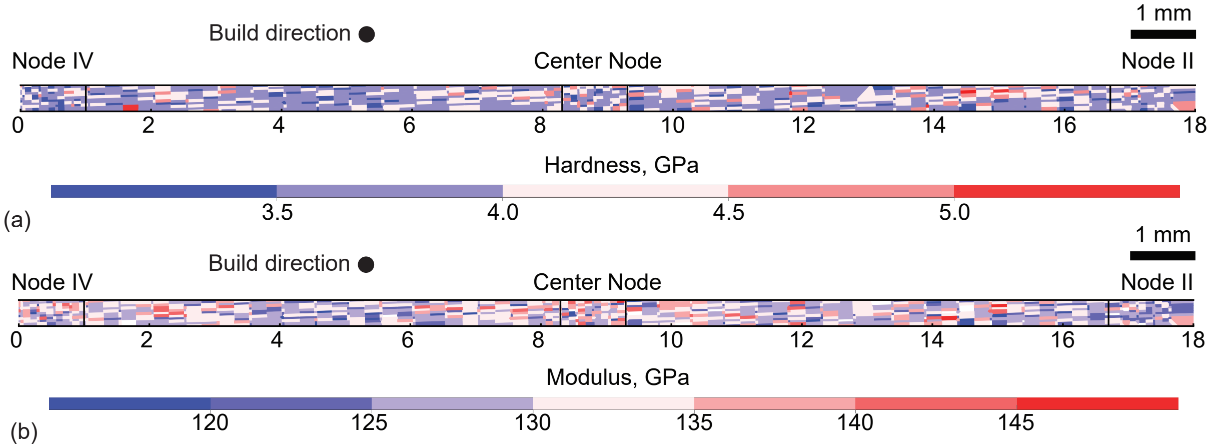

Figure 6.7: Contour maps of (a) hardness and (b) modulus across the indented region of the cell face (⊥BD) with the nodes and build direction labeled.

Comparing the mechanical properties from the cells to those of the isolated struts suggest that struts in isolation may not have the representative mechanical properties of struts that are incorporated into a lattice structure. In comparison to the strut results in Fig. 6.4, the struts of the cells have a lower average hardness and a higher average modulus for struts of the equivalent print orientation. For the 45° orientation, the struts in the cell (||BD) tends to display a more severe gradient in mechanical properties in comparison to the 45° strut primitive. The 90° struts in cell (⊥BD) tended to have greater variation within their mechanical properties in comparison to the 90° isolated strut primitive. Additionally, the average hardness of the 45° struts in cell(||BD) is similar, if not greater, than the average hardness of the 90° struts in cell (⊥BD). This is contrary to the results shown in Fig. 6.4, which demonstrated that the 90° strut primitives are significantly harder than the primitives printed in the other orientations. This highlights the influence of topology upon resultant properties in AM structures.

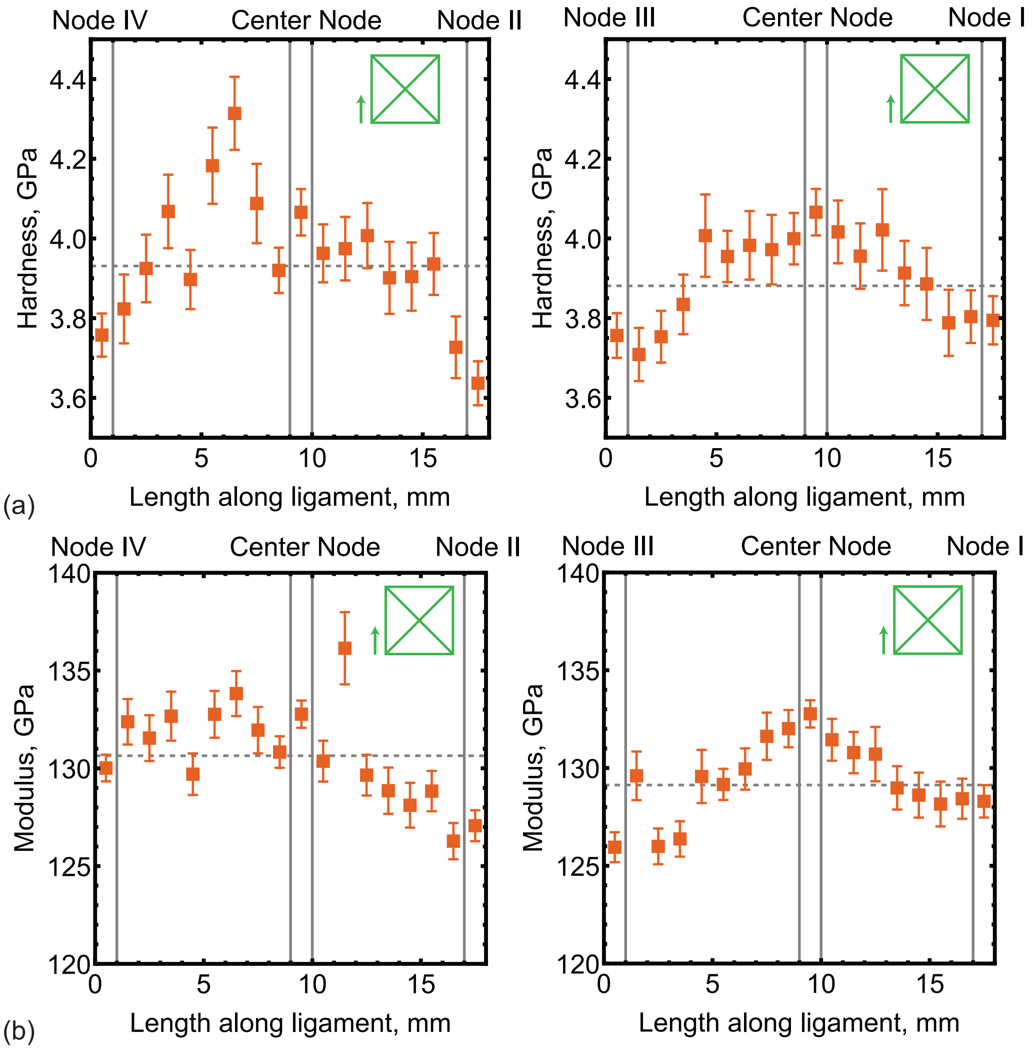

Figure 6.8: The average (a) hardness and (b) modulus within each 1 mm region indented in the cell face (||BD) bounded by the 95% confidence interval. The overall average is given by the dashed line.

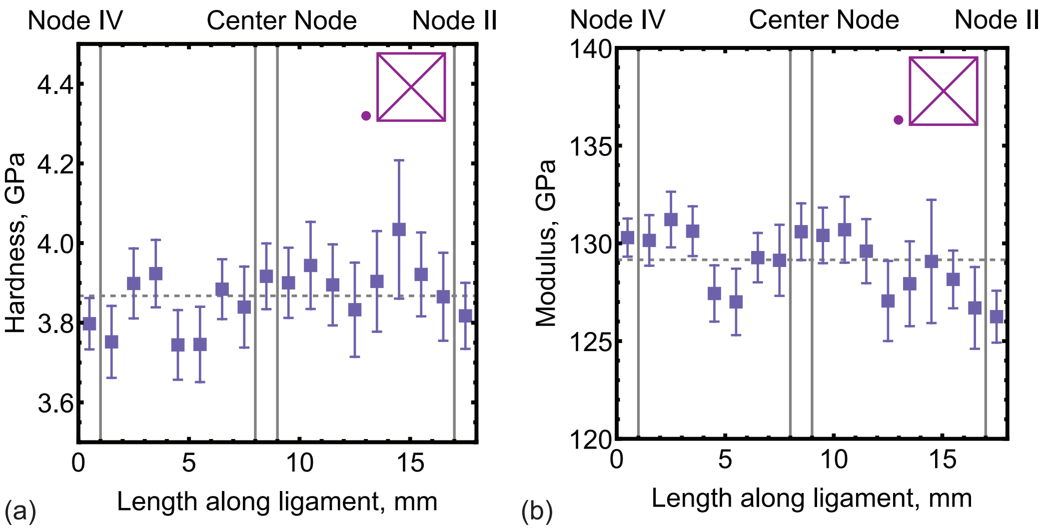

Figure 6.9: The average (a) hardness and (b) modulus within each 1 mm region indented in the cell face (⊥BD) bounded by the 95% confidence interval. The overall average for is given by the dashed line.

6.4 Conclusions

Nanoindentation was used to probe the influence of print orientation and local geometry upon local variations in material properties in struts and nodes. The main conclusions from this work are as follows:

- For EBM Ti6Al4V thin-walled structures, hardness and modulus results are not necessarily correlated to each other. This suggests that the structure consists of varying microstructure that manifest to have similar strength.
- Isolated struts built at a 90° orientation are significantly harder (9-10%) than isolated struts built in the 0° or 45° orientation. This suggests print orientation significantly influences resultant microstructure in a way that manifests higher hardness for thin, strut-based structures built at 90°.
- Struts built at a 45° orientation have a significant gradient in hardness and modulus from one end to the other. In isolated struts, the hardness and modulus varied by

7-9% from end-to-end. In 45° struts within a multi-strut structure, hardness varied by 5-14% while modulus varied by 2-8%.

- Center nodes within a lattice structure built in the plane of the build direction are significantly harder and have a significantly higher modulus than nodes along the exterior. The center nodes have a 8-13% higher hardness and 2-6% higher modulus than exterior nodes.

- Build orientation has a stronger effect on mechanical properties than topology within a build plane. For the same topology, a cell that was built parallel to the build direction had hardness values that varied by 17% and modulus values that varied by 8% while a cell built normal to the build direction hard hardness values that only varied by 7% and modulus values that varied by 5%.

- Isolated struts do not necessarily have the same mechanical properties as struts within a lattice structure. The isolated 45° struts were 10% harder and had a 11% lower modulus than the 45° struts in the cell. The isolated 90° struts were 19% harder and had a 5% lower modulus than the 90° struts in the cell.

Chapter 7

Summary and recommended future work

This dissertation provides important insights into the effect of process-properties coupling upon millimeter-scale features in lattice structures built by powder-bed AM. The techniques and methods presented are broadly applicable to other metallic powder-bed AM lattice structures. The contributions in this dissertation support the following conclusions and recommendations for future work:

Characterization of of strut geometry and mechanical response to identify effective properties as a function of print orientation:

- The resultant geometry of printed struts is highly dependent upon print orientation and can be significantly different from the dictated geometry from CAD files. CT in combination with FEA with validation by mechanical tests were used to demonstrate a method to rigorously determine the effective area of printed struts in two different material systems made by two different processes. This method of determining effective area is straightforward and directly connects to the physical dimensions of the struts. Future studies could use this method in more material systems and processes to evaluate how material and process influence effective geometry in powder-bed AM lattice features.

- The results of this studied demonstrated that different print orientations resulted in different deviations from prescribed area, with orientations more normal to the build direction producing more significant deviations. This study only focused on three different orientations – 0°, 45°, and 90° relative to the build direction. Additional studies that build upon this print orientation effect in combination with orientation within the build plane may be of interest as they may lead to more insight into how other factors, in combination with print orientation, influence geometry.

- The effective area method was further improved by demonstrating that surface roughness measurements could be used to accurately predict the effective area in SLM SS316L nominally square struts. Because fully characterizing these printed structures with CT is a time-consuming process, this method is a promising way to efficiently identify the effective area using surface measurements. Future work should evaluate this method against other material systems and processes as well as with struts with different nominally-shaped cross-sections.

Identification of a method to efficiently extract effective properties from lattice-based structures

- Using the effective area method developed in this work allows for the inference of realistic mechanical properties of printed structures. By correcting for area, simulations to best-fit the macroscopic load-displacement behavior in printed structures can be conducted to infer average, isotropic properties for the materials. This enables accurate comparisons of material properties to those of bulk and to evaluation of any processing, size, or geometric effects. Future work should utilize the effective area methodology demonstrated in this body of work to other printed lattice features to enable accurate characterization of material properties.

- For further studies involving inferred material properties based on macroscopic deformation, the inferred properties should be utilized in simulations to evaluate strain localizations against in situ DIC mechanical tests. These comparisons may allow for one to draw common connections between printed lattice-based structures on where isotropic, macroscopic properties may fall short of predicting the correct behavior.

- Despite being able to infer the average, isotropic material properties in these structures by accounting for geometry, variations in local strain localization still exist. Future work should focus on rigorously measuring property variations in these features by connecting indentation property mapping to constitutive descriptions of microstructure. This kind of work will help determine what local features are integral towards accurate simulation of powder-bed AM lattices.

Understanding the role of strut intersections (nodes) in lattice deformation:

- The analysis presented of the DIC strain maps of two different lattice structures demonstrates that it is necessary to analyze the strains of struts and nodes of a lattice in two different coordinate systems to fully understand local deformation in the lattice. Struts should be analyzed in a coordinate system that has the y direction aligned with the strut axis while nodes should be analyzed in a coordinate system with the y direction aligned with the loading direction. Future work involving DIC strain maps of lattice structures should incorporate this methodology.

- The strain maps of the lattice structures tested showed that strain localizations are heavily influenced by local topology and in some cases, are quite unexpected.

Namely, the large tensile strains observed in nodes with a four-strut connectivity were un-intuitive, given that the lattices were under macroscale compression. Similar results were also observed in the simple “X” lattice structures under tension – they displayed large compressive strains in the interior of the node. Both of these results were validated by simulations. These results necessitate a deeper understanding of nodal topology and strain localization. Future work should focus on simulations of common nodal topology under various loading conditions. This work will further the understanding of how nodes may behave in lattice structures.

- The results of the strain and failure analysis from the CT and DIC of lattice structures demonstrated that the degree of constraint, location within lattice, and orientation within lattice all significantly influence how lattice primitives behave within a lattice. These effects persisted in both topologies tested and in similar manners. Some suggested future work includes simulations of lattices of varying size and topology to determine broad outlines of how topology and boundaries influence local deformation within lattice structures. Care must be taken to select unit cell topologies that are tangentially related to each other to determine the effect of changes in struts.

- Although the strain maps from the FEA of the imaged face broadly agreed with the strain maps from the simulation, there were significant deviations in strain localization locations and deformation patterns near the boundary. To determine whether these were due to only the surface being modeled, it is suggested that 3D FEA of the lattice structures tested be conducted. In addition, indentation property mapping of similar structures should be conducted to evaluate any local property effects.

- It is clear from the studies of node primitives and node deformation in lattice structures that nodes play a significant role in plastic localization of these structures. Being able to efficiently simulate nodal yielding in lattice structures is critical towards building efficient design tools to simulate their performance. Future work should focus on developing efficient nodal yield models that can easily be incorporated into beam-based models.

- While nodal yielding is the main thing unaccounted for in many beam-based simulations of lattices, local variations, such as defects due to surface roughness can also play an important role upon strain localization and deformation in lattice structures. Preliminary work that simulates notch-based defects through use of a single linear beam element that is offset the notch distance has been conducted, though it is not documented in this work. This model, in combination with a nodal yielding model, offers a promising method to simulate lattices and potential defects to identify key defect regions. Future work should explore this venue and involve a complete defect study using simulations.

Quantification of the impact of local intrinsic and surface features to macroscopic performance

- One overarching theme in this dissertation is that nodes play an important role in lattice deformation and they may not necessarily have the same material properties as struts. Additionally, nodal orientation may influence their resultant material properties. Further studies on nodal properties and their influences should be conducted. These studies should include property maps of nodes with different strut connectivity and nodes with different print orientations, with connections to constitutive models based on microstructure. Although the nodes studied may not necessarily perform the same in lattice structures, these studies should draw insight into what factors influence nodal material properties.

- The property maps from the nanoindentation of EBM Ti-6Al-4V struts and cells provide insight into local property variations found within these structures. Additional work should connect these property variations to microstructural observations and material models based upon the microstructure to isolate the source of these property variations.
- Should the connection of nanoindentation property maps to microstructure prove successful, future work should involve similar studies in more geometries within the EBM Ti-6Al-4V and within other material systems, such as L-PBF Ti-6Al-4V and L-PBF SS316L. These studies will provide useful process-properties information for simulation of AM powder-bed lattice structures.

Appendix A

FIJI/ImageJ example macros

All of these macros are saved as *.ijm files and can be run in ImageJ/FIJI by selecting "Plugins → Macros → Run...". ImageJ/FIJI has its own macro scripting language that is distinct from other programming languages and it is advisable to find the reference guide to assist with making macros. In addition, macros can be recorded in ImageJ/FIJI by selecting "Plugins → Macros → Record...".

A.1 Area analysis

Prior to using this script, a stack of images contain the slices of the strut cross-section that needs to be analyzed should be created. The images should be oriented in a way so that the strut axis is pointing in/out of the page.

```
//sample definition
//sample name
strut = "1p5mm_3-2_12p6micronvoxel";
//array that contains the sub-names of individual image stacks of the strut
loc = newArray("bottomLeft_stackMiddletoBottom",
    "bottomRight_stackMiddletoBottom","topLeft_stackMiddletoTop",
    "topRight_stackMiddletoTop");
//folder where image stacks are stored
dir = "1p5mm_tifs_Connie"

for(k=0; k<loc.length; k++) {

    //open file
    open("C:\\MY FOLDER\\CT\\" + dir + "\\Stacks " + strut +
        "\\Area\\" + strut + "_" + loc[k] + ".tif");

    //convert to 8-bit
```

```
run("8-bit");

//set global scale
run("Set Scale...", "distance=1 known=0.0126 pixel=1 unit=mm global");

//duplicate stack
run("Duplicate...", "duplicate");

//auto-threshold image
setAutoThreshold("Huang dark");
setOption("BlackBackground", true);
run("Convert to Mask", "method=Huang background=Dark black");

//calculate area accounting for porosity
run("Set Measurements...", "area centroid perimeter bounding
    redirect=None decimal=3");
run("Analyze Particles...", "size=0.15-Infinity show=Overlay
    display exclude stack");

//Save CSV results
saveAs("Results", "C:\\MY FOLDER\\CT\\" + dir + "\\Stacks " + strut +
    "\\Area\\" + strut + "_" + loc[k] + "_Area.csv");
run("Clear Results");

//calculate area accounting excluding porosity
run("Set Measurements...", "area centroid perimeter bounding
    redirect=None decimal=3");
run("Analyze Particles...", "size=0.15-Infinity show=Overlay display
    exclude include stack");

//Save CSV results
saveAs("Results", "C:\\MY FOLDER\\CT\\" + dir + "\\Stacks " + strut +
    "\\Area\\" + strut + "_" + loc[k] + "_Area_NoPorosity.csv");
run("Clear Results");

//Save outline as TIFF
run("Invert", "stack");
saveAs("Tiff", "C:\\MY FOLDER\\CT\\" + dir + "\\Stacks " + strut +
    "\\Area\\" + strut + "_" + loc[k] + "_Outline.tif");

//Merge original image and fitted ellipse into one image
run("Merge Channels...", "c4=[" + strut + "_"+ loc[k] + ".tif]
```

```
        c5=[" + strut + "_" + loc[k] + "_Outline.tif] create keep");
    run("Invert");

    //save merged image as Tiff
    saveAs("Tiff", "C:\\MY FOLDER\\CT\\" + dir + "\\Stacks " + strut +
        "\\Area\\" + strut + "_" + loc[k] + "_Overlay.tif");

    //close windows
    list = getList("image.titles");
    for (i=0; i <list.length; i++)
    run("Close");

    //close results window
    if (isOpen("Results")) {
        selectWindow("Results");
        run("Close");
    }

}
```

A.2 Inscribed area analysis

Prior to using this script, a stack of images contain the slices of the strut cross-section that needs to be analyzed should be created. The images should be oriented in a way so that the strut axis is pointing in/out of the page.

```
//sample definition
//sample name
strut = "1p5mm_3-2_12p6micronvoxel";
//array that contains the sub-names individual image stacks of the strut
loc = newArray("bottomLeft_stackMiddletoBottom",
    "bottomRight_stackMiddletoBottom","topLeft_stackMiddletoTop",
    "topRight_stackMiddletoTop");
//folder where image stacks are stored
dir = "1p5mm_tifs_Connie"

for(k=0; k<loc.length; k++) {

    //open file
    open("C:\\MY FOLDER\\CT\\" + dir + "\\Stacks " + strut +
        "\\Area\\" + strut + "_" + loc[k] + ".tif");
```

```
//convert to 8-bit
run("8-bit");

//set global scale
run("Set Scale...", "distance=1 known=0.0126 pixel=1 unit=mm global");

//duplicate stack
run("Duplicate...", "duplicate");

//auto-threshold image
setAutoThreshold("Huang dark");
setOption("BlackBackground", true);
run("Convert to Mask", "method=Huang background=Dark black");

//remove surface roughness
run("Options...", "iterations=2 count=1 black do=Close stack");
run("Options...", "iterations=3 count=1 black pad do=Open stack");
run("Options...", "iterations=3 count=1 black do=Close stack");
run("Options...", "iterations=20 count=1 black pad do=Open stack");
run("Options...", "iterations=10 count=1 black pad do=Erode stack");
run("Options...", "iterations=9 count=1 black pad do=Dilate stack");

//calculate area accounting for porosity
run("Set Measurements...", "area centroid perimeter bounding
    redirect=None decimal=3");
run("Analyze Particles...", "size=0.15-Infinity show=Overlay
    display exclude include stack");

//Save CSV results
saveAs("Results", "C:\\MY FOLDER\\CT\\" + dir + "\\Stacks " + strut +
    "\\Area\\Inscribed Area\\" + strut + "_" + loc[k] +
    "_InscribedArea.csv");
run("Clear Results");

//Save outline as TIFF
run("Invert", "stack");
saveAs("Tiff", "C:\\MY FOLDER\\CT\\" + dir + "\\Stacks " + strut +
    "\\Area\\Inscribed Area\\" + strut + "_" + loc[k] +
    "_InscribedOutline.tif");

//Merge original image and fitted ellipse into one image
run("Merge Channels...", "c4=[" + strut + "_"+ loc[k] + ".tif]
```

```
        c5=[" + strut + "_" + loc[k] + "_InscribedOutline.tif]
        create keep");
    run("Invert");

    //save merged image as Tiff
    saveAs("Tiff", C:\\MY FOLDER\\CT\\" + dir + "\\Stacks " + strut +
        "\\Area\\Inscribed    Area\\" + strut + "_" + loc[k] +
        "_InscribedOverlay.tif");

    //close windows
    list = getList("image.titles");
    for (i=0; i <list.length; i++)
    run("Close");

    //close results window
    if (isOpen("Results")) {
        selectWindow("Results");
        run("Close");
    }

}
```

A.3 Surface roughness analysis

Prior to using this script, a stack of images contain the slices of the strut cross-section that needs to be analyzed should be created. The images should be oriented in a way so that the strut axis is pointing horizontally. This script can be adjusted for a vertically oriented strut by adjusting the loops (or one could rotate the vertically oriented struts so that they are horizontal in ImageJ/FIJI).

```
//sample definition
//array of samples that will be analyzed
strut = newArray("1mm_3-7_12p6micronvoxel", "1mm_3-8_12p6micronvoxel");
//array of sample sub-names that will be analyzed
loc = newArray("bottomLeft","bottomRight","topLeft","topRight");
//folder where image stacks are stored
dir = "1mm_tifs_Connie"

for(q=0; q<strut.length; q++){
    for(k=0; k<loc.length; k++){
```

```
    //create table to store coordinates
    Table.create("Coords");

    //Open size summary to determine how many slices there are
    open("C:\\MY FOLDER\\CT\\" + dir + "\\Stacks " + strut[q] +
        "\\Surface Roughness\\" + loc[k] + "\\" + strut[q] + "_" +
        loc[k] + "_SizeSummary.csv");

    //Determine how many slices there are
    n = Table.get("Slice",Table.size-1);

    //Close size summary
    run("Close");

    //Loop to find coordinates of points in all slices
    for(m=1; m<=n; m++){

        //Open pixel grid of slice
        open("C:\\MY FOLDER\\CT\\" + dir + "\\Stacks " + strut[q] +
            "\\Surface Roughness\\" + loc[k] + "\\" + strut[q] + "_"
            + loc[k] + "_Slice" + toString(m,0) + "_PixelGrid.csv");

        //List the column headings and figure out how many
        //columns there are
        cols = split(Table.headings);
        colsLen = lengthOf(cols);

        //Create new arrays to store the top and bottom surface
        //coordinates
        at_x = newArray(0);
        at_y = newArray(0);
        ab_x = newArray(0);
        ab_y = newArray(0);

        //Loop through the table and figure out the coordinates of
        // where the surface is
        for(i=1; i<(colsLen-1); i++){
            for(j=0; j<Math.round(Table.size/2); j++){
                if(Table.get(cols[i],j) == 0){
                    //Split column name so only the column number
                    //is remaining
                    x = split(cols[i],"X");
```

```
                    y = j;
                    //Append coordinate to array to store coordinates
                    at_x = Array.concat(at_x,x);
                    at_y = Array.concat(at_y,y);
                }
            }
            for(j=Math.round(Table.size/2); j<Table.size; j++){
                if(Table.get(cols[i],j) == 0){
                    //Split column name so only the column number
                    //is remaining
                    x = split(cols[i],"X");
                    y = j;
                    //Append coordinate to array to store coordinates
                    ab_x = Array.concat(ab_x,x);
                    ab_y = Array.concat(ab_y,y);
                }
            }
        }

        //Close pixel grid data
        run("Close");

        //Select table to store coordinates
        selectWindow("Coords");

        //Add coordinates to table
        Table.setColumn(toString(m,0)+"_Top_x",at_x);
        Table.setColumn(toString(m,0)+"_Top_y",at_y);
        Table.setColumn(toString(m,0)+"_Bottom_x",ab_x);
        Table.setColumn(toString(m,0)+"_Bottom_y",ab_y);
    }

    //Save table with coordinates for all slices of the sample
    //and close table
    Table.save("C:\\MY FOLDER\\CT\\" + dir + "\\Stacks " + strut[q] +
        "\\Surface Roughness\\" + strut[q] + "_" + loc[k] +
        "_Coordinates.csv")
    run("Close");
  }
}
```

Appendix B

ABAQUS example scripts

These scripts should be saved in *.py file format and then can be run in the ABAQUS GUI by selecting “File → Run Script..”. Tip: you will need to type in

```
session.journalOptions.setValues(replayGeometry=
   COORDINATE, recoverGeometry=COORDINATE)
```

into the ABAQUS kernel command line in order to have the macros print out coordinates instead of ABAQUS’s in-built geometry tracker.

B.1 3D FEA input file

This is an example script for scripting a “X” lattice primitive for 3D FEA.

```
# -*- coding: mbcs -*-
# Do not delete the following import lines
from abaqus import *
from abaqusConstants import *
import __main__
import section
import regionToolset
import displayGroupMdbToolset as dgm
import part
import material
import assembly
import step
import interaction
import load
import mesh
import optimization
import job
```

```
import sketch
import visualization
import xyPlot
import displayGroupOdbToolset as dgo
import connectorBehavior

#units are in mm, MPa, seconds, density is tonne/mm**3

##################################################
# User defined parameters
##################################################

eMesh=10; #number of elements in the thickness of the sample

stime=1.0; #step time, s

disp=1.5; #prescribed tension displacement, mm
hdisp=0.25; #prescribed horizontal displacement, mm

#sample dimensions
#STRUTS HAVE SQUARE CROSS-SECTIONS
#input thickness and then characteristic, e.g., [1.0, 'Nom']
sThickInfo = [[1.0,'Nom'],[[0.9442,'P1_CT_I_Avg']];

#amount of hardening, pre-defined in loop below
jHardList = ['EOS','EOSys_Min']

#nominal strut size
jNomThick = '1MM'; #use '1MM' or '1P5MM'

if jNomThick == '1MM':
    sRadi = 7.98
    sHeight = 31.975
elif jNomThick == '1P5MM':
    sRadi = 7.48
    sHeight = 31.125
else:
    print 'Please input valid nominal thickness.'

fOutput=100; #number of field output requests
hOutput=500; #number of history output requests
```

```
#Encastre for BC 1, Pinned for BC 2
BC=2

#’Y’ for contact and ’N’ for no contact
cont = ’Y’

#’Y’ for medial meshing strategy, ’N’ for advancing front
medialMesh = ’Y’

##################################################
# User-defined functions: DO NOT EDIT
##################################################

#provides x-coordinate of a rotation given a length and angle
def rotXcoord(length,ang,offset):
    return offset+length*cos(ang*pi/180)

#provides y-coordinate of a rotation given a length and angle
def rotYcoord(length,ang,offset):
    return offset+length*sin(ang*pi/180)

#function to convert numbers to text
def jobNameConvert(valueString):
    valueString=str(valueString)
    jname = ’’
    if valueString[-1] == ’0’ and valueString[-2] == ’.’:
        for s in valueString[:-2]:
            jname = jname + s
    else:
        for s in valueString:
            if s != ’.’:
                jname = jname + s
            else:
                jname = jname + ’p’
return jname

##################################################
# Loop for creating input file
##################################################

#iterate over the thicknesses and hardening levels
for sThick in sThickInfo:
```

```
for jHard in jHardList:
    #create new model
    Mdb()

    #create job name
    jobName = 'LANL_3D_'+jNomThick+'_'+sThick[1]+'_hard'+jHard+
        '_asymmDisp';

    #pre-defined dimensions
    strutH = 6.35; #half of the defined sample strut height
    #(see STL drawing dimension of 12.70 mm)
    sWidth = 10.0; #half of the sample width
    #half the node size
    nodeDiag = sThick[0]/sqrt(2);

    #sketch part
    s = mdb.models['Model-1'].ConstrainedSketch(name='__profile__',
        sheetSize=100.0)
    g, v, d, c = s.geometry, s.vertices, s.dimensions, s.constraints
    s.setPrimaryObject(option=STANDALONE)
    #sketch outer dimension limits
    s.Line(point1=(-sWidth, sWidth-nodeDiag), point2=(-sWidth,
        sHeight))
    s.Line(point1=(-sWidth, sHeight), point2=(sWidth, sHeight))
    s.Line(point1=(sWidth, sHeight), point2=(sWidth, sWidth-nodeDiag))
    #sketch horizontal line to mirror sample in the future
    s.Line(point1=(sWidth, 0.0), point2=(-sWidth, 0.0))
    #sketch interior of struts
    s.Line(point1=(0.0, nodeDiag), point2=(strutH-nodeDiag, strutH))
    s.Line(point1=(0.0, nodeDiag), point2=(-(strutH-nodeDiag), strutH))
    #sketch exterior of struts
    s.Line(point1=(nodeDiag, 0.0), point2=(sWidth, sWidth-nodeDiag))
    s.Line(point1=(-nodeDiag, 0.0), point2=(-sWidth, sWidth-nodeDiag))
    #sketch interior arc
    s.Arc3Points(point1=(-(strutH-nodeDiag), strutH),
    point2=(strutH-nodeDiag, strutH),
        point3=(0.0, 2*strutH-nodeDiag+sRadi))
    #mirror part
    s.copyMirror(mirrorLine=g.findAt((0.0, 0.0)), objectList=(
        g.findAt((0.0, sHeight)), g.findAt((nodeDiag, 2*nodeDiag)),
        g.findAt((-nodeDiag, 2*nodeDiag)), g.findAt((sWidth/2,
        sWidth/2-nodeDiag)), g.findAt((-sWidth/2, sWidth/2-nodeDiag)),
```

```
    g.findAt((0.0, 2*strutH-nodeDiag+sRadi)), g.findAt((-sWidth,
    sHeight-1.0)), g.findAt((sWidth, sHeight-1.0))))
#delete mirror line
s.delete(objectList=(g.findAt((0.0, 0.0)), ))
#finish defining part
p = mdb.models['Model-1'].Part(name='LANL_'+jNomThick,
    dimensionality=THREE_D, type=DEFORMABLE_BODY)
p = mdb.models['Model-1'].parts['LANL_'+jNomThick]
p.BaseSolidExtrude(sketch=s, depth=sThick[0])
s.unsetPrimaryObject()
del mdb.models['Model-1'].sketches['__profile__']

#create set of 'All'
p = mdb.models['Model-1'].parts['LANL_'+jNomThick]
c = p.cells
cells = c.findAt(((0.0, 0.0, sThick[0]), ))
p.Set(cells=cells, name='All')

#create partitions on face for where DIC disp measurements were taken
p = mdb.models['Model-1'].parts['LANL_'+jNomThick]
f, e, d = p.faces, p.edges, p.datums
t = p.MakeSketchTransform(sketchPlane=f.findAt(coordinates=(0.0, 0.0,
    sThick[0])),
sketchUpEdge=e.findAt(coordinates=(sWidth, sHeight-1.0, sThick[0])),
sketchPlaneSide=SIDE1, origin=(0.0, 0.0,
    sThick[0]))
s = mdb.models['Model-1'].ConstrainedSketch(name='__profile__',
    sheetSize=150.0, gridSpacing=5.0, transform=t)
g, v1, d1, c = s.geometry, s.vertices, s.dimensions, s.constraints
s.setPrimaryObject(option=SUPERIMPOSE)
p.projectReferencesOntoSketch(sketch=s, filter=COPLANAR_EDGES)
s.Line(point1=(-sWidth, sWidth-nodeDiag),
    point2=(sWidth, sWidth-nodeDiag))
s.Line(point1=(-sWidth, -(sWidth-nodeDiag)),
    point2=(sWidth, -(sWidth-nodeDiag)))
f = p.faces
pickedFaces = f.findAt(((0.0, 0.0, sThick[0]), ))
e1, d2 = p.edges, p.datums
p.PartitionFaceBySketch(sketchUpEdge=e1.findAt(coordinates=(sWidth,
sHeight-1.0, sThick[0])),
faces=pickedFaces, sketch=s)
s.unsetPrimaryObject()
```

```
del mdb.models['Model-1'].sketches['__profile__']

#create partitions halfway through the partitions to get points
#where DIC measurements were taken
p = mdb.models['Model-1'].parts['LANL_'+jNomThick]
e = p.edges
pickedEdges = e.findAt(((-(sWidth-sThick[0]), sWidth-nodeDiag,
    sThick[0]), ),((sWidth-sThick[0], sWidth-nodeDiag, sThick[0]),
    ), ((-(sWidth-sThick[0]), -(sWidth-nodeDiag), sThick[0]), ),
    ((sWidth-sThick[0], -(sWidth-nodeDiag), sThick[0]), ))
edgeLen=pickedEdges[0].getSize(printResults=FALSE)
p.PartitionEdgeByParam(edges=pickedEdges, parameter=0.5)

#create set of the DIC displacement points
p = mdb.models['Model-1'].parts['LANL_'+jNomThick]
v = p.vertices
verts = v.findAt(((-(sWidth-edgeLen/2), sWidth-nodeDiag,
    sThick[0]), ), ((sWidth-edgeLen/2, sWidth-nodeDiag,
    sThick[0]), ), ((-(sWidth-edgeLen/2), -(sWidth-nodeDiag),
    sThick[0]), ), ((sWidth-edgeLen/2, -(sWidth-nodeDiag),
    sThick[0]), ))
p.Set(vertices=verts, name='Disp_Pts')

#create material SS316L
mdb.models['Model-1'].Material(name='SS316L')
mdb.models['Model-1'].materials['SS316L'].Density(table=((7.9e-09,
    ), ))
mdb.models['Model-1'].materials['SS316L'].Elastic(table=((180000,
    0.27), ))

if jHard == 'EOS':
    mdb.models['Model-1'].materials['SS316L'].Plastic(table=(
        (470, 0),(475, 0.001), (494, 0.007), (510, 0.015), (520,
        0.0225), (527, 0.03),(531, 0.038), (534, 0.045), (536,
        0.052), (538, 0.061), (539, 0.066), (540, 0.077), (540,
        0.1), (540, 1.0)))
elif jHard == 'EOS_ysMin':
    mdb.models['Model-1'].materials['SS316L'].Plastic(table=(
        (380, 0), (434, 0.007), (468, 0.015), (488, 0.0225), (502,
        0.03), (514, 0.038), (523, 0.045), (530, 0.052), (539,
        0.075), (540, 0.1), (540, 1.0)))
elif jHard == 'EOS_utsMax':
```

```
        mdb.models['Model-1'].materials['SS316L'].Plastic(table=(
            (470, 0), (514, 0.007), (541, 0.015), (556, 0.0225), (566,
            0.03), (575, 0.038), (582, 0.045), (588, 0.052), (594,
            0.075), (595, 0.1), (595, 1.0)))
    elif jHard == 'EOS_ysMin_utsMax':
        mdb.models['Model-1'].materials['SS316L'].Plastic(table=((380,
            0), (450, 0.007), (496, 0.015), (522, 0.0225), (542, 0.03),
            (558, 0.038), (571, 0.045), (581, 0.052), (594, 0.075),
            (595, 0.1), (595, 1.0)))
    elif jHard == 'EOS_Min':
        mdb.models['Model-1'].materials['SS316L'].Plastic(table=((380,
            0), (417, 0.007), (439, 0.015), (452, 0.0225), (461, 0.03),
            (469, 0.038), (474, 0.045), (479, 0.052), (484, 0.075),
            (485, 0.1), (485, 1.0)))
    elif jHard == 'EOS_Max':
        mdb.models['Model-1'].materials['SS316L'].Plastic(table=((560,
            0), (573, 0.007), (581, 0.015), (585, 0.0225), (588, 0.03),
            (590, 0.038), (592, 0.045), (593, 0.052), (595, 0.075),
            (596, 0.1), (595, 1.0)))
    elif jHard == 'ys410_utsMax':
        mdb.models['Model-1'].materials['SS316L'].Plastic(table=((410,
            0), (472, 0.007), (512, 0.015), (534, 0.0225), (551, 0.03),
            (564, 0.038), (575, 0.045), (584, 0.052), (594, 0.075),
            (595, 0.1), (595, 1.0)))
    elif jHard == 'ys450_utsMax':
        mdb.models['Model-1'].materials['SS316L'].Plastic(table=((450,
            0), (500, 0.007), (531, 0.015), (549, 0.0225), (561, 0.03),
            (572, 0.038), (580, 0.045), (586, 0.052), (594, 0.075),
            (595, 0.1), (595, 1.0)))
    elif jHard == 'ys430_uts655':
        mdb.models['Model-1'].materials['SS316L'].Plastic(table=((430,
            0), (504, 0.007), (552, 0.015), (580, 0.0225), (600, 0.03),
            (617, 0.038), (630, 0.045), (641, 0.052), (654, 0.075),
            (655, 0.1), (655, 1.0)))
    elif jHard == 'EOSys_uts655':
        mdb.models['Model-1'].materials['SS316L'].Plastic(table=((470,
            0), (533, 0.007), (573, 0.015), (595, 0.0225), (611, 0.03),
            (625, 0.038), (635, 0.045), (644, 0.052), (654, 0.075),
            (655, 0.1), (655, 1.0)))
    else:
        print 'Please input valid hardening value.'
```

```
#create section 'NodeSolid' and assign section
mdb.models['Model-1'].HomogeneousSolidSection(name='NodeSolid',
    material='SS316L', thickness=None)
p = mdb.models['Model-1'].parts['LANL_'+jNomThick]
region = p.sets['All']
p.SectionAssignment(region=region, sectionName='NodeSolid',
    offset=0.0, offsetType=MIDDLE_SURFACE, offsetField='',
    thicknessAssignment=FROM_SECTION)

#assign element types and meshing strategy
p = mdb.models['Model-1'].parts['LANL_'+jNomThick]
c = p.cells
pickedRegions = c.findAt(((0.0, 0.0, sThick[0]/2), ))
if medialMesh == 'Y':
    p.setMeshControls(regions=pickedRegions, elemShape=HEX,
        algorithm=MEDIAL_AXIS)
else:
    p.setMeshControls(regions=pickedRegions, elemShape=HEX,
        algorithm=ADVANCING_FRONT)

#mesh part
p = mdb.models['Model-1'].parts['LANL_'+jNomThick]
p.seedPart(size=sThick[0]/eMesh, deviationFactor=0.1,
    minSizeFactor=0.1)
p.generateMesh()

#create assembly
a = mdb.models['Model-1'].rootAssembly
a.DatumCsysByDefault(CARTESIAN)
p = mdb.models['Model-1'].parts['LANL_'+jNomThick]
a.Instance(name='LANL_'+jNomThick+'-1', part=p, dependent=ON)

#create sets 'Top' and 'Bottom'
a = mdb.models['Model-1'].rootAssembly
f1 = a.instances['LANL_'+jNomThick+'-1'].faces
faces1 = f1.findAt(((0.0, sHeight, sThick[0]/2), ))
a.Set(faces=faces1, name='Top')
faces1 = f1.findAt(((0.0, -sHeight, sThick[0]/2), ))
a.Set(faces=faces1, name='Bottom')

#create Dynamic, Implicit step 'Tension'
mdb.models['Model-1'].ImplicitDynamicsStep(name='Tension',
```

```
    previous='Initial', timePeriod=stime, maxNumInc=15000,
    application=QUASI_STATIC, initialInc=stime/10,
    minInc=stime*10**-13, nohaf=OFF, amplitude=RAMP, alpha=DEFAULT,
    initialConditions=OFF, nlgeom=ON)

#create field output request
mdb.models['Model-1'].fieldOutputRequests['F-Output-1'].
    setValues(variables=('S', 'MISES', 'PEEQ', 'E', 'NE', 'LE',
    'U', 'RF', 'NFORC', 'COORD'), numIntervals=fOutput)

#create history output request
mdb.models['Model-1'].historyOutputRequests['H-Output-1'].
    setValues(numIntervals=hOutput)
regionDef=mdb.models['Model-1'].rootAssembly.allInstances['LANL_'
    +jNomThick+'-1'].sets['Disp_Pts']
mdb.models['Model-1'].HistoryOutputRequest(name='H-Output-2',
    createStepName='Tension', variables=('U1', 'U2', 'U3', 'UR1',
    'UR2', 'UR3', 'RF1', 'RF2', 'RF3', 'RM1', 'RM2', 'RM3'),
    numIntervals=hOutput,
region=regionDef, sectionPoints=DEFAULT, rebar=EXCLUDE)
regionDef=mdb.models['Model-1'].rootAssembly.sets['Top']
mdb.models['Model-1'].HistoryOutputRequest(name='H-Output-3',
    createStepName='Tension', variables=('U1', 'U2', 'U3', 'UR1',
    'UR2', 'UR3', 'RF1', 'RF2', 'RF3', 'RM1', 'RM2', 'RM3'),
    numIntervals=hOutput,
region=regionDef, sectionPoints=DEFAULT, rebar=EXCLUDE)
regionDef=mdb.models['Model-1'].rootAssembly.sets['Bottom']
mdb.models['Model-1'].HistoryOutputRequest(name='H-Output-4',
    createStepName='Tension', variables=('U1', 'U2', 'U3', 'UR1',
    'UR2', 'UR3', 'RF1', 'RF2', 'RF3', 'RM1', 'RM2', 'RM3'),
    numIntervals=hOutput, region=regionDef, sectionPoints=DEFAULT,
    rebar=EXCLUDE)

#input contact
if cont == 'Y':
    mdb.models['Model-1'].ContactProperty('Contact')
    mdb.models['Model-1'].interactionProperties['Contact'].
        TangentialBehavior(formulation=FRICTIONLESS)
    mdb.models['Model-1'].interactionProperties['Contact'].
        NormalBehavior(pressureOverclosure=HARD, allowSeparation=ON,
        constraintEnforcementMethod=DEFAULT)
    mdb.models['Model-1'].ContactStd(name='GenContact',
```

```
            createStepName='Initial')
        mdb.models['Model-1'].interactions['GenContact'].
            includedPairs.setValuesInStep(stepName='Initial',
            useAllstar=ON)
        mdb.models['Model-1'].interactions['GenContact'].
            contactPropertyAssignments.appendInStep(stepName='Initial',
            assignments=((GLOBAL, SELF, 'Contact'), ))

    #create fixed bottom BC
    a = mdb.models['Model-1'].rootAssembly
    region = a.sets['Bottom']
    if BC == 1:
        mdb.models['Model-1'].EncastreBC(name='FixedBottom',
            createStepName='Initial',
    region=region, localCsys=None)
    else:
        mdb.models['Model-1'].PinnedBC(name='FixedBottom',
            createStepName='Initial', region=region, localCsys=None)

    #create fixed top BC
    region = a.sets['Top']
    if BC == 1:
        mdb.models['Model-1'].DisplacementBC(name='FixedTop',
            createStepName='Initial', region=region, u1=SET, u2=UNSET,
            ur3=SET, amplitude=UNSET, distributionType=UNIFORM,
            fieldName='', localCsys=None)
    else:
        mdb.models['Model-1'].DisplacementBC(name='FixedTop',
            createStepName='Initial', region=region, u1=SET, u2=UNSET,
            ur3=UNSET, amplitude=UNSET, distributionType=UNIFORM,
            fieldName='', localCsys=None)

    #create tension BC
    mdb.models['Model-1'].DisplacementBC(name='Tension',
        createStepName='Tension', region=region, u1=hdisp, u2=disp,
        ur3=UNSET, amplitude=UNSET, fixed=OFF, distributionType=UNIFORM,
        fieldName='', localCsys=None)

    #create job
    mdb.Job(name=jobName, model='Model-1', description='', type=ANALYSIS,
        atTime=None, waitMinutes=0, waitHours=0, queue=None, memory=90,
        memoryUnits=PERCENTAGE, explicitPrecision=SINGLE,
```

```
            nodalOutputPrecision=SINGLE, echoPrint=OFF, modelPrint=OFF,
            contactPrint=OFF, historyPrint=OFF, userSubroutine='',
            scratch='', resultsFormat=ODB,
            parallelizationMethodExplicit=DOMAIN, numDomains=1,
            activateLoadBalancing=False, multiprocessingMode=DEFAULT,
            numCpus=1)
        mdb.jobs[jobName].writeInput(consistencyChecking=OFF)

print '\n Script Complete!!! ...\n'
```

B.2 2D FEA input files

This script creates an ABAQUS input file of a simple nodal geometry for 2D FEA. It contains an example of how to mesh differently in different regions.

```
# -*- coding: mbcs -*-
# Do not delete the following import lines
from abaqus import *
from abaqusConstants import *
import __main__
import section
import regionToolset
import displayGroupMdbToolset as dgm
import part
import material
import assembly
import step
import interaction
import load
import mesh
import optimization
import job
import sketch
import visualization
import xyPlot
import displayGroupOdbToolset as dgo
import connectorBehavior

#units are in mm, MPa, seconds, density is tonne/mm**3

##################################################
# User defined parameters
```

```
##################################################

#number of elements in each cross-section (not in node),
#optimal mesh 10-20
eleMeshList=[20]
#number of elements in cross-section in node region, optimal mesh 40
nodeMeshList=[40]
#number of elements to put in frame
frMesh=10

stime=1.0; #step time, s

disp=1.0; #prescribed compression displacement, mm

#nominal is 13.97, 0P is 13.0, 90P is 13.7
nodeHeight = 13.97; #distance between two frames, mm

#representative print orientation
jPrint='0P'

#nominal diameter/thickness
jSize='1mm'

#relevant stut information for the job
#STRUTS HAVE SQUARE CROSS-SECTIONS
#diameter/thickness (mm), modulus (wrought is 113800.00 MPa),
#yield stress (wrought is 880.0 MPa), descriptor (e.g., 'Avg')
strutInfoList = [[1.0,120000.00,880.0,'']]

#strut angle, recommended range 15-75 until framelength can be redefined
#as function of length and angle
strutAngList=[60.0]

frameLength=19.05; #frame length, default 20.0

frameThick=2.54; #frame thickness, default 2.5

fOutput=100; #number of field output requests
hOutput=500; #number of history output requests

BC=2; #Encastre for BC 1, Pinned for BC 2
```

```
cont = 'Y'; #'Y' for contact and 'N' for no contact

medialMesh = 'N'; #input 'Y' to use Medial Axis meshing

##################################################
# User-defined functions: DO NOT EDIT
##################################################

#provides x-coordinate of a rotation given a length and angle
def rotXcoord(length,ang,offset):
return offset+length*cos(ang*pi/180)

#provides y-coordinate of a rotation given a length and angle
def rotYcoord(length,ang,offset):
return offset+length*sin(ang*pi/180)

#function to turn numbers into text
def jobNameConvert(valueString):
valueString=str(valueString)
jname = ''
if valueString[-1] == '0' and valueString[-2] == '.':
for s in valueString[:-2]:
jname = jname + s
else:
for s in valueString:
if s != '.':
jname = jname + s
else:
jname = jname + 'p'
return jname

##################################################
# Loop for creating input file
##################################################

#iterate over the element mesh number, node mesh number,
#strut angle, and strut properties
for eleMesh in eleMeshList:
    for nodeMesh in nodeMeshList:
        for strutAng in strutAngList:
            for strutInfo in strutInfoList:
```

```
#create new model
Mdb()

#create job name
#strut angle
if strutAng == 60.0:
    jAng = ''
else:
    jAng = '_ang'+str(int(strutAng))

#element mesh
if eleMesh == 20:
    jEmesh = ''
else:
    jEmesh = '_eM'+str(int(eleMesh))

#node mesh
if nodeMesh == 40:
    jNmesh = ''
else:
    jNmesh = '_nM'+str(int(nodeMesh))

#frame mesh
if frMesh == 10:
    jFmesh = ''
else:
    jFmesh = '_nF'+str(int(frMesh))

#contact
if cont == 'N':
    jCont = '_wOCont'
else:
    jCont = ''

#medial mesh
if medialMesh == 'Y':
    jMedMesh = '_medMesh'
else:
    jMedMesh = ''

#boundary conditions
if BC == 1:
```

```
    jBC = '_BCe'
else:
    jBC = '_BCp'

jobName = '2DPSnodeB'+jAng+jMedMesh+jEmesh+jNmesh+jFmesh+jBC+
    jCont+'_'+jPrint+'_'+jSize+'_New_'+strutInfo[3]

#determine offset from origin
sxDoff=strutInfo[0]/2.0/sin(strutAng*pi/180)
syDoff=strutInfo[0]/2.0/cos(strutAng*pi/180)

#determine strut length based off of node height and
#strut thickness
strutL=(nodeHeight-strutInfo[0]/cos(strutAng*pi/180))
    /(2*sin(strutAng*pi/180))

#sketch part
s = mdb.models['Model-1'].ConstrainedSketch(name=
    '__profile__', sheetSize=100.0)
g, v, d, c = s.geometry, s.vertices, s.dimensions,
    s.constraints
s.setPrimaryObject(option=STANDALONE)
#sketch struts
s.Line(point1=(0.0,syDoff),
point2=(-rotXcoord(strutL,strutAng,0.0),
    rotYcoord(strutL,strutAng,syDoff)))
s.Line(point1=(-sxDoff,0.0),point2=(-rotXcoord(strutL,strutAng,
    2*sxDoff),rotYcoord(strutL,strutAng,syDoff)))
s.Line(point1=(0.0,syDoff),point2=(rotXcoord(strutL,strutAng,
    0.0),rotYcoord(strutL,strutAng,syDoff)))
s.Line(point1=(sxDoff,0.0),point2=(rotXcoord(strutL,strutAng,
    2*sxDoff),rotYcoord(strutL,strutAng,syDoff)))
s.Line(point1=(0.0,-syDoff),point2=(rotXcoord(strutL,strutAng,
    0.0),-rotYcoord(strutL,strutAng,syDoff)))
s.Line(point1=(sxDoff,0.0),point2=(rotXcoord(strutL,strutAng,
    2*sxDoff),-rotYcoord(strutL,strutAng,syDoff)))
s.Line(point1=(0.0,-syDoff),point2=(-rotXcoord(strutL,strutAng,
    0.0),-rotYcoord(strutL,strutAng,syDoff)))
s.Line(point1=(-sxDoff,0.0),point2=(-rotXcoord(strutL,strutAng,
    2*sxDoff),-rotYcoord(strutL,strutAng,syDoff)))
#sketch top frame
s.Line(point1=(-rotXcoord(strutL,strutAng,0.0),
```

```
    rotYcoord(strutL,strutAng,syDoff)),point2=(rotXcoord(
    strutL,strutAng,0.0),rotYcoord(strutL,strutAng,syDoff)))
s.Line(point1=(-rotXcoord(strutL,strutAng,2*sxDoff),
    rotYcoord(strutL,strutAng,syDoff)),point2=(
    -frameLength/2.0,rotYcoord(strutL,strutAng,syDoff)))
s.Line(point1=(-frameLength/2.0,rotYcoord(strutL,strutAng,
    syDoff)),point2=(-frameLength/2.0,rotYcoord(strutL,
    strutAng,syDoff+frameThick)))
s.Line(point1=(-frameLength/2.0,rotYcoord(strutL,strutAng,
    syDoff+frameThick)),point2=(frameLength/2.0,rotYcoord(
    strutL,strutAng,syDoff+frameThick)))
s.Line(point1=(frameLength/2.0,rotYcoord(strutL,strutAng,
    syDoff+frameThick)),point2=(frameLength/2.0,rotYcoord(
    strutL,strutAng,syDoff+0.0)))
s.Line(point1=(frameLength/2.0,rotYcoord(strutL,strutAng,
    syDoff+0.0)),point2=(rotXcoord(strutL,strutAng,2*sxDoff),
    rotYcoord(strutL,strutAng,syDoff)))
#sketch bottom frame
s.Line(point1=(-rotXcoord(strutL,strutAng,0.0),-rotYcoord(
    strutL,strutAng,syDoff)),point2=(rotXcoord(strutL,
    strutAng,0.0),-rotYcoord(strutL,strutAng,syDoff)))
s.Line(point1=(-rotXcoord(strutL,strutAng,2*sxDoff),
    -rotYcoord(strutL,strutAng,syDoff)),point2=(
    -frameLength/2.0,-rotYcoord(strutL,strutAng,syDoff)))
s.Line(point1=(-frameLength/2.0,-rotYcoord(strutL,
    strutAng,syDoff)),point2=(-frameLength/2.0,-rotYcoord(
    strutL,strutAng,syDoff+frameThick)))
s.Line(point1=(-frameLength/2.0,-rotYcoord(strutL,strutAng,
    syDoff+frameThick)),point2=(frameLength/2.0,-rotYcoord(
    strut,strutAng,syDoff+frameThick)))
s.Line(point1=(frameLength/2.0,-rotYcoord(strutL,strutAng,
    syDoff+frameThick)),point2=(frameLength/2.0,-rotYcoord(
    strutL,strutAng,syDoff+0.0)))
s.Line(point1=(frameLength/2.0,-rotYcoord(strutL,strutAng,
    syDoff+0.0)),point2=(rotXcoord(strutL,strutAng,2*sxDoff),
    -rotYcoord(strutL,strutAng,syDoff)))
#finish defining part
p = mdb.models['Model-1'].Part(name='Node-'+str(int(strutAng)),
    dimensionality=TWO_D_PLANAR, type=DEFORMABLE_BODY)
p = mdb.models['Model-1'].parts['Node-'+str(int(strutAng))]
p.BaseShell(sketch=s)
del mdb.models['Model-1'].sketches['__profile__']
```

```
#create partitions for struts
pL=1.5; #partition length
p = mdb.models['Model-1'].parts['Node-'+str(int(strutAng))]
f, e, d = p.faces, p.edges, p.datums
t = p.MakeSketchTransform(sketchPlane=f.findAt(coordinates=
    (0.0, 0.0, 0.0),normal=(0.0, 0.0, 1.0)),
    sketchPlaneSide=SIDE1, origin=(0.0, 0.0, 0.0))
s = mdb.models['Model-1'].ConstrainedSketch(name=
    '__profile__', sheetSize=100.0, gridSpacing=2.0,
    transform=t)
g, v, d1, c = s.geometry, s.vertices, s.dimensions,
    s.constraints
s.setPrimaryObject(option=SUPERIMPOSE)
s.Line(point1=(-rotXcoord(pL+0.5*tan(pi/2-2*strutAng*pi/180),
    strutAng,0.0),rotYcoord(pL+0.5*tan(pi/2-
    2*strutAng*pi/180),strutAng,syDoff)),point2=(-rotXcoord
    (pL-0.5*tan(pi/2-2*strutAng*pi/180),strutAng,sxDoff),
    rotYcoord(pL-0.5*tan(pi/2-2*strutAng*pi/180),
    strutAng,0.0)))
s.Line(point1=(rotXcoord(pL+0.5*tan(pi/2-2*strutAng*pi/180),
    strutAng,0.0),rotYcoord(pL+0.5*tan(pi/2
    -2*strutAng*pi/180),strutAng,syDoff)),point2=(rotXcoord
    (pL-0.5*tan(pi/2-2*strutAng*pi/180),strutAng,sxDoff),
    rotYcoord(pL-0.5*tan(pi/2-2*strutAng*pi/180),
    strutAng,0.0)))
s.Line(point1=(rotXcoord(pL+0.5*tan(pi/2-2*strutAng*pi/180),
    strutAng,0.0),-rotYcoord(pL+0.5*tan(pi/2-
    2*strutAng*pi/180),strutAng,syDoff)),point2=(rotXcoord
    (pL-0.5*tan(pi/2-2*strutAng*pi/180),strutAng,sxDoff),
    -rotYcoord(pL-0.5*tan(pi/2-2*strutAng*pi/180),
    strutAng,0.0)))
s.Line(point1=(-rotXcoord(pL+0.5*tan(pi/2-2*strutAng*pi/180),
    strutAng,0.0),-rotYcoord(pL+0.5*tan(pi/2-
    2*strutAng*pi/180),strutAng,syDoff)),point2=(
    -rotXcoord(pL-0.5*tan(pi/2-2*strutAng*pi/180),
    strutAng,sxDoff),-rotYcoord(pL-0.5*tan(pi/2-
    2*strutAng*pi/180),strutAng,0.0)))
f = p.faces
pickedFaces = f.findAt(((0.0, 0.0, 0.0), ))
e1, d2 = p.edges, p.datums
p.PartitionFaceBySketch(faces=pickedFaces, sketch=s)
```

```
s.unsetPrimaryObject()
del mdb.models['Model-1'].sketches['__profile__']

#create sets of four node angles
p = mdb.models['Model-1'].parts['Node-'+str(int(strutAng))]
v = p.vertices
verts = v.findAt(((-rotXcoord(pL-0.5*tan(pi/2-
    2*strutAng*pi/180),strutAng,sxDoff),rotYcoord
    (pL-0.5*tan(pi/2-2*strutAng*pi/180),strutAng,0.0),
    0.0), ),((-sxDoff, 0.0, 0.0),),((-rotXcoord(pL-0.5*tan
    (pi/2-2*strutAng*pi/180),strutAng,sxDoff),-rotYcoord
    (pL-0.5*tan(pi/2-2*strutAng*pi/180),strutAng,0.0),
    0.0), ))
p.Set(vertices=verts, name='AngleLeft')
verts = v.findAt(((rotXcoord(pL-0.5*tan(pi/2-
    2*strutAng*pi/180),strutAng,sxDoff),rotYcoord(pL-0.5*
    tan(pi/2-2*strutAng*pi/180),strutAng,0.0), 0.0), ),
    ((sxDoff, 0.0, 0.0), ),((rotXcoord(pL-0.5*tan
    (pi/2-2*strutAng*pi/180),strutAng,sxDoff),-rotYcoord
    (pL-0.5*tan(pi/2-2*strutAng*pi/180),strutAng,0.0),
    0.0), ))
p.Set(vertices=verts, name='AngleRight')
verts = v.findAt(((rotXcoord(pL+0.5*tan(pi/2-
    2*strutAng*pi/180),strutAng,0.0),rotYcoord(pL+0.5*tan
    (pi/2-2*strutAng*pi/180),strutAng,syDoff), 0.0), ),
    ((0.0, syDoff, 0.0), ),((-rotXcoord(pL+0.5*tan(pi/2-
    2*strutAng*pi/180),strutAng,0.0),rotYcoord(pL+0.5*
    tan(pi/2-2*strutAng*pi/180),strutAng,syDoff), 0.0), ))
p.Set(vertices=verts, name='AngleTop')
verts = v.findAt(((-rotXcoord(pL+0.5*tan(pi/2-
    2*strutAng*pi/180),strutAng,0.0),-rotYcoord(pL+0.5*tan
    (pi/2-2*strutAng*pi/180),strutAng,syDoff), 0.0), ),
    ((0.0, -syDoff, 0.0), ),((rotXcoord(pL+0.5*tan(pi/2
    -2*strutAng*pi/180),strutAng,0.0),-rotYcoord(pL+0.5*
    tan(pi/2-2*strutAng*pi/180),strutAng,syDoff), 0.0), ))
p.Set(vertices=verts, name='AngleBottom')
#create sets for individual struts
e = p.edges
edges = e.findAt(((-rotXcoord(pL,strutAng,sxDoff/2.0),
    rotYcoord(pL,strutAng,syDoff/2.0), 0.0), ))
p.Set(edges=edges, name='TopLeft')
edges = e.findAt(((rotXcoord(pL,strutAng,sxDoff/2.0),
```

```
        rotYcoord(pL,strutAng,syDoff/2.0), 0.0), ))
    p.Set(edges=edges, name='TopRight')
    edges = e.findAt(((rotXcoord(pL,strutAng,sxDoff/2.0),
        -rotYcoord(pL,strutAng,syDoff/2.0), 0.0), ))
    p.Set(edges=edges, name='BottomRight')
    edges = e.findAt(((-rotXcoord(pL,strutAng,sxDoff/2.0),
        -rotYcoord(pL,strutAng,syDoff/2.0), 0.0), ))
    p.Set(edges=edges, name='BottomLeft')
    #partition top frame for future meshing
    frP = 2*strutInfo[0]; #frame partition length
    e = p.edges
    pickedEdges = e.findAt(((-0.5*(frameLength/2.0+rotXcoord(
        strutL, strutAng,2*sxDoff)), rotYcoord(strutL,strutAng,
        syDoff), 0.0), ))
    p.PartitionEdgeByParam(edges=pickedEdges, parameter=frP/
        (frameLength/2.0-rotXcoord(strutL,strutAng,2*sxDoff)))
    pickedEdges = e.findAt(((0.0, rotYcoord(strutL,strutAng,
        syDoff), 0.0), ))
    p.PartitionEdgeByParam(edges=pickedEdges, parameter=frP/
        (2*rotXcoord(strutL,strutAng,0.0)))
    pickedEdges = e.findAt(((0.0, rotYcoord(
        strutL,strutAng,syDoff), 0.0), ))
    p.PartitionEdgeByParam(edges=pickedEdges, parameter=1-frP/
        (2*rotXcoord(strutL,strutAng,0.0)-frP))
    pickedEdges = e.findAt(((0.5*(frameLength/2.0+rotXcoord(
        strutL,strutAng,2*sxDoff)), rotYcoord(strutL,
        strutAng,syDoff), 0.0), ))
    p.PartitionEdgeByParam(edges=pickedEdges, parameter=1.0-frP/
        (frameLength/2.0-rotXcoord(strutL,strutAng,2*sxDoff)))
    #partition bottom frame for future meshing
    pickedEdges = e.findAt(((-0.5*(frameLength/2.0+rotXcoord(
        strutL,strutAng,2*sxDoff)), -rotYcoord(strutL,
        strutAng,syDoff), 0.0), ))
    p.PartitionEdgeByParam(edges=pickedEdges, parameter=frP/
        (frameLength/2.0-rotXcoord(strutL,strutAng,2*sxDoff)))
    pickedEdges = e.findAt(((0.0, -rotYcoord(strutL,strutAng,
        syDoff), 0.0), ))
    p.PartitionEdgeByParam(edges=pickedEdges, parameter=frP/
        (2*rotXcoord(strutL,strutAng,0.0)))
    pickedEdges = e.findAt(((0.0, -rotYcoord(strutL,
        strutAng,syDoff), 0.0), ))
    p.PartitionEdgeByParam(edges=pickedEdges, parameter=1-frP/
```

```
    (2*rotXcoord(strutL,strutAng,0.0)-frP))
pickedEdges = e.findAt(((0.5*(frameLength/2.0+rotXcoord
    (strutL,strutAng,2*sxDoff)),-rotYcoord(strutL,
    strutAng,syDoff), 0.0), ))
p.PartitionEdgeByParam(edges=pickedEdges, parameter=1.0-frP/
    (frameLength/2.0-rotXcoord(strutL,strutAng,2*sxDoff)))
#create set of ’All’
f = p.faces
faces = f.findAt(((0.0, rotYcoord(strutL,strutAng,syDoff+
    frameThick/2.0), 0.0), ),((0.0, 0.0, 0.0), ), ((0.0,
    -rotYcoord(strutL,strutAng,syDoff+frameThick/2.0),
    0.0), ))
p.Set(faces=faces, name=’All’)
#create set of ’Node’
f = p.faces
faces = f.findAt(((0.0, 0.0, 0.0), ))
p.Set(faces=faces, name=’Node’)
#partition interior of node to define node center
f, e, d = p.faces, p.edges, p.datums
t = p.MakeSketchTransform(sketchPlane=f.findAt(coordinates=
    (0.0, 0.0, 0.0),normal=(0.0, 0.0, 1.0)),
    sketchPlaneSide=SIDE1, origin=(0.0, 0.0, 0.0))
s = mdb.models[’Model-1’].ConstrainedSketch(name=’__profile__’,
    sheetSize=10.0, gridSpacing=0.25, transform=t)
g, v, d1, c = s.geometry, s.vertices, s.dimensions,
    s.constraints
s.setPrimaryObject(option=SUPERIMPOSE)
p = mdb.models[’Model-1’].parts[’Node-’+str(int(strutAng))]
p.projectReferencesOntoSketch(sketch=s, filter=COPLANAR_EDGES)
s.Line(point1=(0.0, syDoff), point2=(sxDoff, 0.0))
s.Line(point1=(sxDoff, 0.0), point2=(0.0, -syDoff))
s.Line(point1=(0.0, -syDoff), point2=(-sxDoff, 0.0))
s.Line(point1=(-sxDoff, 0.0), point2=(0.0, syDoff))
f = p.faces
pickedFaces = f.findAt(((0.0, 0.0, 0.0), ))
e1, d2 = p.edges, p.datums
p.PartitionFaceBySketch(faces=pickedFaces, sketch=s)
s.unsetPrimaryObject()
del mdb.models[’Model-1’].sketches[’__profile__’]

#create material Ti6Al4V
mdb.models[’Model-1’].Material(name=’Ti6Al4V’)
```

```
mdb.models['Model-1'].materials['Ti6Al4V'].Density(
    table=((4.43e-09, ), ))
mdb.models['Model-1'].materials['Ti6Al4V'].Elastic(
    table=((strutInfo[1], 0.342), ))
mdb.models['Model-1'].materials['Ti6Al4V'].Plastic(
    table=((strutInfo[2], 0.0),(strutInfo[2]*(0.5*200+1),
    200.0)))

#create section 'NodeSolid' and assign section
mdb.models['Model-1'].HomogeneousSolidSection(name=
    'NodeSolid', material='Ti6Al4V', thickness=strutInfo[0])
p = mdb.models['Model-1'].parts['Node-'+str(int(strutAng))]
region = p.sets['All']
p.SectionAssignment(region=region, sectionName='NodeSolid',
    offset=0.0, offsetType=MIDDLE_SURFACE, offsetField='',
    thicknessAssignment=FROM_SECTION)

#assign element types
elemType1 = mesh.ElemType(elemCode=CPS8R, elemLibrary=
    STANDARD)
elemType2 = mesh.ElemType(elemCode=CPS6, elemLibrary=STANDARD)
p = mdb.models['Model-1'].parts['Node-'+str(int(strutAng))]
f = p.faces
faces = f.findAt(((0.0, rotYcoord(strutL,strutAng,syDoff+
    frameThick/2.0), 0.0), ),((0.0, 0.0, 0.0), ), ((0.0,
    -rotYcoord(strutL,strutAng,syDoff+frameThick/2.0), 0.0), ))
pickedRegions =(faces, )
p.setElementType(regions=pickedRegions, elemTypes=(elemType1,
    elemType2))
#use medial algorithm?
if medialMesh == 'Y':
pickedRegions = f.findAt(((0.0, rotYcoord(strutL,strutAng,syDoff+
    frameThick/2.0), 0.0), ),((0.0, 0.0, 0.0), ), ((0.0,
    -rotYcoord(strutL,strutAng,syDoff+frameThick/2.0), 0.0), ))
p.setMeshControls(regions=pickedRegions, algorithm=MEDIAL_AXIS)

#mesh node
e = p.edges
pickedEdges = e.findAt(((-rotXcoord(0.95*pL+0.5*tan(pi/2-
    2*strutAng*pi/180),strutAng,0.0),rotYcoord(0.95*pL+
    0.5*tan(pi/2-2*strutAng*pi/180),strutAng,syDoff), 0.0), ),
    ((-rotXcoord(0.95*pL-0.5*tan(pi/2-2*strutAng*pi/180),
```

```
    strutAng,sxDoff),rotYcoord(0.95*pL-0.5*tan(pi/2-
    2*strutAng*pi/180),strutAng,0.0), 0.0),),((rotXcoord(0.95
    *pL+0.5*tan(pi/2-2*strutAng*pi/180),strutAng,0.0),
    rotYcoord(0.95*pL+0.5*tan(pi/2-2*strutAng*pi/180),
    strutAng,syDoff), 0.0),),((rotXcoord(0.95*pL-0.5*tan
    (pi/2-2*strutAng*pi/180),strutAng,sxDoff),rotYcoord
    (0.95*pL-0.5*tan(pi/2-2*strutAng*pi/180),strutAng,0.0),
    0.0),),((rotXcoord(0.95*pL+0.5*tan(pi/2-2*strutAng*
    pi/180),strutAng,0.0),-rotYcoord(0.95*pL+0.5*tan(pi/2-
    2*strutAng*pi/180),strutAng,syDoff), 0.0),),((rotXcoord
    (0.95*pL-0.5*tan(pi/2-2*strutAng*pi/180),strutAng,
    sxDoff),-rotYcoord(0.95*pL-0.5*tan(pi/2-2*strutAng
    *pi/180),strutAng,0.0), 0.0), ),((-rotXcoord(0.95
    *pL+0.5*tan(pi/2-2*strutAng*pi/180),strutAng,0.0),
    -rotYcoord(0.95*pL+0.5*tan(pi/2-2*strutAng*pi/180),
    strutAng,syDoff), 0.0), ),((-rotXcoord(0.95*pL-0.5*
    tan(pi/2-2*strutAng*pi/180),strutAng,sxDoff),
    -rotYcoord(0.95*pL-0.5*tan(pi/2-2*strutAng*pi/180),
    strutAng,0.0), 0.0), ))
p.seedEdgeBySize(edges=pickedEdges, size=strutInfo[0]/nodeMesh,
    deviationFactor=0.1, constraint=FINER)
#mesh struts
pickedEdges = e.findAt(((-rotXcoord(0.5*(strutL-pL)+0.5*
    tan(pi/2-2*strutAng*pi/180),strutAng,0.0),rotYcoord(0.5*
    (strutL-pL)+0.5*tan(pi/2-2*strutAng*pi/180),strutAng,
    syDoff), 0.0), ),((-rotXcoord(0.5*(strutL-pL)-0.5
    *tan(pi/2-2*strutAng*pi/180),strutAng,sxDoff),
    rotYcoord(0.5*(strutL-pL)-0.5*tan(pi/2-2*strutAng*
    pi/180),strutAng,0.0), 0.0), ),((rotXcoord(0.5*(strutL-
    pL)+0.5*tan(pi/2-2*strutAng*pi/180),strutAng,0.0),
    rotYcoord(0.5*(strutL-pL)+0.5*tan(pi/2-2*strutAng*pi/180),
    strutAng,syDoff), 0.0), ),((rotXcoord(0.5*(strutL-pL)-
    0.5*tan(pi/2-2*strutAng*pi/180),strutAng,sxDoff),
    rotYcoord(0.5*(strutL-pL)-0.5*tan(pi/2-2*strutAng*pi/180)
    ,strutAng,0.0), 0.0), ),((rotXcoord(0.5*(strutL-pL)
    +0.5*tan(pi/2-2*strutAng*pi/180),strutAng,0.0),
    -rotYcoord(0.5*(strutL-pL)+0.5*tan(pi/2-2*strutAng*pi/180),
    strutAng,syDoff), 0.0), ),((rotXcoord(0.5*(strutL-pL)
    -0.5*tan(pi/2-2*strutAng*pi/180),strutAng,sxDoff),
    -rotYcoord(0.5*(strutL-pL)-0.5*tan(pi/2-2*strutAng*
    pi/180),strutAng,0.0), 0.0), ),((-rotXcoord(0.5*
    (strutL-pL)+0.5*tan(pi/2-2*strutAng*pi/180),strutAng,0.0),
```

```
    -rotYcoord(0.5*(strutL-pL)+0.5*tan(pi/2-
    2*strutAng*pi/180),strutAng,syDoff), 0.0), ),((
    -rotXcoord(0.5*(strutL-pL)-0.5*tan(pi/2-2*strutAng*
    pi/180),strutAng,sxDoff),-rotYcoord(0.5*(strutL-pL)
    -0.5*tan(pi/2-2*strutAng*pi/180),strutAng,0.0), 0.0), ),
#top frame near struts
    ((-(rotXcoord(strutL,strutAng,0.0)-frP/2), rotYcoord(
    strutL,strutAng,syDoff), 0.0), ),((-(rotXcoord(strutL,
    strutAng,2*sxDoff)+frP/2), rotYcoord(strutL,strutAng,
    syDoff), 0.0), ),((rotXcoord(strutL,strutAng,0.0)-frP/2,
    rotYcoord(strutL,strutAng,syDoff), 0.0), ),((rotXcoord
    (strutL,strutAng,2*sxDoff)+frP/2, rotYcoord(strutL,
    strutAng,syDoff), 0.0), ),
#bottom frame near struts
    ((-(rotXcoord(strutL,strutAng,0.0)-frP/2), -rotYcoord(
    strutL,strutAng,syDoff), 0.0), ),((-(rotXcoord(
    strutL,strutAng,2*sxDoff)+frP/2), -rotYcoord(strutL,
    strutAng,syDoff), 0.0), ),((rotXcoord(strutL,strutAng,
    0.0)-frP/2, -rotYcoord(strutL,strutAng,syDoff), 0.0),
    ),((rotXcoord(strutL,strutAng,2*sxDoff)+frP/2,
    -rotYcoord(strutL,strutAng,syDoff), 0.0), ),)
p.seedEdgeBySize(edges=pickedEdges, size=strutInfo[0]/eleMesh,
    deviationFactor=0.1,
constraint=FINER)
#mesh frames
#top frame
pickedEdges = e.findAt(((0.0, rotYcoord(strutL,strutAng,
    syDoff), 0.0), ),((-frameLength/2.0, rotYcoord(strutL,
    strutAng,syDoff+frameThick/2.0), 0.0), ),((-0.5*
    (frameLength/2+rotXcoord(strutL,strutAng,2*sxDoff)+frP),
    rotYcoord(strutL,strutAng,syDoff), 0.0), ),((0.0,
    rotYcoord(strutL,strutAng,syDoff+frameThick), 0.0),
    ),((0.5*(frameLength/2+rotXcoord(strutL,strutAng,
    2*sxDoff)+frP), rotYcoord(strutL,strutAng,syDoff), 0.0),
    ),((frameLength/2.0, rotYcoord(strutL,strutAng,
    syDoff+frameThick/2.0), 0.0), ),
#bottom frame
    ((0.0, -rotYcoord(strutL,strutAng,syDoff), 0.0), ),
    ((-frameLength/2.0, -rotYcoord(strutL,strutAng,
    syDoff+frameThick/2.0), 0.0), ),((-0.5*(frameLength/2+
    rotXcoord(strutL,strutAng,2*sxDoff)+frP),
    -rotYcoord(strutL,strutAng,syDoff), 0.0), ),((0.0,
```

```
    -rotYcoord(strutL,strutAng,syDoff+frameThick), 0.0), ),
    ((0.5*(frameLength/2+rotXcoord(strutL,strutAng,2*sxDoff)
    +frP), -rotYcoord(strutL,strutAng,syDoff), 0.0), ),
    ((frameLength/2.0, -rotYcoord(strutL,strutAng,
    syDoff+frameThick/2.0), 0.0), ))
p.seedEdgeBySize(edges=pickedEdges, size=frameThick/frMesh,
    deviationFactor=0.1, constraint=FINER)
p.generateMesh()

#create assembly
a = mdb.models['Model-1'].rootAssembly
a.DatumCsysByDefault(CARTESIAN)
p = mdb.models['Model-1'].parts['Node-'+str(int(strutAng))]
a.Instance(name='Node-'+str(int(strutAng))+'-1', part=p,
    dependent=ON)

#create sets 'TopFrame' and 'BottomFrame'
a = mdb.models['Model-1'].rootAssembly
e1 = a.instances['Node-'+str(int(strutAng))+'-1'].edges
edges1 = e1.findAt(((0.0, rotYcoord(strutL,strutAng,
    syDoff+frameThick), 0.0), ))
a.Set(edges=edges1, name='TopFrame')
edges1 = e1.findAt(((0.0, -rotYcoord(strutL,strutAng,
    syDoff+frameThick), 0.0), ))
a.Set(edges=edges1, name='BottomFrame')

#create set 'NodeCenter'
f1 = a.instances['Node-'+str(int(strutAng))+'-1'].faces
faces1 = f1.findAt(((0.0, 0.0, 0.0), ))
a.Set(faces=faces1, name='NodeCenter')

#create Dynamic, Implicit step 'Compress'
mdb.models['Model-1'].ImplicitDynamicsStep(name='Compress',
    previous='Initial', timePeriod=stime, maxNumInc=1500,
    application=QUASI_STATIC, initialInc=stime/10,
    minInc=stime*10**-13, nohaf=OFF, amplitude=RAMP,
    alpha=DEFAULT, initialConditions=OFF, nlgeom=ON)

#create field output request
mdb.models['Model-1'].fieldOutputRequests['F-Output-1'].
    setValues(variables=('S', 'MISES', 'PEEQ', 'E', 'NE',
    'LE', 'U', 'RF', 'NFORC', 'COORD'), numIntervals=fOutput)
```

```
#create history output request
mdb.models['Model-1'].historyOutputRequests['H-Output-1'].
    setValues(numIntervals=hOutput)
regionDef=mdb.models['Model-1'].rootAssembly.sets['TopFrame']
mdb.models['Model-1'].HistoryOutputRequest(name='H-Output-2',
    createStepName='Compress', variables=('U1', 'U2', 'U3',
    'UR1', 'UR2', 'UR3', 'RF1', 'RF2', 'RF3', 'RM1', 'RM2',
    'RM3'), numIntervals=hOutput,
region=regionDef, sectionPoints=DEFAULT, rebar=EXCLUDE)
regionDef=mdb.models['Model-1'].rootAssembly.sets['Node
    Center']
mdb.models['Model-1'].HistoryOutputRequest(name='H-Output-3',
createStepName='Compress', variables=('S11', 'S22', 'S12',
    'E11','E22','E12','LE11','LE22','LE12','EVOL','COOR1',
    'COOR2'), numIntervals=hOutput,
region=regionDef, sectionPoints=DEFAULT, rebar=EXCLUDE)
regionDef=mdb.models['Model-1'].rootAssembly.sets['Bottom
    Frame']
mdb.models['Model-1'].HistoryOutputRequest(name='H-Output-4',
createStepName='Compress', variables=('U1', 'U2', 'U3',
    'UR1', 'UR2', 'UR3', 'RF1', 'RF2', 'RF3', 'RM1',
    'RM2', 'RM3'), numIntervals=hOutput,
region=regionDef, sectionPoints=DEFAULT, rebar=EXCLUDE)

#input contact
if cont == 'Y':
    mdb.models['Model-1'].ContactProperty('Contact')
    mdb.models['Model-1'].interactionProperties['Contact'].
        TangentialBehavior(formulation=FRICTIONLESS)
    mdb.models['Model-1'].interactionProperties['Contact'].
        NormalBehavior(pressureOverclosure=HARD,
        allowSeparation=ON, constraintEnforcementMethod=
        DEFAULT)
    mdb.models['Model-1'].ContactStd(name='GenContact',
        createStepName='Initial')
    mdb.models['Model-1'].interactions['GenContact'].
        includedPairs.setValuesInStep(stepName='Initial',
        useAllstar=ON)
    mdb.models['Model-1'].interactions['GenContact'].
        contactPropertyAssignments.appendInStep(stepName=
        'Initial', assignments=((GLOBAL, SELF, 'Contact'), ))
```

```
#create fixed bottom BC
a = mdb.models['Model-1'].rootAssembly
region = a.sets['BottomFrame']
if BC == 1:
    mdb.models['Model-1'].EncastreBC(name='FixedBottom',
        createStepName='Initial',
region=region, localCsys=None)
else:
    mdb.models['Model-1'].PinnedBC(name='FixedBottom',
        createStepName='Initial', region=region,
        localCsys=None)

#create fixed top BC
region = a.sets['TopFrame']
if BC == 1:
    mdb.models['Model-1'].DisplacementBC(name='FixedTop',
        createStepName='Initial', region=region, u1=SET,
        u2=UNSET, ur3=SET, amplitude=UNSET,
        distributionType=UNIFORM, fieldName='',
        localCsys=None)
else:
    mdb.models['Model-1'].DisplacementBC(name='FixedTop',
        createStepName='Initial', region=region, u1=SET,
        u2=UNSET, ur3=UNSET, amplitude=UNSET,
        distributionType=UNIFORM, fieldName='',
        localCsys=None)

#create compress BC
mdb.models['Model-1'].DisplacementBC(name='Compress',
 createStepName='Compress', region=region, u1=UNSET,
 u2=-disp, ur3=UNSET, amplitude=UNSET, fixed=OFF,
 distributionType=UNIFORM, fieldName='', localCsys=None)

#create job
mdb.Job(name=jobName, model='Model-1',
    description='', type=ANALYSIS, atTime=None,
    waitMinutes=0, waitHours=0, queue=None, memory=90,
    memoryUnits=PERCENTAGE, explicitPrecision=SINGLE,
    nodalOutputPrecision=SINGLE, echoPrint=OFF,
    modelPrint=OFF, contactPrint=OFF, historyPrint=OFF,
    userSubroutine='', scratch='', resultsFormat=ODB,
```

```
                parallelizationMethodExplicit=DOMAIN, numDomains=1,
                activateLoadBalancing=False, multiprocessingMode=DEFAULT,
                numCpus=1)
            mdb.jobs[jobName].writeInput(consistencyChecking=OFF)
print '\n Script Complete!!! ...\n'
```

B.3 Load-displacement report

This is a script that creates a load-displacement curve from a “X” primitive at the specificed set 'DISP_POINTS', which is the location of the displacement taken in the DIC. The file format is *.rpt.

```
# -*- coding: mbcs -*-
# Do not delete the following import lines
from abaqus import *
from abaqusConstants import *
import __main__

import section
import regionToolset
import displayGroupMdbToolset as dgm
import part
import material
import assembly
import step
import interaction
import load
import mesh
import optimization
import job
import sketch
import visualization
import xyPlot
import displayGroupOdbToolset as dgo
import connectorBehavior

import odbAccess
from odbAccess import *

#input jobs
jobs = ['LANL_3D_1MM_P1_CT_I_Avg_hardEOS_asymmDisp',
    'LANL_3D_1MM_P1_CT_I_Avg_hardys410_utsMax_asymmDisp',
```

```
    'LANL_3D_1MM_P3_CT_I_Avg_hardEOS_asymmDisp']

for job in jobs:
#split job name
    jobStrSplit = job.split('_')

#define the part name, which is LANL_1MM in this case
    partName = jobStrSplit[0]+'_'+jobStrSplit[2]

    #opens corresponding odb
    a = mdb.models['Model-1'].rootAssembly
    session.viewports['Viewport: 1'].setValues(displayedObject=a)
    odb = session.openOdb(name='C:/MY SIMULATION FOLDER/'+job+'.odb')
    session.viewports['Viewport: 1'].setValues(displayedObject=odb)
    session.mdbData.summary()

    #define step
    step = odb.steps['Tension']

    #find all defined regions in step
    allitems = step.historyRegions.keys()

    #find nodes in set 'TOP'
    top = odb.rootAssembly.nodeSets['TOP'].nodes[0]

    #find nodes in 'DISP_PTS'
    dispPTS = odb.rootAssembly.instances[partName+'-1'].
        nodeSets['DISP_PTS'].nodes

    #find the order in disp pts of top left, bottom left, top right,
    #bottom right
    order = [0,1,2,3]
    for i in range(len(dispPTS)):
        if dispPTS[i].coordinates[0] < 0 and dispPTS[i].coordinates[1]
            > 0:
            order[0] = i
        elif dispPTS[i].coordinates[0] < 0 and dispPTS[i].coordinates[1]
            < 0:
            order[1] = i
        elif dispPTS[i].coordinates[0] > 0 and dispPTS[i].coordinates[1]
            > 0:
            order[2] = i
```

```
    else:
        order[3] = i

#extract node labels in set ’TOP’ and convert to strings
#this is where the reaction force (RF) is
topLabels = [str(top[i].label) for i in range(len(top))]

#extract node labels in set ’DISP_PTS’ and convert to strings
dispPTSLabels = [str(dispPTS[i].label) for i in range(len(dispPTS))]

#find indices of nodes in ’TOP’ in the history regions
topindices = []
for idx, s in enumerate(allitems):
    if any(s == ’Node ’+partName+’-1.’+lab for lab in topLabels):
topindices.append(idx)

#find indices of nodes in ’DISP_PTS’ in the history regions
dispPTSindices = []
for idx, s in enumerate(allitems):
    if any(s == ’Node ’+partName+’-1.’+lab for lab in dispPTSLabels):
dispPTSindices.append(idx)

dispPTSindices = [dispPTSindices[i] for i in order]

#make a list of time steps throughout step
t = [i[0] for i in step.historyRegions[str(allitems[topindices[0]])].
    historyOutputs[’RF2’].data]

#sum up all RF2 in ’TOP’ and create xy-data
alltRF2 = []
for i in range(len(topindices)):
alltRF2.append([j[1] for j in step.historyRegions[str(allitems
    [topindices[i]])].historyOutputs[’RF2’].data])
tRF2sum = [sum(x) for x in zip(*alltRF2)]
tRF2 = zip(t,tRF2sum)
xy_result = session.XYData(data=tRF2, name=’tRF2’)

#determine U2 based on DIC PTS displacements and create xy-data
dtL = [i[1] for i in step.historyRegions[str(allitems[dispPTSindices
    [0]])].historyOutputs[’U2’].data]
dbL = [i[1] for i in step.historyRegions[str(allitems[dispPTSindices
    [1]])].historyOutputs[’U2’].data]
```

```
    dtR = [i[1] for i in step.historyRegions[str(allitems[dispPTSindices
        [2]])].historyOutputs['U2'].data]
    dbR = [i[1] for i in step.historyRegions[str(allitems[dispPTSindices
        [3]])].historyOutputs['U2'].data]

#displacement at left side
    dL = [dtL[i]-dbL[i] for i in range(len(dtL))]
    #displacement at right side
    dR = [dtR[i]-dbR[i] for i in range(len(dtR))]

#average displacement
    dAvg = [sum(dL[i],dR[i])/2 for i in range(len(dL))]

#create xydata that contains (time, average displacement)
    U2 = zip(t,dAvg)
    xy_result = session.XYData(data=U2, name='Disp_DIC_PTS')

    #create RF2 vs. Disp for DIC points
    #if you wanted
    xy1 = session.xyDataObjects['Disp_DIC_PTS']
    xy2 = session.xyDataObjects['tRF2']
    xy3 = combine(xy1, xy2)
    xy3.setValues(sourceDescription='combine ( "Disp_DIC_PTS", "tRF2" )')
    session.xyDataObjects.changeKey(xy3.name, 'DispDICPtsvstRF2')

    #write to data to rpt file
    x0 = session.xyDataObjects['DispDICPtsvstRF2']
    session.xyReportOptions.setValues(layout=SEPARATE_TABLES)
    session.writeXYReport(fileName='C:/MY SIMULATION FOLDER/Data/'+job+
        '_DICpts_LoadDisp.rpt', xyData=(x0))

    #delete data
    del session.xyDataObjects['DispDICPtsvstRF2']
    del session.xyDataObjects['tRF2']
    del session.xyDataObjects['Disp_DIC_PTS']
```

B.4 Creating a geometry based on a *.CSV file

This is part of a script that allows one to create a 2D part in ABAQUS based on coordinates in a CSV file. It only contains the part definition portion of a script and none of the material definition, step definition, meshing, etc. as that stuff has been thoroughly covered in the previously provided scripts.

```
# -*- coding: mbcs -*-
# Do not delete the following import lines
from abaqus import *
from abaqusConstants import *
import __main__
import section
import regionToolset
import displayGroupMdbToolset as dgm
import part
import material
import assembly
import step
import interaction
import load
import mesh
import optimization
import job
import sketch
import visualization
import xyPlot
import displayGroupOdbToolset as dgo
import connectorBehavior
import csv

filePath='C:\Users\YOUR FILE LOCATION'

fileList=['\\file1.csv','\\file2.csv']

for file in fileList:
    #create new model
    Mdb()

    #open file and read it
    f = open(filePath+file,'rb')
    readFile = csv.reader(f)

    #create a part name based on the file name
    partName ='PART_'+file.split('.')[0][1:]

    #create empty lists to store the coordinates
    xList = []
    yList = []
```

```
    #append coordinates from the file into the empty lists
    for row in readFile:
        xList.append(float(row[0]))
        yList.append(float(row[1]))

    #zip together the separate coordinate lists
    coordList = zip(xList,yList)

    #begin sketch
    s = mdb.models['Model-1'].ConstrainedSketch(name='__profile__',
        sheetSize=100.0)
    g, v, d, c = s.geometry, s.vertices, s.dimensions, s.constraints
    s.sketchOptions.setValues(viewStyle=AXISYM)
    s.setPrimaryObject(option=STANDALONE)
    #sketch points
    for i, coord in enumerate(coordList):
        if i > 0:
            s.Line(point1=coordList[i-1], point2=coordList[i])
    #end sketch
    p = mdb.models['Model-1'].Part(name=partName,
        dimensionality=TWO_D_PLANAR,
        type=DEFORMABLE_BODY)
    p = mdb.models['Model-1'].parts[partName]
    p.BaseShell(sketch=s)
    s.unsetPrimaryObject()
    del mdb.models['Model-1'].sketches['__profile__']
```

B.5 Visualizing von Mises strain contours for a frame

This script allows one to compute von Mises strain contours (based on LE) for individual frames in a simulation. It also has some lines to compute the von Mises strain contours from NE instead. This script is useful for comparisons to DIC.

```
# -*- coding: mbcs -*-
# Do not delete the following import lines
from abaqus import *
from abaqusConstants import *
import __main__
import section
import regionToolset
import displayGroupMdbToolset as dgm
```

```
import part
import material
import assembly
import step
import interaction
import load
import mesh
import optimization
import job
import sketch
import visualization
import xyPlot
import displayGroupOdbToolset as dgo
import connectorBehavior

import odbAccess
from odbAccess import *

#job name
jobName='MY_JOB'

#desired frame numbers to visualize von Mises strains
frNs=[10,20,45,70]

#create session step
currentOdb = session.odbs['C:/MY JOB LOCATION/'+jobName+'.odb']
scratchOdb = session.ScratchOdb(odb=currentOdb)
sessionStep = scratchOdb.Step(name='Session Step', description='Step for
    Viewer non-persistent fields', domain=TIME, timePeriod=1.0)

for frN in frNs:
    #open LE at the frame number
    frN_LE = session.odbs['C:/MY JOB LOCATION/'+jobName+'.odb'].
        steps['Compress'].frames[frN].fieldOutputs['LE']

    #create von Mises strain from LE
    tmpField = sqrt(power(frN_LE.getScalarField(invariant=MAX_PRINCIPAL),2)
        -frN_LE.getScalarField(invariant=MAX_PRINCIPAL)*
        frN_LE.getScalarField(invariant=MIN_PRINCIPAL)+
        power(frN_LE.getScalarField(invariant=MIN_PRINCIPAL),2))*2/3

    #create von Mises strain from LE field output
```

```
if frN == frNs[0]:
    sessionFrame = sessionStep.Frame(frameId=0, frameValue=0.0,
        description='Session Frame')
else:
    sessionFrame = session.scratchOdbs['C:/MY JOB LOCATION/'+jobName
        +'.odb'].steps['Session Step'].frames[0]
    sessionField = sessionFrame.FieldOutput(name='vonMises_LE_'+
        str(frN), description='sqrt(power(frN_LE.getScalarField(
        invariant=MAX_PRINCIPAL),2)-frN_LE.getScalarField(
        invariant=MAX_PRINCIPAL)*frN_LE.getScalarField(
        invariant=MIN_PRINCIPAL)+power(frN_LE.getScalarField(
        invariant=MIN_PRINCIPAL),2))*2/3', field=tmpField)

#open U at frame number
frN_U = session.odbs['C:/MY JOB LOCATION/'+jobName+'.odb'].
    steps['Compress'].frames[frN].fieldOutputs['U']
tmpField = frN_U

#create U field output for session step
#this is necessary to view deformed structure
sessionFrame = session.scratchOdbs['C:/MY JOB LOCATION/'+jobName
    +'.odb'].steps['Session Step'].frames[0]
sessionField = sessionFrame.FieldOutput(name='U_'+str(frN),
    description='U_'+str(frN), field=tmpField)

#create von Mises strain from NE
frN_NE = session.odbs['C:/MY JOB LOCATION/'+jobName+'.odb'].
    steps['Compress'].frames[frN].fieldOutputs['NE']
tmpField = sqrt(power(frN_NE.getScalarField(invariant=MAX_PRINCIPAL),2)
    -frN_NE.getScalarField(invariant=MAX_PRINCIPAL)*
    frN_NE.getScalarField(invariant=MIN_PRINCIPAL)+
    power(frN_NE.getScalarField(invariant=MIN_PRINCIPAL),2))*2/3

#create von Mises strain from NE field output
sessionFrame = session.scratchOdbs[C:/MY JOB LOCATION/'+jobName+
    '.odb'].steps['Session Step'].frames[0]
sessionField = sessionFrame.FieldOutput(name='vonMises_NE_'+str(frN),
    description='sqrt(power(frN_NE.getScalarField(invariant=
    MAX_PRINCIPAL),2)-frN_NE.getScalarField(invariant=MAX_PRINCIPAL)*
    frN_NE.getScalarField(invariant=MIN_PRINCIPAL)+
    power(frN_NE.getScalarField(invariant=MIN_PRINCIPAL),2))*2/3',
    field=tmpField)
```

```
#visualize von Mises strain from LE
odbname = session.viewports['Viewport: 1'].odbDisplay.name
frame1 = session.scratchOdbs[odbname].steps['Session Step'].frames[0]
session.viewports['Viewport: 1'].odbDisplay.setFrame(frame=frame1)
session.viewports['Viewport: 1'].odbDisplay.display.setValues(
    plotState=(DEFORMED, ))
session.viewports['Viewport: 1'].odbDisplay.setDeformedVariable(
    variableLabel='U_'+str(frN), )
session.viewports['Viewport: 1'].odbDisplay.display.setValues(
    plotState=CONTOURS_ON_DEF)
session.viewports['Viewport: 1'].odbDisplay.setPrimaryVariable(
    variableLabel='vonMises_LE_'+str(frN),
    outputPosition=INTEGRATION_POINT, )
```

Appendix C

Surface roughness tables of EBM Ti6Al4V primitives

These tables contain the average, standard deviation, minimum, and maximum values for the surface roughness of the strut primitives in the nodes and cells in Chapter 3.

C.1 Cell primitives

Side		0°		45°		90°	
		1 mm	1.25 mm	1 mm	1.25 mm	1 mm	1.25 mm
Upskin	Mean	52.3 ± 1.9	58.3 ± 1.6	42.3 ± 2.2	49.2 ± 2.3	17.4 ± 1.3	19.4 ± 2.0
	Min	42.5	53.5	31.8	34.5	10.2	10.4
	Max	61.5	63.2	58.5	64.4	27.1	34.2
Downskin	Mean	47.4 ± 1.2	54.4 ± 1.4	48.9 ± 1.8	54.8 ± 3.4	66.0 ± 4.4	57.4 ± 4.8
	Min	42.9	45.4	33.0	25.0	24.1	17.7
	Max	50.3	63.6	96.6	102.5	166.3	116.7
Left	Mean	46.9 ± 1.2	50.3 ± 1.5	48.1 ± 2.6	51.7 ± 4.0	35.3 ± 2.8	40.9 ± 3.9
	Min	41.5	45.9	31.7	29.1	22.0	23.0
	Max	53.8	56.2	63.4	78.1	61.7	81.6
Right	Mean	44.4 ± 2.4	55.7 ± 1.4	49.3 ± 2.8	52.6 ± 4.0	37.6 ± 3.0	37.5 ± 2.6
	Min	39.0	45.4	33.4	33.7	21.4	20.3
	Max	51.9	61.3	74.6	96.5	64.3	55.8

Table C.1: Surface roughness metrics of $\mathrm{R_a}$ in units of µm from the struts of different orientations in the cell primitives. The mean (with standard deviation), maximum, and minimum values are reported. Note that the 0° doesn't have a true "upskin" or "downskin" so the values reported in those rows are just for sides that were arbitrarily labeled "upskin" or "downskin.

Side		0°		45°		90°	
		1 mm	1.25 mm	1 mm	1.25 mm	1 mm	1.25 mm
Upskin	Mean	144.1 ± 12.2	175.6 ± 13.7	105.0 ± 10.9	125.4 ± 10.4	44.7 ± 9.4	47.3 ± 9.1
	Min	109.3	120.6	57.6	75.0	14.9	19.4
	Max	174.0	208.7	157.9	180.2	82.7	86.1
Downskin	Mean	150.5 ± 13.6	177.0 ± 10.6	122.1 ± 14.6	132.5 ± 12.5	203.8 ± 20.5	172.1 ± 20.7
	Min	110.6	146.3	59.9	47.0	54.4	89.5
	Max	230.4	223.1	210.2	249.6	477.3	342.3
Left	Mean	124.3 ± 12.2	152.5 ± 13.6	133.6 ± 12.1	139.1 ± 12.0	105.4 ± 13.7	114.6 ± 14.7
	Min	98.1	110.1	81.3	81.7	63.2	61.0
	Max	158.5	197.3	174.9	205.8	189.6	196.9
Right	Mean	153.6 ± 18.0	162.1 ± 9.0	134.0 ± 10.3	147.0 ± 18.3	109.9 ± 14.2	103.9 ± 11.8
	Min	110.5	125.7	93.8	74.1	42.5	43.4
	Max	206.7	191.6	182.7	269.6	173.1	169.4

Table C.2: Surface roughness metrics of R_{RMS} in units of µm from the struts of different orientations in the cell primitives. The mean (with standard deviation), maximum, and minimum values are reported. Note that the 0° doesn't have a true "upskin" or "downskin" so the values reported in those rows are just for sides that were arbitrarily labeled "upskin" or "downskin.

Side		0°		45°		90°	
		1 mm	1.25 mm	1 mm	1.25 mm	1 mm	1.25 mm
Upskin	Mean	144.1 ± 12.2	175.6 ± 13.7	105.0 ± 10.9	125.4 ± 10.4	44.7 ± 9.4	47.3 ± 9.1
	Min	109.3	120.6	57.6	75.0	14.9	19.4
	Max	174.0	208.7	157.9	180.2	82.7	86.1
Downskin	Mean	150.5 ± 13.6	177.0 ± 10.6	122.1 ± 14.6	132.5 ± 12.5	203.8 ± 20.5	172.1 ± 20.7
	Min	110.6	146.3	59.9	47.0	54.4	89.5
	Max	230.4	223.1	210.2	249.6	477.3	342.3
Left	Mean	124.3 ± 12.2	152.5 ± 13.6	133.6 ± 12.1	139.1 ± 12.0	105.4 ± 13.7	114.6 ± 14.7
	Min	98.1	110.1	81.3	81.7	63.2	61.0
	Max	158.5	197.3	174.9	205.8	189.6	196.9
Right	Mean	153.6 ± 18.0	162.1 ± 9.0	134.0 ± 10.3	147.0 ± 18.3	109.9 ± 14.2	103.9 ± 11.8
	Min	110.5	125.7	93.8	74.1	42.5	43.4
	Max	206.7	191.6	182.7	269.6	173.1	169.4

Table C.3: Surface roughness metrics of R_v in units of µm from the struts of different orientations in the cell primitives. The mean (with standard deviation), maximum, and minimum values are reported. Note that the 0° doesn't have a true "upskin" or "downskin" so the values reported in those rows are just for sides that were arbitrarily labeled "upskin" or "downskin.

Side		0°		45°		90°	
		1 mm	1.25 mm	1 mm	1.25 mm	1 mm	1.25 mm
Upskin	Mean	197.4 ± 16.8	183.5 ± 24.0	155.5 ± 18.1	180.2 ± 16.9	42.5 ± 6.5	51.0 ± 9.2
	Min	123.0	139.5	88.4	93.9	11.9	17.6
	Max	257.9	250.0	266.9	259.0	65.5	87.2
Downskin	Mean	158.7 ± 14.6	184.8 ± 16.6	156.9 ± 13.6	186.5 ± 18.0	211.0 ± 25.6	171.4 ± 20.8
	Min	123.9	144.2	86.9	60.9	50.9	34.5
	Max	186.4	221.6	275.8	356.1	535.0	482.0
Left	Mean	161.9 ± 17.7	194.5 ± 25.9	152.8 ± 16.1	173.0 ± 25.8	104.2 ± 13.2	116.3 ± 18.8
	Min	124.7	155.7	70.0	104.3	48.9	59.0
	Max	218.1	285.5	253.2	376.7	187.1	273.9
Right	Mean	133.9 ± 10.3	209.2 ± 18.6	163.2 ± 16.4	163.9 ± 25.8	113.1 ± 13.9	109.8 ± 13.9
	Min	115.6	140.3	93.0	87.9	56.6	63.5
	Max	181.6	310.5	279.1	405.4	210.5	201.3

Table C.4: Surface roughness metrics of R_p in units of µm from the struts of different orientations in the cell primitives. The mean (with standard deviation), maximum, and minimum values are reported. Note that the 0° doesn't have a true "upskin" or "downskin" so the values reported in those rows are just for sides that were arbitrarily labeled "upskin" or "downskin.

C.2 Node primitives

Side		0°		90°	
		1 mm	1.25 mm	1 mm	1.25 mm
Upskin	Mean	50.7 ± 3.1	46.2 ± 5.2	18.6 ± 2.2	33.6 ± 9.2
	Min	40.9	34.8	14.8	11.0
	Max	63.0	61.8	23.4	65.7
Downskin	Mean	33.3 ± 2.9	34.6 ± 3.7	77.7 ± 5.6	63.4 ± 9.8
	Min	23.6	24.6	31.2	38.7
	Max	41.5	46.7	114.1	97.0
Left	Mean	35.1 ± 2.2	53.2 ± 2.2	25.2 ± 2.8	28.6 ± 2.2
	Min	29.3	43.5	20.7	23.9
	Max	41.5	61.1	35.3	34.9
Right	Mean	37.5 ± 1.4	51.8 ± 2.3	27.0 ± 2.2	27.9 ± 2.5
	Min	26.1	43.3	18.9	12.3
	Max	45.3	58.3	31.4	35.8

Table C.5: Surface roughness metrics of R_a in units of µm from the struts of different orientations in the node primitives. The mean (with standard deviation), maximum, and minimum values are reported.

Side		0°		90°	
		1 mm	1.25 mm	1 mm	1.25 mm
Upskin	Mean	64.7 ± 4.2	56.9 ± 6.4	23.1 ± 1.7	48.3 ± 12.8
	Min	50.5	42.0	20.3	19.0
	Max	82.6	74.2	27.8	97.1
Downskin	Mean	41.7 ± 2.8	43.7 ± 3.3	101.6 ± 6.7	83.5 ± 14.6
	Min	30.7	34.3	42.3	50.0
	Max	50.9	53.5	144.9	134.2
Left	Mean	43.7 ± 2.4	65.6 ± 2.6	31.4 ± 3.1	36.4 ± 2.1
	Min	35.0	52.4	26.9	33.0
	Max	50.2	74.4	45.4	42.6
Right	Mean	46.6 ± 1.2	63.4 ± 2.1	34.0 ± 2.2	34.8 ± 2.8
	Min	34.9	54.3	27.0	21.1
	Max	56.0	71.8	40.3	45.6

Table C.6: Surface roughness metrics of R_{RMS} in units of µm from the struts of different orientations in the node primitives. The mean (with standard deviation), maximum, and minimum values are reported.

Side		0°		90°	
		1 mm	1.25 mm	1 mm	1.25 mm
Upskin	Mean	119.4 ± 15.7	128.9 ± 18.7	47.4 ± 12.6	59.2 ± 13.9
	Min	82.2	77.5	20.1	31.2
	Max	180.3	172.3	72.7	90.8
Downskin	Mean	104.7 ± 14.5	91.4 ± 14.5	168.9 ± 13.6	167.5 ± 23.9
	Min	78.0	66.1	86.6	96.3
	Max	130.1	124.4	241.8	271.0
Left	Mean	103.4 ± 9.7	136.8 ± 15.7	63.0 ± 13.1	86.2 ± 15.6
	Min	83.7	90.1	36.3	52.7
	Max	124.2	178.2	95.1	123.2
Right	Mean	104.7 ± 11.4	127.9 ± 12.0	83.2 ± 12.5	82.0 ± 15.0
	Min	79.8	93.3	52.3	47.1
	Max	130.5	203.4	129.4	120.2

Table C.7: Surface roughness metrics of R_v in units of µm from the struts of different orientations in the node primitives. The mean (with standard deviation), maximum, and minimum values are reported.

Side		0°		90°	
		1 mm	1.25 mm	1 mm	1.25 mm
Upskin	Mean	196.9 ± 23.3	130.7 ± 23.9	43.9 ± 9.7	164.2 ± 49.6
	Min	134.3	94.4	28.3	58.0
	Max	280.4	193.3	64.0	346.1
Downskin	Mean	94.7 ± 12.0	102.9 ± 11.3	277.1 ± 19.9	236.3 ± 60.3
	Min	63.2	71.6	103.1	104.9
	Max	131.0	155.1	397.0	392.4
Left	Mean	108.1 ± 14.9	146.8 ± 11.4	85.1 ± 16.6	84.0 ± 14.5
	Min	82.6	115.4	58.5	52.6
	Max	138.5	175.2	146.0	119.2
Right	Mean	111.9 ± 12.6	143.7 ± 9.7	77.0 ± 13.5	88.2 ± 12.1
	Min	61.7	92.9	46.9	51.8
	Max	154.1	186.8	130.5	112.9

Table C.8: Surface roughness metrics of R_p in units of µm from the struts of different orientations in the node primitives. The mean (with standard deviation), maximum, and minimum values are reported.

Bibliography

[1] 4WEB Medical, “Anterior spine truss system,” 2018. [Online; accessed April 20, 2018].

[2] X. Wang, S. Xu, S. Zhou, W. Xu, M. Leary, P. Choong, M. Qian, M. Brandt, and Y. M. Xie, “Topological design and additive manufacturing of porous metals for bone scaffolds and orthopaedic implants: A review,” *Biomaterials*, vol. 83, pp. 127–141, 2016.

[3] Y. Tian, D. Tomus, P. Rometsch, and X. Wu, “Influences of processing parameters on surface roughness of Hastelloy X produced by selective laser melting,” *Additive Manufacturing*, vol. 13, pp. 103–112, 2017.

[4] L. E. Murr, S. M. Gaytan, D. A. Ramirez, E. Martinez, J. Hernandez, K. N. Amato, P. W. Shindo, F. R. Medina, and R. B. Wicker, “Metal fabrication by additive manufacturing using laser and electron beam melting technologies,” *Journal of Materials Science & Technology*, vol. 28, no. 1, pp. 1–14, 2012.

[5] S. Li, Q. Xu, Z. Wang, W. Hou, Y. Hao, R. Yang, and L. Murr, “Influence of cell shape on mechanical properties of Ti–6Al–4V meshes fabricated by electron beam melting method,” *Acta biomaterialia*, vol. 10, no. 10, pp. 4537–4547, 2014.

[6] C. I. Hammetter, R. G. Rinaldi, and F. W. Zok, “Pyramidal lattice structures for high strength and energy absorption,” *Journal of Applied Mechanics*, vol. 80, no. 4, 2013.

[7] L. Facchini, E. Magalini, P. Robotti, and A. Molinari, “Microstructure and mechanical properties of Ti–6Al–4V produced by electron beam melting of pre-alloyed powders,” *Rapid Prototyping Journal*, 2009.

[8] L. Murr, E. Esquivel, S. Quinones, S. Gaytan, M. Lopez, E. Martinez, F. Medina, D. Hernandez, E. Martinez, J. Martinez, *et al.*, “Microstructures and mechanical properties of electron beam-rapid manufactured Ti–6Al–4V biomedical prototypes compared to wrought Ti–6Al–4V,” *Materials characterization*, vol. 60, no. 2, pp. 96–105, 2009.

[9] H. Rafi, N. Karthik, H. Gong, T. L. Starr, and B. E. Stucker, "Microstructures and mechanical properties of Ti6Al4V parts fabricated by selective laser melting and electron beam melting," *Journal of Materials Engineering and Performance*, vol. 22, no. 12, pp. 3872–3883, 2013.

[10] Y. Zhai, H. Galarraga, and D. A. Lados, "Microstructure, static properties, and fatigue crack growth mechanisms in Ti–6Al–4V fabricated by additive manufacturing: LENS and EBM," *Engineering Failure Analysis*, vol. 69, pp. 3–14, 2016.

[11] X. Tan, Y. Kok, Y. J. Tan, M. Descoins, D. Mangelinck, S. B. Tor, K. F. Leong, and C. K. Chua, "Graded microstructure and mechanical properties of additive manufactured Ti–6Al–4V via electron beam melting," *Acta Materialia*, vol. 97, pp. 1–16, 2015.

[12] H. Gong, K. Rafi, H. Gu, G. J. Ram, T. Starr, and B. Stucker, "Influence of defects on mechanical properties of Ti–6Al–4V components produced by selective laser melting and electron beam melting," *Materials & Design*, vol. 86, pp. 545–554, 2015.

[13] N. Hrabe and T. Quinn, "Effects of processing on microstructure and mechanical properties of a titanium alloy (Ti–6Al–4V) fabricated using electron beam melting (EBM), part 1: Distance from build plate and part size," *Materials Science and Engineering: A*, vol. 573, pp. 264–270, 2013.

[14] N. Hrabe and T. Quinn, "Effects of processing on microstructure and mechanical properties of a titanium alloy (Ti–6Al–4V) fabricated using electron beam melting (EBM), part 2: Energy input, orientation, and location," *Materials Science and Engineering: A*, vol. 573, pp. 271–277, 2013.

[15] H. Galarraga, D. A. Lados, R. R. Dehoff, M. M. Kirka, and P. Nandwana, "Effects of the microstructure and porosity on properties of Ti–6Al–4V ELI alloy fabricated by electron beam melting (EBM)," *Additive Manufacturing*, vol. 10, pp. 47–57, 2016.

[16] C. de Formanoir, S. Michotte, O. Rigo, L. Germain, and S. Godet, "Electron beam melted Ti–6Al–4V: Microstructure, texture and mechanical behavior of the as-built and heat-treated material," *Materials Science and Engineering: A*, vol. 652, pp. 105–119, 2016.

[17] A. M. Hosseini, S. Masood, D. Fraser, and M. Jahedi, "Mechanical properties investigation of HIP and as-built EBM parts," in *Advanced Materials Research*, vol. 576, pp. 216–219, Trans Tech Publ, 2012.

[18] J. J. Lewandowski and M. Seifi, "Metal additive manufacturing: a review of mechanical properties," *Annual review of materials research*, vol. 46, pp. 151–186, 2016.

[19] M. Svensson, U. Ackelid, and A. Ab, "Titanium alloys manufactured with electron beam melting mechanical and chemical properties," in *Proceedings of the Materials and Processes for Medical Devices Conference*, pp. 189–194, ASM International, 2010.

[20] T. Persenot, G. Martin, R. Dendievel, J.-Y. Buffiére, and E. Maire, "Enhancing the tensile properties of EBM as-built thin parts: effect of HIP and chemical etching," *Materials Characterization*, vol. 143, pp. 82–93, 2018.

[21] S. Murchio, M. Dallago, F. Zanini, S. Carmignato, G. Zappini, F. Berto, D. Maniglio, and M. Benedetti, "Additively manufactured Ti–6Al–4V thin struts via laser powder bed fusion: Effect of building orientation on geometrical accuracy and mechanical properties," *Journal of the Mechanical Behavior of Biomedical Materials*, vol. 119, p. 104495, 2021.

[22] P. Wang, J. Song, M. L. S. Nai, and J. Wei, "Experimental analysis of additively manufactured component and design guidelines for lightweight structures: A case study using electron beam melting," *Additive Manufacturing*, vol. 33, p. 101088, 2020.

[23] J. Dzugan, M. Seifi, R. Prochazka, M. Rund, P. Podany, P. Konopik, and J. Lewandowski, "Effects of thickness and orientation on the small scale fracture behaviour of additively manufactured Ti-6Al-4V," *Materials Characterization*, vol. 143, pp. 94–109, 2018.

[24] L. Gibson and M. Ashby, *Cellular Solids: Structure and Properties.* Cambridge Solid State Science Series, Cambridge University Press, 1999.

[25] M. F. Ashby, "The properties of foams and lattices," *Philosophical Transactions of the Royal Society A: Mathematical, Physical and Engineering Sciences*, vol. 364, no. 1838, pp. 15–30, 2006.

[26] N. A. Fleck, V. S. Deshpande, and M. F. Ashby, "Micro-architectured materials: past, present and future," *Proceedings of the Royal Society A: Mathematical, Physical and Engineering Sciences*, vol. 466, no. 2121, pp. 2495–2516, 2010.

[27] V. Deshpande, M. Ashby, and N. Fleck, "Foam topology: bending versus stretching dominated architectures," *Acta materialia*, vol. 49, no. 6, pp. 1035–1040, 2001.

[28] T. Maconachie, M. Leary, B. Lozanovski, X. Zhang, M. Qian, O. Faruque, and M. Brandt, "SLM lattice structures: Properties, performance, applications and challenges," *Materials & Design*, vol. 183, p. 108137, 2019.

[29] M. Suard, G. Martin, P. Lhuissier, R. Dendievel, F. Vignat, J.-J. Blandin, and F. Villeneuve, "Mechanical equivalent diameter of single struts for the stiffness

prediction of lattice structures produced by Electron Beam Melting," *Additive Manufacturing*, vol. 8, pp. 124–131, 2015.

[30] H. D. Carlton, J. Lind, M. C. Messner, N. A. Volkoff-Shoemaker, H. S. Barnard, N. R. Barton, and M. Kumar, "Mapping local deformation behavior in single cell metal lattice structures," *Acta Materialia*, vol. 129, pp. 239–250, 2017.

[31] O. Cansizoglu, O. Harrysson, D. Cormier, H. West, and T. Mahale, "Properties of Ti–6Al–4V non-stochastic lattice structures fabricated via electron beam melting," *Materials Science and Engineering: A*, vol. 492, no. 1-2, pp. 468–474, 2008.

[32] X. Tan, Y. Tan, C. Chow, S. Tor, and W. Yeong, "Metallic powder-bed based 3d printing of cellular scaffolds for orthopaedic implants: A state-of-the-art review on manufacturing, topological design, mechanical properties and biocompatibility," *Materials Science and Engineering: C*, vol. 76, pp. 1328–1343, 2017.

[33] A. Safdar, H. He, L.-Y. Wei, A. Snis, and L. E. C. de Paz, "Effect of process parameters settings and thickness on surface roughness of EBM produced Ti-6Al-4V," *Rapid Prototyping Journal*, 2012.

[34] X. Cheng, S. Li, L. Murr, Z. Zhang, Y. Hao, R. Yang, F. Medina, and R. Wicker, "Compression deformation behavior of Ti–6Al–4V alloy with cellular structures fabricated by electron beam melting," *Journal of the mechanical behavior of biomedical materials*, vol. 16, pp. 153–162, 2012.

[35] S. Zhao, S. Li, W. Hou, Y. Hao, R. Yang, and R. Misra, "The influence of cell morphology on the compressive fatigue behavior of Ti-6Al-4V meshes fabricated by electron beam melting," *Journal of the mechanical behavior of biomedical materials*, vol. 59, pp. 251–264, 2016.

[36] J. Parthasarathy, B. Starly, S. Raman, and A. Christensen, "Mechanical evaluation of porous titanium (Ti6Al4V) structures with electron beam melting (EBM)," *Journal of the mechanical behavior of biomedical materials*, vol. 3, no. 3, pp. 249–259, 2010.

[37] P. Heinl, L. Müller, C. Körner, R. F. Singer, and F. A. Müller, "Cellular Ti–6Al–4V structures with interconnected macro porosity for bone implants fabricated by selective electron beam melting," *Acta biomaterialia*, vol. 4, no. 5, pp. 1536–1544, 2008.

[38] A. Safdar, L.-Y. Wei, A. Snis, and Z. Lai, "Evaluation of microstructural development in electron beam melted Ti-6Al-4V," *Materials Characterization*, vol. 65, pp. 8–15, 2012.

[39] A. Mertens, S. Reginster, H. Paydas, Q. Contrepois, T. Dormal, O. Lemaire, and J. Lecomte-Beckers, "Mechanical properties of alloy Ti–6Al–4V and of stainless steel 316L processed by selective laser melting: influence of out-of-equilibrium microstructures," *Powder Metallurgy*, vol. 57, no. 3, pp. 184–189, 2014.

[40] T. Ishimoto, S. Wu, Y. Ito, S.-H. Sun, H. Amano, and T. Nakano, "Crystallographic orientation control of 316L austenitic stainless steel via selective laser melting," *ISIJ International*, vol. 60, no. 8, pp. 1758–1764, 2020.

[41] R. R. Dehoff, M. Kirka, W. Sames, H. Bilheux, A. Tremsin, L. Lowe, and S. Babu, "Site specific control of crystallographic grain orientation through electron beam additive manufacturing," *Materials Science and Technology*, vol. 31, no. 8, pp. 931–938, 2015.

[42] J. Gockel and J. Beuth, "Understanding Ti-6Al-4V microstructure control in additive manufacturing via process maps," in *Solid freeform fabrication proceedings*, pp. 666–674, Univ. Tex. Austin, 2013.

[43] S. P. Narra, R. Cunningham, J. Beuth, and A. D. Rollett, "Location specific solidification microstructure control in electron beam melting of Ti-6Al-4V," *Additive Manufacturing*, vol. 19, pp. 160–166, 2018.

[44] A. A. Antonysamy, J. Meyer, and P. Prangnell, "Effect of build geometry on the β-grain structure and texture in additive manufacture of Ti6Al4V by selective electron beam melting," *Materials characterization*, vol. 84, pp. 153–168, 2013.

[45] X. Tan, Y. Kok, Y. J. Tan, G. Vastola, Q. X. Pei, G. Zhang, Y.-W. Zhang, S. B. Tor, K. F. Leong, and C. K. Chua, "An experimental and simulation study on build thickness dependent microstructure for electron beam melted Ti–6Al–4V," *Journal of Alloys and Compounds*, vol. 646, pp. 303–309, 2015.

[46] Y. Kok, X. Tan, S. B. Tor, and C. K. Chua, "Fabrication and microstructural characterisation of additive manufactured Ti-6Al-4V parts by electron beam melting: This paper reports that the microstructure and micro-hardness of an EMB part is thickness dependent," *Virtual and Physical Prototyping*, vol. 10, no. 1, pp. 13–21, 2015.

[47] J. K. Algardh, T. Horn, H. West, R. Aman, A. Snis, H. Engqvist, J. Lausmaa, and O. Harrysson, "Thickness dependency of mechanical properties for thin-walled titanium parts manufactured by Electron Beam Melting (EBM)," *Additive Manufacturing*, vol. 12, pp. 45–50, 2016.

[48] X. Zhao, S. Li, M. Zhang, Y. Liu, T. B. Sercombe, S. Wang, Y. Hao, R. Yang, and L. E. Murr, "Comparison of the microstructures and mechanical properties of Ti–6Al–4V fabricated by selective laser melting and electron beam melting," *Materials & Design*, vol. 95, pp. 21–31, 2016.

[49] U. S. Bertoli, A. J. Wolfer, M. J. Matthews, J.-P. R. Delplanque, and J. M. Schoenung, “On the limitations of volumetric energy density as a design parameter for selective laser melting,” *Materials & Design*, vol. 113, pp. 331–340, 2017.

[50] N. T. Aboulkhair, N. M. Everitt, I. Ashcroft, and C. Tuck, “Reducing porosity in AlSi10Mg parts processed by selective laser melting,” *Additive manufacturing*, vol. 1, pp. 77–86, 2014.

[51] D. Buchbinder, W. Meiners, K. Wissenbach, and R. Poprawe, “Selective laser melting of aluminum die-cast alloy—correlations between process parameters, solidification conditions, and resulting mechanical properties,” *Journal of Laser Applications*, vol. 27, no. S2, p. S29205, 2015.

[52] W. Di, Y. Yongqiang, S. Xubin, and C. Yonghua, “Study on energy input and its influences on single-track, multi-track, and multi-layer in SLM,” *The International Journal of Advanced Manufacturing Technology*, vol. 58, no. 9, pp. 1189–1199, 2012.

[53] K. Monroy, J. Delgado, and J. Ciurana, “Study of the pore formation on CoCrMo alloys by selective laser melting manufacturing process,” *Procedia Engineering*, vol. 63, pp. 361–369, 2013.

[54] Q. S. Wei, X. Zhao, L. Wang, R. D. Li, J. Liu, and Y. S. Shi, “Effects of the processing parameters on the forming quality of stainless steel parts by selective laser melting,” in *Advanced Materials Research*, vol. 189, pp. 3668–3671, Trans Tech Publ, 2011.

[55] B. Zhang, L. Dembinski, and C. Coddet, “The study of the laser parameters and environment variables effect on mechanical properties of high compact parts elaborated by selective laser melting 316L powder,” *Materials Science and Engineering: A*, vol. 584, pp. 21–31, 2013.

[56] S. M. Yusuf and N. Gao, “Influence of energy density on metallurgy and properties in metal additive manufacturing,” *Materials Science and Technology*, vol. 33, no. 11, pp. 1269–1289, 2017.

[57] E. O. Olakanmi, K. W. Dalgarno, and R. F. Cochrane, “Laser sintering of blended Al-Si powders,” *Rapid Prototyping Journal*, 2012.

[58] C. Guo, W. Ge, and F. Lin, “Effects of scanning parameters on material deposition during electron beam selective melting of Ti-6Al-4V powder,” *Journal of Materials Processing Technology*, vol. 217, pp. 148–157, 2015.

[59] W. Yan, W. Ge, J. Smith, S. Lin, O. L. Kafka, F. Lin, and W. K. Liu, “Multi-scale modeling of electron beam melting of functionally graded materials,” *Acta Materialia*, vol. 115, pp. 403–412, 2016.

[60] H. Gong, K. Rafi, H. Gu, T. Starr, and B. Stucker, “Analysis of defect generation in Ti–6Al–4V parts made using powder bed fusion additive manufacturing processes,” *Additive Manufacturing*, vol. 1, pp. 87–98, 2014.

[61] J. Cherry, H. Davies, S. Mehmood, N. Lavery, S. Brown, and J. Sienz, “Investigation into the effect of process parameters on microstructural and physical properties of 316L stainless steel parts by selective laser melting,” *The International Journal of Advanced Manufacturing Technology*, vol. 76, no. 5-8, pp. 869–879, 2015.

[62] T. Peng and C. Chen, “Influence of energy density on energy demand and porosity of 316L stainless steel fabricated by selective laser melting,” *International Journal of Precision Engineering and Manufacturing-Green Technology*, vol. 5, no. 1, pp. 55–62, 2018.

[63] K. V. Yang, P. Rometsch, T. Jarvis, J. Rao, S. Cao, C. Davies, and X. Wu, “Porosity formation mechanisms and fatigue response in Al-Si-Mg alloys made by selective laser melting,” *Materials Science and Engineering: A*, vol. 712, pp. 166–174, 2018.

[64] G. Kasperovich, J. Haubrich, J. Gussone, and G. Requena, “Correlation between porosity and processing parameters in TiAl6V4 produced by selective laser melting,” *Materials & Design*, vol. 105, pp. 160–170, 2016.

[65] J. Dilip, S. Zhang, C. Teng, K. Zeng, C. Robinson, D. Pal, and B. Stucker, “Influence of processing parameters on the evolution of melt pool, porosity, and microstructures in Ti-6Al-4V alloy parts fabricated by selective laser melting,” *Progress in Additive Manufacturing*, vol. 2, no. 3, pp. 157–167, 2017.

[66] A. H. Maamoun, Y. F. Xue, M. A. Elbestawi, and S. C. Veldhuis, “Effect of selective laser melting process parameters on the quality of Al alloy parts: Powder characterization, density, surface roughness, and dimensional accuracy,” *Materials*, vol. 11, no. 12, p. 2343, 2018.

[67] D. Wang, Y. Liu, Y. Yang, and D. Xiao, “Theoretical and experimental study on surface roughness of 316L stainless steel metal parts obtained through selective laser melting,” *Rapid Prototyping Journal*, 2016.

[68] T. Yang, T. Liu, W. Liao, E. MacDonald, H. Wei, X. Chen, and L. Jiang, “The influence of process parameters on vertical surface roughness of the AlSi10Mg parts fabricated by selective laser melting,” *Journal of Materials Processing Technology*, vol. 266, pp. 26–36, 2019.

[69] D. Gu and Y. Shen, “Balling phenomena in direct laser sintering of stainless steel powder: Metallurgical mechanisms and control methods,” *Materials & Design*, vol. 30, no. 8, pp. 2903–2910, 2009.

[70] R. Li, J. Liu, Y. Shi, L. Wang, and W. Jiang, “Balling behavior of stainless steel and nickel powder during selective laser melting process,” *The International Journal of Advanced Manufacturing Technology*, vol. 59, no. 9, pp. 1025–1035, 2012.

[71] K. Prashanth, S. Scudino, T. Maity, J. Das, and J. Eckert, “Is the energy density a reliable parameter for materials synthesis by selective laser melting?,” *Materials Research Letters*, vol. 5, no. 6, pp. 386–390, 2017.

[72] ISO/ASTM52900-15, *Standard Terminology for Additive Manufacturing – General Principles – Terminology.* ASTM International, West Conshohocken, PA, 2015.

[73] T. Niendorf, F. Brenne, and M. Schaper, “Lattice structures manufactured by SLM: On the effect of geometrical dimensions on microstructure evolution during processing,” *Metallurgical and materials transactions B*, vol. 45, no. 4, pp. 1181–1185, 2014.

[74] J. Bruno, A. Rochman, and G. Cassar, “Effect of build orientation of electron beam melting on microstructure and mechanical properties of Ti-6Al-4V,” *Journal of Materials Engineering and Performance*, vol. 26, no. 2, pp. 692–703, 2017.

[75] A. Leicht, U. Klement, and E. Hryha, “Effect of build geometry on the microstructural development of 316L parts produced by additive manufacturing,” *Materials Characterization*, vol. 143, pp. 137–143, 2018.

[76] Z. Dong, Y. Liu, W. Li, and J. Liang, “Orientation dependency for microstructure, geometric accuracy and mechanical properties of selective laser melting AlSi10Mg lattices,” *Journal of Alloys and Compounds*, vol. 791, pp. 490–500, 2019.

[77] R. Wauthle, B. Vrancken, B. Beynaerts, K. Jorissen, J. Schrooten, J.-P. Kruth, and J. Van Humbeeck, “Effects of build orientation and heat treatment on the microstructure and mechanical properties of selective laser melted Ti6Al4V lattice structures,” *Additive Manufacturing*, vol. 5, pp. 77–84, 2015.

[78] S. Al-Bermani, M. Blackmore, W. Zhang, and I. Todd, “The origin of microstructural diversity, texture, and mechanical properties in electron beam melted Ti-6Al-4V,” *Metallurgical and materials transactions a*, vol. 41, no. 13, pp. 3422–3434, 2010.

[79] G. Strano, L. Hao, R. M. Everson, and K. E. Evans, “Surface roughness analysis, modelling and prediction in selective laser melting,” *Journal of Materials Processing Technology*, vol. 213, no. 4, pp. 589–597, 2013.

[80] F. Cabanettes, A. Joubert, G. Chardon, V. Dumas, J. Rech, C. Grosjean, and Z. Dimkovski, “Topography of as built surfaces generated in metal additive manufacturing: a multi scale analysis from form to roughness,” *Precision Engineering*, vol. 52, pp. 249–265, 2018.

[81] D. Ahn, H. Kim, and S. Lee, "Surface roughness prediction using measured data and interpolation in layered manufacturing," *Journal of materials processing technology*, vol. 209, no. 2, pp. 664–671, 2009.

[82] B. Vandenbroucke and J.-P. Kruth, "Selective laser melting of biocompatible metals for rapid manufacturing of medical parts," *Rapid Prototyping Journal*, 2007.

[83] P. Das, R. Chandran, R. Samant, and S. Anand, "Optimum part build orientation in additive manufacturing for minimizing part errors and support structures," *Procedia Manufacturing*, vol. 1, pp. 343–354, 2015.

[84] T. Persenot, A. Burr, G. Martin, J.-Y. Buffiere, R. Dendievel, and E. Maire, "Effect of build orientation on the fatigue properties of as-built Electron Beam Melted Ti-6Al-4V alloy," *International Journal of Fatigue*, vol. 118, pp. 65–76, 2019.

[85] T. DebRoy, H. Wei, J. Zuback, T. Mukherjee, J. Elmer, J. Milewski, A. M. Beese, A. Wilson-Heid, A. De, and W. Zhang, "Additive manufacturing of metallic components–process, structure and properties," *Progress in Materials Science*, vol. 92, pp. 112–224, 2018.

[86] W. J. Sames, F. List, S. Pannala, R. R. Dehoff, and S. S. Babu, "The metallurgy and processing science of metal additive manufacturing," *International materials reviews*, vol. 61, no. 5, pp. 315–360, 2016.

[87] V. Bhavar, P. Kattire, V. Patil, S. Khot, K. Gujar, and R. Singh, "A review on powder bed fusion technology of metal additive manufacturing," in *Additive manufacturing handbook*, pp. 251–253, CRC Press, 2017.

[88] C. Qiu, C. Panwisawas, M. Ward, H. C. Basoalto, J. W. Brooks, and M. M. Attallah, "On the role of melt flow into the surface structure and porosity development during selective laser melting," *Acta Materialia*, vol. 96, pp. 72–79, 2015.

[89] S. Rahmati and E. Vahabli, "Evaluation of analytical modeling for improvement of surface roughness of FDM test part using measurement results," *The International Journal of Advanced Manufacturing Technology*, vol. 79, no. 5, pp. 823–829, 2015.

[90] J.-P. Kruth, L. Froyen, J. Van Vaerenbergh, P. Mercelis, M. Rombouts, and B. Lauwers, "Selective laser melting of iron-based powder," *Journal of materials processing technology*, vol. 149, no. 1-3, pp. 616–622, 2004.

[91] H. Niu and I. Chang, "Instability of scan tracks of selective laser sintering of high speed steel powder," *Scripta materialia*, vol. 41, no. 11, pp. 1229–1234, 1999.

[92] J.-P. Kruth, G. Levy, F. Klocke, and T. Childs, "Consolidation phenomena in laser and powder-bed based layered manufacturing," *CIRP annals*, vol. 56, no. 2, pp. 730–759, 2007.

[93] K. Mumtaz and N. Hopkinson, "Top surface and side roughness of Inconel 625 parts processed using selective laser melting," *Rapid Prototyping Journal*, 2009.

[94] C. Korner, A. Bauereiss, and E. Attar, "Fundamental consolidation mechanisms during selective beam melting of powders: Modelling and simulation in materials science and engineering," 2013.

[95] A. Fathi, E. Toyserkani, A. Khajepour, and M. Durali, "Prediction of melt pool depth and dilution in laser powder deposition," *Journal of Physics D: Applied Physics*, vol. 39, no. 12, p. 2613, 2006.

[96] I. Anderson, R. Figliola, and H. Morton, "Flow mechanisms in high pressure gas atomization," *Materials Science and Engineering: A*, vol. 148, no. 1, pp. 101–114, 1991.

[97] R. G. Bourdeau, "Rotary atomizing process," Nov. 15 1983. US Patent 4,415,511.

[98] A. Ozols, H. Sirkin, and E. Vicente, "Segregation in stellite powders produced by the plasma rotating electrode process," *Materials Science and Engineering: A*, vol. 262, no. 1-2, pp. 64–69, 1999.

[99] Y. Seki, S. Okamoto, H. Takigawa, and N. Kawai, "Effect of atomization variables on powder characteristics in the high-pressured water atomization process," *Metal Powder Report*, vol. 45, no. 1, pp. 38–40, 1990.

[100] W. Sames, F. Medina, W. Peter, S. Babu, and R. Dehoff, "Effect of process control and powder quality on Inconel 718 produced using electron beam melting," in *8th Int. Symp. Superalloy 718 Deriv*, pp. 409–423, 2014.

[101] A. J. Pinkerton and L. Li, "Direct additive laser manufacturing using gas-and water-atomised H13 tool steel powders," *The International Journal of Advanced Manufacturing Technology*, vol. 25, no. 5, pp. 471–479, 2005.

[102] E. J. Parteli and T. Pöschel, "Particle-based simulation of powder application in additive manufacturing," *Powder Technology*, vol. 288, pp. 96–102, 2016.

[103] C. T. Schade, T. F. Murphy, and C. Walton, "Development of atomized powders for additive manufacturing," in *Powder Metallurgy Word Congress, Accessed on 2nd July*, 2014.

[104] B. Liu, R. Wildman, C. Tuck, I. Ashcroft, and R. Hague, "Investigation the effect of particle size distribution on processing parameters optimisation in selective laser melting process," *Additive manufacturing research group, Loughborough University*, pp. 227–238, 2011.

[105] H. Qi, M. Azer, and A. Ritter, “Studies of standard heat treatment effects on microstructure and mechanical properties of laser net shape manufactured Inconel 718,” *Metallurgical and Materials Transactions A*, vol. 40, no. 10, pp. 2410–2422, 2009.

[106] C. Meier, R. Weissbach, J. Weinberg, W. A. Wall, and A. J. Hart, “Critical influences of particle size and adhesion on the powder layer uniformity in metal additive manufacturing,” *Journal of Materials Processing Technology*, vol. 266, pp. 484–501, 2019.

[107] J. Gockel, L. Sheridan, B. Koerper, and B. Whip, “The influence of additive manufacturing processing parameters on surface roughness and fatigue life,” *International Journal of Fatigue*, vol. 124, pp. 380–388, 2019.

[108] W. E. King, H. D. Barth, V. M. Castillo, G. F. Gallegos, J. W. Gibbs, D. E. Hahn, C. Kamath, and A. M. Rubenchik, “Observation of keyhole-mode laser melting in laser powder-bed fusion additive manufacturing,” *Journal of Materials Processing Technology*, vol. 214, no. 12, pp. 2915–2925, 2014.

[109] S. A. Khairallah, A. T. Anderson, A. Rubenchik, and W. E. King, “Laser powder-bed fusion additive manufacturing: Physics of complex melt flow and formation mechanisms of pores, spatter, and denudation zones,” *Acta Materialia*, vol. 108, pp. 36–45, 2016.

[110] P. Wang, W. J. Sin, M. L. S. Nai, and J. Wei, “Effects of processing parameters on surface roughness of additive manufactured Ti-6Al-4V via electron beam melting,” *Materials*, vol. 10, no. 10, p. 1121, 2017.

[111] D. Systémes, *Abaqus Analysis User’s Guide, Version 6.14.* Dassault Systémes, Providence, RI, 2014.

[112] R. D. Cook *et al.*, *Concepts and applications of finite element analysis.* John wiley & sons, 2007.

[113] L. Andersen and S. Nielsen, “Elastic beams in three dimensions,” *Aalborg University*, 2008.

[114] R. M. Gorguluarslan, U. N. Gandhi, R. Mandapati, and S.-K. Choi, “Design and fabrication of periodic lattice-based cellular structures,” *Computer-Aided Design and Applications*, vol. 13, no. 1, pp. 50–62, 2016.

[115] G. Labeas and M. Sunaric, “Investigation on the static response and failure process of metallic open lattice cellular structures,” *Strain*, vol. 46, no. 2, pp. 195–204, 2010.

[116] M. Smith, Z. Guan, and W. Cantwell, “Finite element modelling of the compressive response of lattice structures manufactured using the selective laser melting technique,” *International Journal of Mechanical Sciences*, vol. 67, pp. 28–41, 2013.

[117] J. Schindelin, I. Arganda-Carreras, E. Frise, V. Kaynig, M. Longair, T. Pietzsch, S. Preibisch, C. Rueden, S. Saalfeld, B. Schmid, *et al.*, "Fiji: an open-source platform for biological-image analysis," *Nature methods*, vol. 9, no. 7, pp. 676–682, 2012.

[118] E. H. Meijering, W. J. Niessen, and M. A. Viergever, "Quantitative evaluation of convolution-based methods for medical image interpolation," *Medical image analysis*, vol. 5, no. 2, pp. 111–126, 2001.

[119] B. Schmid, J. Schindelin, A. Cardona, M. Longair, and M. Heisenberg, "A high-level 3d visualization API for java and imagej," *BMC bioinformatics*, vol. 11, no. 1, pp. 1–7, 2010.

[120] T. Ferreira and W. Rasb, *ImageJ user guide: IJ 1.46 r*, 2012.

[121] H. Schreier, J.-J. Orteu, M. A. Sutton, *et al.*, *Image correlation for shape, motion and deformation measurements: Basic concepts, theory and applications*, vol. 1. Springer, 2009.

[122] V. Rajan, M. Rossol, and F. Zok, "Optimization of digital image correlation for high-resolution strain mapping of ceramic composites," *Experimental mechanics*, vol. 52, no. 9, pp. 1407–1421, 2012.

[123] W. S. LePage, S. H. Daly, and J. A. Shaw, "Cross polarization for improved digital image correlation," *Experimental Mechanics*, vol. 56, no. 6, pp. 969–985, 2016.

[124] K. L. Johnson and K. L. Johnson, *Contact mechanics.* Cambridge university press, 1987.

[125] K. Johnson, "The correlation of indentation experiments," *Journal of the Mechanics and Physics of Solids*, vol. 18, no. 2, pp. 115–126, 1970.

[126] M. Mata, O. Casals, and J. Alcala, "The plastic zone size in indentation experiments: The analogy with the expansion of a spherical cavity," *International Journal of Solids and Structures*, vol. 43, no. 20, pp. 5994–6013, 2006.

[127] J. Chen and S. Bull, "On the relationship between plastic zone radius and maximum depth during nanoindentation," *Surface and Coatings Technology*, vol. 201, no. 7, pp. 4289–4293, 2006.

[128] A. Giannakopoulos and S. Suresh, "Determination of elastoplastic properties by instrumented sharp indentation," *Scripta materialia*, vol. 40, no. 10, pp. 1191–1198, 1999.

[129] D. Kramer, H. Huang, M. Kriese, J. Robach, J. Nelson, A. Wright, D. Bahr, and W. Gerberich, "Yield strength predictions from the plastic zone around nanocontacts," *Acta Materialia*, vol. 47, no. 1, pp. 333–343, 1998.

[130] S. Chiang, D. Marshall, and A. Evans, "The response of solids to elastic/plastic indentation. I. Stresses and residual stresses," *Journal of Applied Physics*, vol. 53, no. 1, pp. 298–311, 1982.

[131] E. Yoffe, "Elastic stress fields caused by indenting brittle materials," *Philosophical Magazine A*, vol. 46, no. 4, pp. 617–628, 1982.

[132] C. K. Dolph, D. J. da Silva, M. J. Swenson, and J. P. Wharry, "Plastic zone size for nanoindentation of irradiated Fe–9% Cr ODS," *Journal of Nuclear Materials*, vol. 481, pp. 33–45, 2016.

[133] D. Tabor, "A simple theory of static and dynamic hardness," *Proceedings of the Royal Society of London. Series A. Mathematical and Physical Sciences*, vol. 192, no. 1029, pp. 247–274, 1948.

[134] P. Zhang, S. Li, and Z. Zhang, "General relationship between strength and hardness," *Materials Science and Engineering: A*, vol. 529, pp. 62–73, 2011.

[135] M. F. Ashby and D. R. Jones, *Engineering materials 1: an introduction to properties, applications and design*, vol. 1. Elsevier, 2012.

[136] H. E. Boyer and T. L. Gall, *Metals handbook; desk edition*, 1985.

[137] W. D. Callister and D. G. Rethwisch, *Materials science and engineering*, vol. 5. John Wiley & Sons NY, 2011.

[138] Y.-T. Cheng and C.-M. Cheng, "Scaling, dimensional analysis, and indentation measurements," *Materials Science and Engineering: R: Reports*, vol. 44, no. 4-5, pp. 91–149, 2004.

[139] J. Cahoon, W. Broughton, and A. Kutzak, "The determination of yield strength from hardness measurements," *Metallurgical transactions*, vol. 2, no. 7, pp. 1979–1983, 1971.

[140] E. Pavlina and C. Van Tyne, "Correlation of yield strength and tensile strength with hardness for steels," *Journal of materials engineering and performance*, vol. 17, no. 6, pp. 888–893, 2008.

[141] C. Hickey Jr, "Tensile strength-hardness correlation for Titanium alloys.," tech. rep., Watertown Arsenal Labs MA, 1961.

[142] J. S. Keist and T. A. Palmer, "Development of strength-hardness relationships in additively manufactured titanium alloys," *Materials Science and Engineering: A*, vol. 693, pp. 214–224, 2017.

[143] N. Hrabe, T. Gnäupel-Herold, and T. Quinn, “Fatigue properties of a titanium alloy (Ti–6Al–4V) fabricated via electron beam melting (EBM): Effects of internal defects and residual stress,” *International Journal of Fatigue*, vol. 94, pp. 202–210, 2017.

[144] C. Smith, F. Derguti, E. H. Nava, M. Thomas, S. Tammas-Williams, S. Gulizia, D. Fraser, and I. Todd, “Dimensional accuracy of Electron Beam Melting (EBM) additive manufacture with regard to weight optimized truss structures,” *Journal of Materials Processing Technology*, vol. 229, pp. 128–138, 2016.

[145] A. Pérez-Sánchez, A. Yánez, A. Cuadrado, O. Martel, and N. Nuño, “Fatigue behaviour and equivalent diameter of single Ti–6Al–4V struts fabricated by Electron Bean Melting orientated to porous lattice structures,” *Materials & Design*, vol. 155, pp. 106–115, 2018.

[146] C. Dong, R. Collino, S. Donegan, J. Miller, and M. Begley, “Effective properties for millimeter-scale struts and strut intersections (nodes) in lattice primitives fabricated via ebm,” *Submitted to Additive Manufacturing*, 2021.

[147] ASTM International, *Standard Specification for Additive Manufacturing Titanium-6 Aluminum-4 Vanadium ELI (Extra Low Interstitial) with Powder Bed Fusion.* ASTM International, West Conshohocken, PA, 2014.

[148] Arcam AB, *Ti6Al4V Titanium Alloy.* Arcam EBM System, Mölndal, Sweden, 2019.

[149] C. Dong, S. Messina, G. Balbus, J. Shin, D. Gianola, and M. Begley, “Variations in local geometric and mechanical properties in EBM Ti–6Al–4V lattice structure primitives,” *Manuscript in preparation*, 2021.

[150] S. C. Wehmeyer, B. G. Compton, J. W. Pro, F. Zok, and M. R. Begley, “Damping in cellular structures made from composite struts and walls with elastic and viscoelastic phases,” *Journal of the Mechanics and Physics of Solids*, vol. 145, p. 104106, 2020.

[151] C. Britt, C. J. Montgomery, M. J. Brand, Z.-K. Liu, J. S. Carpenter, and A. M. Beese, “Effect of processing parameters and strut dimensions on the microstructures and hardness of stainless steel 316L lattice-emulating structures made by powder bed fusion,” *Additive Manufacturing*, p. 101943, 2021.

[152] E. Liverani, S. Toschi, L. Ceschini, and A. Fortunato, “Effect of selective laser melting (SLM) process parameters on microstructure and mechanical properties of 316L austenitic stainless steel,” *Journal of Materials Processing Technology*, vol. 249, pp. 255–263, 2017.

[153] P. Hanzl, M. Zetek, T. Bakša, and T. Kroupa, "The influence of processing parameters on the mechanical properties of SLM parts," *Procedia Engineering*, vol. 100, pp. 1405–1413, 2015.

[154] A. A. Zadpoor, "Mechanical performance of additively manufactured meta-biomaterials," *Acta biomaterialia*, vol. 85, pp. 41–59, 2019.

[155] S. L. Sing, F. E. Wiria, and W. Y. Yeong, "Selective laser melting of lattice structures: A statistical approach to manufacturability and mechanical behavior," *Robotics and Computer-Integrated Manufacturing*, vol. 49, pp. 170–180, 2018.

[156] Y. Kok, X. Tan, N. Loh, S. Tor, and C. Chua, "Geometry dependence of microstructure and microhardness for selective electron beam-melted Ti–6Al–4V parts," *Virtual and Physical Prototyping*, vol. 11, no. 3, pp. 183–191, 2016.

[157] O. Andreau, I. Koutiri, P. Peyre, J.-D. Penot, N. Saintier, E. Pessard, T. De Terris, C. Dupuy, and T. Baudin, "Texture control of 316L parts by modulation of the melt pool morphology in selective laser melting," *Journal of Materials Processing Technology*, vol. 264, pp. 21–31, 2019.

[158] A. Deev, P. Kuznetcov, and S. Petrov, "Anisotropy of mechanical properties and its correlation with the structure of the stainless steel 316L produced by the SLM method," *Physics Procedia*, vol. 83, pp. 789–796, 2016.

[159] G. Ziółkowski, E. Chlebus, P. Szymczyk, and J. Kurzac, "Application of X-ray CT method for discontinuity and porosity detection in 316L stainless steel parts produced with SLM technology," *Archives of civil and mechanical engineering*, vol. 14, pp. 608–614, 2014.

[160] J. Suryawanshi, K. Prashanth, and U. Ramamurty, "Mechanical behavior of selective laser melted 316L stainless steel," *Materials Science and Engineering: A*, vol. 696, pp. 113–121, 2017.

[161] M. Montero Sistiaga, S. Nardone, C. Hautfenne, and J. Van Humbeeck, "Effect of heat treatment of 316L stainless steel produced by selective laser melting (SLM)," in *Proceedings of the 27th Annual International Solid Freeform Fabrication Symposium-An Additive Manufacturing Conference*, pp. 558–565, Solid Freeform Fabrication, 2016.

[162] T. Kurzynowski, W. Stopyra, K. Gruber, G. Ziółkowski, B. Kuźnicka, and E. Chlebus, "Effect of scanning and support strategies on relative density of SLM-ed H13 steel in relation to specimen size," *Materials*, vol. 12, no. 2, p. 239, 2019.

[163] E. Yasa and J.-P. Kruth, "Microstructural investigation of Selective Laser Melting 316L stainless steel parts exposed to laser re-melting," *Procedia Engineering*, vol. 19, pp. 389–395, 2011.

[164] D. Wang, S. Wu, Y. Yang, W. Dou, S. Deng, Z. Wang, and S. Li, "The effect of a scanning strategy on the residual stress of 316L steel parts fabricated by selective laser melting (SLM)," *Materials*, vol. 11, no. 10, p. 1821, 2018.

[165] H. Gu, H. Gong, D. Pal, K. Rafi, T. Starr, B. Stucker, *et al.*, "Influences of energy density on porosity and microstructure of selective laser melted 17-4PH stainless steel," in *2013 Solid Freeform Fabrication Symposium*, vol. 474, 2013.

[166] W. M. Tucho, V. H. Lysne, H. Austbø, A. Sjolyst-Kverneland, and V. Hansen, "Investigation of effects of process parameters on microstructure and hardness of SLM manufactured SS316L," *Journal of Alloys and Compounds*, vol. 740, pp. 910–925, 2018.

[167] R. Li, Y. Shi, Z. Wang, L. Wang, J. Liu, and W. Jiang, "Densification behavior of gas and water atomized 316L stainless steel powder during selective laser melting," *Applied surface science*, vol. 256, no. 13, pp. 4350–4356, 2010.

[168] T. Larimian, M. Kannan, D. Grzesiak, B. AlMangour, and T. Borkar, "Effect of energy density and scanning strategy on densification, microstructure and mechanical properties of 316L stainless steel processed via selective laser melting," *Materials Science and Engineering: A*, vol. 770, p. 138455, 2020.

[169] T. Kurzynowski, K. Gruber, W. Stopyra, B. Kuźnicka, and E. Chlebus, "Correlation between process parameters, microstructure and properties of 316 L stainless steel processed by selective laser melting," *Materials Science and Engineering: A*, vol. 718, pp. 64–73, 2018.

[170] T. Zhong, K. He, H. Li, and L. Yang, "Mechanical properties of lightweight 316L stainless steel lattice structures fabricated by selective laser melting," *Materials & Design*, vol. 181, p. 108076, 2019.

[171] C. Yan, L. Hao, A. Hussein, P. Young, and D. Raymont, "Advanced lightweight 316L stainless steel cellular lattice structures fabricated via selective laser melting," *Materials & Design*, vol. 55, pp. 533–541, 2014.

[172] P. Li, "Constitutive and failure behaviour in selective laser melted stainless steel for microlattice structures," *Materials Science and Engineering: A*, vol. 622, pp. 114–120, 2015.

[173] L. Liu, P. Kamm, F. García-Moreno, J. Banhart, and D. Pasini, "Elastic and failure response of imperfect three-dimensional metallic lattices: the role of geometric defects induced by Selective Laser Melting," *Journal of the Mechanics and Physics of Solids*, vol. 107, pp. 160–184, 2017.

[174] H. Lei, C. Li, J. Meng, H. Zhou, Y. Liu, X. Zhang, P. Wang, and D. Fang, "Evaluation of compressive properties of SLM-fabricated multi-layer lattice structures by experimental test and μ-ct-based finite element analysis," *Materials & Design*, vol. 169, p. 107685, 2019.

[175] P. Koehnen, C. Haase, J. Bueltmann, S. Ziegler, J. H. Schleifenbaum, and W. Bleck, "Mechanical properties and deformation behavior of additively manufactured lattice structures of stainless steel," *Materials & Design*, vol. 145, pp. 205–217, 2018.

[176] Z. Xiao, Y. Yang, R. Xiao, Y. Bai, C. Song, and D. Wang, "Evaluation of topology-optimized lattice structures manufactured via selective laser melting," *Materials & Design*, vol. 143, pp. 27–37, 2018.

[177] C. Yan, L. Hao, A. Hussein, and D. Raymont, "Evaluations of cellular lattice structures manufactured using selective laser melting," *International Journal of Machine Tools and Manufacture*, vol. 62, pp. 32–38, 2012.

[178] P. Płatek, J. Sienkiewicz, J. Janiszewski, and F. Jiang, "Investigations on mechanical properties of lattice structures with different values of relative density made from 316L by Selective Laser Melting (SLM)," *Materials*, vol. 13, no. 9, p. 2204, 2020.

[179] X. Cao, S. Duan, J. Liang, W. Wen, and D. Fang, "Mechanical properties of an improved 3D-printed rhombic dodecahedron stainless steel lattice structure of variable cross section," *International Journal of Mechanical Sciences*, vol. 145, pp. 53–63, 2018.

[180] A. Röttger, J. Boes, W. Theisen, M. Thiele, C. Esen, A. Edelmann, and R. Hellmann, "Microstructure and mechanical properties of 316L austenitic stainless steel processed by different SLM devices," *The International Journal of Advanced Manufacturing Technology*, vol. 108, pp. 769–783, 2020.

[181] R. Gümrük, R. Mines, and S. Karadeniz, "Determination of strain rate sensitivity of micro-struts manufactured using the selective laser melting method," *Journal of Materials Engineering and Performance*, vol. 27, no. 3, pp. 1016–1032, 2018.

[182] X. Wang, J. A. Muniz-Lerma, O. Sánchez-Mata, M. A. Shandiz, and M. Brochu, "Microstructure and mechanical properties of stainless steel 316L vertical struts manufactured by laser powder bed fusion process," *Materials Science and Engineering: A*, vol. 736, pp. 27–40, 2018.

[183] S. Tsopanos, R. Mines, S. McKown, Y. Shen, W. Cantwell, W. Brooks, and C. Sutcliffe, "The influence of processing parameters on the mechanical properties of selectively laser melted stainless steel microlattice structures," *Journal of Manufacturing Science and Engineering*, vol. 132, no. 4, 2010.

[184] Y. Shen, S. McKown, S. Tsopanos, C. Sutcliffe, R. Mines, and W. Cantwell, "The mechanical properties of sandwich structures based on metal lattice architectures," *Journal of Sandwich Structures & Materials*, vol. 12, no. 2, pp. 159–180, 2010.

[185] J. Bültmann, S. Merkt, C. Hammer, C. Hinke, and U. Prahl, "Scalability of the mechanical properties of selective laser melting produced micro-struts," *Journal of Laser Applications*, vol. 27, no. S2, p. S29206, 2015.

[186] P. Li, Z. Wang, N. Petrinic, and C. Siviour, "Deformation behaviour of stainless steel microlattice structures by selective laser melting," *Materials Science and Engineering: A*, vol. 614, pp. 116–121, 2014.

[187] E. Abele, H. A. Stoffregen, M. Kniepkamp, S. Lang, and M. Hampe, "Selective laser melting for manufacturing of thin-walled porous elements," *Journal of Materials Processing Technology*, vol. 215, pp. 114–122, 2015.

[188] U. Hossain, S. Ghouse, K. Nai, and J. Jeffers, "Mechanical and morphological properties of additively manufactured SS316L and Ti6Al4V micro-struts as a function of build angle," *Additive Manufacturing*, p. 102050, 2021.

[189] Z. Wang and P. Li, "Characterisation and constitutive model of tensile properties of selective laser melted Ti-6Al-4V struts for microlattice structures," *Materials Science and Engineering: A*, vol. 725, pp. 350–358, 2018.

[190] D. J. Whitehouse, *Surfaces and their Measurement.* CRC Press, 2002.

[191] J. Hollomon, "Time-temperature relations in tempering steel," *Trans. AIME*, vol. 162, pp. 223–249, 1945.

[192] EOS GmbH - Electro Optical Systems, *EOS StainlessSteel 316L - Material data sheet.* EOS GmbH, Robert-Stirling-Ring 1, D-82152 Krailling/München, Germany, 2019.

[193] G. Mohr, S. J. Altenburg, and K. Hilgenberg, "Effects of inter layer time and build height on resulting properties of 316L stainless steel processed by laser powder bed fusion," *Additive Manufacturing*, vol. 32, p. 101080, 2020.

[194] A. E. Wilson-Heid, S. Qin, and A. M. Beese, "Multiaxial plasticity and fracture behavior of stainless steel 316L by laser powder bed fusion: Experiments and computational modeling," *Acta Materialia*, vol. 199, pp. 578–592, 2020.

[195] S. Messina, C. Dong, G. Balbus, J. Shin, T. Pollock, D. Gianola, and M. Begley, "The impact of geometry and microstructure on the failure of milli-meter scale EBM Ti-6Al-4V struts," *In Preparation*, 2021.

[196] N. Vanderesse, A. Richter, N. Nuño, and P. Bocher, “Measurement of deformation heterogeneities in additive manufactured lattice materials by digital image correlation: strain maps analysis and reliability assessment,” *Journal of the mechanical behavior of biomedical materials*, vol. 86, pp. 397–408, 2018.

[197] F. J. Q. González and N. Nuno, “Finite element modeling of manufacturing irregularities of porous materials,” *Biomater. Biomech. Bioeng*, vol. 3, no. 1, pp. 1–14, 2016.

[198] G. Pyka, G. Kerckhofs, I. Papantoniou, M. Speirs, J. Schrooten, and M. Wevers, “Surface roughness and morphology customization of additive manufactured open porous Ti6Al4V structures,” *Materials*, vol. 6, no. 10, pp. 4737–4757, 2013.

[199] I. Koutiri, E. Pessard, P. Peyre, O. Amlou, and T. De Terris, “Influence of SLM process parameters on the surface finish, porosity rate and fatigue behavior of as-built Inconel 625 parts,” *Journal of Materials Processing Technology*, vol. 255, pp. 536–546, 2018.

[200] C. Dong, A. Samuel, L. Kuettner, B. Patterson, C. Montgomery, C. Britt, F. Zok, A. Beese, J. Carpenter, and M. Begley, “Influence of energy density on effective properties of SLM stainless steel 316L thin strut intersections (nodes),” *Submitted to Additive Manufacturing*, 2021.

[201] B. Gorny, T. Niendorf, J. Lackmann, M. Thoene, T. Troester, and H. Maier, “In situ characterization of the deformation and failure behavior of non-stochastic porous structures processed by selective laser melting,” *Materials Science and Engineering: A*, vol. 528, no. 27, pp. 7962–7967, 2011.

[202] Q. Feng, Q. Tang, Y. Liu, R. Setchi, S. Soe, S. Ma, and L. Bai, “Quasi-static analysis of mechanical properties of Ti6Al4V lattice structures manufactured using selective laser melting,” *The International Journal of Advanced Manufacturing Technology*, vol. 94, no. 5, pp. 2301–2313, 2018.

[203] T. Tancogne-Dejean, A. B. Spierings, and D. Mohr, “Additively-manufactured metallic micro-lattice materials for high specific energy absorption under static and dynamic loading,” *Acta Materialia*, vol. 116, pp. 14–28, 2016.

[204] M. Mazur, M. Leary, S. Sun, M. Vcelka, D. Shidid, and M. Brandt, “Deformation and failure behaviour of Ti-6Al-4V lattice structures manufactured by selective laser melting (SLM),” *The International Journal of Advanced Manufacturing Technology*, vol. 84, no. 5, pp. 1391–1411, 2016.

[205] T. Yu, H. Hyer, Y. Sohn, Y. Bai, and D. Wu, “Structure-property relationship in high strength and lightweight AlSi10Mg microlattices fabricated by selective laser melting,” *Materials & Design*, vol. 182, p. 108062, 2019.

[206] A. Ferrigno, F. Di Caprio, R. Borrelli, F. Auricchio, and A. Vigliotti, “The mechanical strength of Ti-6Al-4V columns with regular octet microstructure manufactured by electron beam melting,” *Materialia*, vol. 5, p. 100232, 2019.

[207] G. Campoli, M. Borleffs, S. A. Yavari, R. Wauthle, H. Weinans, and A. A. Zadpoor, “Mechanical properties of open-cell metallic biomaterials manufactured using additive manufacturing,” *Materials & Design*, vol. 49, pp. 957–965, 2013.

[208] S. A. Yavari, S. Ahmadi, R. Wauthle, B. Pouran, J. Schrooten, H. Weinans, and A. Zadpoor, “Relationship between unit cell type and porosity and the fatigue behavior of selective laser melted meta-biomaterials,” *Journal of the mechanical behavior of biomedical materials*, vol. 43, pp. 91–100, 2015.

[209] M. A. Sutton, J. J. Orteu, and H. Schreier, *Image correlation for shape, motion and deformation measurements: basic concepts, theory and applications.* Springer Science & Business Media, 2009.

[210] C. Tang, J. Liu, Y. Yang, Y. Liu, S. Jiang, and W. Hao, “Effect of process parameters on mechanical properties of 3d printed PLA lattice structures,” *Composites Part C: Open Access*, vol. 3, p. 100076, 2020.

[211] L. Xiao and W. Song, “Additively-manufactured functionally graded Ti-6Al-4V lattice structures with high strength under static and dynamic loading: Experiments,” *International Journal of Impact Engineering*, vol. 111, pp. 255–272, 2018.

[212] M.-W. Wu, J.-K. Chen, B.-H. Lin, P.-H. Chiang, and M.-K. Tsai, “Compressive fatigue properties of additive-manufactured Ti-6Al-4V cellular material with different porosities,” *Materials Science and Engineering: A*, vol. 790, p. 139695, 2020.

[213] F. Brenne, T. Niendorf, and H. Maier, “Additively manufactured cellular structures: Impact of microstructure and local strains on the monotonic and cyclic behavior under uniaxial and bending load,” *Journal of Materials Processing Technology*, vol. 213, no. 9, pp. 1558–1564, 2013.

[214] R. Goodall, E. Hernandez-Nava, S. N. Jenkins, L. Sinclair, E. Tyrwhitt-Jones, M. A. Khodadadi, D. H. Ip, and H. Ghadbeigi, “The effects of defects and damage in the mechanical behavior of Ti6Al4V lattices,” *Frontiers in Materials*, vol. 6, p. 117, 2019.

[215] N. Soro, N. Saintier, J. Merzeau, M. Veidt, and M. S. Dargusch, “Quasi-static and fatigue properties of graded Ti–6Al–4V lattices produced by Laser Powder Bed Fusion (LPBF),” *Additive Manufacturing*, vol. 37, p. 101653, 2021.

[216] L. Huynh, J. Rotella, and M. D. Sangid, “Fatigue behavior of IN718 microtrusses produced via additive manufacturing,” *Materials & Design*, vol. 105, pp. 278–289, 2016.

[217] J. Song, Y. Wang, W. Zhou, R. Fan, B. Yu, Y. Lu, and L. Li, "Topology optimization-guided lattice composites and their mechanical characterizations," *Composites Part B: Engineering*, vol. 160, pp. 402–411, 2019.

[218] M. A. Sutton, J. H. Yan, V. Tiwari, H. Schreier, and J.-J. Orteu, "The effect of out-of-plane motion on 2D and 3D digital image correlation measurements," *Optics and Lasers in Engineering*, vol. 46, no. 10, pp. 746–757, 2008.

[219] W. Radlof, C. Benz, and M. Sander, "Numerical and experimental investigations of additively manufactured lattice structures under quasi-static compression loading," *Material Design & Processing Communications*, vol. 3, no. 3, p. e164, 2021.

[220] W.-M. Chen, Y. M. Xie, G. Imbalzano, J. Shen, S. Xu, S.-J. Lee, and P. V. S. Lee, "Lattice Ti structures with low rigidity but compatible mechanical strength: Design of implant materials for trabecular bone," *International Journal of Precision Engineering and Manufacturing*, vol. 17, no. 6, pp. 793–799, 2016.

[221] F. Brenne and T. Niendorf, "Load distribution and damage evolution in bending and stretch dominated Ti-6Al-4V cellular structures processed by selective laser melting," *International Journal of Fatigue*, vol. 121, pp. 219–228, 2019.

[222] L. Boniotti, S. Foletti, S. Beretta, and L. Patriarca, "Analysis of strain and stress concentrations in micro-lattice structures manufactured by SLM," *Rapid Prototyping Journal*, 2019.

[223] C. Dong, A. Samuel, M. Leary, F. Zok, J. Miller, and M. Begley, "Strain maps and failure analysis of SLM Ti-6Al-4V lattices measured by in situ DIC on a primitive scale," *Manuscript in preparation*, 2021.

[224] S. Van Bael, Y. C. Chai, S. Truscello, M. Moesen, G. Kerckhofs, H. Van Oosterwyck, J.-P. Kruth, and J. Schrooten, "The effect of pore geometry on the in vitro biological behavior of human periosteum-derived cells seeded on selective laser-melted Ti6Al4V bone scaffolds," *Acta biomaterialia*, vol. 8, no. 7, pp. 2824–2834, 2012.

[225] J. C. Maxwell, "On the calculation of the equilibrium and stiffness of frames," *The London, Edinburgh, and Dublin Philosophical Magazine and Journal of Science*, vol. 27, no. 182, pp. 294–299, 1864.

[226] R. M. Latture, R. X. Rodriguez, L. R. Holmes Jr, and F. W. Zok, "Effects of nodal fillets and external boundaries on compressive response of an octet truss," *Acta Materialia*, vol. 149, pp. 78–87, 2018.

[227] N. A. Fleck and X. Qiu, "The damage tolerance of elastic–brittle, two-dimensional isotropic lattices," *Journal of the Mechanics and Physics of Solids*, vol. 55, no. 3, pp. 562–588, 2007.

[228] M. C. Messner, "Optimal lattice-structured materials," *Journal of the Mechanics and Physics of Solids*, vol. 96, pp. 162–183, 2016.

[229] R. M. Latture, M. R. Begley, and F. W. Zok, "Design and mechanical properties of elastically isotropic trusses," *Journal of Materials Research*, vol. 33, no. 3, pp. 249–263, 2018.

[230] A. Ataee, Y. Li, D. Fraser, G. Song, and C. Wen, "Anisotropic Ti-6Al-4V gyroid scaffolds manufactured by electron beam melting (EBM) for bone implant applications," *Materials & Design*, vol. 137, pp. 345–354, 2018.

[231] E. Sallica-Leva, A. Jardini, and J. Fogagnolo, "Microstructure and mechanical behavior of porous Ti–6Al–4V parts obtained by selective laser melting," *Journal of the mechanical behavior of biomedical materials*, vol. 26, pp. 98–108, 2013.

[232] V. Weißmann, P. Drescher, R. Bader, H. Seitz, H. Hansmann, and N. Laufer, "Comparison of single Ti6Al4V struts made using selective laser melting and electron beam melting subject to part orientation," *Metals*, vol. 7, no. 3, p. 91, 2017.

[233] G. Kasperovich and J. Hausmann, "Improvement of fatigue resistance and ductility of TiAl6V4 processed by selective laser melting," *Journal of Materials Processing Technology*, vol. 220, pp. 202–214, 2015.

[234] B. Song, S. Dong, B. Zhang, H. Liao, and C. Coddet, "Effects of processing parameters on microstructure and mechanical property of selective laser melted Ti6Al4V," *Materials & Design*, vol. 35, pp. 120–125, 2012.

[235] A. Ataee, Y. Li, M. Brandt, and C. Wen, "Ultrahigh-strength titanium gyroid scaffolds manufactured by selective laser melting (SLM) for bone implant applications," *Acta Materialia*, vol. 158, pp. 354–368, 2018.

[236] W. Zhang, P. Qin, Z. Wang, C. Yang, L. Kollo, D. Grzesiak, and K. G. Prashanth, "Superior wear resistance in EBM-Processed TC4 alloy compared with SLM and forged samples," *Materials*, vol. 12, no. 5, p. 782, 2019.

[237] M. Neikter, P. Åkerfeldt, R. Pederson, M.-L. Antti, and V. Sandell, "Microstructural characterization and comparison of Ti-6Al-4V manufactured with different additive manufacturing processes," *Materials Characterization*, vol. 143, pp. 68–75, 2018.

[238] W. Q. Toh, P. Wang, X. Tan, M. L. S. Nai, E. Liu, and S. B. Tor, "Microstructure and wear properties of electron beam melted Ti-6Al-4V parts: A comparison study against as-cast form," *Metals*, vol. 6, no. 11, p. 284, 2016.

[239] P. Wang, X. Tan, M. L. S. Nai, S. B. Tor, and J. Wei, "Spatial and geometrical-based characterization of microstructure and microhardness for an electron beam melted Ti–6Al–4V component," *Materials & Design*, vol. 95, pp. 287–295, 2016.

[240] J. Wang, Q. Sun, H. Wang, J. Liu, and J. Feng, "Effect of location on microstructure and mechanical properties of additive layer manufactured Inconel 625 using gas tungsten arc welding," *Materials Science and Engineering: A*, vol. 676, pp. 395–405, 2016.

[241] A. Ataee, Y. Li, and C. Wen, "A comparative study on the nanoindentation behavior, wear resistance and in vitro biocompatibility of SLM manufactured CP–Ti and EBM manufactured Ti64 gyroid scaffolds," *Acta biomaterialia*, vol. 97, pp. 587–596, 2019.

[242] C. Li, Z. Liu, X. Fang, and Y. Guo, "Residual stress in metal additive manufacturing," *Procedia Cirp*, vol. 71, pp. 348–353, 2018.

[243] Y. Choi and D.-G. Lee, "Correlation between surface tension and fatigue properties of Ti-6Al-4V alloy fabricated by EBM additive manufacturing," *Applied Surface Science*, vol. 481, pp. 741–746, 2019.

[244] S. Özerinç, B. Kaygusuz, M. Kaş, A. Motallebzadeh, Ş. Nesli, Ö. Duygulu, and O. Yilmaz, "Micromechanical characterization of additively manufactured Ti-6Al-4V parts produced by electron beam melting," *JOM*, vol. 73, no. 10, pp. 3021–3033, 2021.

[245] M. Todai, T. Nakano, T. Liu, H. Y. Yasuda, K. Hagihara, K. Cho, M. Ueda, and M. Takeyama, "Effect of building direction on the microstructure and tensile properties of Ti-48Al-2Cr-2Nb alloy additively manufactured by electron beam melting," *Additive Manufacturing*, vol. 13, pp. 61–70, 2017.

[246] N. M. Everitt, N. T. Aboulkhair, I. Maskery, C. Tuck, and I. Ashcroft, "Nanoindentation shows uniform local mechanical properties across melt pools and layers produced by selective laser melting of AlSi10Mg alloy," *Advanced Materials Letters*, vol. 7, no. 1, 2016.

[247] A. Reichardt, R. P. Dillon, J. P. Borgonia, A. A. Shapiro, B. W. McEnerney, T. Momose, and P. Hosemann, "Development and characterization of Ti-6Al-4V to 304L stainless steel gradient components fabricated with laser deposition additive manufacturing," *Materials & Design*, vol. 104, pp. 404–413, 2016.

[248] C. Han, Y. Li, Q. Wang, D. Cai, Q. Wei, L. Yang, S. Wen, J. Liu, and Y. Shi, "Titanium/hydroxyapatite (Ti/HA) gradient materials with quasi-continuous ratios fabricated by SLM: material interface and fracture toughness," *Materials & Design*, vol. 141, pp. 256–266, 2018.